**This document is downloaded from DR-NTU (https://dr.ntu.edu.sg)
Nanyang Technological University, Singapore.**

Effects of interfacial reactions and electromigration on the Cu/electroless Ni-P/Sn-3.5Ag solder joint strength

Aditya Kumar

2007

Aditya, K. (2007). Effects of interfacial reactions and electromigration on the Cu/electroless Ni-P/Sn-3.5Ag solder joint strength. Doctoral thesis, Nanyang Technological University, Singapore.

https://hdl.handle.net/10356/5119

https://doi.org/10.32657/10356/5119

Nanyang Technological University

Downloaded on 04 Apr 2024 20:52:47 SGT

NANYANG
TECHNOLOGICAL
UNIVERSITY

EFFECTS OF INTERFACIAL REACTIONS AND ELECTROMIGRATION ON THE CU/ELECTROLESS NI-P/SN-3.5AG SOLDER JOINT STRENGTH

ADITYA KUMAR

SCHOOL OF MATERIALS SCIENCE & ENGINEERING

2007

Effects of Interfacial Reactions and Electromigration on the Cu/Electroless Ni-P/Sn-3.5Ag Solder Joint Strength

Aditya Kumar

School of Materials Science & Engineering

A thesis submitted to the Nanyang Technological University
in fulfilment of the requirement for the degree of
Doctor of Philosophy

2007

Acknowledgments

I would like to take this opportunity to acknowledge the guidance, support, and assistance received during this work.

First of all, I sincerely express my great gratitude to my supervisor, Dr. Chen Zhong, for his invaluable guidance, advice, and encouragement throughout the course of this study. I would also like to thank my co-supervisor, Dr. V. Kripesh (IME). Without their supervision and constant support, this work could not be possible.

Next, I thank Prof. A. Gusak (CSU, Ukraine) and Prof. K. N. Tu (UCLA, US) for their sound advice. I would also like to thank Dr. C. C. Wong and Dr. S. Mhaisalkar, for their constant support and advice.

I am thankful to all of my colleagues in the School of Materials Science and Engineering, Nanyang Technological University, for their friendship and inspiration. In particular, I thank Dr. K. S. Ramakanth for reviewing my papers and his invaluable suggestions. I am also thankful to the technical staff: Mr. Eric, Ms. Fen, Ms. Fiona, Mr. Goo Jon, Ms. Jing Li, Ms. Irene, Ms. Mastura, Mr. Patrick, Mr. Pay, Mr. Sin, Mr. Thomas, Ms. Tay, and Ms. Yenni, for their great assistance.

I express my deepest gratitude to my parents and sisters for their great love and support at every moment of my life. I am also grateful to my wife, Ity Singh, for her love and patience. Finally, I close by thanking God for getting me through this phase of life.

Table of Contents

Acknowledgements ······ i

Table of Contents ······ ii

Abstract ······ ix

List of Figures ······ xi

List of Tables ······ xx

List of Abbreviations ······ xxii

Chapter 1. Introduction

1.1 Background and Motivation ······ 1

1.2 Objectives ······ 5

1.2.1 Study of Cu/Electroless Ni-P/Sn-3.5Ag Interfacial Reactions and their Effect on Solder Joint Strength ······ 7

1.2.2 Investigation of Influence of Ni-P Thickness on Cu/Electroless Ni-P/Sn-3.5Ag Interfacial Reactions and Solder Joint Strength ······ 7

1.2.3 Investigation of Effect of P Concentration on Cu/Electroless Ni-P/Sn-3.5Ag Interfacial Microstructure and Solder Joint Strength ······ 8

1.2.4 Development of a Mathematical Model for the Growth of Ni_3P and Ni_3Sn_4 Compounds ······ 8

1.2.5 Study of Effect of Electromigration on the Interfacial Microstructure and Mechanical Properties of UBM/Solder Joints ······ 8

1.3 Organization of the Thesis ········· 9

Chapter 2. Literature Review

2.1 Interfacial Reactions between Electroless Ni-P and Sn-bearing Solder ········· 10

2.1.1 Morphology of Intermetallic Compound ········· 14

2.1.2 Growth Kinetics of Intermetallic Compound ········· 15

2.1.3 Other Phenomena Associated with Interfacial Reactions ········· 17

2.1.4 Interfacial Elemental Diffusion and Reaction Mechanism ········· 20

2.1.5 Kirkendall Void Formation at the Electroless Ni-P/Solder Interface ········· 23

2.2 Mechanical Properties of Ni-P/Solder Joints ········· 24

2.2.1 Mechanical Testing of Electroless Ni-P/Solder Joints ········· 28

2.2.2 Factors Causing the Brittle Failure of Ni-P/Solder Joints ········· 31

2.3 Electromigration ········· 33

2.4 Electromigration Effect in Solder Joint ········· 41

2.4.1 Electromigration-Induced Electrical Failure of Solder Joint ········· 41

2.4.2 Electromigration-Induced UBM/Solder Interfacial Reactions ········· 42

2.4.3 Effect of Electric Current on the Mechanical Behavior of Solder Joints ········· 44

2.5 Summary and Remarks ········· 44

Chapter 3. Cu/Electroless Ni-P/Sn-3.5Ag Interfacial Reactions and their Effect on Solder Joint Strength

3.1 Introduction ··· 47

3.2 Experimental Procedures ··· 48

3.2.1 Preparation of Test Samples ··· 48

3.2.2 Thermal Aging of Test Samples ··· 49

3.2.3 Tensile Testing of Test Samples ··· 50

3.2.4 Microstructural Observations ··· 50

3.3 Results ··· 50

3.3.1 Interfacial Microstructure Analysis ··· 50

3.3.2 Growth of Interfacial Compounds ··· 55

3.3.3 Growth Kinetics of Interfacial Compounds ··· 57

3.3.4 Tensile Strength and Failure Modes ··· 62

3.3.5 Fracture Analysis ··· 63

3.4 Discussion ··· 68

3.4.1 Reaction between Sn and Ni_3P forming Ni-Sn-P Layer ··· 68

3.4.2 Elemental Diffusion and Kirkendall Void Formation in Ni-P Layer ··· 70

3.4.3 Thermodynamics and Kinetics of Interfacial Compound Formation ··· 73

3.4.4 Transition of Ni-Sn-P Growth Kinetics ··· 77

3.4.5 Growth Mechanism of Interfacial Compounds ··· 78

3.4.6 Transition of Ni_3Sn_4 Morphology ··· 79

3.4.7 Diffusion of Cu through Ni-P Layer ······81

3.4.8 Factors Affecting the Mechanical Properties of Solder Joint ······83

3.5 Conclusions ······87

Chapter 4. Influence of Ni-P Thickness on Cu/Electroless Ni-P/Sn-3.5Ag Interfacial Reactions and Solder Joint Strength

4.1 Introduction ······90

4.2 Experimental Procedures ······90

4.3 Results ······91

4.3.1 Interfacial Microstructure Analysis ······91

4.3.2 Tensile Strength and Fracture Analysis ······97

4.4 Discussion ······104

4.4.1 Growth Mechanism of Ni-Cu-Sn and Cu-Sn IMCs ······104

4.4.2 Effect of Ni-P Thickness on the Mechanical Strength of Solder Joint ······106

4.5 Conclusions ······109

Chapter 5. Influence of P Concentration on Cu/Electroless Ni-P/Sn-3.5Ag Interfacial Microstructure and Solder Joint Strength

5.1 Introduction ······111

5.2 Experimental Procedures ······112

5.3 Results and Discussion ······112

5.3.1 Influence of P Concentration on Interfacial Microstructure ······112

5.3.2 Influence of P Concentration on Mechanical Properties ··························· 118

5.4 Conclusions ··························· 123

Chapter 6. Mathematical Model for the Growth of Ni_3P and Ni_3Sn_4 Compounds

6.1 Introduction ··························· 125

6.2 Derivation of Growth Model ··························· 126

6.3 Comparison with Experimental Results ··························· 133

6.3.1 Growth Kinetics of Ni_3P and Ni_3Sn_4 Compounds ··························· 133

6.3.2 Influence of P Concentration on the Growth of Ni_3P and Ni_3Sn_4 ··························· 134

6.4 Conclusions ··························· 137

Chapter 7. Effect of Electromigration on the Interfacial Microstructure and Mechanical Properties of UBM/Solder Joints

7.1. Introduction ··························· 138

7.2. Experimental Procedures ··························· 139

7.2.1 Preparation of Test Samples ··························· 139

7.2.2 Thermal Aging and Electrical Stressing of Test Samples ··························· 139

7.2.3 Mechanical Testing of Test Samples ··························· 141

7.2.4 Microstructural Observations ··························· 141

7.3. Results ··························· 141

7.3.1. Tensile Strength of UBM/Solder Joints ··························· 141

7.3.2. Fracture Energy of UBM/Solder Joints ···· 142

7.3.3. Fracture Analysis ···· 145

7.3.4. Nano-indentation Test ···· 150

7.3.5. Microstructural Analysis ···· 152

7.3.6. Growth of Ni_3Sn_4 IMC ···· 156

7.4. Discussion ···· 158

7.4.1. Electromigration-Induced Brittle Failure of Solder Joints ···· 158

7.4.2. Effect of Electromigration on Ni_3Sn_4 Growth ···· 160

7.5. Conclusions ···· 162

Chapter 8. Conclusions and Recommendations

8.1 Conclusions ···· 164

8.2 Recommendations for Future Work ···· 166

References ···· 167

List of Publications ···· 182

Appendix A. Typical Load-Extension Curves ···· 184

Appendix B. Quantitative EDS Analysis ···· 186

B.1 ZAF Factors in X-Ray Microanalysis ···· 187

B.2 Procedure for ZAF Matrix Correction ···· 189

B.3 Quantitative EDS Analysis using Standard ZAF Correction Method ···· 190

B.3.1 Experimental Procedures for Standard ZAF Correction Method……………190

B.3.2 Quantitative EDS Analyses of Compounds Observed in Present Study ….193

B.3.3 Comparison between the Results from Standard and Standardless ZAF Correction Methods……………………………………………………………………196

Abstract

In this work, the effects of interfacial reactions and electromigration on the mechanical properties of Cu/electroless Ni-P/Sn-3.5Ag solder joint were investigated. The effects of interfacial reactions were investigated for different aging temperatures, Ni-P layer thicknesses, and P concentrations of Ni-P layer. The aging results showed that during interfacial reactions, Ni_3Sn_4 intermetallic compound (IMC) grows at the Ni-P/Sn-3.5Ag interface, along with the transformation of Ni-P layer into the Ni_3P compound. A ternary Ni-Sn-P compound also grew in between the Ni_3Sn_4 and Ni_3P due to the reaction of Sn with Ni_3P. The Ni-Sn-P grew slowly as long as the Ni-P layer was present at the reaction interface; however, after its complete transformation into Ni_3P, Ni-Sn-P grew rapidly in conjunction with Cu depletion from the Cu surface. Initially, Ni_3Sn_4, Ni-Sn-P, and Ni_3P followed $t^{1/3}$ growth kinetics; however, after the complete transformation of Ni-P layer, the Ni-Sn-P followed linear growth kinetics. The activation energy for the growth of Ni_3Sn_4, Ni-Sn-P, and Ni_3P was found to be 98.9, 42.2, and 94.3 kJ/mol, respectively. Interfacial reactions were found to degrade solder joint strength due to the extensive growth of Ni_3Sn_4 and depletion of Cu from the Cu surface. The Cu depletion resulted in the formation of a layer of Kirkendall voids at the Ni_3P/Cu interface and thereby resulted in the loss of adhesion between the Ni_3P and Cu surface.

The Ni-P layer thickness was found to influence the Cu/Ni-P/Sn-3.5Ag interfacial reactions and solder joint strength. Several additional IMCs such as Cu_3Sn, Cu_6Sn_5, and $(Ni_{1-x}Cu_x)_6Sn_5$ grew in the thin (3.9 μm) Ni-P sample as compared to the thicker Ni-P (7.3 and 9.9 μm) samples. In the thin Ni-P sample, brittle failure at the interface between IMCs occurred at a lower aging temperature and within a shorter aging duration than that in the thicker Ni-P samples. The complete transformation of the Ni-P layer into Ni_3P and Ni-Sn-P compounds was found to be the main cause for the growth of additional IMCs and brittle failure. Across the Ni_3P and Ni-Sn-P, diffusion of Cu and Sn took place, which resulted in the formation of additional IMCs and a layer of Kirkendall voids.

The P concentration of Ni-P layer was found to affect the Cu/Ni-P/Sn-3.5Ag interfacial microstructure as well as the solder joint strength after multiple reflows. The low P (6.1 wt.%) samples exhibited the highest joint strength after multiple reflows, while the strengths of medium P (8.8 wt.%) and high P (12.3 wt.%) samples decreased more rapidly. Microstructural analysis revealed that the Ni_3Sn_4 IMC particles formed in the low P sample adhere to the reaction interface, whereas most of the Ni_3Sn_4 IMC particles formed in the medium and high P samples spall into the molten solder. The spallation of Ni_3Sn_4 IMC speeded up the consumption of Ni-P layer, leading to the extensive formation of Cu-Sn and Ni-Cu-Sn IMCs and Kirkendall voids. The greater reduction of the strength of medium and high P samples was found to be due to the larger amounts of Cu-Sn IMCs, Ni-Cu-Sn IMCs, and voids formed between the solder and Cu substrate.

A mathematical model that describes Ni_3P and Ni_3Sn_4 growth was developed. This model explained various experimental findings such as the variation in Ni_3P and Ni_3Sn_4 growth kinetics and the influence of P concentration on their growth very well. The model revealed that Ni_3P and Ni_3Sn_4 growth kinetics could vary from $t^{1/2}$ to $t^{1/(2+m)}$ $(m > 0)$ due to the lateral growth of Ni_3P grain. The P concentration of Ni-P layer was found to be a crucial factor that affects Ni_3Sn_4 and Ni_3P growth.

The effect of electromigration on the mechanical properties of three different solder joints, Ni-P/Sn-3.5Ag, Ni/Sn-3.5Ag, and Ni-P/Sn-37Pb, was investigated. It was found that electromigration causes the brittle failure of the solder joint and the tendency of brittle failure increases with current density. In most of the electrically stressed samples, fracture occurred at the brittle solder/IMC interface rather than inside the ductile solder. Microstructural analysis revealed that electromigration influences the growth of Ni_3Sn_4 IMC and Sn-37Pb grain coarsening. The electromigration-induced Ni_3Sn_4 growth was found to depend upon the metallization. This effect was more prominent in the Ni samples than in the Ni-P samples.

List of Figures

Fig. 1.1. Schematic of typical (a) solder flip chip package and (b) solder interconnect…..3

Fig. 2.1. The equilibrium phase diagram of Ni-Sn binary alloy……………..…...……...11

Fig. 2.2. The equilibrium phase diagram of Ni-P binary alloy ……..………..…...……...12

Fig. 2.3. Schematic illustration of an electronic package (a) with zero strain and (b) with thermal load, showing the generation of shear and tensile stresses in the solder joints between chip and substrate……………………………………..……………………25

Fig. 2.4. Drift of four aluminium stripes of various lengths annealed at 350°C in the presence of current of 3.7 ×10^5 A/cm^2 density for 15 h ……….……………..……..….36

Fig. 2.5. TTF as a function of current stress for different samples for a criterion of ΔR/R = 100 %: (a) at 300°C and (b) at different temperatures…………….……...……. ………..38

Fig. 3.1. Schematic of metallization layout on the Cu plate………………..…….………48

Fig. 3.2. Schematic illustration of joining the Ni-P coated Cu plates…………….…..……49

Fig. 3.3. Schematic diagram of test sample..……...………………………...……...……49

Fig. 3.4. (a) Cross-sectional and (b) top views of compounds formed at the Sn-3.5Ag/electroless Ni-P interface of as-prepared sample…………...…..……...………51

Fig. 3.5. Back-scattered SEM images showing the growth of Ni_3Sn_4, Ni-Sn-P, and Ni_3P compounds at the Sn-3.5Ag/electroless Ni-P/Cu interfaces of the samples aged for 225 h at temperatures of (a) 140°C, (b) 160°C, (c) 180°C, and (d) 200°C………….…………...53

Fig. 3.6. Top view of Ni_3Sn_4 IMC in the samples aged for 225 h at temperatures of (a) 140°C, (b) 160°C, (c) 180°C, and (d) 200°C………………..………....…………….………..54

Fig. 3.7. Line-scanned SEM images of the Cu/electroless Ni-P/Sn-3.5Ag interfaces in the samples aged at 200 °C for (a) 48 h, (b) 100 h, (c) 225 h, and (d) 400 h ………...……55

Fig. 3.8. Thickness of Ni_3Sn_4, Ni-Sn-P, and Ni_3P compounds as a function of aging time at temperatures of (a) 140°C, (b) 160°C, (c) 180°C, and (d) 200°C………….………….....…..57

Fig. 3.9. Ln-ln plot of increment in compound thickness versus aging time at various temperatures for (a) Ni_3Sn_4, (b) Ni-Sn-P, and (c) Ni_3P……………..….………..…..……59

Fig. 3.10. Arrhenius plot of (a) Ni_3Sn_4, (b) Ni-Sn-P, and (c) Ni_3P compounds growth used to estimate apparent activation energy……………………………………….…………..…..61

Fig. 3.11. Tensile strength of Cu/electroless Ni-P/Sn-3.5Ag solder joint as a function of aging duration at various temperatures…………………………………….….….………62

Fig. 3.12. Typical curves of tensile strength versus extension associated with different types of the failures of solder joint…………………………………………………..…………..63

Fig. 3.13. (a) Fracture path and (b) fracture surface of the as-prepared sample...….…...……64

Fig. 3.14. Fracture surfaces of the samples aged for 400 h at temperature of (a) 160°C (one side), (b) 160°C (other side), (c) 180°C (one side), (d) 180°C (other side), (e) 200°C (one side), and (f) 200°C (other side)……………..…………………………….….….………..65

Fig. 3.15. Fracture surfaces of the solder joint aged at 180°C for 48 h showing mixed failure at the interface between (a) Ni_3Sn_4 and (b) solder……………………..………...…….66

Fig. 3.16. Cross-sectional SEM image showing fracture at the solder/Ni_3Sn_4 interface in the solder joint aged at 180°C for 48 h………….………………………..…..……………....66

Fig. 3.17. Fracture surfaces of the solder joints aged for varied hours at 200°C………..…..67

Fig. 3.18. Cross-sectional SEM images showing (a) formation of a layer of Kirkendall voids at the Ni_3P/Cu interface and (b) fracture at the Ni_3P/Cu interface in the solder joint aged at 200°C for 100 h……………….……………………………………………….………...…68

Fig. 3.19. Fracture surface of solder joint aged at 200°C for 48 h...………..……….…..……68

Fig. 3.20. EDS element mapping analysis of Sn-3.5Ag/Ni-P/Cu interfaces of the sample aged at 160 °C for 400 h: (a) SEM image, (b) mapping for P, (c) mapping for Ni, and (d) mapping for Sn. The concentration of element decreases with an increase in intensity of black color. ...…….…………………………………….……………..………….…..71

Fig. 3.21. EDS element mapping analysis of Sn-3.5Ag/Ni-P/Cu interfaces of the sample aged at 200 °C for 100 h: (a) SEM image, (b) mapping for P, (c) mapping for Ni, (d) mapping for Sn. The concentration of element decreases with an increase in intensity of black color. ...……..…………………………………………………..………..….72

Fig. 3.22. Schematic illustration of the growth of multiple compounds at the Sn-3.5Ag/electroless Ni-P/Cu interfaces………………………………….………..……79

Fig. 3.23. Fracture surface of the Cu/electroless Ni-P/Sn-3.5Ag solder joint aged at 200°C for 100 h ……………………..……………………………….………………..……....82

Fig. 3.24. Schematic illustration of Cu diffusion through the Ni_3P layer: (a) Growth of Ni_3P layer in between Ni_3Sn_4 intermetallic and electroless Ni-P layer and (b) Diffusing of Cu through the grain boundaries of Ni_3P layer……………………………………………..83

Fig. 3.25. Schematic illustration for the effect of Ni_3Sn_4 spallation on the interfacial microstructure of solder joint: (a) Ni_3Sn_4 spallation during reflow and (b) Accumulation of spalled Ni_3Sn_4 particles at the solder/Ni_3Sn_4 interface……………………..………….…86

Fig. 4.1. Back-scattered SEM images of Sn-3.5Ag/Ni-P/Cu interfaces in the as-prepared samples having electroless Ni-P layers of different thicknesses ……………..…………..92

Fig. 4.2. Back-scattered SEM images of Sn-3.5Ag/Ni-P/Cu interfaces in the solder joints aged at 160°C for 225 h and having Ni-P layers of different thicknesses……..…......…..93

Fig. 4.3. Back-scattered SEM images of Sn-3.5Ag/Ni-P/Cu interfaces in the samples aged at 180°C for 225 h and having Ni-P layers of different thicknesses ……..………….…..…94

Fig. 4.4. Back-scattered SEM images of Sn-3.5Ag/Ni-P/Cu interfaces in the samples aged at 200°C for 400 h and having Ni-P layers of different thicknesses...……………….……..95

Fig. 4.5. EDS element mapping analysis of Sn-3.5Ag/Ni-P/Cu interfaces of the sample having thin (3.9 μm) Ni-P layer and aged at 200°C for 400 h: (a) SEM image, (b) mapping for P, (c) mapping for Ni, (d) mapping for Cu, (e) mapping for Sn, and (f) mapping for Ag. The concentration of element decreases with the increase in intensity of black color……………………………………………………………………….……………...96

Fig. 4.6. Fracture surfaces of the as-prepared sample having thin (3.9 µm) Ni-P layer showing ductile fracture inside the bulk solder…………………...…………….……………..…97

Fig. 4.7. Tensile strength of test samples having Ni-P layers of different thicknesses as a function of aging duration at 160°C……………….……………....……………..…………98

Fig. 4.8. Fracture energy of test samples having Ni-P layers of different thicknesses as a function of aging duration at 160 °C ………………………………….….……..……………..98

Fig. 4.9. Fracture surfaces of the aged (at 160 °C for 100 h) samples having Ni-P layers of different thicknesses…………………………………...……...…………..……………..…99

Fig. 4.10. Fracture surfaces of the aged samples having thin (3.9 µm) Ni-P layer and aged for varied hours at 160°C. ……….…………………..………………………….…………….100

Fig. 4.11. SEM images showing fracture of the sample aged at 160°C for 400 h and having thin (3.9 µm) Ni-P layer (a) Fracture occurring at the Ni_3P/Cu interface and (b) Fracture transmitting to the $(Ni_{1-x}Cu_x)_3Sn_4$/Ni-Sn-P interface through the Ni_3P layer…………….100

Fig. 4.12. Tensile strength of test samples having Ni-P layers of different thicknesses as a function of aging duration at 180°C………………….……….……...…………………..…101

Fig. 4.13. SEM image showing fracture at the solder/Ni_3Sn_4 interface (a and b) and Ni_3P/Cu interface (c and d) in the medium (7.3 µm) Ni-P samples aged at 180°C for 48 h……....102

Fig. 4.14. SEM image showing fracture in the layer of Kirkendall voids between Cu and Ni-Sn-P layer in the thin (3.4 µm) Ni-P sample aged at 180°C for 400 h……….…..…..102

Fig. 4.15. Tensile strength of test samples having Ni-P layer of different thicknesses as a function of aging duration at 200°C……………………….……….……….....……..…103

Fig. 4.16. Cross-sectional SEM images showing fracture path of the sample having thin (3.9

µm) Ni-P layer and aged at 200°C for (a) 48 h, (b) 100 h, and (c) 400 h. ...……………..…..103

Fig. 4.17. Schematic illustration for the growth of interfacial compounds in Sn-3.5Ag/electroless Ni-P/Cu system showing different stages of growth……….….….105

Fig. 4.18. Schematic illustrations correlating the fracture behavior with the interfacial microstructure of Cu/electroless Ni-P/Sn-3.5Ag solder joint: (a) fracture inside the bulk solder and (b) fracture at the interfaces between two compounds………………………..107

Fig. 4.19. Magnified view of Ni_3P layer inside the rectangle frame in Figure 4.10c illustrating the Cu diffusion paths in the Ni_3P layer by the arrows…………….………..……..107

Fig. 4.20. (a) Top view and (b) titled view of fracture surface of the thin Ni-P sample aged at 180°C for 225 h …………………………………………………….………………......109

Fig. 5.1. Cross-section of electroless Ni-P plated Cu substrate…………………………..…113

Fig. 5.2. Interfacial microstructures of as-prepared samples having electroless Ni-P layers of different P concentrations…………………………...……………...…...……..…114

Fig. 5.3. Interfacial microstructures of the test samples having electroless Ni-P layers of different P concentrations after 5 reflows……………...………………….……….…117

Fig. 5.4. Interfacial microstructures of the test samples having electroless Ni-P layers of different P concentrations after 20 reflows……………………………….………..……..118

Fig. 5.5. The tensile strength of low, medium, and high P samples after multiple reflows……………………………………………………………………..…………119

Fig. 5.6. Fracture path in low P sample (a) after 2 reflows, (b) after 20 reflows………...120

Fig. 5.7. Fracture surfaces of high P sample (a) after 2 reflows, (b) after 20 reflows...…120

Fig. 5.8. Fracture surfaces of medium P samples after reflow for (a) 5 cycles (solder side), (b) 5 cycles (Cu substrate side), (c) 15 cycles (solder side), (d) 15 cycles (Cu substrate side), (e) 30 cycles (solder side), and (f) 30 cycles (Cu substrate side)……………………………121

Fig. 5.9. SEM image of fracture path in the medium P sample reflowed for 30 cycles...….......122

Fig. 5.10. Fracture surfaces of low P sample after 20 reflows (a) solder side, (b) Cu substrate side, (c) magnified image of solder side, (d) magnified image of Cu substrate side………………………………... ……………………………………….…….….…..123

Fig. 6.1. Schematic illustration of the growth of Ni_3P grain in the electroless Ni-P layer……………………………………………………………………………..……….127

Fig. 6.2. A plot of Ni_3Sn_4/Ni_3P thickness ratio versus P concentration of electroless Ni-P UBM………………………………………………………………………..…....135

Fig. 7.1. Schematic of metallization layout on Ni plate…………………….………..…..139

Fig. 7.2. Schematic diagram of Ni/Sn-3.5Ag test sample……………………….….……139

Fig. 7.3. Schematic diagram of experimental setup used to pass the electric current through test samples during thermal aging in oven……………………….………….…...…....140

Fig. 7.4. Tensile strength of (a) Ni-P/Sn-3.5Ag (b) Ni-P/Sn-37Pb and (c) Ni/Sn-3.5Ag solder joints as a function of current density ………………………...……..……….…..142

Fig. 7.5. Fracture energy of (a) Ni-P/Sn-3.5Ag (b) Ni-P/Sn-37Pb and (c) Ni/Sn-3.5Ag solder joints as a function of current density ……………………………….…..……..143

Fig. 7.6. Load vs. Extension curves of the Ni-P/Sn-3.5Ag solder joints aged with (a) 1×10^3 A/cm^2 and (b) 3×10^3 A/cm^2 current densities. ……………………….…………….…………..154

Fig. 7.7. Load vs. Extension curves of the Ni/Sn-3.5Ag solder joints aged with (a) 1×10^3 A/cm^2 and (b) 2×10^3 A/cm^2 current densities……………………………………….………..144

Fig. 7.8. SEM images showing fracture in the electroless Ni-P/Sn-3.5Ag solder joint aged at 160°C for 100 h with 1×10^3 A/cm^2 current density: (a) Anode side top view, (b) cathode side tope view, and (c) cross-sectional view. ……………………………………………145

Fig. 7.9. SEM images showing fracture in the electroless Ni-P/Sn-3.5Ag solder joint aged at 160°C for 100 h with 3×10^3 A/cm^2 current density: (a) Anode side top view, (b) cathode side tope view, and (c) cross-sectional view……...…………………….…………..………146

Fig. 7.10. Fracture surfaces of the electroless Ni-P/Sn-3.5Ag solder joint aged at 160 °C for 100 h with 3 × 10^3 A/cm^2 current density: (a) Anode side and (b) cathode side………..146

Fig. 7.11. Fracture in the Ni/Sn-3.5Ag solder joint aged at 160°C for 100 h without current…………………………………………………………….…………..………..147

Fig. 7.12. Fracture surfaces of the Ni/Sn-3.5Ag solder joint aged at 160°C for 100 h without current: (a) solder side and (b) Ni side..……………………………………......……147

Fig. 7.13. SEM images showing mixed fracture in the Ni/Sn-3.5Ag solder joint aged at 160°C for 100 h with 2 × 10^3 A/cm^2 current density: (a) Anode side top view, (b) cathode side tope view, and (c) cross-sectional view……………………………………..….148

Fig. 7.14. Fracture surfaces of the Ni/Sn-3.5Ag solder joint aged at 160°C for 100 h with 3 × 10^3 A/cm^2 current density...……………………………………………….…………...148

Fig. 7.15. Fracture in the Ni-P/Sn-37Pb solder joint aged at 160°C for 100 h with 1 × 10^3 A/cm^2 current density………………………………….……………..…...…………..149

Fig. 7.16. SEM images showing fracture in the electroless Ni-P/Sn-37Pb solder joint aged at 160°C for 100 h with 3 × 10^3 A/cm^2 current density: (a) Anode side top view, (b) cathode side tope view, and (c) cross-sectional view………………………………………..149

Fig. 7.17. SEM images showing nano-indentation marks in the Ni/Sn-3.5Ag sample aged at 160°C for 100 h with 2 × 10^3 A/cm^2 current density: (a) Anode side, (b) cathode side, and (c) magnified view of a single mark……………………………………………..………152

Fig. 7.18. Cross-sectional SEM images of electroless Ni-P/Sn-3.5Ag interfaces of the sample aged at 160°C for 100 h without current…….…………………….…………153

Fig. 7.19. Cross-sectional SEM images of electroless Ni-P/Sn-3.5Ag interfaces of the sample aged at 160°C for 100 h with 2 × 10^3 A/cm^2 current density: (a) anode side and (b) cathode side ………………………………………………………..………………....153

Fig. 7.20. Cross-sectional SEM images of Ni/Sn-3.5Ag interfaces of the sample aged at 160

°C for 100 h without current……………………………..……………………………154

Fig. 7.21. Cross-sectional SEM images of Ni/Sn-3.5Ag interfaces of the sample aged at 160°C for 100 h with 2 × 10^3 A/cm^2 current density: (a) anode side and (b) cathode side..154

Fig. 7.22. Cross-sectional SEM images of electroless Ni-P/Sn-37Pb interfaces of the sample aged at 160°C for 100 h without current………………………………………………155

Fig. 7.23. Cross-sectional SEM images of electroless Ni-P/Sn-37Pb interfaces of the sample aged at 160°C for 100 h with 2 × 10^3 A/cm^2 current density: (a) anode side and (b) cathode side ………………………………………….……….…………….….….………...155

Fig. 7.24. Microstructure of Sn-37Pb solder in the samples aged at 160°C for 100 h with different current densities……………………………..……..…………….……………156

Fig. 7.25. Thickness of Ni_3Sn_4 IMC in the (a) electroless Ni-P/Sn-3.5Ag, (b) Ni/Sn-3.5Ag, and (c) electroless Ni-P/Sn-37Pb samples aged at 160°C for 100 h, as a function of current density……………………………………………………..…..…………………….…....157

Fig. 7.26. Schematic illustration for electromigration effect on the growth of Ni_3Sn_4 IMC in (a) Ni/solder and (b) electroless Ni-P/solder systems……………………………….....162

Fig. A.1. Load-extension curves of the samples having 9.9 μm thick Ni-P layer and aged for 225 h at (a) 160 °C, (b) 180 °C, and (c) 200 °C…………………………………….……....184

Fig. A.2. Load-extension curves of the samples aged at 160°C for 225 h and having (a) thin (3.9 μm), (b) medium (7.3 μm), and (c) thick (9.9 μm) Ni-P layers…...……………..….185

Fig. B.1. EDS spectra from (a) pure Cu, (b) pure Sn, (c) pure Ni, and (d) GaP standards…………………………………………………………………….……..……....192

Fig. B.2. EDS spectrum from the Ni/Sn-3.5Ag sample aged at 160 °C for 100 h showing formation of Ni-Sn IMC…………………………………………….…...…………......192

Fig. B.3. ZAF (a) standard and (b) standardless quantitative analyses of Ni-Sn spectrum from the sample aged at 160 °C for 100 h, indicating the formation of Ni_3Sn_4 IMC….....193

Fig. B.4. SEM images of the Sn-3.5Ag/Ni-P/Cu interfaces of the samples having 9.9 μm electroless Ni-P layer and aged at (a) 160 °C for 400 h and (b) 200 °C for 100 h…….....194

Fig. B.5. EDS analyses of the points (a) 1, (b) 2, and (c) 3 that shown in the Fig B.4, indicating the formation of Ni_3Sn_4, Ni_3P, and Ni_2SnP phases, respectively..…………….....194

Fig. B.6. SEM image of the Sn-3.5Ag/Ni-P/Cu interfaces of the sample having 3.9 μm electroless Ni-P layer and aged at 200 °C for 400 h..……….…………………….…..….....195

Fig. B.7. EDS analyses of the points (a) 1, (b) 2, (c) 3, and (d) 4 that shown in the Fig B.6, indicating the formation of $(Ni_{1-x}Cu_x)_3Sn_4$, $(Ni_{1-x}Cu_x)_6Sn_5$, Cu_6Sn_5, Cu_3Sn IMCs, respectively……………………………….………………………………..……....195

List of Tables

Table 2.1. Growth kinetic parameters and proposed growth mechanism of various compounds in different electroless Ni-P/solder systems……………………..…..……….18

Table 3.1. EDS results showing the chemical composition (at.%) of compounds formed at the Sn-3.5Ag/Ni-P/Cu interfaces of the as-prepared sample. ……..…………….………...…..52

Table 3.2. EDS results showing the chemical composition (at.%) of compounds formed at the Sn-3.5Ag/Ni-P/Cu interfaces of the sample aged at 200 °C ……..…………….…….….54

Table 3.3. Thickness ratio of Ni_3Sn_4 to Ni_3P layers measured at different aging conditions……………………………………………………………………..…………..57

Table 3.4. Kinetic parameters of the growth of Ni_3Sn_4, Ni-Sn-P, and Ni_3P compounds at various temperatures……………………..……………………………………………..…60

Table 3.5. Activation energies (Q) of the growth of compound in the electroless Ni-P/solder system reported in different studies………………………………..……………..…….61

Table 3.6. Comparison between the thermodynamic driving forces (Gibbs free energy change, ΔG) for the formation of different Ni-P compounds…………………….…..…….74

Table 3.7. Comparison between the thermodynamic driving forces (Gibbs free energy change, ΔG) for the formation of different Ni-Sn compounds………..…………….……74

Table 3.8. Comparison between the thermodynamic driving forces (Gibbs free energy change, ΔG) for the self-crystallization and solder reaction-assisted crystallization of electroless Ni-P……………………..……..…………………….…………………….…….76

Table 3.9. Density of reacting materials and resulting compounds in the Cu/electroless Ni-P/Sn-3.5Ag solder joint…………………..……………………………….……..….…84

Table 4.1. EDS results showing the chemical composition (at.%) of compounds formed at the Sn-3.5Ag/Ni-P/Cu interfaces in Fig. 4.4a……………..………………...……...…..…95

Table 6.1. Thickness ratio of Ni_3Sn_4 to Ni_3P layers obtained from previous interfacial studies that used electroless Ni-P UBM of different P concentrations……………..….….136

Table 7.1. Reduced modulus and hardness of solders in different solder joints at different experimental conditions…………………………………………………..…………..151

Table B.1. Elemental composition (at.%) of different compounds that measured using standard and standardless ZAF matrix corrections……………………..…….……...…..196

List of Abbreviations

AC	Alternating Current
BGA	Ball Grid Array
C4	Control Collapse Chip Connection
CTE	Coefficient of Thermal Expansion
DC	Direct Current
DSC	Differential Scanning Calorimetry
EDS	Energy Dispersive X-ray Spectroscopy
EMPA	Electron Probe Micro Analyzer
IC	Integrated Circuit
IMC	Intermetallic Compound
I/O	Input/Output
PCB	Printed Circuit Board
SEM	Scanning Electron Microscope
TEM	Transmission Electron Microscope
TTF	Time To Failure
UBM	Under Bump Metallization
VLSI	Very Large Scale Integrated

Chapter 1

Introduction

1.1. Background and Motivation

Electronic packaging is one of the greatest challenges faced by the semiconductor industry because of the strict requirements on packaging technology, such as high I/O counts, fine pitch, limited usage of toxic materials, enhanced heat dissipation, and reliable interconnects. The primary function of a package is to make the electrical connections between semiconductor device and printed circuit board (PCB) to provide paths for power to be applied to the chip and for data signals to be transmitted into and out of the chip. Its secondary function is to house and protect the fragile chip from harsh environmental conditions like moisture, light, and dust that might hinder its performance. The first function is becoming increasingly important and more difficult to achieve as the number of I/O counts are increasing and the pitch (or bump size) is decreasing steadily. Solder flip chip packaging technology has been proved to be a future technology to achieve this requirement (Tummala, 2001). In this technology, solder bumps are built on the chip's I/O pads using wafer-bumping process. The wafer-bumping process includes deposition of solder by one of the processes of evaporation, electroplating, and stencil printing, on the wafer I/O pads, then heating the wafer together with solder to a temperature well above the melting point of solder, and finally cooling the wafer. During melting, the shape of solder changes into a ball because of surface tension and it remains in the same shape even after cooling. The process of melting the solder to achieve ball-shaped solder bump is called as reflow. After the wafer-bumping process, the wafer is cut into a number of small chips. Then the chip is flipped over and finally the flipped chip is joined with the substrate having a matching pad's pattern using solder interconnects with the help of reflow process.

Fig. 1.1 shows the schematic of typical solder flip chip package and solder interconnect. In the solder flip chip package, solder interconnect joins the IC chip metallization, which is usually known as under bump metallization (UBM), to the substrate metallization. The UBM is a combination of thin metallic layers whose function is to provide good solderable surface and protect underlying IC metallization from reacting with solder. The under bump and substrate metallizations react with solder and form intermetallic compounds (IMCs). These IMCs connect the solder ball to metallizations to form a complete solder interconnect (Fig. 1.1b). The solder interconnects in the flip chip package not only provide electrical and thermal interconnections between chip and board but also mechanically support the package. Thus, the failure of a single solder interconnect can cause the failure of a device, or even of an entire electronic system. Therefore, the reliability of a solder interconnect in the electronic packages has become a critical issue for the reliability of the entire electronic system.

Solder flip chip technology was developed by IBM in 1960s and named C4 (Controlled Collapse Chip Connection) technology (Lau, 1996). In this technology, high-Pb Sn-Pb solder was used with Cu-based Cr-Cu UBM and ceramic substrate. Later on, polymer substrate was used in the flip chip package to reduce the package cost. Due to the low glass transition temperature of polymer, solders with low melting temperature have been developed for the flip chip packages with polymer substrate. Eutectic Sn-Pb alloy with a melting temperature of 183ºC has been the solder of choice since the last few decades. Recently, due to the legislative and environmental concerns on toxic lead, the packaging industry is promoting the use of lead-free solders (Bruinsma, 2001; WEEE, 2000). However, unlike the eutectic Sn-Pb alloy, the lead-free solders are high-Sn alloys constituting one or two more elements such as Ag, Cu, Au, and Bi. These high-Sn solders react more rapidly with Cu-based UBM and substrate metallization as compared to the Sn-Pb solders and thus result not only in the extensive growth of brittle Cu-Sn IMCs and Kirkendall voids but also in the spalling of Cu-Sn IMCs (Kim *et al.*, 1996; Liu *et al.*, 1996; Tu and Zeng, 2001; Zeng and Tu, 2002).

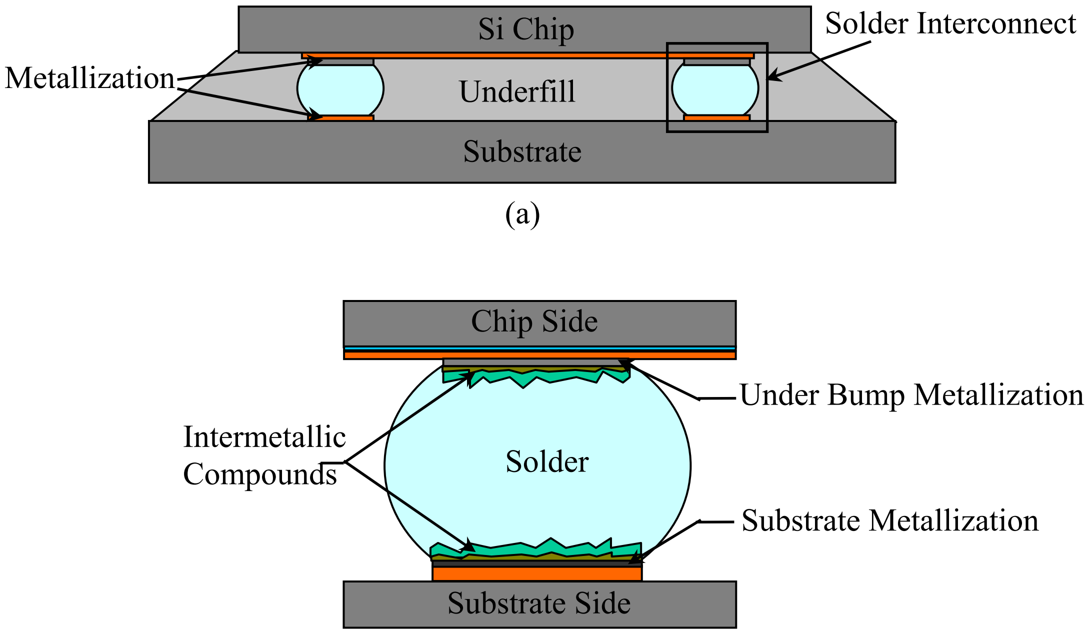
Si Chip
Solder Interconnect
Metallization
Underfill
Substrate
Chip Side
Under Bump Metallization
Intermetallic Compounds
Solder
Substrate Metallization
Substrate Side

(a)

(b)

Fig. 1.1 Schematic of typical (a) solder flip chip package and (b) solder interconnect.

The IMC growth has been found to minimize in the case of Ni-based UBM as the reaction between Ni and Sn is much slower than between Cu and Sn (Kim *et al.*, 1999; Tu and Zeng, 2001). Several Ni-based UBM are available depending on deposition techniques, such as sputtered nickel, electrolytic nickel, and electroless nickel. Among them, electroless nickel (Ni-P) with a thin layer of immersion gold has been considered as one of the promising candidates for UBM and substrate metallization due to its various advantages such as mask-less selective deposition, strong adhesion, low residual stress, good solderability, good uniformity, excellent corrosion resistance, and low processing cost (Jeon *et al.*, 2001; Mallory and Hajdu, 1990; Stepniak, 1997).

Electroless Ni-P is an amorphous alloy containing 12-19 at.% P. The presence of P in electroless Ni-P makes its soldering reactions more complicated than one with pure Ni. Many studies have been performed on the interaction between electroless Ni-P and

Sn-bearing solders (Ahat *et al.*, 2000; Alam *et al.*, 2003; Chonan *et al.*, 2002a; Hung and Chan, 2000; Hung *et al.*, 2000a, b; Jang *et al.*, 1999; Jang *et al.*, 2000; Jeon and Paik, 2002; Kulojarvi *et al.*, 1998; Lee and Lin, 1994; Lee and Lin, 1995; Lin and Liu, 1999; Liu *et al.*, 2000b; Liu and Shang, 2000a; Mei and Dauskardt, 1999). Topics of these studies include the formation and growth of Ni-Sn and Ni-P compounds at the interface between molten solder and Ni-P UBM (Lee and Lin, 1994; Lin and Liu, 1999; Mei and Dauskardt, 1999), solder reaction-assisted crystallization of electroless Ni-P metallization (Hung and Chan, 2000; Hung *et al.*, 2000b; Jang *et al.*, 1999), influence of P-concentration of electroless Ni-P on the solder joint strength (Chonan *et al.*, 2002a; Alam *et al.*, 2003), and influences of IMCs on the mechanical properties of solder joints (Ahat *et al.*, 2000; Kulojarvi *et al.*, 1998; Lee and Lin, 1995; Liu and Shang, 2000a).

In most of the reported electroless Ni-P/solder interfacial studies, the main focus was given to solder and much less was reported on electroless Ni-P UBM. Though, due to the difference in composition of different solders, differences are expected in the IMC formation, IMC morphology, IMC growth rate, and mechanical properties of solder joint, less or nothing can be expected for the effect of change in thickness and composition of electroless Ni-P UBM on the mechanical properties of solder owing to the limited studies on it. Thus, more efforts have to be made to systematically examine the effect of interfacial reactions on the mechanical properties of electroless Ni-P/Sn-rich solder joints with focusing electroless Ni-P. More specifically, there are still many outstanding issues that need further investigation, such as:

a) The understanding of interfacial reactions between electroless Ni-P and Sn-bearing solder is still incomplete. The growth kinetics of IMC reported in different studies is not consistent. Moreover, nothing has been reported about the growth kinetics of ternary Ni-Sn-P compound. The discussion on the reaction mechanism is still quite limited and incomplete. Thus, a thorough investigation is required with a wide range of aging conditions that corresponds to the large variation of interfacial conditions.

b) The understanding of the formation of Kirkendall voids in the Cu/electroless Ni-P/Sn-3.5Ag solder joint and its influence on the reliability of solder joint is still not clear. There are discrepancies in the published literatures on where these voids are formed and how they affect the solder joint strength. As a result, there is no agreement on the main causes of the brittle failure of solder joint.

c) Little has been reported on the influence of thickness and P concentration of electroless Ni-P UBM on the mechanical properties of solder joint. As the presence of P in electroless Ni-P causes complex soldering reactions resulting in the formation of multiple IMCs, these two parameters of electroless Ni-P layer can play an important role in determining the reliability of solder joint. However, not much has been reported on it in published studies.

Apart from the usage of lead-free solders, other challenges faced by electronic packaging industry due to the development of small but high-powered integrated circuit (IC) chip are the high service temperature and fine pitch of electronic package. Although, the problem of high service temperature can be tackled by the selection of proper UBM/solder system, the effect of fine pitch or in other words, small solder bump, on the reliability of solder joint is not clear. It is known that the fine pitch (< 200 μm) of solder flip-chip package results in a high current density ($>10^3$ A/cm^2) in the solder interconnects. At very high current density ($\sim10^4$ A/cm^2), electromigration-induced electrical failure of solder interconnect has been reported by several researchers (Lee *et al.*, 2001a,b; Yeh *et al.*, 2002). Even at low current density (10^2-10^3 A/cm^2), electric current has been found to influence interfacial reactions, IMC formation, and grain growth in the solder joints and different material systems (Chen *et al.*, 1998; Conrad, 2000; Chen and Chen, 2001; Gan and Tu, 2005). Recently, electric current has also been found to influence the mechanical properties of solder joints (Ren *et al.*, 2005; Ye *et al.*, 2003b). Though, a number of studies have been done on electromigration effect in solder joints, there are still several issues that have to be addressed such as:

a) No systematic comparison of electroless Ni-P with pure Ni UBMs has been reported in terms of electromigration effect on UBM/solder interfacial reactions. Moreover, the effect of P on the electromigration phenomena is still not clear. The comparison between electroless Ni-P/solder and Ni/solder systems would be helpful in understanding the performance of Ni-based UBMs in solder-bumped flip chip technology.

b) Although, the effect of electromigration on the electrical reliability of solder joints has been well studied, little is known about its effect on the mechanical reliability of the solder joints. Thus, more efforts are required to systematically examine the effect of electromigration on the mechanical properties of solder joints.

c) No comparison of lead solder with lead-free solder has been reported in literature. The comparison between these solders would help in understanding their performances as package level solder interconnects stressing with high current density.

1.2. Objectives

This thesis reports mainly an experimental study of the effects of interfacial reactions and electromigration on the mechanical properties of Cu/electroless Ni-P/Sn-3.5Ag solder joint. The study of interfacial reactions covers the effects of solid-state thermal aging, Ni-P thickness, P concentration of electroless Ni-P layer, on the interfacial microstructure and mechanical properties of the solder joint. Electrical study aims at a systematic and comprehensive understanding of the solid-solid interaction of different UBM/solder systems stressed with high-density electric current. Moreover, an effort has been made to understand the influence of high-density electric current on the mechanical properties of different UBM/solder systems. Such understanding would provide guidance to the selection of working conditions as well as the materials of electronic packages in order to produce better and reliable products. The work covers several separate but inter-related sub-topics, as detailed below.

1.2.1. Study of Cu/Electroless Ni-P/Sn-3.5Ag Interfacial Reactions and their Effect on Solder Joint Strength

The objective of this part of the work is to make a comprehensive understanding of the solid-state interaction of Sn-3.5Ag solder with electroless Ni-P UBM plated on Cu substrate at the temperatures ranging from low (140 °C) to very high (200 °C). In the interfacial study, the morphology and growth kinetics of all the major compounds, Ni_3Sn_4, Ni-Sn-P, and Ni_3P are investigated. Along with the compounds growth, other evolution of interfacial microstructure such as the formation of Kirkendall void is also investigated. The effects of state of interaction (liquid and solid) on the morphology of Ni_3Sn_4 and the growth mechanisms of compounds and Kirkendall void are discussed. In the mechanical study, tensile strength and fracture behavior of thermally aged solder joint are investigated to identify the factors that affect the mechanical properties of solder joint.

1.2.2. Investigation of Influence of Ni-P Thickness on Cu/Electroless Ni-P/Sn-3.5Ag Interfacial Reactions and Solder Joint Strength

In this part of the work, solid-state Cu/electroless Ni-P/Sn-3.5Ag solder interfacial reactions and their effect on the mechanical properties of solder joint are investigated for different Ni-P thicknesses. The objectives are to understand the influence of UBM thickness on the formation of IMCs, on the evolution of interfacial microstructure, and on the mechanical reliability of solder joint. The growth mechanism of additional IMCs such as Cu-Sn and Ni-Cu-Sn is discussed. A correlation is established between the evolution of interfacial microstructure and the mechanical properties of solder joint.

1.2.3. Investigation of Effect of P Concentration on Cu/Electroless Ni-P/Sn-3.5Ag Interfacial Microstructure and Solder Joint Strength

In this part of the work, the interfacial microstructure and mechanical properties of multiple-reflowed Cu/electroless Ni-P/Sn-3.5Ag solder joints are investigated for different P concentrations of electroless Ni-P layer. An understanding of the effect of P concentration on the evolution of interfacial microstructure such as Ni_3Sn_4 spallation and Cu-Sn IMCs growth is made. A correlation between the Ni_3Sn_4 spallation and the mechanical properties of the solder joints is established. Understanding of the correlation would provide direct insight into how the Ni_3Sn_4 spallation affects the package's mechanical reliability.

1.2.4. Development of a Mathematical Model for the Growth of Ni_3P and Ni_3Sn_4 Compounds

In this part of the work, a mathematical model is developed which can describe the growth of Ni_3P and Ni_3Sn_4 in the electroless Ni-P/solder joint. An effort is made to explain various experimental findings such as variation in Ni_3P and Ni_3Sn_4 growth kinetics, relationship between the growth of Ni_3P and Ni_3Sn_4, and the influence of P concentration on compounds growth with the help of model.

1.2.5. Study of Effect of Electromigration on the Interfacial Microstructure and Mechanical Properties of UBM/Solder Joints

The objective of this part of the work is to understand the influence of electromigration on the UBM/solder interfacial reactions and mechanical properties of solder joint. The mechanical properties of electrically stressed UBM/solder joints are investigated with the help of tensile testing and nano-indentation methods. Three UBM/solder systems, electroless Ni-P/Sn-3.5Ag, Ni/Sn-3.5Ag, and electroless Ni-P/Sn-37Pb, are compared in terms of IMC formation and mechanical properties. The polarity effect of electric current on the formation of Ni_3Sn_4 IMC and the electromigration-induced brittle failure of solder joints are discussed.

1.3. Organization of the Thesis

This thesis is divided into 8 chapters and organized in the following manner:

Chapter 2 presents a review of the interfacial reactions between electroless Ni-P and Sn-bearing solders that include the formation of intermetallic compounds, IMC morphology, and IMC growth kinetics. Other phenomena associated with interfacial reactions, such as IMC grain coarsening, IMC grain spalling, and Kirkendall void formation are also discussed. A review of mechanical properties of electroless Ni-P/solder joint is also done. Prior work on electromigration effect in solder joints is also discussed.

Chapter 3 covers a study of Cu/Electroless Ni-P/Sn-3.5Ag interfacial reactions and their effect on solder joint strength.

Chapter 4 presents a study of the influence of Ni-P thickness on Cu/Electroless Ni-P/Sn-3.5Ag interfacial reactions and solder joint strength.

Chapter 5 covers an investigation of the effect of P concentration on Cu/Electroless Ni-P/Sn-3.5Ag interfacial microstructure and solder joint strength.

Chapter 6 presents the development of a mathematical model for the growth of Ni_3P and Ni_3Sn_4 layers.

Chapter 7 presents a study of the effect of electromigration on the interfacial microstructure and mechanical properties of UBM/Solder joints.

Finally, Chapter 8 covers the conclusions and recommendations for future work.

Chapter 2

Literature Review

The interfacial reactions and electromigration are the inevitable phenomena that occur in solder joints. The present work investigates the effects of interfacial reactions and electromigration on the Cu/electroless Ni-P/Sn-3.5Ag solder joint strength. This chapter reviews the literature on the interfacial reactions between electroless Ni-P and Sn-bearing solder, mechanical properties of solder joint, electromigration phenomenon, and electromigration effect in solder joint.

2.1. Interfacial Reactions between Electroless Ni-P and Sn-bearing Solder

In solder flip chip package, the interfacial reactions between solder and UBM take place not only during the manufacturing process (the reflow process) but also during service. In the reflow process, the solder experiences a temperature cycle during which it melts and then solidifies quickly. Thus liquid-state reactions take place during reflow process, whereas solid-state reactions during service. In both types of interfacial reactions, interfacial compounds nucleate and/or grow between solder and UBM. The phase of interfacial compound that will form between a known composition of solder and UBM at certain process condition can be predicted with the help of a phase diagram.

According to the phase diagram shown in Fig. 2.1, three kinds of intermetallic compounds (IMCs) can form between Ni and Sn: Ni_3Sn_4, Ni_3Sn_2 and Ni_3Sn. However, during normal reflow or soldering process with the temperature range of 200-250ºC, Ni_3Sn_4 is found to be the primary product of reactions between Sn-bearing solder (eutectic Sn-Pb solder or lead-free solder without copper) and electroless Ni-P (Hung and Chan, 2000; Hung *et al.*, 2000b; Jang *et al.*, 2000; Kulojarvi *et al.*, 1998; Lee and Lin, 1994, 1995; Lin and Liu, 1999; Liu *et al.*, 2000b; Liu and Shang, 2000a, b; Mei and Dauskardt, 1999). Besides the predominant Ni_3Sn_4 layer, there are a few studies that report the formation of thin (submicron) layer of other kind(s) of Ni-Sn IMC such as Ni_3Sn_2 (Hwang *et al.*, 2003; Liu *et al.*, 2000b) and $Ni_{48}Sn_{52}$ (Matsuki *et al.*, 2002). Thus it can be understood that the small thickness of other Ni-Sn IMCs which is due to their slow nucleation and/or growth makes them difficult to be observed by SEM and even by TEM.

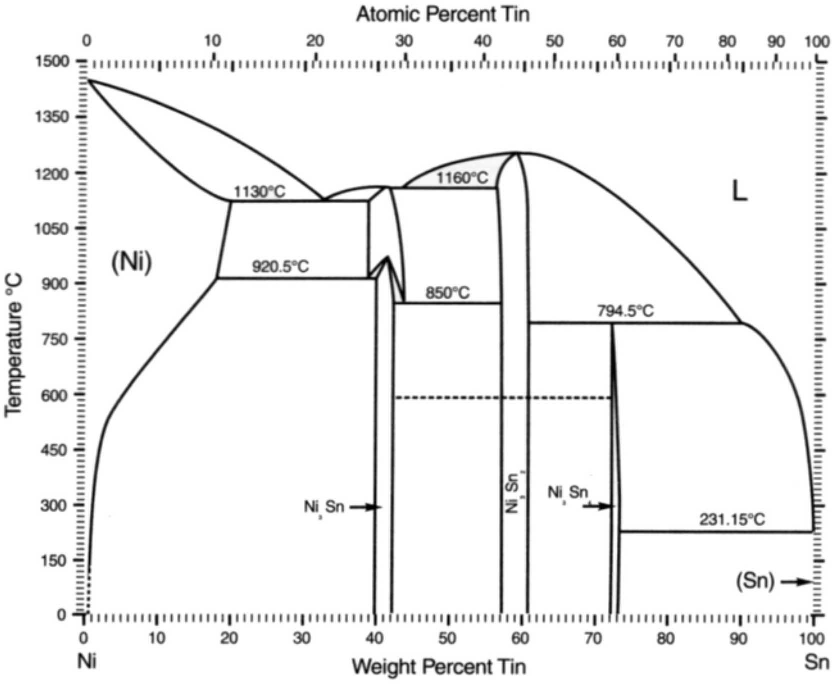

Fig. 2.1. The equilibrium phase diagram of Ni-Sn binary alloy (Massalski, 1986).

Since electroless plated nickel is a Ni-P alloy that gets P from hypophosphite ($H_2PO_2^-$) reducing agent during the reduction of Ni from an ionic Ni solution (Mallory and Hajdu, 1990), the presence of P influences the microstructure of Ni-P and make its soldering reaction more complicated than that one with pure Ni. It is known that if P concentration of electroless Ni-P is less than 12.5 at.%, then its structure is microcrystalline, otherwise it is amorphous (Haseeb *et al.*, 1996; Mallory and Hajdu, 1990; Sohn *et al.*, 2003; Li *et al.*, 1998). The electroless Ni-P UBM used in electronic packaging normally has more than 12.5 at.% of P and therefore has amorphous structure.

The amorphous Ni-P alloys are thermodynamically unstable, thus their crystallization occurs spontaneously during thermal treatment when temperature reaches their crystallization temperature of about 280 ºC (Li *et al.*, 1998). The thermodynamics equilibrium phases present near the composition of electroless Ni-P, i. e. Ni and Ni_3P (Fig. 2.2), form during the crystallization. Microstructure of amorphous electroless Ni-P also changes during self-crystallization process. While amorphous electroless Ni-P is comprised of thousands of nano-size particles distributed homogeneously, these particles gather gradually into big particles during crystallization process in order to decrease surface energy (Li *et al.*, 1998). The microstructure of amorphous Ni-P finally changes into a fine crystalline structure.

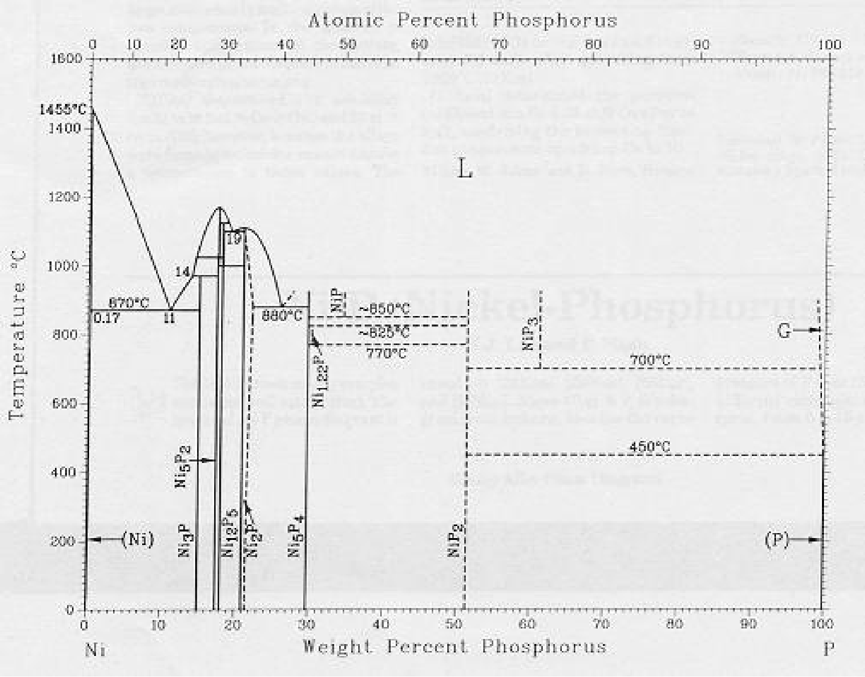

Fig. 2.2. The equilibrium phase diagram of Ni-P binary alloy (Massalski, 1986).

When electroless Ni-P comes into contact with solder, the soldering reaction triggers the crystallization of amorphous Ni-P at reflow temperature (200-250 °C), that is well below the self-crystallization temperature of Ni-P (280-300 °C) (Jang *et al.*, 1999). Moreover, in the solder reaction-assisted crystallization of amorphous electroless Ni-P, along with primary Ni_3P phase, additional Ni-P phase such as $Ni_{12}P_5$ (Liu *et al.*, 2000b) and Ni_2P (Sohn *et al.*, 2004b) have been also reported to form in the crystallized Ni-P layer. These reports indicate that the interfacial reactions between electroless Ni-P and Sn-bearing solders are highly complicated due to the presence of P in electroless Ni-P.

Solder reaction-assisted crystallization of electroless Ni-P is quite different from its self-crystallization owing to a few unique characteristics. The first is that the products of solder reaction-assisted crystallization do not have the same elemental composition as the amorphous phase. The thermodynamic equilibrium phases in Ni-P alloy with 12-19 at.% of P (usual composition of Ni-P used for UBM) are Ni_3P and Ni. These two phases are the final products of self-crystallization of amorphous Ni-P alloy during thermal aging (Li *et al.*, 1998; Vafaei-Makhsoos, 1980). However, in the case of solder reaction-assisted crystallization of amorphous Ni-P alloy, the product is either only Ni_3P phase (Hung and Chan, 2000; Hung *et al.*, 2000b; Jang *et al.*, 1999) or a mixture of Ni_3P and Ni with an elemental composition closed to Ni_3P phase (Chen *et al.*, 2004; Hwang *et al.*, 2003; Liu *et al.*, 2000b). The reason for this is that Ni diffuses out from the crystallized Ni-P layer to react with Sn to form Ni_3Sn_4. Secondly, the solder reaction-assisted crystallization occurs selectively adjacent to the solder. It leads to the formation of a distinguishable layer in contact with original electroless Ni-P layer instead of a homogeneous crystallization of whole Ni-P layer. Third, a clear microstructural difference exists in the two types of crystallized Ni-P. Highly directional, well-developed, and fine columnar structure has been observed in the solder reaction-assisted crystallized Ni-P layer (Liu *et al.*, 2000b; Jang *et al.*, 1999; Zeng *et al.*, 2002). However, self-crystallized Ni-P has been reported to have small evenly distributed dark particles, which are the coherent precipitate (Mallory and Hajdu, 1990).

In addition to primary Ni_3P compound, other Ni-P compounds have been reported to form in different electroless Ni-P/solder joints at different experimental conditions. Under extended annealing conditions, two separate layers of Ni_3P and $Ni_{12}P_5$ were reported to form in electroless Ni-P/Sn-Pb solder joint after aging at 150ºC for 30 days (Liu *et al.*, 2000b). Sohn *et al.* (2004b) reported the formation of Ni_2P compound in the high P concentration (9 wt.%) electroless Ni-P/ Sn-3.5Ag solder joint after 30 min liquid state reaction at 250 ºC. The Ni_3P was the only compound initially present, however during prolonged reflow, a new

Ni_2P phase formed. Leaving these fine details aside, all the evidences show that solder reaction-assisted crystallization of electroless Ni-P UBM leads to the formation of Ni-P compounds, which is dominated by Ni_3P.

Besides Ni-Sn and Ni-P compounds, in a few recent studies (Chen *et al.*, 2004; Hwang *et al.*, 2003; Matsuki *et al.*, 2002; Sohn *et al.*, 2004b), a ternary Ni-Sn-P compound has been also reported to form in between Ni-Sn and Ni-P compounds. The thin (a few hundred nm) layer of this ternary Ni-Sn-P compound has been identified to consist of Ni_2SnP (Chen *et al.*, 2004; Matsuki *et al.*, 2002) and Ni_3SnP (Hwang *et al.*, 2003; Sohn *et al.*, 2004b) phase using TEM, whereas thick (a few micron) layer of Ni-Sn-P has been found to be of Ni_2SnP phase using electron probe micro analyzer (EPMA) and scanning electron microscope (SEM) (Wang and Liu, 2003; Yoon and Jung, 2005). These studies suggest that mainly the Ni_2SnP phase forms during electroless Ni-P/solder interfacial reactions and the Ni_3SnP phase exists as a minor phase.

2.1.1. Morphology of Intermetallic Compound

The formation of intermetallic compounds at the solder/UBM interface can be attributed to a surface reaction occurring between solder and UBM. Both liquid-state and solid-state reactions lead to the change in morphology of intermetallic compounds (Tu *et al.*, 2001a). Other than state of reactions, there are several material and processing factors that affect the morphology of intermetallic compounds. Material factors are the quantity of solute in Sn-matrix and the microstructure of solder and UBM (He *et al.*, 2004b; Tu *et al.*, 2003; Sohn *et al.*, 2004b). Processing factors are the reflow parameters such as the peak temperature, the dwell time over melting temperature of solder, and the post-reflow cooling rate (He *et al.*, 2004b, c).

Ni_3Sn_4 IMC with two types of morphologies, needle-type and chunky-type, have been reported to form at the electroless Ni-P/solder interface during reflow (He *et al.*, 2004b, d;

Hung *et al.*, 2000a, b; Jang *et al.*, 1999, 2000; Yokomine *et al.*, 2001). At the beginning of reflow, the formation of needle-type Ni_3Sn_4 grains dominates; however, more chunky-type Ni_3Sn_4 grains form and grow at the expense of needle-type Ni_3Sn_4 grains when the reflow time is prolonged (Jang *et al.*, 1999; He *et al.*, 2004b, d). It has been also reported (Hung *et al.*, 2000a, b) that the variation of the P concentration of electroless Ni-P layer does not affect the morphology of Ni_3Sn_4 IMC grown at the electroless Ni-P/solder interface.

There are a few studies in which the morphology of intermetallics is also affected in terms of size as well as shape by cooling rate (Chan *et al.*, 2003; Fan *et al.*, 2001; He *et al.*, 2004c; Mei and Dauskardt, 1999; Yao and Shang, 1996). However, most of these studies focus on the change of IMC morphology in bulk solder rather than at solder/UBM interface. The effect of cooling rate on IMC morphology has been reported to be more significant in the case of electroless Ni-P UBM than that of pure Ni (Mei and Dauskardt, 1999). Mei and Dauskardt (1999) studied the electrolytic Ni/Sn-Pb and electroless Ni-P/Sn-Pb interfacial microstructures after liquid-state reflow with air-cooled and water-quenched cooling processes. In the case of electrolytic Ni, no significant difference was observed between IMC layers formed with air-cooled and water-quenched processes. However in the case of electroless Ni-P, IMC grain size was around 6 μm with air-cooled cooling process and it was 2.5 μm with water-quenched cooling process.

In solid-state reactions, the morphology of Ni_3Sn_4 IMC becomes quite different as compared to liquid-state reactions. A continuous layer of Ni_3Sn_4 IMC with curved chunky-type or more appropriately scallop-type morphology has been reported to form during solid-state reaction instead of needle-type and chunky-type grains with channels that formed in the case of liquid-state reflow (He *et al.*, 2004a).

2.1.2. Growth Kinetics of Intermetallic Compound

Kinetic parameters of IMC growth are obtained to find out the controlling mechanism and activation energy of IMC growth. The growth of IMC layer can be represented by the following empirical power law

$$X = X_0 + kt^{1/n} \tag{2.1}$$

where, X is the thickness of IMC layer at the time t, X_0 is the initial thickness, n is the time exponent, and k is the temperature dependent rate constant. The variation in k with temperature can be represented by the following Arrhenius equation

$$k = A\exp(-Q/RT) \tag{2.2}$$

where, A is the prefactor, T is the absolute temperature, R is the gas constant and Q is the apparent activation energy of IMC growth. The activation energy can be determined from the slope of the straight line obtained by plotting ln k against $1/T$,

$$\ln k = \ln A - \frac{Q}{R} \cdot \frac{1}{T} \tag{2.3}$$

The growth of IMC is controlled by various mechanisms such as the diffusion of reacting element and the rate of reaction and this can be predicted by the value of n in the Eq. 2.1. If n is 1, then IMC growth is controlled by the rate of reaction, and if n is 2, then the diffusion of reacting element is the growth controlling mechanism. However, these are the ideal values. In practice, n may deviate from the ideal values due to the several factors such as the formation of multiple IMC layers, different diffusion mechanism, and time dependent apparent diffusivity. Moreover, n can be close to 3 if growth of IMC takes place in conjunction with the grain growth and/or coarsening of IMC (Ghosh, 2000a; Gusak and Tu, 2002).

For the growth of IMCs in electroless Ni-P/solder systems, different values of n and different controlling mechanisms have been reported in different studies (see Table 2.1). Such a wide variation of n values and different reported mechanisms indicate that electroless Ni-P/solder interfacial reactions are quite complex in nature. Although in most of the electroless Ni-P/solder interfacial studies, the growth of IMC has been assumed to follow diffusion-controlled kinetics (He *et al.*, 2004b; Hung *et al.*, 2000b; Jang *et al.*, 1999; Sharif *et al.*, 2005; Tu and Zeng, 2001; Yoon and Jung, 2004), the wide variation in the measured n values indicates that IMC growth kinetics in electroless Ni-P/solder systems is not as simple as assumed in many studies. In most of the electroless Ni-P/solder interfacial studies, either Ni_3Sn_4 or Ni_3P growth kinetics has been reported, which is due to their inter-related growths (Jang *et al.*, 1999; He *et al.*, 2004b; Sharif *et al.*, 2005; Yoon and Jung, 2004). However, no study reports the growth kinetics of ternary Ni-Sn-P compound.

In solid-state reactions, the growth rate of IMC layer becomes quite low as compared to liquid-state reactions. The growth rate of IMC in solid-state reactions has been reported to be about 4 orders of magnitude lower than that in liquid-state reactions (Lee *et al.*, 2002; Tu and Zeng, 2001). One of the main reasons for this is the formation of continuous IMC layer in the case of solid-state reactions as compared to the grains of IMC with solder channels in between them in the case of liquid-state reactions. The continuous layer of IMC acts as a barrier for elemental inter-diffusion between solder and metallization.

2.1.3. Other Phenomena Associated with Interfacial Reactions

Ripening or Coarsening of IMC Grains

During IMC growth in UBM/solder system, IMC grains experience ripening, too. During ripening, bigger grains grow at the expense of smaller grains. The driving force for the ripening of IMC grains has been reported to be the reduction of surface energy (Lifshitz and Slyozov, 1961) and/or the gain of bulk free energy (Gusak and Tu, 2002). In the case of pure Ni UBM, ripening of scallop-type Ni_3Sn_4 grains has been reported during liquid-state as well as solid-state aging (Ghosh, 2000a; Ghosh, 2000b). Also, in electroless Ni-P/solder systems, big chunky-type Ni_3Sn_4 gains have been reported to grow at the expense of small needle-type Ni_3Sn_4 grains due to the grain ripening during liquid-state reactions (Jang *et al.*, 1999; He *et al.*, 2004b; He *et al.*, 2004d).

Table 2.1. Growth kinetic parameters and proposed growth mechanism of various compounds in different electroless Ni-P/solder systems.

Solder	Experimental Conditions (Temperature/Time)	Compound	Value of n		Proposed growth mechanism of compound	Activation Energy (kJ/mol)	Reference
			Measured	Assumed			
Sn-37Pb	200-240°C/Up to 40 min	Ni_3P	---	2	Diffusion controlled process	31.8	Jang *et al.*, 1999
Sn-3.5Ag	130-170°C/Up to 625 h	Ni_3Sn_4	---	2	Diffusion controlled process	110	He *et al.*, 2004b
Sn-37Pb	130-170°C/Up to 625 h	Ni_3Sn_4	---	2	Diffusion controlled process	141	He *et al.*, 2004b
Sn-3.5Ag	251°C/Up to 5 h	Ni_3Sn_4	3.57	---	Complex process involving grain boundary diffusion, grain grooving, and grain coarsening	---	He *et al.*, 2004d
Sn-3.5Ag	260-300°C/Up to 8 min	Ni_3Sn_4	1.54-2.03	---	Ideal (lattice) diffusion controlled	---	Jeon *et al.*, 2003b
Sn-3.5Ag	125-175°C/Up to 2000 h	Ni_3Sn_4	2.65-4.52	---	Grain boundary diffusion controlled	---	Jeon *et al.*, 2003b
Sn-3.5Ag	100-170°C/Up to 60 days	Ni_3Sn_4	2.5	2	Diffusion controlled process	49	Yoon and Jung, 2004
Sn-3.5Ag	100-170°C/Up to 60 days	Ni_3P	---	2	Diffusion controlled process	---	Yoon and Jung, 2004
Sn-3.5Ag	240-270°C/Up to 120 min	Ni_3P	---	2	Diffusion controlled process	75	Sharif *et al.*, 2005
Sn-3.5Ag-0.5Cu	240-270°C/Up to 120 min	Ni_3P	---	2	Diffusion controlled process	103	Sharif *et al.*, 2005
Sn-0.7Cu	240-270°C/Up to 120 min	Ni_3P	---	2	Diffusion controlled process	131	Sharif *et al.*, 2005

There are a few theoretical and experimental studies in which IMC grain ripening or coarsening has been reported to influence the IMC growth kinetics (Ghosh, 2000a, b; Kim and Tu, 1996; Gusak and Tu, 2002). Kim and Tu (1996) proposed that there are two types of elemental flux in soldering reactions. One is the reaction flux, which is the diffusion of atoms from metallization to solder and vice-versa and the other is the ripening flux, which is the diffusion of atoms from small size IMC grains to large size grains. They proposed that the resulting flux of these two fluxes leads to a $t^{1/3}$ growth kinetics of IMC layer. The decrease of surface energy was considered as a driving force for ripening flux. Gusak and Tu (2002) also proposed a model that predicts $t^{1/3}$ growth kinetics of IMC grains by considering the flux-driven ripening. They considered the gain of bulk energy a driving force for ripening flux. On the other hand, Ghosh (2000a, b) found that radial growth of IMC gains could be described by empirical power laws, which could yield time exponent n greater than three. The values of n for radial growth of Ni_3Sn_4 gains were reported to be 4.77 with Sn-3.5Ag solder at 260 ºC temperature and 6.56 with Sn-38Pb solder at 200 ºC temperature. The corresponding values of n for the growth of Ni_3Sn_4 layer were found to be 4.69 with Sn-3.5Ag solder and 3.14 with Sn-38Pb solder (Ghosh, 2000b). Ghosh (2000a, b) attributed the large time exponent of Ni_3Sn_4 grain growth to the faceting process of grains as faceted surface is energetically singular. All these studies indicate that the IMC growth could follow $t^{1/3}$ growth kinetics if IMC growth takes place along with grain coarsening process. However, the $t^{1/3}$ growth kinetics may not be related to a particular set of mechanisms owing to the various mechanisms involved in the soldering reaction such as lattice and grain boundary diffusion, grain coarsening, faceting, and competitive growth of grains.

Spallation of IMC Grains

Spallation of IMC grains from reaction interface to the molten solder occurs due to two things: the mechanical stresses generated by the volume change between reacting materials and resulting IMC, and the dewetting of IMC due to the complete consumption of underlying metallization layer. However, from the literature, it is difficult to understand the IMC spallation phenomenon in electroless Ni-P/solder systems owing to the different materials and processes used and different explanations provided. Jang *et al.* (2000) reported the spallation of needle-type Ni_3Sn_4 grains in the electroless Ni-P/Sn-3.5Ag solder joint after two reflows of 60 s each over the melting temperature of the solder. They explained the Ni_3Sn_4 spallation as a result of the large volume change between Ni_3Sn_4 and Ni_3P. However, the similar kind of Ni_3Sn_4 spallation was not observed with Sn-Pb solder even after reflow at 240ºC for 40 min (Jang *et al.*, 1999). Moreover, Sohn et al. (2004b) observed that the spallation of Ni_3Sn_4 IMC grains in electroless Ni-P/Sn-3.5Ag solder joints is influenced by the solder-deposition method, the P concentration, and the reaction time and is increased with increasing the P concentration, the reaction time, and the solder volume. They attributed the spallation of Ni_3Sn_4 grains to the growth of ternary Ni-Sn-P layer in between Ni_3Sn_4 and Ni_3P layers and the needle type morphology of Ni_3Sn_4 grains.

2.1.4. Interfacial Elemental Diffusion and Reaction Mechanism

The growth of compounds during interfacial reactions between solder and electroless Ni-P requires the diffusion of all the constituent atoms. The growth of a compound itself involves several complex interfacial processes such as elemental diffusion, elemental dissolution in solder, phase nucleation, and creation and/or annihilation of defects. Moreover, the growth of multiple compounds in electroless Ni-P/solder joint makes the interfacial elemental diffusion and reaction mechanism much more complicated. As a result, the interfacial elemental diffusion and reaction mechanism of electroless Ni-P/solder joint has not been fully understood yet.

Although the interfacial elemental diffusion and reactions accompanying the electroless

Ni-P crystallization in electroless Ni-P/solder system have been investigated by a number of researchers (He *et al.*, 2004b, d; Jeon *et al.*, 2002; Liu *et al.*, 2000b; Matsuki *et al.*, 2002; Tu and Zeng, 2001), their results do not agree with each other. In different studies, different elements such as Ni and/or Sn and/or P were considered to be the dominant diffusing species. Jang *et al.* (1999) proposed two possibilities of elemental diffusion for solder reaction-assisted crystallization of electroless Ni-P. They proposed that during Ni_3Sn_4 growth either Ni diffuses out of electroless Ni-P layer to Ni_3P/Ni_3Sn_4 interface through the grain boundaries of Ni_3P layer or Ni_3P decomposes into P and Ni at Ni_3P/Ni_3Sn_4 interface and then P atom diffuses back interstitially to Ni_3P/electroless Ni-P interface to grow Ni_3P layer. However, they supported the latter mechanism as the grain boundary diffusion of Ni must be accompanied by the back diffusion of vacancies and they did not find any Kirkendall voids in the Ni_3P layer. Alternatively, He *et al.* (2004a, d) observed that Ni_3P layer has small Kirkendall voids, whose size and number increase with the duration of solid-state and liquid-state aging and thus they concluded that Ni is the dominant diffusing element in Ni_3P layer. Moreover, Matsuki *et al.* (2002) reported that the inter-diffusion of Ni and Sn takes place during Ni-P/Sn-Pb interfacial reactions and Ni acts as a dominant diffusing element in Ni-20mass%P and Ni_2SnP layers.

Other researchers claimed that Sn is the dominant diffusing element. Lee and Lin (1994) used W marker in the electroless Ni-P/Sn-Pb solder joint to study the elemental diffusion and concluded that Sn is the dominant diffusing element that reaches the Ni-P layer, whereas Ni remains in the Ni-P layer or diffuses slowly relative to Sn. Liu et al. (2000b) reported the formation of two new phases, Ni_3Sn_2 and $Ni_{12}P_5$ after prolonged aging and explained their formation to be due to the reaction of Sn with Ni_3P as the diffusion of Sn in Ni_3Sn_4 is much faster than that of Ni (Lee and Lin, 1994). However, one ambiguity was that if Sn reacts with Ni_3P instead of Ni, it should react at the beginning of the reaction and there was no evidence of such layers at that point. They also proposed that P diffusions away from electroless Ni-P to the Ni_3P layer to grow the Ni_3P layer. Further, Jeon et al. (2002) also suggested that the diffusion of Sn into P-rich Ni-P layer is faster than the diffusion of Ni or P to Ni_3Sn_4 IMC during Ni-P/solder interfacial reactions.

Some other researchers described Ni as a primary diffusing element. Ahat *et al.* (2001) reported the diffusion of Ni from electroless Ni-P to the solder. They found that owing to the diffusion of Ni from the Ni-P/Cu interface through the remaining Ni-P layer, many vacancies are left in Ni-P especially near the Ni-P/Cu interface. However, they didn't observe any voids in the remaining Ni-P layer due to the depletion of Ni. As before solder reaction-assisted crystallization, Ni-P layer has amorphous structure, it is very hard for element to diffuse through it because of lack of grain boundaries. Thus, Ni atoms that present in the lower part of Ni-P layer cannot compensate the consumption of Ni from the upper part of Ni-P layer. So if voids form in Ni-P layer, they should distribute not only at the Ni-P/Cu interface but also other parts of Ni-P layer.

Although none of the existing work presents the complete elemental diffusion process of electroless Ni-P/solder system, a partial but common understanding of interfacial elemental diffusion and reaction mechanism can be made. In electroless Ni-P/solder interfacial reactions, the growth of Ni_3Sn_4 IMC requires Ni atoms from electroless Ni-P UBM and Sn atoms from solder (Lee and Lin, 1994; Ahat *et al.*, 2001). During the diffusion of these atoms, P atoms retain in the Ni-P layer (Ahat *et al.*, 2001; He *et al.*, 2004a; Matsuki *et al.*, 2002) and as a result a higher P containing Ni-P (Ni_3P) layer forms in between Ni_3Sn_4 and Ni-P layers (Jang *et al.*, 1999). The out diffusion of Ni from electroless Ni-P moves the Ni_3Sn_4/Ni_3P interface toward the electroless Ni-P layer (Liu *et al.*, 2000b).

In fact, electroless Ni-P/solder interfacial elemental diffusion and reactions are the complicated inter-diffusion processes of all the elements of the system such as Ni, Sn, and P and thus the existence of all the compounds should be considered in this. Accordingly, a detailed analysis will be carried out in the present work.

2.1.5. Kirkendall Void Formation at the Electroless Ni-P/Solder Interface

Kirkendall voids form in a material system due to the unbalanced atomic diffusion. However if there is an intermediate layer between two materials, it may act as a diffusion barrier for the atoms of one material, which in turn can cause the rapid diffusion of other material into this. As there is a counter diffusion of vacancies, these vacancies accumulate in the other material and finally form voids. These voids are called as Kirkendall voids.

The formation of Kirkendall voids is a reliability issue for solder interconnects, as the excessive voiding degrades the mechanical properties of solder joints. The formation of Kirkendall voids at the electroless Ni-P/solder interface has been reported in several interfacial studies (Ahat *et al.*, 2001; Goyal *et al.*, 2002; He *et al.*, 2004a, d; Jeon *et al.*, 2002; Matsuki *et al.*, 2002; Zeng and Tu, 2002). Goyal *et al.* (2002) observed Kirkendall void formation at the interface between Ni_3Sn_4 IMC and P-rich (Ni_3P) layer and explained their formation to be due to the faster Sn diffusion into the Ni-P layer than Ni diffusion into the solder. Jeon *et al.* (2002) used TEM to study the liquid-state reactions of electroless Ni-P UBM with Sn-Pb and Sn-Ag solders. They also reported the formation of Kirkendall voids inside the Ni_3Sn_4 layer at the locations close to Ni_3P layer. This result also indicates that Sn diffuses into P-rich layer faster than Ni or P diffusion into IMC. However, Zeng and Tu (2002) reported Kirkendall voids in the Ni-Sn-P layer of electroless Ni-P/SnAgCu solder joint reflowed for five times.

Matsuki *et al.* (2002) found two types of Kirkendall voids at electroless Ni-P/SnPb interface. The first were spherical voids that formed at the $Ni_{48}Sn_{52}/Ni_2SnP$ interface due to the slow diffusion of Ni in Ni_2SnP as compared to in Ni_3Sn_4. The second were columnar voids that formed at the Ni_2SnP/Ni-20mass%P interface due to the slower diffusion of Sn in Ni_2SnP that that of Ni. On the other hand, Ahat *et al.* (2001) reported that Kirkendall voids form near the interface between Ni-P and Cu substrate of Cu/Ni-P/SnAgCu solder joint.

Recently, He *et al.* (2004a, d) examined the liquid-state and solid-state interfacial reactions of Ni-P UBM with Sn-37Pb and Sn-3.5Ag solders. They found that Kirkendall voids form in the Ni_3P layer and attributed their formation to the unbalanced elemental diffusion of Ni and Sn in the growth of Ni_3P layer. In summary, though various findings and explanations have been reported on the formation of Kirkendall voids in electroless Ni-P/solder systems, however inconsistency exists among them. As in some reliability studies (Ahat *et al.*, 2001; Jeon *et al.*, 2002; Goyal *et al.*, 2002), Kirkendall voids have been observed at the fracture surfaces of Ni-P/solder joints, these voids may have detrimental effect on the strength of solder joint and thus should be studied in detail.

2.2. Mechanical Properties of Ni-P/Solder Joints

The mechanical reliability of solder joints is a critical issue for the reliability of flip chip and BGA packages as the solder joint makes the thermal and electrical interconnection between IC chip and substrate. Since the failure of a single solder interconnect can cause the failure of a complete device or even the malfunction of entire system, thus to keep the interconnection working well, solder joint must be able to bear the mechanical stresses that generate in the electronic packages. As shown in Fig. 2.3, shear and tensile stresses generate in an electronic package during thermal loading (because of reflow or service temperature) due to the coefficient of thermal expansion (CTE) mismatch between constituting materials. The mechanical stresses vary when the packages experiences thermal cycle either during reflow process or during service and such thermal cycle causes the fatigue of solder joint. Moreover, the excessive growth of IMCs makes the solder joint more prone to failure as IMCs are brittle in nature and their growth itself generates intrinsic stresses in the solder joint. It is, therefore, crucial to understand all the factors that can affect the mechanical properties of solder joint to avoid unexpected failure of the device or system.

Various testing methods such as tensile, shear, fatigue, indentation are used to investigate the mechanical properties of solder joint. Tensile and shear strength of solder joint are the important parameters to know the load-bearing capacity of the joint. Whereas, the fatigue testing of solder joint is helpful to determine the lifetime of the joint as the electronic components usually undergo thermal or mechanical cycles during service. The indentation method is used to determine the micro-mechanical properties such as hardness and modulus of solder, metallization, and interfacial compounds. Moreover, there are some other mechanical tests such as three and four point bending tests, which are used for failure analysis of the solder joints in a package. In these types of tests, a package experiences the mixed (tensile + shear) stresses that are very common in actual practice. However, these tests cannot find out load-bearing capacity or life time of a solder joint or package.

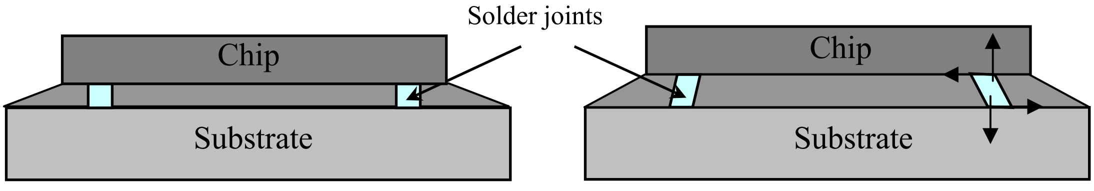

(a) (b)

Fig. 2.3. Schematic illustration of an electronic package (a) with zero strain and (b) with thermal load, showing the generation of shear and tensile stresses in the solder joints between chip and substrate.

In the current work, tensile testing and nono-indentation methods have been used to investigate the mechanical properties of electroless Ni-P/solder joint, hence a brief description of these testing methods is given below:

Tensile Testing

Tensile testing is an appropriate method to identify the interfacial factors that affect the strength of solder joint. The reason for this is the sensitivity of the tensile strength of a solder joint to the changes that take place at various interfaces in the solder joint. Tensile testing is also a useful method to determine the adhesive strength between UBM and underlying chip metallization.

Normally during tensile testing, if the solder is weaker than the UBM/solder interface, deformation occurs inside the solder rather than in the IMC layers. In this case, strain energy is accommodated by the deformation and the gradual ductile rupture of the solder. On the other hand, if solder is stronger than the UBM/solder interface, only a limited amount of strain energy is accommodated by the solder and the rest is transferred to the IMC layers. Thus, the tensile behavior of solder joint depends mainly upon the interfacial reactions or microstructure. Moreover, it has been reported that if IMC is thin, fracture occurs inside the solder and as the IMC grows, fracture occurs either at the solder/IMC interface or inside the IMC layers (He *et al.*, 2005; Frear *et al.*, 1991).

In tensile testing, the strength of solder joint is significantly influenced by the thickness of solder in between the metallizations. If the solder layer thickness in between the metallizations is too low, then the strong metallizations restrain the deformation of solder and thus the tensile strength of solder joint appears much higher than that of bulk solder strength. He *et al.* (2005) observed that because of the constrains from adjacent stronger metallizations, in the case of thin Sn-3.5Ag solder layer in between Ni-P metallizations, the tensile strength of Ni-P/Sn-3.5Ag solder joint (76 MPa) was much higher than that of bulk Sn-3.5Ag solder (40 MPa). Another testing parameter that influences the tensile strength of solder joint is the strain rate. The tensile strength of bulk solder (Vianco, 1999) and solder joint (Kawashima *et al.*, 1992; Takemoto and Matsunawa, 1997) have been reported to be higher with the higher strain rate. In real practice, solder interconnect experiences slow deformation, hence a low deformation rate is preferred for measuring the tensile strength of solder joint.

Nano-indentation

The nano-indentation technique is used to measure the mechanical properties such as Young’s modulus and hardness of materials. Recently, this technique has been extensively used to measure the mechanical properties of solder, metallizations, and interfacial compounds of solder joint. The reason for this is the ability of this technique to test small volume and the solder joint is usually of a few hundreds microns.

In the nano-indentation method, the analysis of load-depth data is done preferably using Oliver and Pharr method (Oliver and Pharr, 1992). In this method, the unloading data is fitted by a power law function instead of linear function. The power law function can be expressed as

$$P = a(h - h_c)^m \tag{2.4}$$

where, h is the depth at any stage of loading, h_c is the depth through which contact is made (contact depth), and a and m are constants. The contact depth is determined from the expression:

$$h_c = h_{\max} - \varepsilon(CP_{\max}) \tag{2.5}$$

where, h_{max} is the maximum depth, P_{max} is the maximum load, C is the contact compliance which is equal to the tangent to the unloading curve at maximum load. The value of ε depends on the indenter geometry. For a Berkovich indenter, ε is 0.75. The diamond area function A(h) for a Berkovich indenter is given by

$$A = 24.5h^2 \tag{2.6}$$

The elastic modulus is calculated by analyzing the unloading portion of the load-depth curve according to the following equation:

$$C = \frac{1}{2E_r}\frac{\sqrt{\pi}}{\sqrt{A}} \tag{2.7}$$

where, E_r is the reduced modulus, which is given by the following equation:

$$\frac{1}{E_r} = \left.\frac{1-\nu^2}{E}\right|_{sample} + \left.\frac{1-\nu^2}{E}\right|_{indenter} \tag{2.8}$$

where, E is the Young's modulus, ν is Poisson's ratio.

The hardness H is determined from the maximum load P_{max} and the projected area of contact $A(h_c)$ as

$$H = \frac{P_{\max}}{A(h_c)} \tag{2.9}$$

Similar to the tensile testing method, the results of nano-indentation test are also influenced by the testing parameters and sample geometry. For the nano-indentation test, the sample surface must be very flat and smooth. The rough surface of Sn-Pb solder has been reported to cause inaccurate measurement of the mechanical properties of solder (Ye *et al.*, 2003b). Gao and Takemoto (2006) investigated the effect of nano-indentation testing parameters on the mechanical properties of Sn-3.5Ag solder. They reported that the modulus value of solder does not depend on the loading rate, however higher loading rate results in higher hardness. Usually, a low loading rate of equal or less than 0.5 mN/s, is used for the solders (Kumar *et. al.*, 2006; Xu and Pang, 2006).

2.2.1. Mechanical Testing of Electroless Ni-P/Solder Joints

Many studies have been done on the mechanical reliability of electroless Ni-P/solder joints. However, different testing methods and sample geometries have been used in these studies, which lead to the conflicting results and explanations. Therefore, it is difficult to compare the mechanical testing results reported in different studies.

He *et al.* (2005) investigated the tensile strength of thermally aged electroless Ni-P/Sn-3.5Ag solder joints. They observed that ductile fracture occurs inside the bulk solder in the as-soldered solder joint. However, fracture moves to the solder/Ni_3Sn_4 interface and then brittle fracture occurs in the Ni_3Sn_4 layer with the growth of Ni_3Sn_4 IMC. They also reported that the tensile strength of electroless Ni-P/Sn-3.5Ag solder joint decreases severely with a brittle fracture at the Ni_3P/Ni interface due to the stress caused by the volume changes during the phase transformation of electroless Ni-P layer.

Chonan *et al.* (2002a, b) studied the strength of Ni-P/Sn-Ag, Ni-P/Sn-Ag-Cu, and Ni-P/Sn-Pb solder joints using a cold bump pull tester. Solder joints having different thicknesses and P concentrations of Ni-P layer were studied. They observed that the strength of solder joints decreases with the increase in P concentration in Ni-P layer. They also observed that independent of the solder materials, the solder joint strength is very sensitive to the thickness of P-rich (Ni_3P) layer and the strength deceases with the thickness of P-rich layer. They observed that brittle failure of solder joints occurs partially inside the P-rich layer and attributed this failure to the voids in the P-rich layer. Alam *et al.* (2003) also studied the effect of P concentration of Ni-P layer on the mechanical strength of Cu/Ni-P/Sn-Ag solder by performing shear testing of solder balls; however they also used Ni-P layers of different thicknesses. The Ni-P thickness used was the higher in the case of lower P containing Ni-P layer. They reported nearly the same conclusions as Chonan *et al.* (2002a) reported. Ball shear testing method was also used by Jeon *et al.* (2002) to study the mechanical properties of electroless Ni-P/Sn-3.5Ag and electroless Ni-P/Sn-37Pb solder joints after reflow for 1 to 16 min. They observed that in both types of solder joints, fracture occurs always inside the solder, but as the reflow time increases, the point of fracture initiation moves to the Ni_3Sn_4 IMC. They observed some Kirkendall voids in the Ni_3Sn_4 IMC and concluded that these Kirkendall voids and Ni_3Sn_4 IMC are responsible for the shift in the point of fracture initiation.

Besides the ball shear test, other shear tests such as lap-shear (Sohn *et al.*, 2005) or direct-shear (Ahat *et al.*, 2000) of components were also used in a few reliability studies of electroless Ni-P/solder joints. Sohn *et al.* (2005) observed two fracture modes in the reflowed Ni-P/Sn-3.5Ag solder joints; ductile fracture passing through the bulk solder and brittle fracture passing through the interface between Ni_3Sn_4 and Ni-P layers. They observed the spalling of Ni_3Sn_4 IMC and claimed the brittle fracture occurs due to the Ni_3Sn_4 spalling and the growth of Ni-Sn-P layer. Nonetheless, no brittle-fracture area matched directly with the spalling area. Ahat *et al.* (2000) also observed two fracture modes in the Sn-36Pb-2Ag/Ni-P/Cu and Sn-3.5Ag/Ni-P/Cu joints. They observed ductile fracture mode that occurred in the bulk solder of as-prepared solder joint and brittle fracture mode that occured at different locations depending upon the thermal aging duration. Brittle fracture occurred at three locations, in the solder, in the Ni_3Sn_4 layer, and at the solder/Ni-P interface, in the joints aged for 250 h and it occurred at the Ni-P/Cu interface in the joints aged for 1000 h. They related the brittle failure of solder joint to the excessive depletion of Ni characterized by a rapid accumulation of P in the remaining Ni-P layer that resulted in poor adhesion between Ni-P layer and Cu substrate due to the crack formation at the Ni-P/Cu interface.

Liu and Shang (2000a, b) examined the interfacial fatigue resistance of thermally aged Sn-37Pb/Ni-P solder joint using flexural peel specimen. In the as-reflowed specimen and the specimen mild-aged at 170ºC for 15 days, the fatigue-crack-growth occurred predominantly along the interface between the solder and the Ni_3Sn_4 IMC. Whereas in the specimen over-aged at 170ºC for 30 days, the fatigue-crack-growth depended strongly on the applied strain energy release rate. At low to medium rate, the fatigue-crack-growth followed the same trend as it followed at shorter aging condition. However, the high rate resulted in the brittle fracture passing through the Ni_3Sn_2 layer that located underneath the Ni_3Sn_4 IMC layer. The over aging of solder joint resulted in a sharp drop in the fatigue resistance of the Sn-37Pb/Ni-P interface. They attributed this sharp drop in interfacial fatigue resistance to the brittle fracture of the Ni_3Sn_2 IMC that grew in the over-aged specimen.

There are also some studies (Goyal *et al.*, 2002; Mei *et al.*, 1998) that used three and four point bending tests to analyze failure mechanism of electroless Ni-P/solder joints in a BGA package. Goyal *et al.* (2002) reported that brittle failure occurs in the electroless Ni-P/Sn-Pb solder joint due to the Kirkendall voids formed at the interface between P-rich

Ni-P layer and Ni-Sn IMC, segregation of P in P-rich Ni-P layer, and density of mudflat crack in the P-rich Ni-P layer. However Mei *et al.* (1998) reported that the brittle failure of Cu/electroless Ni-P/Au/Sn-Pn joints occurs owing to the one or more failure mechanism(s) such as P segregation in Ni-P, contamination or oxidation of Au/Ni-P metallization, and extensive cracking in Ni-P.

2.2.2. Factors Causing the Brittle Failure of Ni-P/Solder Joints

In general, the mechanical behavior of solder joint can be affected by several factors such as reflow and service temperatures, reflow and service durations, and the microstructural and physical properties of solder and metallization materials. Though all these factors are different, each of these factors influences the microstructure and intrinsic stresses of solder joints and thereby changes their mechanical behavior.

The solder joint is actually comprised of solder, metallization layers, and IMCs that form between solder and metallization. The formation of IMCs in a solder joint is closely related to the reflow and service conditions such as temperature and duration. The physical properties of these IMCs differ a lot from those of solder and metallization materials. The IMCs are much harder compared to the solder and metallization materials and this indicates their high brittleness (Frear *et al.*, 1994; Mallory and Hajdu, 1990). The growth of IMCs can be beneficial or detrimental for the reliability of solder joint. Formation of a thin layer of IMCs during soldering is desirable and beneficial to achieve good metallurgical bond between solder and metallization. However, the excessive growth of IMCs can affect the mechanical reliability of solder joint as they are very brittle in nature and can act as initiation site for micro-cracks. In addition, the difference of density among the IMCs, metallization, and solder can cause the development of intrinsic stresses in the solder joint due to the excess growth of IMCs.

The microstructure of solder joint is also related to the process and service conditions such as temperature and time. However, the change in the microstructure of solder and metallization with the process and service conditions depends upon solder and metallization materials itself. Thus, it is imperative to understand the evolution of the microstructure (interfacial as well as bulk) of solder joint and its effect on the mechanical properties of the solder joint.

A number of studies have reported the brittle failure of electroless Ni-P/solder joints; however, no conclusive factors that cause the brittle failure have been identified. This is because of the different results reported in different studies. Goyal *et al.* (2002) and Mei *et al.* (1998) observed brittle fracture at the Ni_3Sn_4/Ni-P interface of electroless Ni-P/Sn-Pb solder joint and identified several possible failure mechanisms such as P segregation in Ni-P, contamination or oxidation of Au/Ni-P metallization, and extensive cracking in Ni-P. Alam *et al.* (2003) also observed brittle fracture in the Sn-Ag/Au/Ni-P/Cu joint and concluded that the formation of crystalline P-rich Ni layer at the interface between Sn-Ag solder and Au/Ni-P/Cu pad deteriorates the mechanical strength of the joint. However, Ahat *et al.* (2000) reported that the brittle failure occurs at the Ni-P/Cu interface of Sn-Ag/Ni-P/Cu joint due to the Kirkendall voids, which form due to the excessive depletion of Ni in the remaining Ni-P layer or the rapid accumulation of P. On the other hand, He *et al.* (2005) reported that the formation of Kirkendall voids in the Ni_3P layer do not affect the Ni-P/Sn-3.5Ag solder joint strength. Nevertheless, the change in Ni-P volume during its transformation and growth of Ni_3Sn_4 were reported to be the reasons for deterioration in the joint strength (He *et al.*, 2005). Further, some studies reported that the formation of Ni_3Sn_2 (Liu and Shang, 2000a) or Ni_2SnP (Matsuki *et al.*, 2002) layer at the Ni-P/Ni_3Sn_4 interface causes the brittle fracture of electroless Ni-P/Sn-Pb solder joint. Recently, Sohn *et al.* (2005) claimed that the spalling of Ni_3Sn_4 IMC takes place in the Ni-P/Sn-Ag solder joint due to the growth of Ni_3SnP layer, and these together cause the brittle failure of solder joint. However, they could not correlate their claim with the location of fracture surfaces. Although all these studies indicate that the interfacial reactions and microstructure of electroless Ni-P/solder joint are the critical factors for the mechanical reliability of solder joint, the main factors causing the brittle failure of electroless Ni-P/solder joints are still not clear. Thus, more work has to be done to identify these factors.

2.3. Electromigration

Electromigration is defined as a mass transport phenomenon caused by the high density of electric current in a media where charge transport is electronic rather than ionic (Golopentia and Huntington, 1978). When an electric field is applied to a conductor, the electromigration force on the activated ion constitutes two forces and is given by

$$F_{em} = F_{es} + F_{wd} \tag{2.10}$$

where, F_{es} and F_{wd} are the electrostatic field force and the wind force, respectively. The electrostatic field force is due to the field interaction with the effective ionic charge. As the effective ionic charge is diminished by the screening effect of ion's bound-electrons, the magnitude of the electrostatic field force is small. On the other hand, the wind force, which is due to the momentum transfer between moving charge carriers and activated ions, is of significant magnitude. These two forces act in opposite directions, the electrostatic force in the direction of electric field, and the wind force in the opposite direction as it is brought by electrons flowing in the direction opposite to the applied field. The resulting electromigration force F_{em} is written as

$$F_{em} = eEZ^* = e\rho jZ^* \tag{2.11}$$

where, Z^* is the effective charge number and it represents the net effect of the electrostatic field force and the wind force, ρ is the resistivity, and j is the current density.

Electromigration-induced Mass flux

In the case of high density electric current, the effect of electromigration gives rise to the movement of ions along with the electron current (Campbell and Huntington, 1969; Christon 1994; Golopentia and Huntington, 1978; Hsieh and Huntington, 1978; Huntington *et al.*, 1984; Sullivan, 1967; Routbort, 1968). If μ and C are the mobility and the concentration of moving ions, respectively, then the resulting ionic flux due to electromigration force, F_{em}, is given by

$$J_{em} = CF_{em}\mu = Cv_d \tag{2.12}$$

where, v_d is the drift velocity. From the Nernst-Einstein relation, the mobility is

$$\mu = D/kT \tag{2.13}$$

where, D is the diffusivity, k is the Boltzmann's constant, and T is the absolute temperature.

and Ho, 1988).

When an electric current passes through a polycrystalline metallic thin film, the ionic flux *J* comes primarily from electromigration occurring in lattice and at the grain boundary. For the lattice, the lattice electromigration flux (Gupta and Ho, 1988) is

$$J_l = \frac{1}{kT} C_l D_l Z_l^* j \rho e \tag{2.15}$$

and for an ideal grain structure, the grain boundary electromigration flux (Gupta and Ho, 1988) is

$$J_b = \frac{1}{kT} \frac{C_b \delta}{d} D_b Z_b^* j \rho e \tag{2.16}$$

where, the subscripts *l* and *b* denote the parameters of lattice and grain boundary, respectively. The quantity δ is the effective boundary width (~10 Å) for mass transport and d is the average gain size. Gupta and Ho (1988) calculated the relative contribution of J_l anf J_b in the electromigration with the help of their ratio

$$\frac{J_l}{J_b} = \frac{N_l}{N_b} \frac{d}{\delta} \frac{D_l}{D_b} \frac{Z_l^*}{Z_b^*} \tag{2.17}$$

They showed that for a thin film with 1 μm grain size at moderate temperature (~0.5 T_m), the ionic flux from the lattice diffusion is very small (~0.01 %) as compared to the grain boundary diffusion. Thus, the latter becomes the dominant mode of mass transfer and distinguishes the effect of electromigration in thin films from bulk materials.

In thin film interconnects, electromigration-induced damages usually appear in the form of voids and hillocks (Durkan *et al.*, 1999; Gupta and Ho, 1988; Pierce and Brusius, 1997). Voids grow and link together to cause electrical discontinuity in conductor line, which lead to open circuit failure. Hillocks also grow and extrude out materials to cause short-circuit failure. This phenomenon can be observed from the response of a short Al strip deposited on TiN. This type of structure is called as Blech structure for electromigration test (Blech, 1976; Blech and Herring, 1976). Fig. 2.4 is a micrograph of aluminium stripes deposited on TiN and annealed at 350°C in the presence of current of 3.7×10^5 A/cm^2 density for 15 h (Blech, 1976). The strips deplete at the cathode (-ve) end and extrude at the anode (+ve) end.

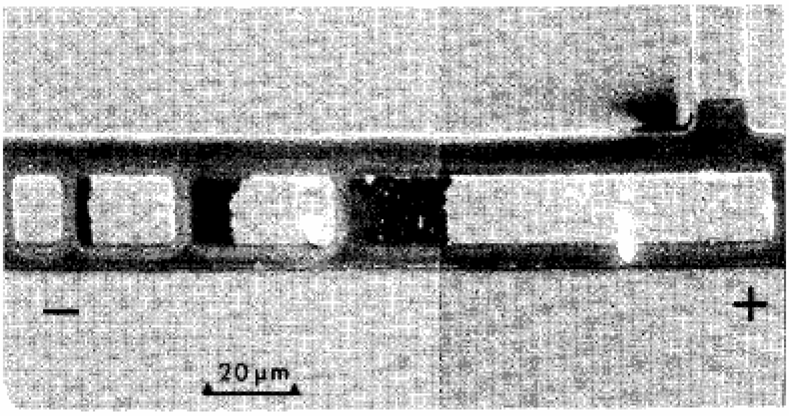

Fig. 2.4. Drift of four aluminium stripes of various lengths annealed at 350°C in the presence of current of 3.7×10^5 A/cm^2 density for 15 h (Blech, 1976).

Effect of Electromigration on Interfacial Reactions

When two different materials are kept in contact, atoms diffuse from one material to another due to concentration gradients (more precisely, chemical potential gradients) and new phases form as well if the thermodynamic and kinetic conditions are appropriate. The reactions that take place in the vicinity of the contact are called as interfacial reactions. At the initial stage of the interfacial reactions, new phases nucleate, and then the associated mass transport governs their growth. The diffusion flux resulted from concentration gradient is described by Fick's first law

$$j_c = -D\frac{\partial C}{\partial x} \tag{2.18}$$

where D is the diffusivity, $\partial C/\partial x$ is the concentration gradient, and x is the axis parallel to the concentration gradient. From Eqs. 2.14 and 2.18, the total ionic flux due to the concentration gradient and electromigration is

$$j_T = j_c + j_{em} = -D\frac{\partial C}{\partial x} + \frac{CDZ^* e\rho j}{kT} \tag{2.19}$$

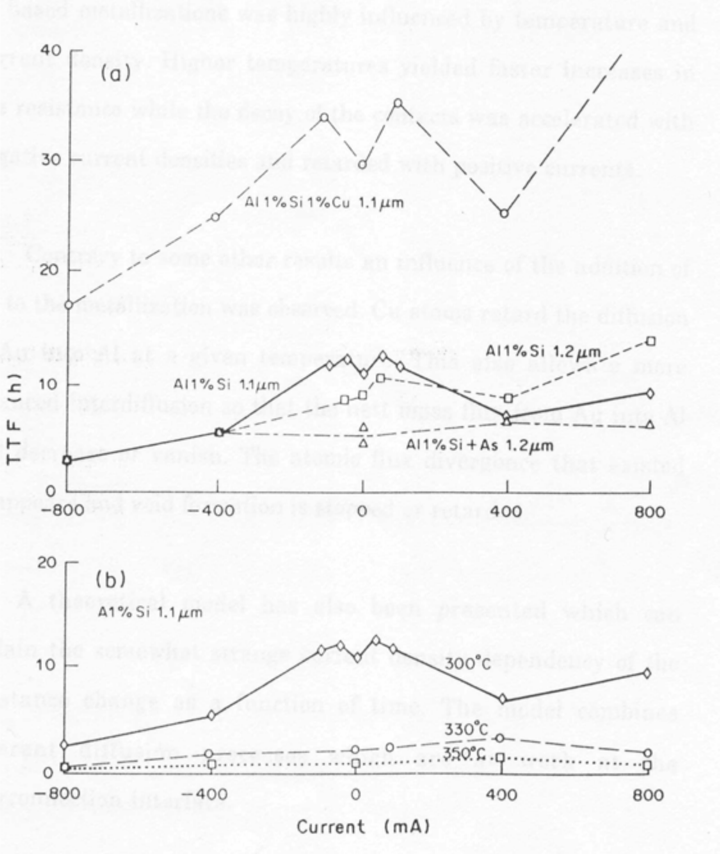

Fig. 2.5. TTF as a function of current stress for different samples for a criterion of ΔR/R = 100 %: (a) at 300 °C and (b) at different temperatures (Vanhecke *et al.*, 1993).

Liu *et al.* (1998) investigated the influence of electric current on Al/Ni interfacial reactions. They observed that the same IMCs, Al_3Ni and Al_3Ni_2, form at the interfaces with and without the passage of electric current, however, the current significantly influences the thickness of Al_3Ni_2 phase. The Al_3Ni_2 IMC grew three times thicker in the sample aged with current of 10^3 A/cm^2 density than in the sample aged without current. However, the thickness of Al_3Ni layer did not change significantly due to the current. A long incubation period was reported to require for the formation of Al_3Ni_2 phase in the absence of current. Chen *et al.* (1998) studied the same effect on Sn/Cu and Sn/Ni interfacial reactions. A DC current of 5×10^2 A/cm^2 was passed through the samples at 200°C for 72 to 480 hrs. They observed a dependence of IMC formation on the direction of the flow of electrons. In Sn/Ni system, the formation of Ni_3Sn_4 layer was enhanced when the flow of electrons was in one direction (from Sn to Ni) and inhibited when flow was in the opposite direction. However, no significant effect of electromigration was observed on the Sn/Cu interactions. Further in the similar Sn-3.8Ag-0.7Cu/Cu system, Gan and Tu (2005) observed the effect of electromigration on the Cu-Sn IMC growth, but at relatively higher (~ 10^4 A/cm^2) current density.

In an electromigration study on Sn/Ag system, Chen and Chen (1999) passed the DC current of 5×10^2 A/cm^2 density at 140°C and 200°C for 1 to 20 days and observed that the effect of electromigration depends upon temperature. The electromigration had significant effect on IMC growth at low temperature (140°C) but no effect at higher temperature (200°C). They explained this observation using the difference in the temperature dependence of the two terms of Eq. 2.19. They also investigated the effect of electromigration upon Sn/Ag and Sn/Ni interfacial reactions at various temperatures and current densities (Chen and Chen, 2002). The current densities used were 5×10^2 and 1×10^3 A/cm^2. They observed that the effect of electromigration increases with increasing the current density and decreases with increasing the temperature.

Chan and Chan (2003) reported the effect of electromigration on Sn/Ni interfacial reaction at low (100°C) temperature and 4×10^3 A/cm^2 current density. They reported that while two Ni-Sn phases, stable Ni_3Sn_4 and metastable $NiSn_3$, form at both the Sn/Ni and Ni/Sn interfaces due to the aging without current, only one Ni_3Sn_4 phase forms at the Sn/Ni interface and very thick $NiSn_3$ phase with Ni_3Sn_4 phase form at the Ni/Sn interface due to the aging with current. They explained that in the presence of current, at the Sn/Ni interface (where electrons flow opposite to the direction of Ni diffusion) the nucleation of $NiSn_3$ phase is inhibited, whereas at the Ni/Sn interface (where the electrons flow in the same direction as that of Ni diffusion) the nucleation and growth of the $NiSn_3$ phase is enhanced.

Bertolino *et al.* (2001) investigated the effect of electromigration in Al-Au multi-layered sample by passing the DC current of densities of 0.0, 5.09×10^2 A/cm^2, and

1.09×10^3 A/cm^2 at 450°C for up to 8 h. They observed the same nature and sequence of the formation of Al-Au IMCs in the samples aged with and without current. However, the growth rates of the IMC layers were different from each other. In the presence of current, all four Al-Au IMCs, Au_5Al_2, Au_2Al, AuAl, and $AuAl_2$ formed even for the shortest reaction time, but their thicknesses differed from each other considerably with time. The Au_2Al phase grew at the expense of Au and when Au is consumed completely, the thickness of Au_5Al_2 phase began decreasing. However, there was negligible change in the thickness of AuAl and $AuAl_2$. The authors attributed this phenomenon to the effect of electromigration on nucleation as well as growth processes.

Shi *et al.* (2000) investigated the effect of electromigration on the interface evolution of nano-scale Au-Ag bimetal film on SiO_2 substrate. The experiments were conducted at 140°C for 5 and 30 min with a current of 2 A/cm^2 density. It was observed that the electromigration alters the aggregation states of metal atoms in Au-Ag film from continuous islands to isolated islands and further to a corrugated sheet structure. It was also found that electromigration induces the chemical reaction occurring at the interface between Au-Ag film and SiO_2 layer. They claimed that the electromigration in Au-Ag bimetal film on SiO_2 surface is accompanied with chemical interfacial reaction.

Effect of Electric Current on the Phenomena related to Microstructure

Conrad (2000) reported several examples of effect of electric current on solid-state phase transformations such as IMC formation and growth, precipitation, crystallization of amorphous alloys, and recrystallization and grain growth of cold worked metals. It was reported that an electric current of density greater than 10^3 A/cm^2 accelerates the solid-state transformations in some metals and alloys, whereas it retards in others. This effect depends upon the composition, prior heat treatment of the materials, and the strength and frequency of current. The effect of current on the nucleation rate was also reported.

There are several studies (Lai *et al.*, 1989; Lai *et al.*, 1995; Teng *et al.*, 1996) on the electric current-induced crystallization behavior of rapidly quenched amorphous Fe-Si-B alloys. It was reported that the electric current accelerates the Fe-Si-B crystallization. Koppenaal and Simcoe (1963) studied the effect of DC current on the precipitation rate of Al-4wt.% Cu alloy with the help of resistivity measurements and reported that beyond a critical value of the current density of around 10^3 A/cm^2, current increases the precipitation rate of the alloy linearly. Though several examples of the effect of electric current on the microstructural behavior of materials and alloys are available, but our understating of the mechanisms associated with these effects is still not complete.

2.4. Electromigration Effect in Solder Joint

2.4.1. Electromigration-Induced Electrical Failure of Solder Joint

Brandenbery and Yeh (1998) observed that the electromigration-induced electrical failure occurs in eutectic Sn-Pb solder interconnect within a few hundred hours of aging at 150°C under a current of 8×10^3 A/cm^2 density. This current density is about one order of magnitude less than that used in wafer level interconnects such as Al and Cu metallic lines (Blech, 1976; Blech and Herring, 1976; Christon, 1994; Gupta and Ho, 1988). Electromigration rate in solder alloys has been reported to be very fast even at room temperature (Liu *et al.*, 1999; Liu *et al.*, 2000a). The reasons for fast electromigration rate in solder alloys are their low melting point and high atomic diffusivity. Moreover, the line-to-bump configuration in flip chip package produces very high current density change when current flows from the IC metallic line into the solder interconnect and vice versa. This change in current density results in current crowding in solder joint, which further enhances the electromigration-induced electrical failure of solder joint (Yeh *et al.*, 2002; Yeh and Tu, 2000). Yeh *et al.* (2002) investigated the current crowding effect on the electromigration failure of eutectic Sn-Pb solder joint. They observed that electromigration-induced electrical failure of eutectic Sn-Pb solder joint occurs within 40 h of aging at 125°C with a current of 2.25×10^4 A/cm^2 density. During the failure, voids nucleated near the current crowding region and then propagated throughout the cross-section. The nucleation of voids took long incubation time but they propagated very fast. The position of voids was reported to depend strongly on the current crowding region.

Lee *et al.* (2001b) studied electromigration effect in the eutectic Sn-Pb solder interconnect aged at 120°C for various durations up to 324 h with a current of 10^4 A/cm^2 density. It was reported that during electromigration, voids and Pb rich hillocks form at the cathode (-ve) side and the anode (+ve) side of the solder interconnect, respectively. A very large compositional redistribution occurred in the Sn-Pb solder, where a Pb-rich layer formed at the anode side suggesting that Pb was the dominant diffusing species at low temperature (120°C). The same authors also investigated the electromigration effect in the Sn-3.8Ag-0.7Cu flip chip solder joint (Lee *et al.*, 2001a). The UBM on chip side was electroless Ni-P and on board side it was electroplated Cu. The experiments were performed at 120°C and at current density of 3.8×10^4 A/cm^2. They observed that unlike in eutectic Sn-Pb solder, electromigration has very small affect in Sn-3.8Ag-0.7Cu solder. The void formation was negligible in the case of Sn-3.8Ag-0.7Cu solder, but some hillocks of IMC formed at the anode side.

2.4.2. Electromigration-Induced UBM/Solder Interfacial Reactions

As mentioned previously, an important electromigration effect is its polarity effect on IMC growth in a reaction couple. Since solder joint is a reaction couple between solder and metallization, nearly the same polarity effect of electromigration is observed in the solder joint, and this effect will be covered in this section

Chen and Chen (2001) studied the effect of electromigration on the Sn-0.7Cu/Ni and Sn-3.5Ag/Ni interfacial reactions. Sandwich-type reaction couples of

Sn-0.7Cu/Ni/Sn-0.7Cu and Sn-3.5Ag/Ni/Sn-3.5Ag were used in the studies. The annealing was carried out at 160, 180 and 200°C for 120 to 480 h, with and without electric current of 5×10^2 A/cm^2 density. They observed that electromigration influences the phase formation and growth of IMC in the case of Sn-0.7Cu/Ni reaction couple. During annealing without current only one Ni_3Sn_4 phase formed, with only small solubility of Cu at both the interfaces. Whereas with current, at the Sn-0.7Cu/Ni interface (where electrons flow from solder to Ni), two IMC phases, Cu_6Sn_5 (dark) and Ni_3Sn_4 (bright) formed and at the Ni/Sn-0.7Cu interface (where electrons flow from Ni to solder), only one Ni_3Sn_4 phase formed. They also observed that current enhances the growth of IMC at the Sn-0.7Cu/Ni interface and retards at the Ni/Sn-0.7Cu interface. This difference in the interfacial reactions in the case of passage of current was attributed to the electromigration, which enhanced the flux of Sn and Cu in the direction of movement of electrons. Similar effect of electromigration was reported in Sn-3.5Ag/Ni couple, but in this case only one Ni_3Sn_4 phase formed at both the interfaces with different thicknesses in the case of passage of electric current. They also reported that the effect of electromigration decreases with increasing the temperature.

Gan and Tu (2005) investigated the polarity effect of electromigration in Cu/Sn-3.8Ag-0.7Cu solder joint at different temperatures (120, 150, and 180 °C) and current densities (10^3-10^4 A/cm^2). They observed that while the same Cu-Sn IMCs form at the solder/Cu interface independent of the passage of electric current, the growth of IMC is enhanced by the electric current at the anode (where electrons flow from solder to Cu) and inhibited at the cathode (where electrons flow from Cu to solder), in comparison without current. Kirkendall voids formed at the cathode side solder/Cu interface at high current density (~10^4 A/cm^2). Dissolution of Cu-Sn IMC at the cathode side solder/Cu interface was observed at high current density (~10^4 A/cm^2) and low temperature (120 °C).

2.4.3. Effect of Electric Current on the Mechanical Behavior of Solder Joints

In real practice, solder joints work under both thermal stress as well as electrical stress. While the influence of thermal stress on the mechanical properties of solder joint has been extensively investigated, the effect of electrical current on the mechanical behavior of solder joint has been investigated only in a recent study (Ren *et al.*, 2005). Ren *et al.* (2005) studied the effect of electromigration on mechanical behavior of Sn-3.8Ag-0.7Cu and Sn-Pb solder joints with Cu and Ni metallizations at 100-155°C temperatures and 10^3-10^4 A/cm^2 current densities. They observed that without applying current, the solder joint breaks at the middle of solder, however after applying current, failure occurs at the cathode side of solder joint. They also observed a decrease in the tensile strength of Sn-3.8Ag-0.7Cu solder joint with the increase in current density. However, no detailed explanation has been given about the failure mechanism.

As the presence of electrical current in solder joint is inevitable and the electric current significantly influences the interfacial as well as bulk microstructure, thus more systematic work is needed for thorough understanding of electric current effect on the mechanical properties of solder joint.

2.5. Summary and Remarks

From the literature, it is apparent that the interfacial reactions between electroless Ni-P UBM and solder are highly complex due to the presence of P in Ni-P. Multilayered interfacial compounds such as Ni_3Sn_4, Ni_3P, and Ni-Sn-P form during interfacial reactions. Needle-type and chunk-type Ni_3Sn_4 IMCs have been reported in reflowed Ni-P/solder joint, while scallop-type Ni_3Sn_4 IMC in solid state aged solder joint. Growth kinetics of Ni_3Sn_4 and Ni_3P has been investigated in several studies, but there is wide inconsistency in the published results. Moreover, nothing has been reported about the growth kinetics of ternary Ni-Sn-P layer.

The formation of Kirkendall voids at electroless Ni-P/solder interface has been reported in many studies; however, there is a disagreement of the location and the formation mechanism of Kirkendall voids. In addition, interfacial elemental diffusion and reaction mechanism are also not clear yet. Thus, it can be said that though many studies have investigated morphology, growth kinetics, and growth mechanism of interfacial compounds in electroless Ni-P/solder joint, there are still many issues that need to be investigated either due to inadequate attention or discrepancies among these investigations. Moreover, no systematic comparison of electroless Ni-P/solder interfacial reactions has been done with different Ni-P thicknesses and P concentrations.

Many studies have reported the brittle failure of the electroless Ni-P/solder joints. However in different studies, different factors have been reported to cause the brittle failure of the joint. As a result, it is difficult to identify the main cause(s) of brittle failure and to correlate the interfacial reactions with the mechanical properties of electroless Ni-P/solder joint. In the current work, efforts have been made to identify the factor(s) causing the brittle failure of the joint and to correlated the mechanical behavior of solder joint with interfacial reactions and/or microstructure. To achieve this, some material parameters such as the thickness and P concentration of Ni-P UBM (which influence the interfacial reactions) have been varied and tensile testing method (which is sensitive to interfacial changes) has been used.

From electromigration related literature, it is clear that electromigration significantly influences the elemental diffusion in the bulk material and reaction couple. The unbalanced elemental diffusion not only results in the formation of voids and hillocks in the bulk material and reaction couple but also influences the interfacial reactions in reaction couple. The effect of electromigration becomes more severe in solder joint due to the low melting point and high diffusivity of solder alloy, and the presence of concentration gradient at UBM/solder interface. Therefore, electromigration effect in solder joint can be seen at relatively low current densities (<10^3 A/cm^2). It is also clear that electromigration effect increases with current density and time and depends upon the materials system. Thus, it is imperative to study the effect of electromigration on the interfacial reactions and mechanical behavior of electroless Ni-P/solder joint, which is an extensively used solder joint in electronic packages.

Chapter 3

Cu/Electroless Ni-P/Sn-3.5Ag Interfacial Reactions and their Effect on Solder Joint Strength

3.1. Introduction

The presence of P in the electroless Ni-P causes complex electroless Ni-P/solder interfacial reactions resulting in the formation of multiple interfacial compounds (Chen *et al.*, 2004; Hwang *et al.*, 2003; Jang *et al.*, 1999; Liu *et al.*, 2000, 2000b; Matsuki *et al.*, 2002; Sohn *et al.*, 2004b; Wang and Liu, 2003; Yoon and Jung, 2005; Zeng and Tu, 2002). The growth of multiple interfacial compounds in the electroless Ni-P/solder system is of great interest, as in many reliability studies brittle fracture has been found to occur in between these compounds (Ahat *et al.*, 2000; Alam *et al.*, 2003; He *et al.*, 2005; Liu and Shang, 2000a; Matsuki *et al.*, 2002; Mei *et al.*, 1998).

Although several studies have examined the interfacial reactions and joint strength between electroless Ni-P and solder, little is known about the growth kinetics and mechanism of interfacial compounds and the factors that affect the mechanical properties of solder joint. The reason for this limited knowledge is that most of the studies have been carried out either under solid-state aging (usually at temperatures below 150°C) or under liquid-state aging (usually at temperatures above 210°C). At these aging conditions, interfacial reactions are either too slow or too fast to understand well. Thus, a thorough investigation is required for intermediate aging conditions that can represent sufficient window of aging conditions. Accordingly in this investigation, solid-state aging of Cu/electroless Ni-P/Sn-3.5Ag solder joint has been carried out at high temperatures ranging from 140°C to 200°C. An effort has been made to identify the factors that affect the mechanical properties of solder joint.

3.2. Experimental Procedures

3.2.1. Preparation of Test Samples

Cu (99.98 wt.%) plate of size of 70 mm × 25 mm × 6 mm was used to fabricate multi-layered test samples Cu/electroless Ni-P/Sn-3.5Ag/electroless Ni-P/Cu. The Cu plate was surface cleaned, first by polishing down to 1 μm finish, then by ultrasonically cleaning with acetone for 10 min, then by etching with 20 vol.% HNO_3 solution for a few seconds, and finally by cleaning with de-ionized water. Electroless Ni-P was plated on the surface cleaned Cu plate in two steps. In the first step, Cu surface was activated using the ruthenium-based pre-initiator. Then, electroless Ni-P was plated on the activated Cu surface. Thin layer (~0.05 μm) of non-cyanide immersion gold was also deposited on electroless Ni-P surface to protect the surface from oxidation. The schematic of metallization layer(s) on the Cu plate is shown in Fig. 3.1.

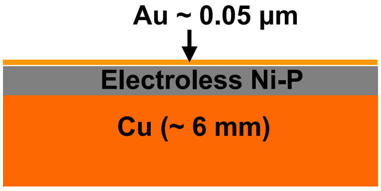

Fig. 3.1. Schematic of metallization layout on the Cu plate.

Electroless Ni-P/Sn-3.5Ag solder joint was prepared by cutting the electroless Ni-P coated Cu plate into two plates of sizes of 40 mm × 25 mm × 6 mm and 30 mm × 25 mm × 6 mm, and then joining them with each other using Sn-3.5Ag solder wires, as shown in Fig. 3.2. The joint was formed during the reflow process by placing a number of small pieces of solder wires on the smaller piece of electroless Ni-P coated Cu plate and pressing them by the bigger plate. “No-clean” paste flux was applied on both the plates before placing the

Sn-3.5Ag wires. The reflow process was carried out in IR reflow oven (ESSEMTEC RO-06E) which involved preheating at 150°C for 100 s, then reflowing at 250°C for 60 s, and finally cooling down to 160°C in the oven. Alumina spacers of thickness of around 650 µm were used to maintain the uniform thickness of Sn-3.5Ag solder in between the plates. The joined plates were cut into a number of small test samples of cross-sectional area of around 600 µm × 650 µm with the help of a diamond saw. Fig. 3.3 shows the schematic diagram of test sample.

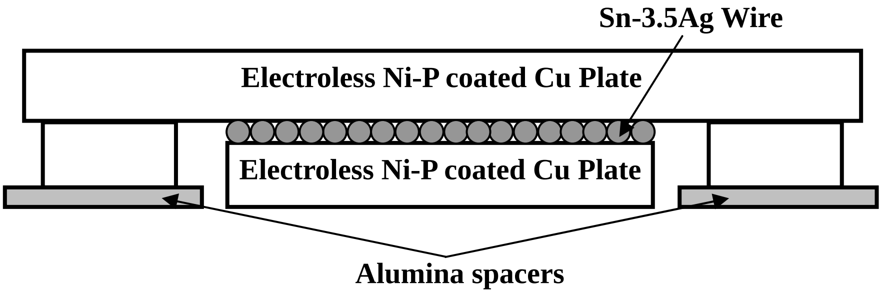
Sn-3.5Ag Wire
Electroless Ni-P coated Cu Plate
Electroless Ni-P coated Cu Plate
Alumina spacers

Fig. 3.2. Schematic illustration of joining the Ni-P coated Cu plates.

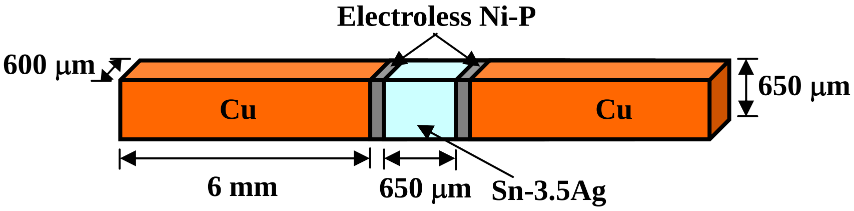
Electroless Ni-P
600 µm
650 µm
Cu
Cu
6 mm
650 µm
Sn-3.5Ag

Fig. 3.3. Schematic diagram of test sample.

3.2.2. Thermal Aging of Test Samples

Solid-state thermal aging at 150 °C for 1000 h is a required reliability test for solder/UBM joint (Tu and Zeng, 2001). In this work, solid-state aging was carried out at higher temperatures (160-200 °C) to shorten down the aging duration. For thermal aging, as-prepared test samples were kept in the oven (Lenton WHT4/30) at 140, 160, 180, and 200 °C for 48, 100, 225, and 400 h. After aging, the samples were removed from the oven and cooled in air to room temperature.

3.2.3. Tensile Testing of Test Samples

Tensile testing of test samples was performed using INSTRON 5567 tensile tester. Five samples from each condition were tensile tested to obtain the average and the standard deviation. The tensile test was done at room temperature with a constant crosshead speed of 0.05 mm/min to a complete fracture.

Strain compatibility is an issue in inhomogeneous solids. As a result, a thin layer of solder in a solder joint results in a high mechanical strength of the solder joint (He *et al.*, 2005). To eliminate this effect, a thick (650 μm) solder layer with a cross-sectional area of 600 μm × 650 μm was used in the present work.

3.2.4. Microstructural Observations

JEOL JSM-6360A Scanning electron microscope (SEM) was used for microstructure analysis. For the cross-sectional SEM, the samples were cold mounted in epoxy and polished down to 1 μm finish. After polishing, solder etching was carried out with 4 vol.% HCl acid for a few seconds to reveal the microstructure. To observe top-view of interfacial compound, the sample was soaked in 5 vol.% HNO_3 acid for a few minutes to dissolve all the solder. Energy dispersive X-ray spectroscopy (EDS) was performed in the SEM to analyze the chemical composition of interfacial compounds. Image processing and analysis software was used to measure the area and length of interfacial compound from the SEM images. The thickness of interfacial compound was determined by dividing the area with the length. The thickness was measured at six different locations in a sample to estimate the average value.

3.3. Results

3.3.1. Interfacial Microstructure Analysis

SEM and EDS analyses of as-prepared and thermally aged samples were carried out to analyze the formation of interfacial compounds as well as to understand the evolution of interfacial microstructure.

As-prepared Sample

Thickness and P-concentration of as-plated electroless Ni-P layer were measured to be around 9.9 μm and 16 at.%, respectively. Fig. 3.4a and b, respectively, are the cross-sectional and top view of compounds formed at the Sn-3.5Ag/electroless Ni-P interface of as-prepared sample. From the figures, it is clear that needle-type and chunky-type Ni_3Sn_4 intermetallics formed at the Sn-3.5Ag/electroless Ni-P interface during reflow, some of which spalled off into the molten solder. Underneath the Ni_3Sn_4 intermetallics, a ternary Ni-Sn-P layer formed, whose composition was difficult to measure by EDS in the SEM owing to its submicron thickness (Table 3.1). Underneath the Ni-Sn-P layer, a dark thin Ni_3P layer having a large number of columnar voids formed within the electroless Ni-P layer. Formation of these compounds is in agreement with the results of previous interfacial studies between electroless Ni-P and different solders (Jang *et al.*, 1999; Zeng and Tu, 2002; Matsuki *et al.*, 2002; Chen *et al.*, 2004; Wang and Liu, 2003). The immersion Au layer that plated on the electroless Ni-P layer completely dissolved in the molten solder during reflow, as no Au or Au–Sn intermetallic was found at the Sn-3.5Ag/electroless Ni-P interface.

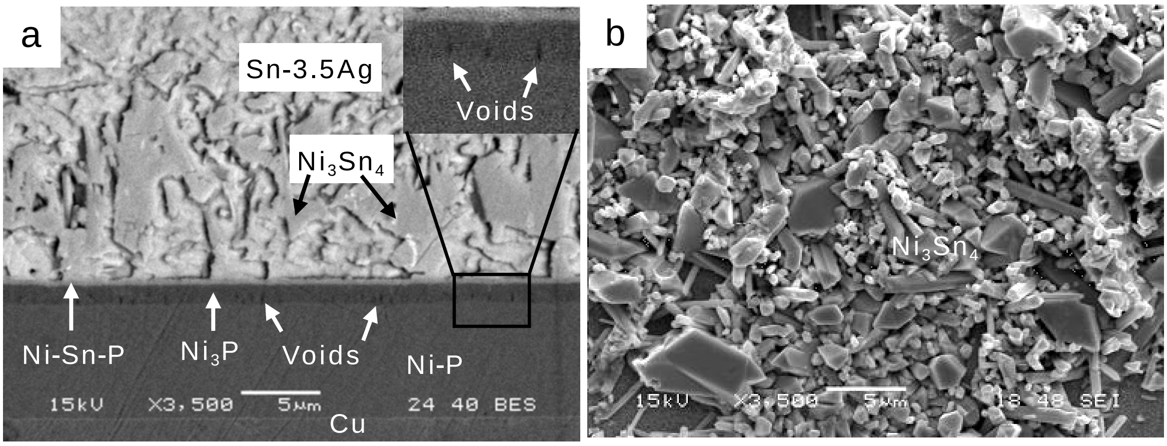

Fig. 3.4. (a) Cross-sectional and (b) top views of compounds formed at the Sn-3.5Ag/electroless Ni-P interface of as-prepared sample.

Table 3.1. EDS results showing the chemical composition (at.%) of compounds formed at the Sn-3.5Ag/Ni-P/Cu interfaces of the as-prepared sample.

Compounds	Ni	Sn	P
Ni-P	84±1.5	-	16±1.5
Ni_3Sn_4	41±1.5	59±1.5	-
Ni-Sn-P	-	-	-
Ni_3P	74±1.5	-	26±1.5

Thermally aged samples

Fig. 3.5 is the back-scattered SEM images showing the growth of various compounds at the Sn-3.5Ag/electroless Ni-P/Cu interfaces in the samples aged at different temperatures. It can be observed that mainly three compounds, Ni_3Sn_4, Ni-Sn-P, and Ni_3P, grew during aging. With the growth of compounds, columnar voids present in the Ni_3P layer also grew in size as well as in number. Owing to the aging, the morphology of Ni_3Sn_4 changed into the scallop-type (Fig. 3.6). In the sample aged at 180 °C, most of the electroless Ni-P layer transformed into Ni_3P layer as shown in Fig. 3.5c. The thickness of this transformed electroless Ni-P layer (~ 5.2 μm) is much smaller than that of as-plated electroless Ni-P layer (~ 9.9 μm). This shrinkage in Ni-P layer indicates that during aging, Ni diffused out from the electroless Ni-P ($Ni_{84}P_{16}$) layer to form Ni_3Sn_4 leaving behind a higher P containing Ni-P (Ni_3P) layer within the electroless Ni-P layer.

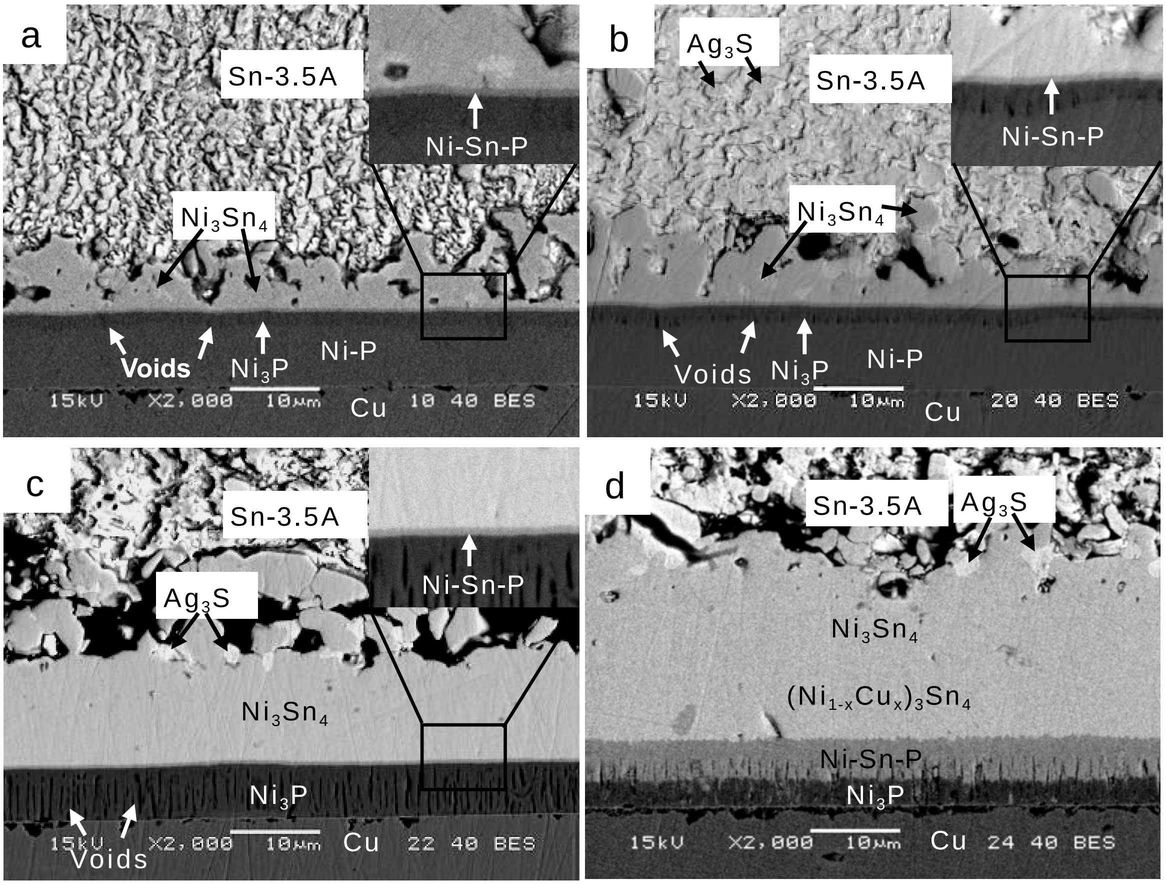
a
Sn-3.5A
Ni-Sn-P
Ni_3Sn_4
Voids
Ni_3P
Ni-P
15kV X2,000 10µm Cu 10 40 BES
b
Ag_3S
Sn-3.5A
Ni-Sn-P
Ni_3Sn_4
Voids
Ni_3P
Ni-P
15kV X2,000 10µm Cu 20 40 BES
c
Sn-3.5A
Ni-Sn-P
Ag_3S
Ni_3Sn_4
Ni_3P
Voids
15kV X2,000 10µm Cu 22 40 BES
d
Sn-3.5A
Ag_3S
Ni_3Sn_4
$(Ni_{1-x}Cu_x)_3Sn_4$
Ni-Sn-P
Ni_3P
15kV X2,000 10µm Cu 24 40 BES

Fig. 3.5. Back-scattered SEM images showing the growth of Ni_3Sn_4, Ni-Sn-P, and Ni_3P compounds at the Sn-3.5Ag/electroless Ni-P/Cu interfaces of the samples aged for 225 h at temperatures of (a) 140 °C, (b) 160 °C, (c) 180 °C, and (d) 200 °C.

In the samples aged at 180 °C and 200 °C, Sn-3.5Ag/Ni_3Sn_4 interface became more even and some particles of Ag_3Sn and spalled Ni_3Sn_4 IMCs accumulated at the Sn-3.5Ag/Ni_3Sn_4 interface due to the large growth of Ni_3Sn_4 layer (Figs. 3.5c, 3.5d, 3.6c, and 3.6d). Other differences observed among the samples aged at different temperatures were the relatively large growth of Ni-Sn-P layer and the presence of small amount of Cu (up to 5 at.%) in the Ni_3Sn_4 IMC grown near the Ni-Sn-P layer in the samples aged at 200°C (Fig. 3.5d). The elemental composition of this Ni-Sn-P layer was found similar to that of Ni_2SnP compound (Table 3.2). The Cu amount in the $(Ni_{1-x}Cu_x)_3Sn_4$ layer was gradually decreasing to zero from the $(Ni_{1-x}Cu_x)_3Sn_4$/Ni-Sn-P interface to the Ni_3Sn_4/$(Ni_{1-x}Cu_x)_3Sn_4$

interface (Fig. 3.5d).

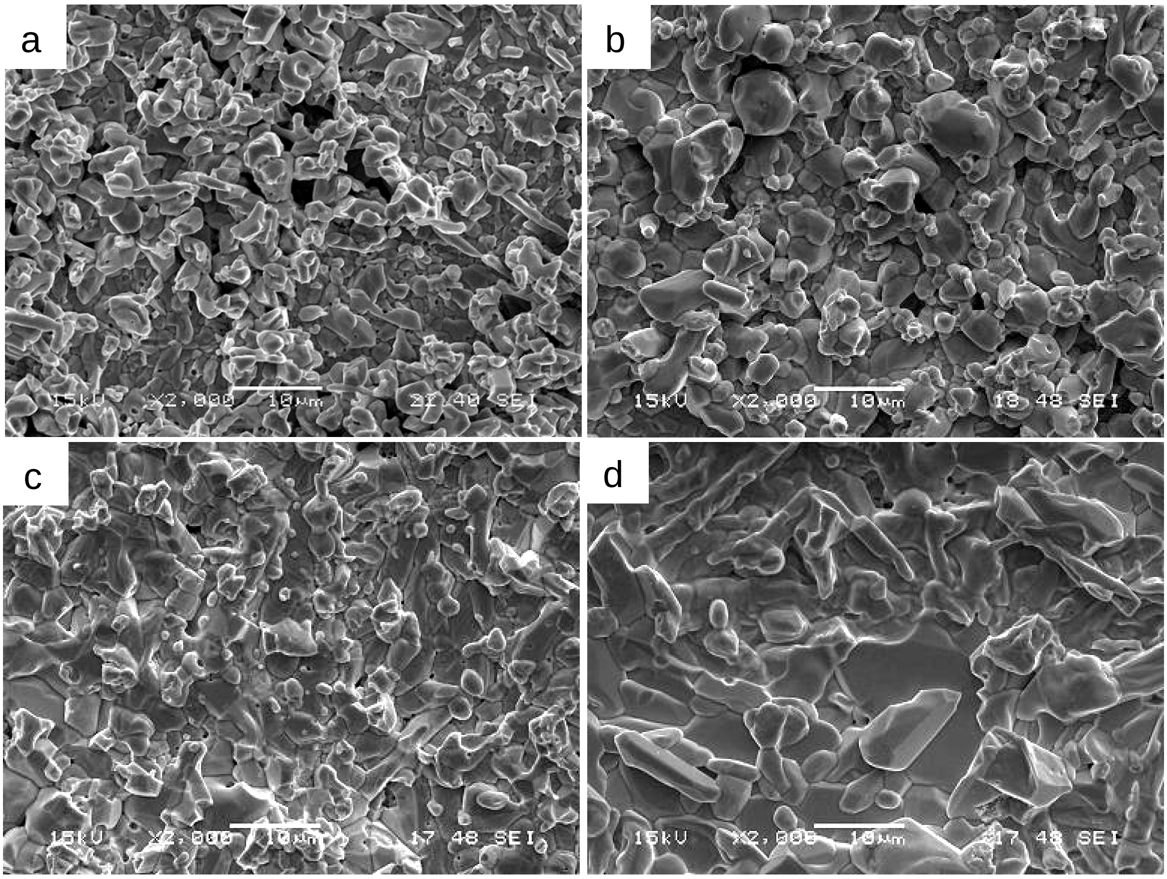
a
15kU X2,000 10µm 21 40 SEI
b
15kU X2,000 10µm 18 48 SEI
c
15kU X2,000 10µm 17 48 SEI
d
15kU X2,000 10µm 17 48 SEI

Fig. 3.6. Top view of Ni_3Sn_4 IMC in the samples aged for 225 h at temperatures of (a) 140 °C, (b) 160 °C, (c) 180 °C, and (d) 200 °C, showing scallop-type morphology.

Table 3.2. EDS results showing the chemical composition (at.%) of compounds formed at the Sn-3.5Ag/Ni-P/Cu interfaces of the sample aged at 200 °C.

Compounds	Ni	Cu	Sn	P
Ni_3Sn_4	41±1.5	<1	58±1.5	-
Ni-Sn-P	47±2	<2	29±2	22±2
Ni_3P	72±2	<2	<4	27±2
$(Ni_{1-x}Cu_x)_3Sn_4$	37±1.5	4±1.5	59±1.5	-

Fig. 3.7 shows the line-scanned images of the Cu/electroless Ni-P/Sn-3.5Ag interfaces of the samples aged at 200 °C for different durations. From the figure it is clear that in the samples aged at 200 °C, the electroless Ni-P layer completely transformed into Ni_3P layer

within 48 h of aging and then Ni-Sn-P layer started growing at the expense of Ni_3P layer. Concurrent with this, a layer of voids also grew at the Cu/Ni_3P interface. The growth of layer of voids and the presence of Cu in Ni_3Sn_4 imply that after the complete transformation of electroless Ni-P layer into Ni_3P, the diffusion of Cu takes place from the Cu/Ni_3P interface to the Ni-Sn-P/Ni_3Sn_4 interface and that results in the growth of layer of voids and $(Ni_{1-x}Cu_x)_3Sn_4$ intermetallics at the Cu/Ni_3P and Ni-Sn-P/Ni_3Sn_4 interfaces, respectively. The extreme case of Cu diffusion will be discussed in the next chapter.

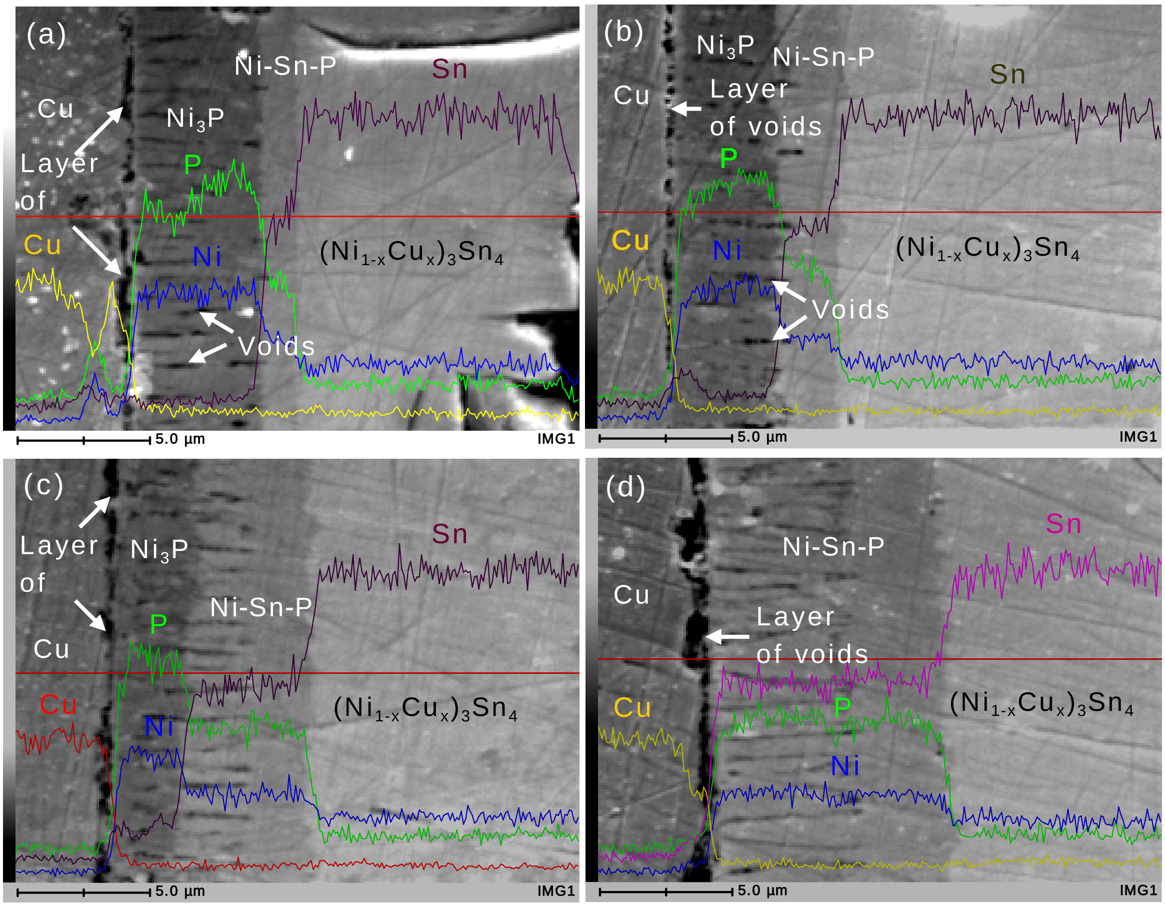
(a)
Ni-Sn-P
Sn
Cu
Ni3P
Layer of Cu
P
Cu
Ni
(Ni1-xCux)3Sn4
Voids
5.0 µm
IMG1
(b)
Ni3P
Ni-Sn-P
Sn
Cu
Layer of voids
P
Cu
Ni
(Ni1-xCux)3Sn4
Voids
5.0 µm
IMG1
(c)
Layer of Cu
Ni3P
Sn
Ni-Sn-P
P
Cu
Ni
(Ni1-xCux)3Sn4
5.0 µm
IMG1
(d)
Ni-Sn-P
Sn
Cu
Layer of voids
Cu
P
Ni
(Ni1-xCux)3Sn4
5.0 µm
IMG1

Fig. 3.7. Line-scanned SEM images of the Cu/electroless Ni-P/Sn-3.5Ag interfaces in the samples aged at 200 °C for (a) 48 h, (b) 100 h, (c) 225 h, and (d) 400 h, showing the growth of Ni-Sn-P layer at the expense of Ni_3P layer.

3.3.2. Growth of Interfacial Compounds

Fig. 3.8 shows the thickness of Ni_3Sn_4, Ni-Sn-P, and Ni_3P compound layers as a function of aging time at different temperatures. It can be observed that in the samples aged at 140 °C and 160 °C, all the layers grew with aging; however, the growth of Ni-Sn-P layer was negligible as compared to the growth of Ni_3Sn_4 and Ni_3P layers. Similar trend of compound growth was observed in the samples aged at 180 °C, however in these samples, compound growth became sluggish at the later stage (after 225 h) of aging. The reason for this sluggish compound growth was the complete transformation of electroless Ni-P layer into Ni_3P layer at most of the places of Sn-3.5Ag/Ni-P/Cu interfaces (Fig. 3.5c), which subsequently reduced the supply of Ni from the remaining electroless Ni-P layer. A different trend of compound growth was observed in the samples aged at 200 °C, where Ni_3Sn_4+ $(Ni_{1-x}Cu_x)_3Sn_4$ and Ni-Sn-P layers grew and Ni_3P layer diminished with aging (Fig. 3.8d). As mentioned earlier, in these samples, electroless Ni-P layer completely transformed into Ni_3P layer within 48 h of aging and then Ni-Sn-P layer started growing rapidly at the expense of Ni_3P layer (Fig. 3.7).

It has been reported (Jang *et al.*, 1999; Sharif *et al.*, 2005) that the Ni_3Sn_4 and Ni_3P compounds grown at the electroless Ni-P/solder (Sn-Pb and Sn-Ag) interface are the reaction products of a mass conservative reaction between Sn and electroless Ni-P and have a constant relation between their thicknesses. In this investigation also, we observed a constant relation between thickness of Ni_3Sn_4 and Ni_3P layers. Table 3.3 shows the thickness ratio of Ni_3Sn_4 to Ni_3P layers measured at different aging conditions. It can be seen that except for the samples aged at 200 °C, the thickness ratio of Ni_3Sn_4 to Ni_3P layers are within the narrow range of 2.2-2.9. The higher thickness ratio in the case of samples aged at 200 °C is understood to be due to the diminishing of the Ni_3P layer (see Fig. 3.8d). Although the thickness ratio of Ni_3Sn_4 to Ni_3P layers measured in this investigation is similar to the previously reported thickness ratio (Jang *et al.*, 1999), this ratio can vary widely depending upon the P concentration of electroless Ni-P layer, which will be discussed in the coming chapter.

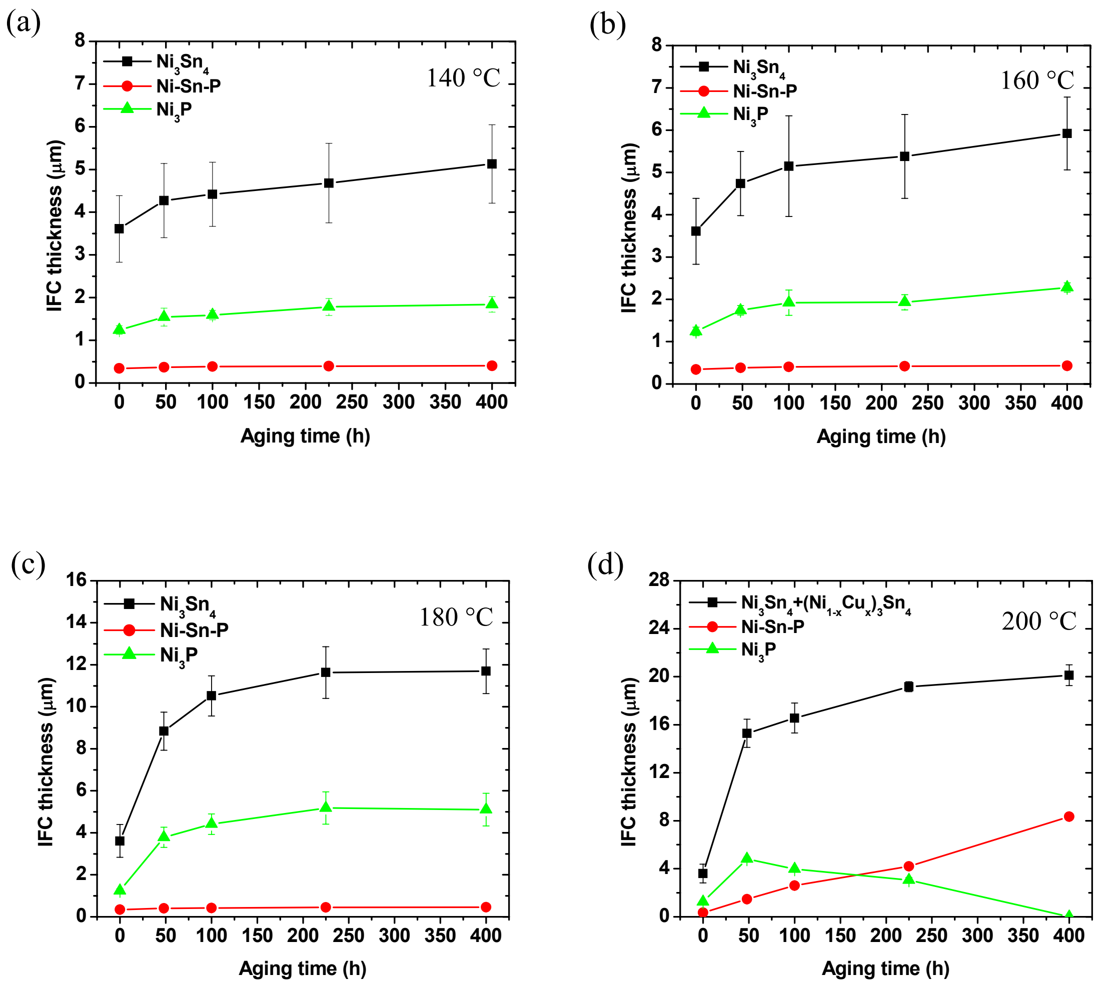

Fig. 3.8. Thickness of Ni_3Sn_4, Ni-Sn-P, and Ni_3P compounds as a function of aging time at temperatures of (a) 140 °C, (b) 160 °C, (c) 180 °C, and (d) 200 °C.

Table 3.3. Thickness ratio of Ni_3Sn_4 to Ni_3P layers measured at different aging conditions.

Aging conditions	Thickness ratio of Ni_3Sn_4 to Ni_3P layers			
Time (h)\Temperature (°C)	140	160	180	200
0 (As-prepared)	2.9	2.9	2.9	2.9
48	2.8	2.7	2.3	3.2
100	2.8	2.7	2.4	4.2
225	2.6	2.8	2.2	6.3
400	2.8	2.6	2.3	NA

3.3.3. Growth Kinetics of Interfacial Compounds

As shown in Fig. 3.9, based on equation 2.1, the thickness data of interfacial compounds were plotted as $ln\ (X\text{-}X_0\ in\ \mu m)$ versus $ln\ (t\ in\ h)$ to determine the kinetic parameters k and n. The values of $1/n$ and $ln\ (k\ in\ \mu m/h^{1/n})$, respectively, are represented by the slope and the y-axis intercept of the best-fit line of thickness data. The measured kinetic parameters for the growth of Ni_3Sn_4, Ni-Sn-P, and Ni_3P layers at different temperatures are tabulated in the Table 3.4. The kinetic parameters for Ni_3Sn_4 and Ni_3P growth at 200 °C could not be obtained because of the presence of Cu in Ni_3Sn_4 and decrease in Ni_3P thickness, respectively (Figs. 3.7 and 3.8d). For the Ni_3Sn_4 and Ni_3P growth at 180 °C, kinetic parameters were obtained by considering the compound growth up to 225 h of aging, as by 225 h, electroless Ni-P layer was completely transformed into Ni_3P layer at most of the places of Sn-3.5Ag/Ni-P/Cu interfaces (Fig. 3.5c). From Table 3.4, it can be seen that in most of the cases, value of n is close to 3, which indicate that the compound growth in the electroless Ni-P/Sn-3.5Ag system is controlled by the diffusion of reacting elements. Similar kinetic result for the growth of Ni_3Sn_4 IMC in the electroless Ni-P/Sn-3.5Ag solder joint has been reported in the previous interfacial studies (He *et al*., 2004d; Yoon and Jung, 2004; Jeon *et al*., 2003). The values of n obtained from Ni-Sn-P growth imply that its growth was diffusion controlled in the samples aged at 140, 160 and 180 °C and it became reaction controlled in the samples aged at 200 °C. In the present work, the deviation of n from its ideal values 3 and 1 could be due to the formation of multiple compound layers and time dependent apparent diffusivity.

According to equation 2.3, Arrhenius plots shown in Fig. 3.10 were obtained for different compounds to estimate the apparent activation energy for compound growth. The activation energies for Ni_3Sn_4, Ni-Sn-P, and Ni_3P growth were estimated to be 98.9, 42.2, and 94.3 kJ/mol, respectively and the prefactors were estimated to be 4.1×10^{11}, 1.5×10^{3}, and 5.2×10^{10} $\mu m/h^{1/n}$ (n~3), respectively. The activation energies for Ni_3Sn_4 and Ni_3P growths are very close to each other, which are expected to be due to a constant relation between their growths (see Table 3.3). However interestingly despite of slow Ni-Sn-P growth, the activation energy of Ni-Sn-P growth (42.2 kJ/mol) was found to be lower than that of Ni_3Sn_4 and Ni_3P growth. Though the low activation energy of compound growth indicates the ease in overcoming the barrier of compound growth, there is another factor, the prefactor, which also contributes to the compound growth. And in the case of Ni-Sn-P, the value of prefactor was found to be much lower that that of Ni_3Sn_4 and Ni_3P. Table 3.5 lists the activation energies of the growth of compounds in the electroless Ni-P/solder systems reported in different studies. Considering the fact that activation energy of compound growth varies widely depending upon solder's composition and experimental conditions, our results for Ni_3Sn_4 and Ni_3P compounds are in agreement with previously reported results. However for the ternary Ni-Sn-P compound, no comparison could be made, as this is the first study that reports Ni-Sn-P growth kinetics.

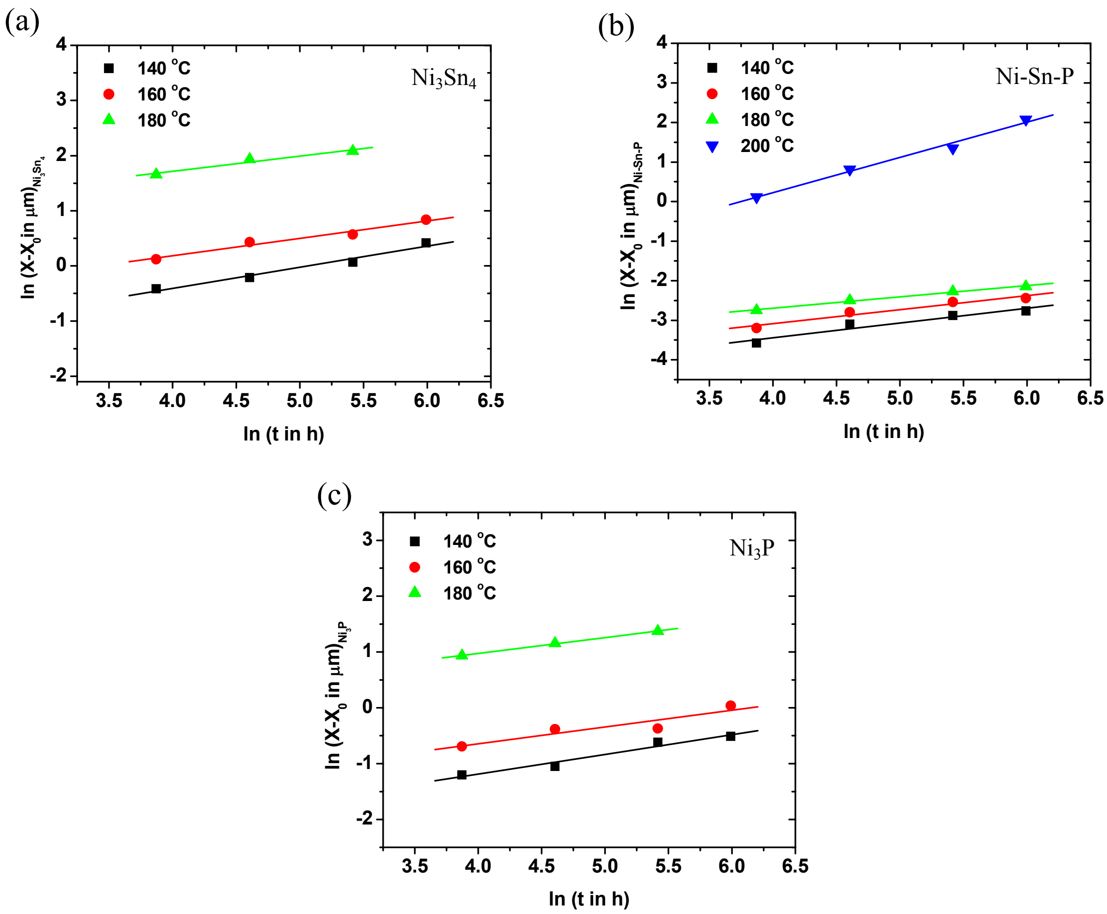

Fig. 3.9. Ln-ln plot of increment in compound thickness versus aging time at various temperatures for (a) Ni_3Sn_4, (b) Ni-Sn-P, and (c) Ni_3P.

Table 3.4. Kinetic parameters of the growth of Ni_3Sn_4, Ni-Sn-P, and Ni_3P compounds at various temperatures.

Temperature (°C)	Ni_3Sn_4			Ni-Sn-P			Ni_3P		
	ln (k in µm/$h^{1/n}$)	1/n	n	ln (k in µm/$h^{1/n}$)	1/n	n	ln (k in µm/$h^{1/n}$)	1/n	n
140	-1.94	0.38	2.63	-4.93	0.37	2.70	-2.60	0.35	2.86
160	-1.08	0.32	3.13	-4.50	0.35	2.86	-1.85	0.30	3.33
180	0.62	0.28	3.57	-3.84	0.29	3.45	-0.16	0.28	3.57
200	NA	NA	NA	-3.34	0.89	1.12	NA	NA	NA

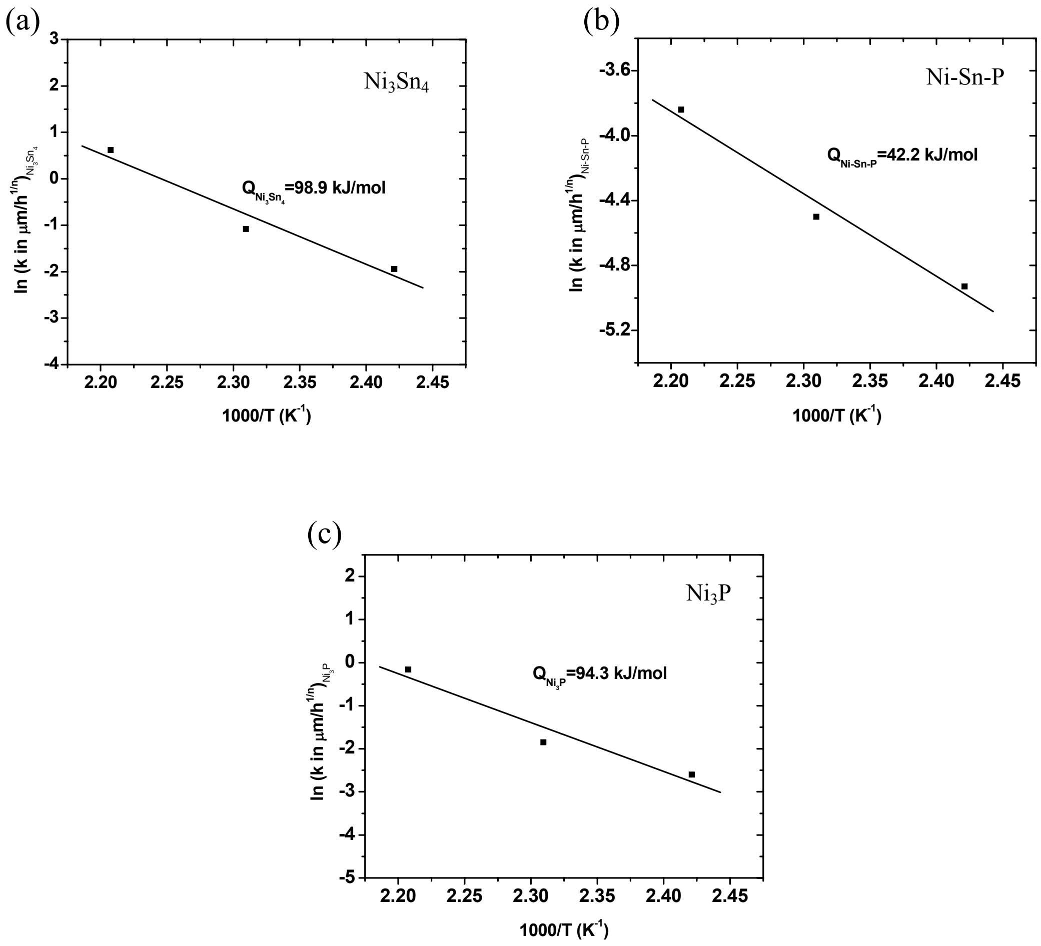

Fig. 3.10. Arrhenius plot of (a) Ni_3Sn_4, (b) Ni-Sn-P, and (c) Ni_3P growth used to estimate apparent activation energy.

Table 3.5. Activation energies (Q) of the growth of compound in the electroless Ni-P/solder systems reported in different studies.

Solder (wt.%)	Experimental Conditions (Temperature/Time)	Compound	Q (kJ/mol)	Reference
Sn-3.5Ag	140 to 180°C/Up to 400 h	Ni_3Sn_4	98.9	Present work
Sn-3.5Ag	140 to 180°C/Up to 400 h	Ni-Sn-P	42.2	Present work
Sn-3.5Ag	140 to 180°C/ Up to 400 h	Ni_3P	94.3	Present work
Sn-37Pb	200 to 240°C/Up to 40 min	Ni_3P	31.8	Jang *et al.*, 1999
Sn-3.5Ag	130 to 170°C/Up to 625 h	Ni_3Sn_4	110	He *et al.*, 2004b
Sn-37Pb	130 to 170°C/Up to 625 h	Ni_3Sn_4	141	He *et al.*, 2004b
Sn-3.5Ag	100 to 170°C/Up to 60 days	Ni_3Sn_4	49	Yoon and Jung, 2004
Sn-3.5Ag	240 to 270°C/Up to 120 min	Ni_3P	75	Sharif *et al.*, 2005
Sn-3.5Ag-0.5Cu	240 to 270°C/Up to 120 min	Ni_3P	103	Sharif *et al.*, 2005
Sn-0.7Cu	240 to 270°C/Up to 120 min	Ni_3P	131	Sharif *et al.*, 2005

3.3.4. Tensile Strength and Failure Modes

Tensile strength of Cu/electroless Ni-P/Sn-3.5Ag solder joint as a function of aging duration at various aging temperatures is shown in Fig. 3.11. It can be seen that for a fixed aging duration, the strength decreased drastically with the increase in aging temperature. The effect of increase in aging duration on the strength, however, varied with aging temperature. In the case of samples aged at 160°C, the tensile strength increased slightly with the increase in aging duration, whereas, it decreased considerably in the case of samples aged at 180 and 200°C. The decrease in tensile strength was very large in the case of samples aged at 200°C as compared to the samples aged at 180°C, however, in both the cases, the strength decreased severely in the initial 48 h of aging and after that it remained nearly constant.

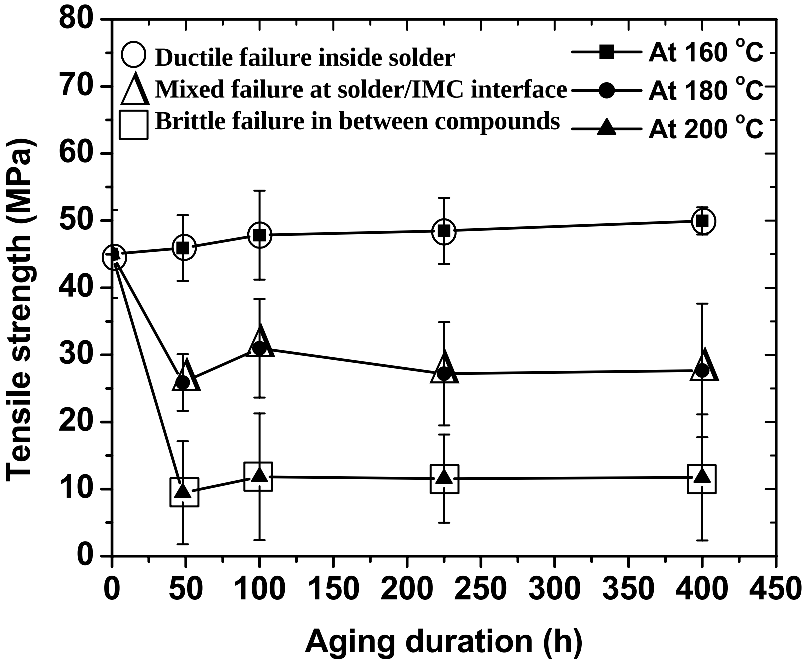

Fig. 3.11. Tensile strength of Cu/electroless Ni-P/Sn-3.5Ag solder joint as a function of aging duration at various temperatures (typical load-extension curves are shown in the Fig. A.1 of appendix A).

As shown in Fig. 3.12, based on strength verses extension curve, failure modes of solder joint were categorized into three categories, ductile, mixed, and brittle. As depicted in Fig. 3.11, ductile failure was observed in the as-prepared samples and the samples aged at 160°C. The failure mode changed into mixed in the samples aged at 180°C and became brittle in the samples aged at 200°C.

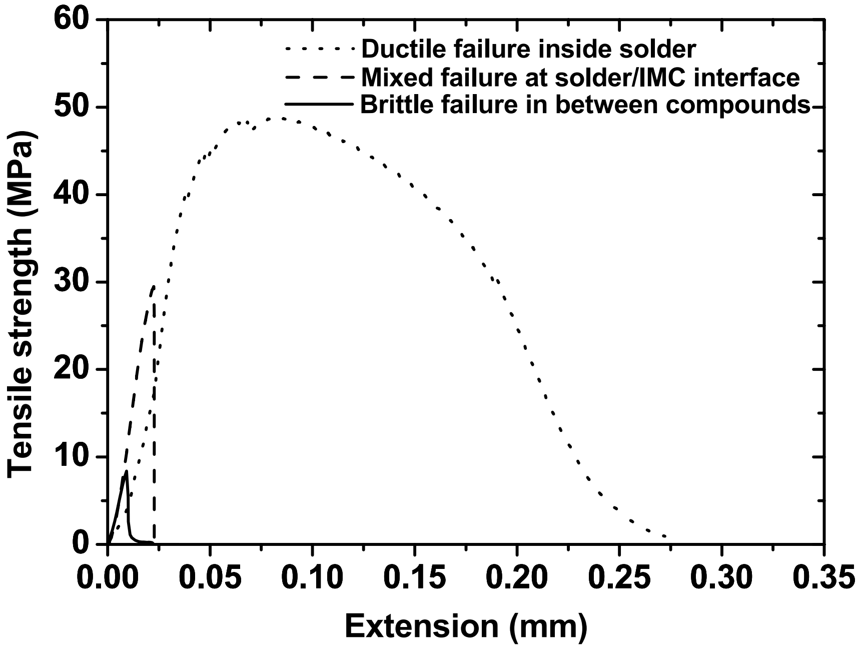

Fig. 3.12. Typical curves of tensile strength versus extension associated with different types of the failures of solder joint.

3.3.5 Fracture Analysis

Figs. 3.13 and 3.14 show the fracture surfaces of the test samples after different aging conditions. Similar to failure mode, a clear difference can be observed in the fracture surfaces of the samples subjected to different aging conditions. As shown in Fig. 3.13a and b, ductile fracture occurred inside the bulk solder in the as-prepared sample. The ductile failure inside the bulk solder became more prominent in the samples aged at 160°C, as shown in Fig. 3.14a and b by a clear necking in the bulk solder. The fracture occurred at the Ni_3Sn_4/Sn-3.5Ag interface in the samples aged at 180°C (Fig. 3.14c and d). This fracture was corresponding to the mixed failure mode shown in Fig. 3.12. In depth fracture analysis of the samples aged at 180°C revealed that though in these samples fracture was macroscopically brittle, dimple (dotted ellipses in Fig. 3.15b) formed at the solder surface were clearly suggesting a microscopically ductile fracture. A large number of Ni_3Sn_4 particles were observed to accumulate at the edges of dimples formed in the solder. The accumulation of Ni_3Sn_4 particles was very large at some specific locations, see ellipses with solid line in Fig. 3.15b, where edge of many dimples met with each other. The cross-sectional SEM image (Fig. 3.16) revealed that these Ni_3Sn_4 particles were the spalled Ni_3Sn_4 particles, which accumulated at the Sn-3.5Ag/Ni_3Sn_4 interface due to the large growth of Ni_3Sn_4 at 180 °C.

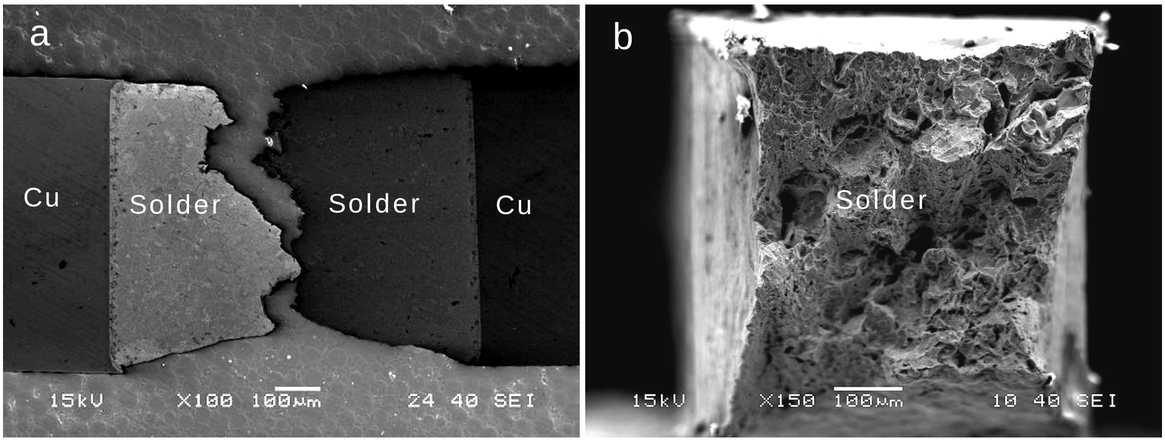

Fig. 3.13. (a) Fracture path and (b) fracture surface of the as-prepared sample. The neck formation in the bulk solder indicates the ductile failure.

In the solder joints aged at 200°C, as shown in Fig. 3.14 e and f, fracture occurred neither inside the bulk solder nor at Ni_3Sn_4/Sn-3.5Ag interface. A detailed fracture analysis (Fig. 3.17) revealed that in these samples fracture occurred at various compound/compound interfaces such as $(Ni_{1-x}Cu_x)_3Sn_4$/Ni-Sn-P, Ni-Sn-P/Ni_3P, and Ni_3P/Cu. The fracture at these interfaces suggests that the adhesion between interfacial compounds became very weak in the solder joints aged at 200°C. After careful analysis, it was found that though fracture occurred at various interfaces, the Ni_3P/Cu interface was more prone to fracture as in most of the samples fracture occurred mainly at the Ni_3P/Cu interface (Fig. 3.17). This was further confirmed from the cross-sectional SEM analysis shown in Fig. 3.18. Interestingly, the Ni_3P layer having a large number of columnar voids was found not to be prone to fracture, as no fracture surface was observed to contain the Kirkendall voids of Ni_3P layer (Fig. 3.17). However, columnar Kirkendall voids in the Ni_3P layer and fine grains of Ni-Sn-P layer helped the fracture to transmit from the Ni_3P/Cu interface to the $(Ni_{1-x}Cu_x)_3Sn_4$/Ni-Sn-P and/or Ni-Sn-P/Ni_3P interfaces as shown in Figs. 3.17a, b, and 3.19.

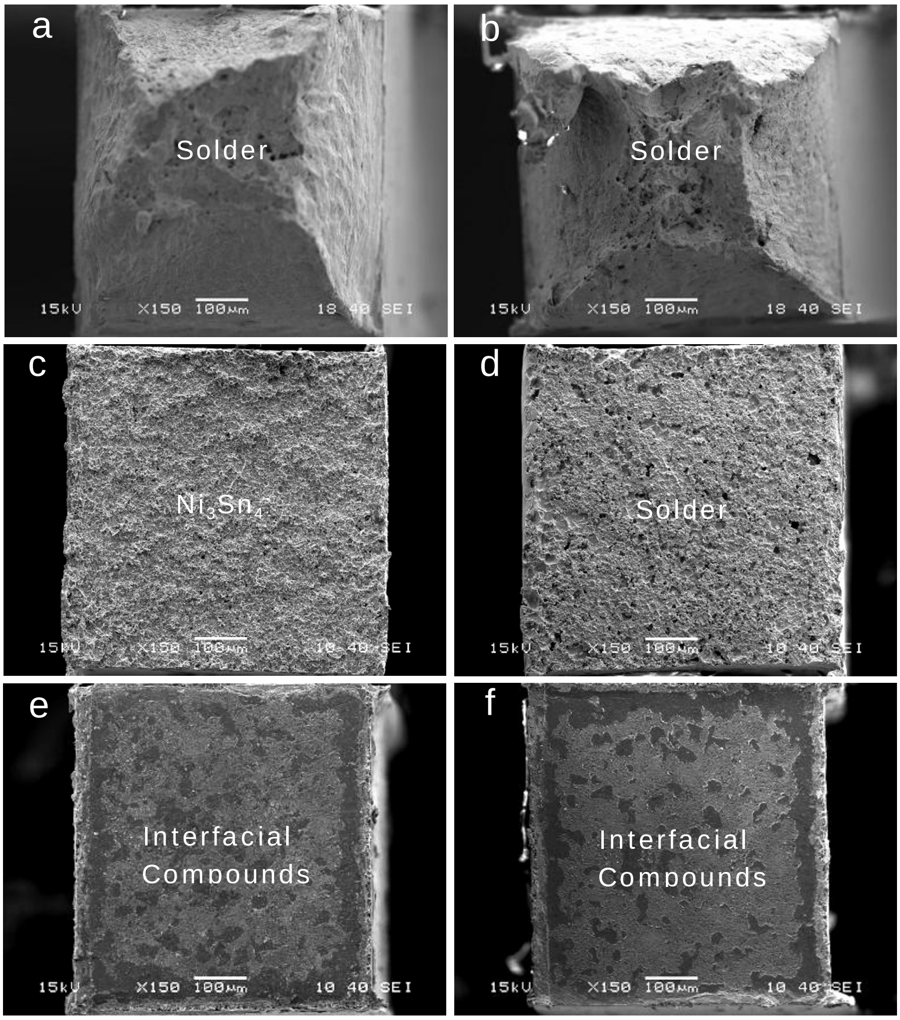
a
Solder
15kV X150 100µm 10 40 SEI
b
Solder
15kV X150 100µm 10 40 SEI
c
Ni3Sn4
15kV X150 100µm 10 40 SEI
d
Solder
15kV X150 100µm 10 40 SEI
e
Interfacial Compounds
15kV X150 100µm 10 40 SEI
f
Interfacial Compounds
15kV X150 100µm 10 40 SEI

Fig. 3.14. Fracture surfaces of the samples aged for 400 h at temperature of (a) 160°C (one side), (b) 160°C (other side), (c) 180°C (one side), (d) 180°C (other side), (e) 200°C (one side), and (f) 200°C (other side).

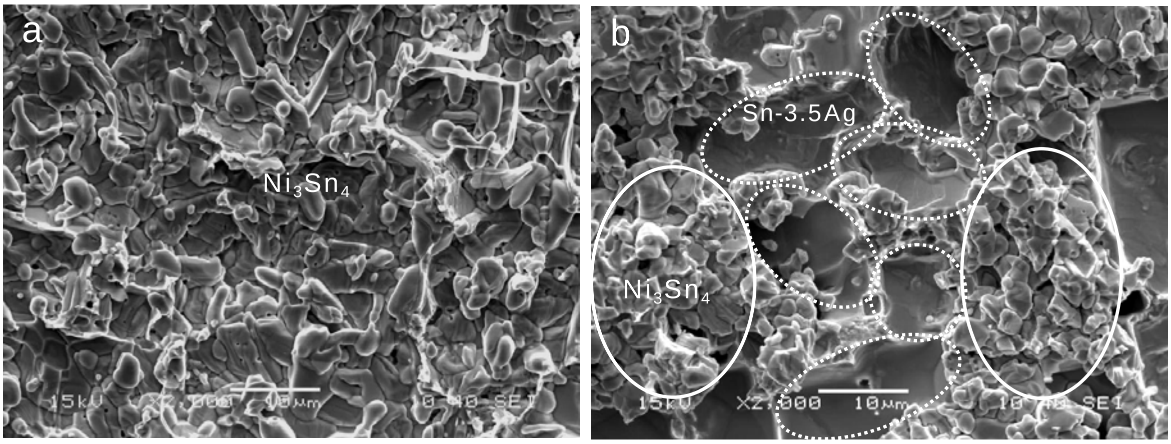
a
Ni_3Sn_4
15kV X2,000 10μm 10 40 SEI
b
Sn-3.5Ag
Ni_3Sn_4
15kV X2,000 10μm 10 40 SEI

Fig. 3.15. Fracture surfaces of the solder joint aged at 180°C for 48 h showing mixed failure (macroscopically brittle while microscopically ductile) at the interface between (a) Ni_3Sn_4 and (b) solder.

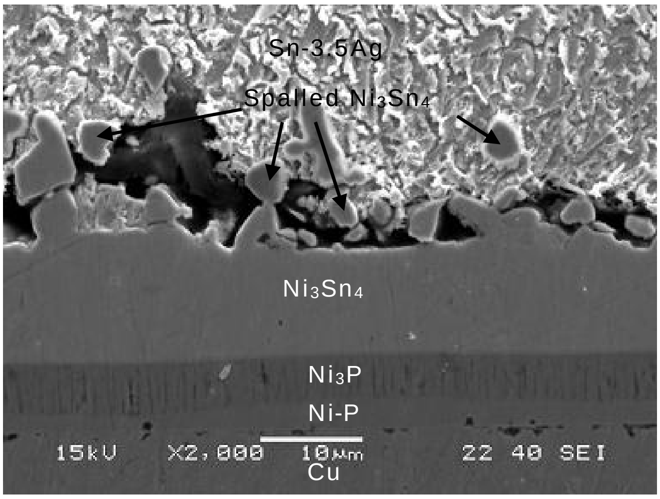
Sn-3.5Ag
Spalled Ni_3Sn_4
Ni_3Sn_4
Ni_3P
Ni-P
Cu
15kV X2,000 10μm 22 40 SEI

Fig. 3.16. Cross-sectional SEM image showing fracture at the solder/Ni_3Sn_4 interface in the solder joint aged at 180°C for 48 h.

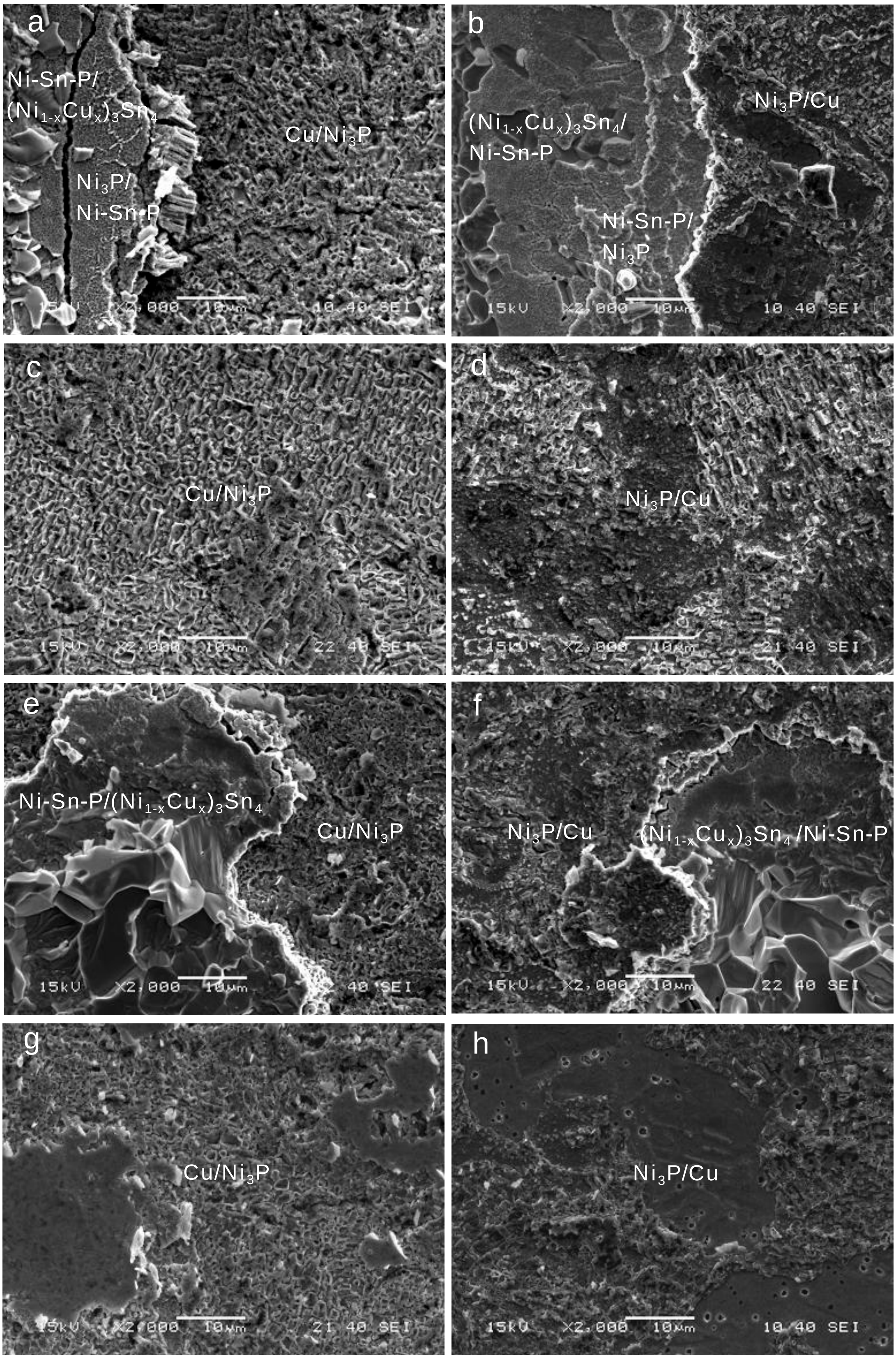
a
Ni-Sn-P/ $(Ni_{1-x}Cu_x)_3Sn_4$
Ni_3P/ Ni-Sn-P
Cu/Ni_3P
15kV X2,000 10µm 10 40 SEI
b
Ni_3P/Cu
$(Ni_{1-x}Cu_x)_3Sn_4$/ Ni-Sn-P
Ni-Sn-P/ Ni_3P
15kV X2,000 10µm 10 40 SEI
c
Cu/Ni_3P
15kV X2,000 10µm 22 40 SEI
d
Ni_3P/Cu
15kV X2,000 10µm 21 40 SEI
e
Ni-Sn-P/$(Ni_{1-x}Cu_x)_3Sn_4$
Cu/Ni_3P
15kV X2,000 10µm 40 SEI
f
Ni_3P/Cu
$(Ni_{1-x}Cu_x)_3Sn_4$/Ni-Sn-P
15kV X2,000 10µm 22 40 SEI
g
Cu/Ni_3P
15kV X2,000 10µm 21 40 SEI
h
Ni_3P/Cu
15kV X2,000 10µm 10 40 SEI

Fig. 3.17. Fracture surfaces of the solder joints aged at 200°C for (a) 48 h (Cu side), (b) 48 h (solder side), (c) 100 h (Cu side), (d) 100 h (solder side), (e) 225 h (Cu side), (f) 225 h (solder side), (g) 400 h (Cu side), and (h) 400 h (solder side). Fracture occured mainly at the Ni_3P/Cu interface.

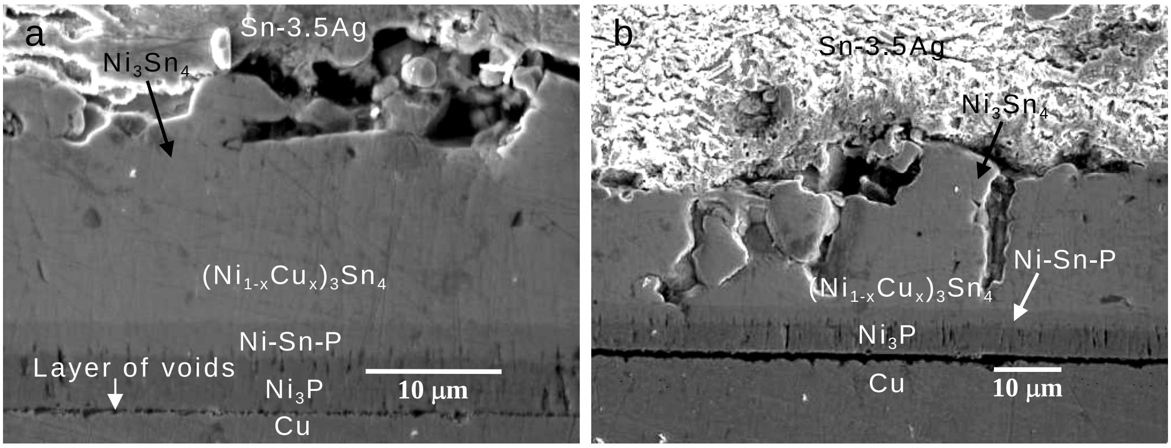
a
Sn-3.5Ag
Ni3Sn4
(Ni1-xCux)3Sn4
Ni-Sn-P
Layer of voids
Ni3P
Cu
10 μm
b
Sn-3.5Ag
Ni3Sn4
Ni-Sn-P
(Ni1-xCux)3Sn4
Ni3P
Cu
10 μm

Fig. 3.18. Cross-sectional SEM images showing (a) formation of a layer of Kirkendall voids at the Ni_3P/Cu interface and (b) fracture at the Ni_3P/Cu interface in the solder joint aged at 200°C for 100 h.

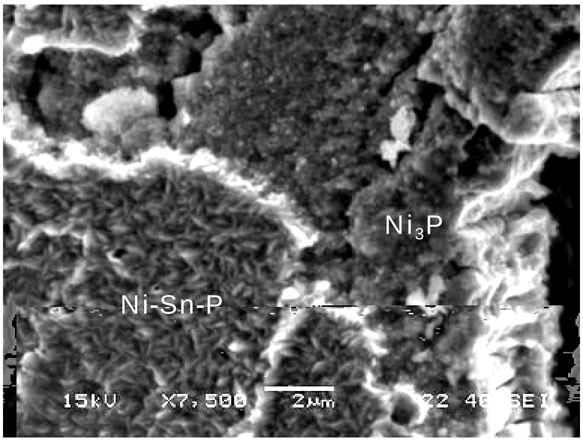
Ni3P
Ni-Sn-P
15kV X7,500 2μm

Fig. 3.19. Fracture surface of solder joint aged at 200°C for 48 h showing the fine grains of Ni-Sn-P compound grown on the columnar-grained Ni_3P layer.

3.4. Discussion

3.4.1. Reaction between Sn and Ni_3P forming Ni-Sn-P Layer

In this study, it was observed that in the samples aged at 200°C, Ni-Sn-P and Ni_3Sn_4+$(Ni_{1-x}Cu_x)_3Sn_4$ layers grow at the expanse of Ni_3P layer (Figs. 3.7 and 3.8d). This indicates that the thickness of Ni-Sn-P and Ni_3Sn_4+$(Ni_{1-x}Cu_x)_3Sn_4$ layers increases due to the diminishing of Ni_3P layer. However, there is another factor, the inclusion of Cu that comes from Ni_3P/Cu interface, which also increases the Ni_3Sn_4+$(Ni_{1-x}Cu_x)_3Sn_4$ layer thickness. Taking the account of maximum Cu concentration in Ni_3Sn_4+$(Ni_{1-x}Cu_x)_3Sn_4$ layer (average value is 2.5 at.% in the sample aged for 400 h), the maximum possible growth in Ni_3Sn_4+ $(Ni_{1-x}Cu_x)_3Sn_4$ layer due to the inclusion of Cu is calculated to be around 1.2 µm. However, the growth in Ni_3Sn_4+ $(Ni_{1-x}Cu_x)_3Sn_4$ layer during the diminishing of Ni_3P layer (from 48 to 400 h of aging) was 4.8 µm (see Fig. 3.8d). Thus, it can easily be understood that during the diminishing of the Ni_3P layer a large amount of Ni was supplied for the growth of Ni_3Sn_4+ $(Ni_{1-x}Cu_x)_3Sn_4$ layer. Based on this analysis, we propose the following reaction between Sn and Ni_3P

$$\mathrm{Sn} + \mathrm{Ni}_3\mathrm{P} \rightarrow \mathrm{Ni}_2\mathrm{SnP} + \mathrm{Ni} \qquad (3.1)$$

To prove the reaction between Sn and Ni_3P, the law of conservation of mass is applied on the growth of compound layers in the samples aged at 200°C. In these samples, electroless Ni-P layer completely transformed into Ni_3P layer within 48 h of aging (Fig. 3.7a) and then Ni_3P layer completely transformed into Ni-Sn-P layer within 400 h of aging (Fig. 3.7d). Thus, according to the equation 3.1, if Ni_3P layer is transformed into Ni_2SnP layer due to its reaction with Sn, then the moles of Ni in the Ni_3P layer existed after 48 h of aging, must be equal to the moles of Ni in the Ni_2SnP layer grown after 48 h of aging and the moles of free Ni. Since free Ni is used to grow Ni_3Sn_4 intermetallic, the moles of free Ni must be equal to the moles of Ni in the Ni_3Sn_4 layer grown after 48 h of aging. To make the mass balance calculation easier, the small presence of Cu in $(Ni_{1-x}Cu_x)_3Sn_4$ ($0 \leq x \leq 0.12$) intermetallics is neglected and Ni_3Sn_4+ $(Ni_{1-x}Cu_x)_3Sn_4$ layer is assumed to be of Ni_3Sn_4 intermetallic only.

From Fig. 3.8d, the thickness of Ni_3P layer at 48 h of aging is 4.8 µm and the growth in Ni_2SnP and Ni_3Sn_4 layers from 48 to 400 h of aging are 6.9 and 4.8 µm, respectively. The moles of Ni in a compound layer of thickness t_{IFC} per unit interfacial area can be determined by

$$\mathrm{Ni}_{\mathrm{IFC}} = m \times \frac{t_{IFC}\, d_{IFC}}{M_{IFC}} \qquad (3.2)$$

where, m is the number of moles of Ni in one mole of compound, M_{IFC} is the molecular weight, and d_{IFC} is the density of compound. Thus, by inserting the values of m (3 for Ni_3P, 2 for Ni_2SnP, and 3 for Ni_3Sn_4), densities (d_{Ni_3P} = 7.82 g/cm^3 (Jang *et al.*, 1999), d_{Ni_2SnP} = 7.56 g/cm^3 (Furuseth and Fjellvag, 1985), and $d_{Ni_3Sn_4}$ = 8.64 g/cm^3 (Jang *et al.*, 1999)), molecular weights, and layer thicknesses in the equation 3.2, the Ni_{Ni_3P}, Ni_{Ni_2SnP}, and $Ni_{Ni_3Sn_4}$ are determined to be 0.54, 0.39, and 0.19 mole/cm^2. From these values it is clear that $Ni_{Ni_3P} \approx Ni_{Ni_2SnP} + Ni_{Ni_3Sn_4}$. Thus, it is proved that Sn reacts with Ni_3P layer to form Ni_2SnP and Ni_3Sn_4 compounds. The slightly higher value of $Ni_{Ni_2SnP} + Ni_{Ni_3Sn_4}$ than that of Ni_{Ni_3P} can be understood to be due to the presence of small amount of Cu in $(Ni_{1-x}Cu_x)_3Sn_4$ intermetallics, which we neglected in the mass balance calculation.

3.4.2. Elemental Diffusion and Kirkendall Void Formation in Ni-P Layer

A large number of small columnar voids were observed in the Ni_3P layer formed in the as-prepared sample (Fig. 3.4a). The size and number of these voids increased with the increase in Ni_3P thickness during aging (Fig. 3.5). This implies that the voids in Ni_3P layer form in conjunction with the transformation of electroless Ni-P layer into Ni_3P layer. During this transformation, as shown in Fig. 3.20b, P remains in the Ni-P layer. However, Ni diffuses out from the Ni-P layer, which causes a reduction in the thickness of Ni-P layer (Fig. 3.5c). Interestingly, Sn does not diffuse into the Ni_3P layer (Fig. 3.20d) and stops at the interface between Ni-Sn-P and Ni_3P layers (Fig. 3.21d).

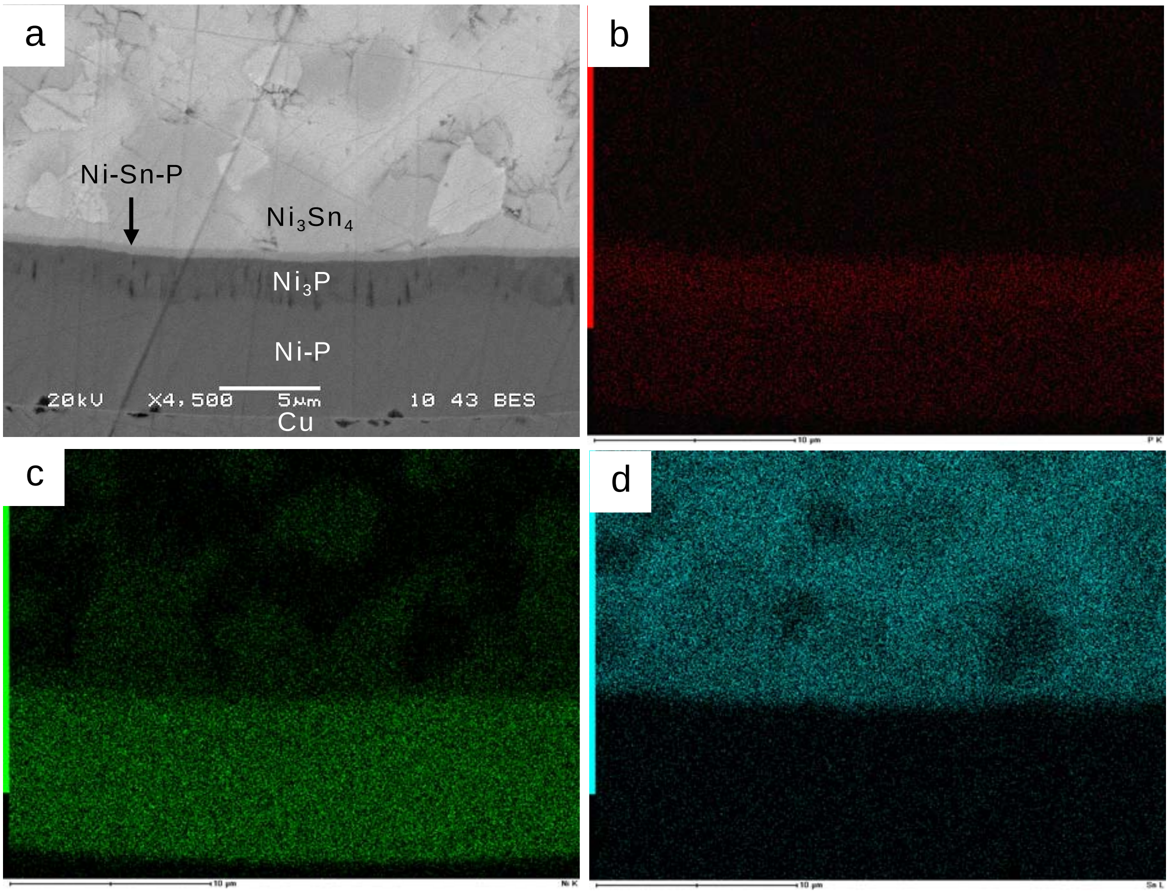

Fig. 3.20. EDS element mapping analysis of Sn-3.5Ag/Ni-P/Cu interfaces of the sample aged at 160 °C for 400 h: (a) SEM image, (b) mapping for P, (c) mapping for Ni, and (d) mapping for Sn. The concentration of element decreases with an increase in intensity of black color.

Though, the Sn-3.5Ag/electroless Ni-P interfacial reactions result in the depletion of Ni from the electroless Ni-P layer, the diffusion species in Ni-P layer could be either P or Ni. Jang *et al.* (1999) proposed that during solder/electroless Ni-P interfacial reactions, either Ni diffuses out from the electroless Ni-P layer through the grain boundaries of Ni_3P layer or Ni_3P decomposes into P and Ni at the reaction front and then P diffuses interstitially back to grow Ni_3P at the Ni_3P/electroless Ni-P interface. However, they supported the interstitial diffusion of P because the grain boundary diffusion of Ni from the electroless Ni-P layer must be accompanied by the back diffusion of vacancies and no Kirkendall void was observed in their study. On the other hand, He *et al.* (2004a) observed the Kirkendall void formation in the Ni_3P layer and thus supported the diffusion of Ni thorough the grain boundaries of Ni_3P layer. In the present work also, a large number of columnar voids formed in the Ni_3P layer and they grew with the growth of Ni_3P layer. These observations confirm that during solder/electroless Ni-P interfacial reactions, Ni diffuses out from the electroless Ni-P layer through the grain boundaries of Ni_3P layer to form Ni_3Sn_4. This out diffusion of Ni assists electroless Ni-P to transform into Ni_3P and results in a counter diffusion of vacancies. With aging, these vacancies agglomerate and form voids in the Ni_3P layer. The reason behind the invisibility of Kirkendall voids in the Ni_3P layer in the case of Jang *et al.* (1999) study could be the insufficient reaction temperature (< 240 ° C) and time (< 40 min) given to the vacancies to nucleate and/or grow into voids.

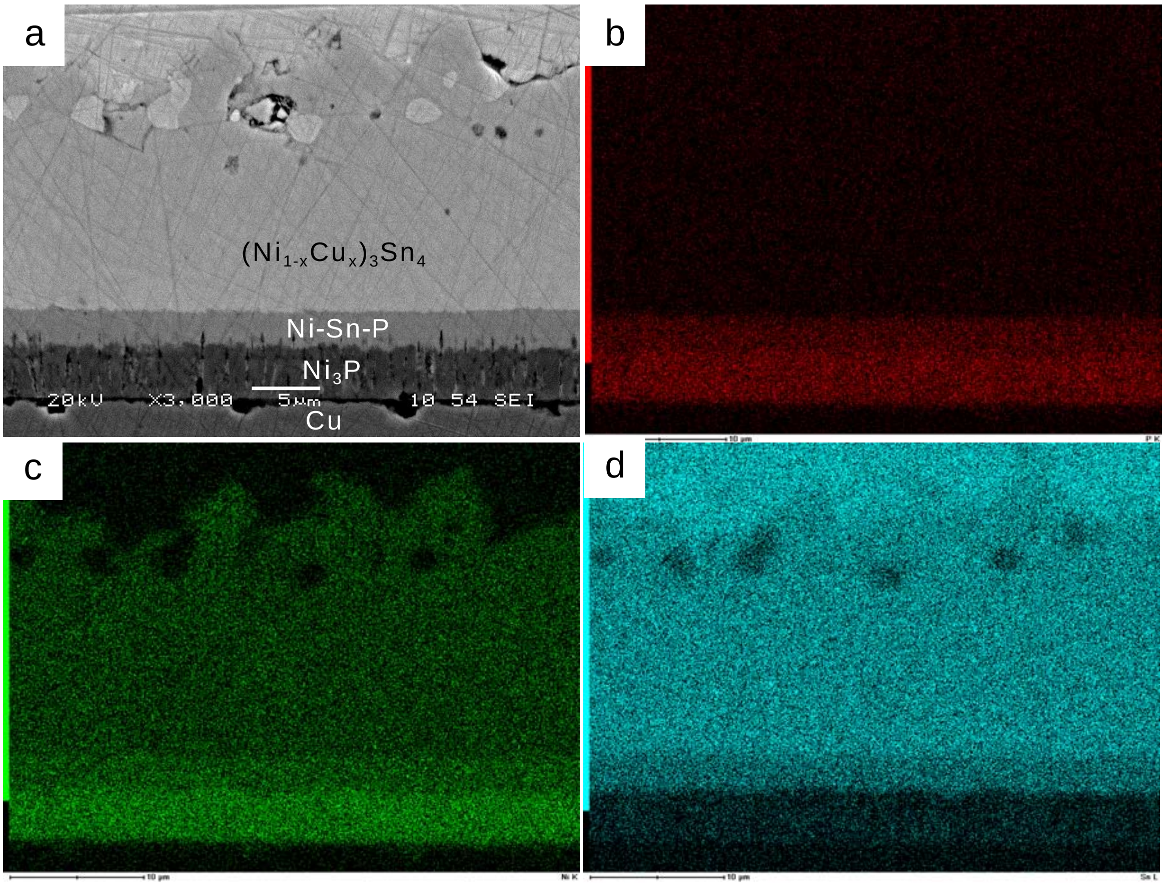

Fig. 3.21. EDS element mapping analysis of Sn-3.5Ag/Ni-P/Cu interfaces of the sample aged at 200 °C for 100 h: (a) SEM image, (b) mapping for P, (c) mapping for Ni, (d) mapping for Sn. The concentration of element decreases with an increase in intensity of black color.

3.4.3. Thermodynamics and Kinetics of Interfacial Compound Formation

From this study it is clear that the Sn-3.5Ag/electroless Ni-P interfacial reactions result in the formation of multiple Ni_3Sn_4, Ni-Sn-P, and Ni_3P compounds. However, Ni-Sn and Ni-P phase diagrams (Massalski, 1986) suggest that other Ni-Sn (Ni_3Sn_2 and Ni_3Sn) and Ni-P (Ni_5P_2, $Ni_{12}P_5$, Ni_2P, Ni_5P_4, and NiP_2) compounds should also form during the interfacial reactions. Thus, to understand the formation of Ni_3Sn_4 and Ni_3P compounds, thermodynamic calculations were carried out to compare the thermodynamic driving force for the formation of different Ni-Sn and Ni-P compounds. Only Ni_3Sn_2, Ni_3Sn, Ni_5P_2, Ni_2P compounds were considered for the thermodynamic calculations due to a lack of thermodynamic data for other Ni-P and ternary Ni-Sn-P compounds (Binnewies and Mike, 2002; Kubaschewski *et al.*, 1993).

For transformation that occurs at constant temperature and pressure, the relative stability of a system is determined by its Gibbs free energy (G). The Gibbs free energy of a system is defined by the equation (Porter and Easterling, 1991; Kubaschewski *et al.*, 1993)

$$G = H - TS \qquad (3.3)$$

where, H is the enthalpy, S is the entropy, and T is the absolute temperature of the system. In a system, any phase transformation that results in a decrease in Gibbs free energy is possible. Therefore, for a phase transformation, a necessary criterion is $\Delta G = G_{\text{products}} - G_{\text{reactants}} < 0$, where ΔG is thermodynamic driving force (Porter and Easterling, 1991; Kubaschewski *et al.*, 1993).

The thermodynamic driving forces for the formation of different Ni-Sn and Ni-P compounds were calculated considering the reaction between Ni and Sn and the depletion of Ni from electroless Ni-P ($Ni_{84}P_{16}$), respectively. The reaction between Ni and Sn and the transformation of electroless Ni-P into Ni-P compound can be represented in a general form as

$$a\text{Ni} + \text{bSn} \rightarrow \text{Ni}_{\text{a}}\text{Sn}_{\text{b}} \qquad (3.4)$$

$$\mathrm{Ni_{84}P_{16}} \rightarrow a\mathrm{Ni_bP_c} + (86 - a \cdot b)\mathrm{Ni} \qquad \text{, where a} \cdot \text{c} = 16 \qquad (3.5)$$

Based on the reactions 3.4 and 3.5, a change in Gibbs free energies for the formation of all the possible Ni-Sn and Ni-P compounds were calculated. Since the thermodynamic data for $Ni_{84}P_{16}$ alloy is unknown (Binnewies and Mike, 2002; Kubaschewski *et al.*, 1993), $G_{Ni_{84}P_{16}}$ is used for $Ni_{84}P_{16}$. The calculated ΔG values for Ni-P and Ni-Sn compounds are tabulated in the Table 3.6 and 3.7, respectively. From these values it is clear that at all the aging temperatures the thermodynamic driving force (negative value of ΔG) is largest for the formation Ni_3Sn_4 and Ni_3P compound.

Table 3.6. Comparison between the thermodynamic driving forces (Gibbs free energy change, ΔG) for the formation of different Ni-P compounds. The ΔG is calculated for the transformation of one mole of electroless Ni-P ($Ni_{84}P_{16}$). The $G_{Ni_{84}P_{16}}$ is unknown.

Aging temperature (°C)	ΔG for Ni_3P formation (kJ/mole)	ΔG for Ni_5P_2 formation (kJ/mole)	ΔG for Ni_2P formation (kJ/mole)
140	$-4714.42-G_{Ni_{84}P_{16}}$	$-4690.18-G_{Ni_{84}P_{16}}$	$-4160.60-G_{Ni_{84}P_{16}}$
160	$-4786.97-G_{Ni_{84}P_{16}}$	$-4763.26-G_{Ni_{84}P_{16}}$	$-4233.91-G_{Ni_{84}P_{16}}$
180	$-4861.85-G_{Ni_{84}P_{16}}$	$-4838.71-G_{Ni_{84}P_{16}}$	$-4309.62-G_{Ni_{84}P_{16}}$
200	$-4938.99-G_{Ni_{84}P_{16}}$	$-4916.45-G_{Ni_{84}P_{16}}$	$-4387.66-G_{Ni_{84}P_{16}}$

Table 3.7. Comparison between the thermodynamic driving forces (Gibbs free energy change, ΔG) for the formation of different Ni-Sn compounds. The ΔG is calculated for the formation of one mole of Ni-Sn compound.

Aging temperature (°C)	ΔG for Ni_3Sn_4 formation (kJ/mole)	ΔG for Ni_3Sn_2 formation (kJ/mole)	ΔG for Ni_3Sn formation (kJ/mole)
140	-158.31	-148.71	-105.11
160	-156.21	-148.13	-110.34
180	-153.92	-147.51	-116.28
200	-151.44	-146.86	-122.90

From the thermodynamic calculations, it is clear that the thermodynamic driving force for the formation Ni_3P and Ni_3Sn_4 compound is largest. Their exact formation reactions can be written as

$$3\mathrm{Ni} + 4\mathrm{Sn} \rightarrow \mathrm{Ni}_3\mathrm{Sn}_4 \tag{3.6}$$

$$\mathrm{Ni}_{84}\mathrm{P}_{16} \rightarrow 16\mathrm{Ni}_3\mathrm{P} + 36\mathrm{Ni} \tag{3.7}$$

The reaction 3.7 also represents the self-crystallization of amorphous electroless Ni-P, which occurs only at and above 280 °C (Li *et al.*, 1998). However, in the present study we observed the growth of Ni_3P at very low temperature of 140 °C. Moreover, we observed a constant relation between the growth of Ni_3P and Ni_3Sn_4 layers (Table 3.3). These observations indicate that the reactions 3.6 and 3.7 do not take place independently. Jang *et al.* (1999) also observed that the transformation (crystallization) of electroless Ni-P layer takes place at much lower temperature and in shorter duration of annealing in the case of soldering reaction as compared to the self-crystallization. They called this phenomenon as “solder reaction-assisted crystallization of electroless Ni-P”. The solder reaction-assisted crystallization of electroless Ni-P can be understood by combining the reactions 3.6 and 3.7 into one as

$$\mathrm{Ni}_{84}\mathrm{P}_{16} + 48\mathrm{Sn} \rightarrow 16\mathrm{Ni}_3\mathrm{P} + 12\mathrm{Ni}_3\mathrm{Sn}_4 \tag{3.8}$$

Now, on comparing the thermodynamic driving force for the self-crystallization and solder reaction-assisted crystallization of electroless Ni-P (Table 3.8), it can be seen that the thermodynamic driving force for electroless Ni-P crystallization is much higher in the case of soldering reaction. Thus, the high thermodynamic driving force is the reason for low temperature crystallization of electroless Ni-P during soldering reaction.

Table 3.8. Comparison between the thermodynamic driving forces (Gibbs free energy change, ΔG) for the self-crystallization and solder reaction-assisted crystallization of electroless Ni-P. The ΔG is calculated for the transformation of one mole of electroless Ni-P ($Ni_{84}P_{16}$). The $G_{Ni_{84}P_{16}}$ is unknown.

Aging temperature (°C)	ΔG for self-crystallization (3.7) (kJ/mole)	ΔG for solder-assisted crystallization (3.8) (kJ/mole)
140	$-4714.42-G_{Ni_{84}P_{16}}$	$-6614.11-G_{Ni_{84}P_{16}}$
160	$-4786.97-G_{Ni_{84}P_{16}}$	$-6661.44-G_{Ni_{84}P_{16}}$
180	$-4861.85-G_{Ni_{84}P_{16}}$	$-6708.84-G_{Ni_{84}P_{16}}$
200	$-4938.99-G_{Ni_{84}P_{16}}$	$-6756.28-G_{Ni_{84}P_{16}}$

So far in this section, thermodynamic driving force or a change in Gibbs free energy has been discussed to explain the formation of compound. Though a decrease in Gibbs free energy provides information about phase formation, the rate at which a phase will form cannot be determined by classical thermodynamics. Thus, it is possible that a phase which has a low thermodynamic driving force grows very fast, and vice-versa. The study of the rate of phase formation belongs to the science of kinetics. According to kinetic theory, the rate of phase formation depends upon the probability of an atom to reach activated state and the frequency with which atoms reach the activated state (Porter and Easterling, 1991). The rate of phase formation can be represented by Arrhenius equation (equation 2.2), in which $exp(-Q/RT)$ is the probability and A is the frequency factor.

Since kinetic data for Ni_3Sn_4 and Ni_3P compounds are only available in the cited literature on solder/electroless Ni-P system (Table 2.1), it can be understood that at the experimental conditions, the growth of other Ni-P and Ni-Sn compounds in this system is too slow to be measured. In the present study, kinetic parameters are determined for the growth of Ni_3Sn_4, Ni-Sn-P, and Ni_3P compounds and tabulated in the Table 3.4. Considering the fact that kinetic parameters vary widely with solder's composition and experimental conditions, the kinetic parameters for the Ni_3Sn_4 and Ni_3P compounds that obtained in this study are in agreement with the results of previous studies (Table 3.5). However, no comparison could be made for ternary Ni-Sn-P compound due to a lack of kinetic data (Jang *et al.*, 1999; He *et al.*, 2004b; Yoon and Jung, 2004; Sharif *et al.*, 2005).

3.4.4. Transition of Ni-Sn-P Growth Kinetics

From this study, we know that though Ni-Sn-P growth is diffusion controlled, in some circumstances it can be a reaction rate controlled such as in the case of samples aged at 200 °C. As the excessive growth of Ni-Sn-P layer can influence the mechanical reliability of electroless Ni-P/solder joint, it is necessary to understand this transition of Ni-Sn-P growth kinetics so that its growth can be controlled. It is known that in the electroless Ni-P/solder system, Sn is the dominant diffusing element in Ni_3Sn_4 (Lee and Lin, 1994) and Ni diffuses from electroless Ni-P layer through Ni_3P and Ni-Sn-P layers to form Ni_3Sn_4 (Jang *et al.*, 1999; Matsuki *et al.*, 2002; Chen *et al.*, 2004; He *et al.* 2004a). Thus, it can be understood that in the samples aged at 140, 160 and 180 °C, where sufficient Ni was available from electroless Ni-P, most of the Sn coming from solder was consumed by Ni to from Ni_3Sn_4 and therefore the growth of Ni-Sn-P layer was slow. However in the samples aged at 200 °C, owing to the complete transformation of electroless Ni-P layer into Ni_3P (Figs. 3.7 and 3.8d), the supply of Ni became insufficient and thus all the Sn started reacting with Ni_3P, which resulted in a rapid growth of Ni-Sn-P layer. From this, it can be said that as long as electroless Ni-P layer is present underneath the Ni_3P layer, the growth of Ni-Sn-P is controlled by the diffusion of Ni through Ni_3P, otherwise by the rate of reaction between Sn and Ni_3P. Thus, the growth of ternary Ni-Sn-P compound can be suppressed by ensuring continuous supply of Ni from electroless Ni-P layer. The continuous supply of Ni from electroless Ni-P can be easily extended either by increasing the thickness or by decreasing the P concentration of electroless Ni-P layer.

3.4.5. Growth Mechanism of Interfacial Compounds

In this work, it was found that mainly three compounds, Ni_3Sn_4, Ni-Sn-P, and Ni_3P, form during electroless Ni-P/Sn-3.5Ag interfacial reactions. The formation of these compounds has been reported in several studies (Jang *et al.*, 1999; Zeng and Tu, 2002; Matsuki *et al.*, 2002; Chen *et al.*, 2004; He *et al.*, 2004a; Wang and Liu, 2003; Yoon and Jung, 2005). Nonetheless, the understanding made on their growth mechanism is incomplete. It is known that during electroless Ni-P/solder interfacial reactions, Sn of solder reacts with Ni of electroless Ni-P and forms Ni_3Sn_4 intermetallic (Jang *et al.*, 1999; Zeng and Tu, 2002; Lee and Lin, 1994). The depletion of Ni from electroless Ni-P layer results in its transformation into higher P containing Ni-P (Ni_3P) layer (Jang *et al.*, 1999; Matsuki *et al.*, 2002; Chen *et al.*, 2004). For the further growth of Ni_3Sn_4, Sn diffuses from solder through Ni_3Sn_4 layer and Ni diffuses from electroless Ni-P layer through Ni_3P layer (Jang *et al.*, 1999; Lee and Lin, 1994; Matsuki *et al.*, 2002; He *et al.*, 2004a).

From the present investigation, it is clear that during electroless Ni-P/solder interfacial reactions, Sn of solder also reacts with Ni_3P layer and forms Ni_2SnP compound in between the Ni_3Sn_4 and Ni_3P layers. The growth of Ni_2SnP compounds remains slow as long as Ni is available from the electroless Ni-P layer. Once the electroless Ni-P layer is completely transformed into Ni_3P, there is no Ni to react with Sn and thus, all the Sn starts reacting with the Ni_3P layer to form Ni_2SnP and therefore the Ni_2SnP layer starts growing rapidly at the expense of the Ni_3P layer (Fig. 3.7). The Cu present underneath the Ni_3P layer tries to compensate the supply of Ni; however, the layer of Kirkendall voids that formed at the Ni_3P/Cu interface due to the depletion of Cu (Fig. 3.7) restricts further supply of Cu from the Cu surface.

Based on previous and present investigations, the growth mechanism of compounds formed at the Sn-3.5Ag/electroless Ni-P/Cu interfaces can now be understood well and is depicted in Fig. 3.22. There are mainly three reactions, reaction between Sn and Ni forming Ni_3Sn_4 intermetallic, transformation of electroless Ni-P into Ni_3P, and reaction between Sn and Ni_3P forming Ni_2SnP compound, which take place during electroless Ni-P/solder interfacial reactions. For these reactions, Sn diffuses from the solder and first reaches the Ni_3Sn_4/Ni_2SnP interface, where it reacts with Ni and forms Ni_3Sn_4. Sn then reaches the Ni_2SnP/Ni_3P interface and forms Ni_2SnP compound due to its reaction with Ni_3P. Thus, at the beginning of the interfacial reactions, growth of Ni_3Sn_4 and Ni_3P layers dominates the growth of Ni_2SnP compound as most of the Sn coming from the solder is consumed by Ni at the Ni_3Sn_4/Ni_2SnP interface and only a small part of Sn reaches the Ni_2SnP/Ni_3P interface to react with Ni_3P. However, once the supply of Ni becomes low, the Ni_2SnP compound starts growing rapidly because most of the Sn starts reacting with the Ni_3P layer.

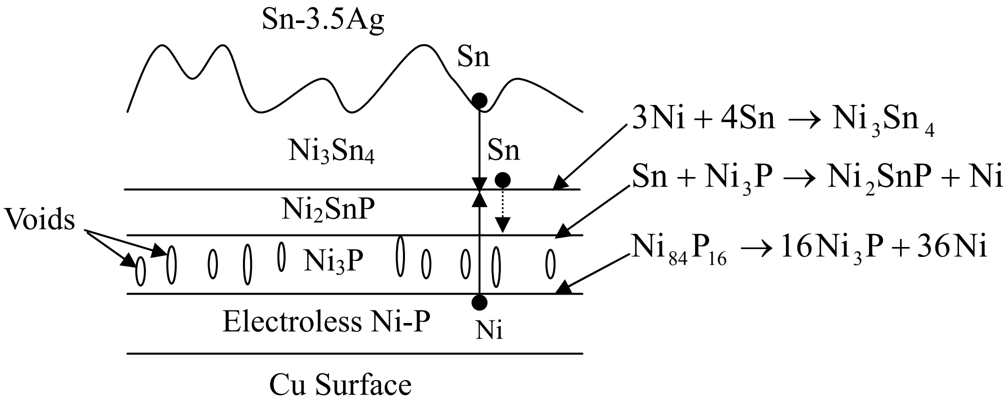
Sn-3.5Ag
Sn
$3Ni + 4Sn \rightarrow Ni_3Sn_4$
Ni_3Sn_4
Sn
$Sn + Ni_3P \rightarrow Ni_2SnP + Ni$
Voids
Ni_2SnP
$Ni_{84}P_{16} \rightarrow 16Ni_3P + 36Ni$
Ni_3P
Electroless Ni-P
Ni
Cu Surface

Fig. 3.22. Schematic illustration of the growth of multiple compounds at the Sn-3.5Ag/electroless Ni-P/Cu interfaces showing all the interfacial reactions.

3.4.6. Transition of Ni_3Sn_4 Morphology

Several studies (Jang *et al.*, 1999, 2000; He *et al.*, 2004b, d) have examined the morphology of Ni_3Sn_4 IMC in the electroless Ni-P/solder systems. It has been reported that Ni_3Sn_4 grains having needle-type and chunky-type morphologies form at the electroless Ni-P/solder interface after reflow (Jang *et al.*, 1999, 2000; He *et al.*, 2004b, d). The formation of needle-type Ni_3Sn_4 grains dominates at the beginning of reflow; however, needle-type Ni_3Sn_4 grains disappear and the number and size of chunky-type Ni_3Sn_4 grains increase with increasing the reflow duration (He *et al*., 2004b, d). In this study also, Ni_3Sn_4 IMC with needle-type and chunky-type morphologies formed in the as-prepared or reflowed sample (Fig. 3.4b) and their morphologies changed into "scallop-type" after solid-state aging (Fig. 3.6).

Although much has been reported about the morphology of Ni_3Sn_4 IMC in the electroless Ni-P/solder systems, little is known about its transition. In general, other than crystallography, the morphology of IMC formed during soldering reaction mainly depends upon the state of reaction (solid or liquid) (Tu *et al.*, 2001a), solder and UBM compositions (He *et al.*, 2004b; Tu *et al.*, 2003), and processing or more accurately the microstructure of reacting materials (Sohn *et al.*, 2004b). Other factors such as reaction temperature and time also influence the IMC morphology; however, their influence is more on grain growth rather than on grain shape (He *et al.* 2004b). Since Ni_3Sn_4 with needle-type morphology has been reported to form with electroless Ni-P UBM and not with sputtered Ni (He *et al.* 2004b), it can be easily understood that the needle-type morphology of Ni_3Sn_4 is related to the microstructure of electroless Ni-P. The electroless Ni-P UBM (12.5 at.% < P < 19 at.%) used in the electronic industry normally has amorphous structure (Mallory and Hajdu, 1990), however it transforms into crystalline Ni_3P and Ni-Sn-P layers due to the soldering reaction (Chen *et al.*, 2004; He *et al.* 2004a; Jang *et al.*, 1999). The crystallized electroless Ni-P layer has fine columnar grains of nm size (Chen *et al.*, 2004; He *et al.*, 2004a; Jang *et al.*, 1999). Thus, considering the microstructure of Ni_3P layer, the formation of needle-type Ni_3Sn_4 IMC in the electroless Ni-P/solder system can be understood. At the beginning of soldering reaction when the Ni_3P grain is of a few tens of nm and the thickness of Ni-Sn-P layer is negligible, the formation of a large number of needle-type Ni_3Sn_4 IMC can be understood to be due to a large number of grain boundaries in Ni_3P layer. These grain boundaries are perpendicular to reaction interface and Ni atoms diffuse out from electroless

Ni-P layer through them (Chen *et al.*, 2004; He *et al.*, 2004a; Jang *et al.*, 1999; Matsuki *et al.*, 2002). Therefore, at the beginning of soldering reaction, Ni atoms are trapped by Sn atoms at the exit of Ni_3P grain boundaries and unidirectional flow of Ni from Ni_3P grain boundaries results in the needle-type morphology of Ni_3Sn_4. After the formation of needle-type Ni_3Sn_4, as soldering reaction precedes, needle-type Ni_3Sn_4 grains disappear and chunky-type Ni_3Sn_4 grains grow due to the well-known grain-coarsening phenomenon (Gusak and Tu, 2002; Lifshitz and Slyozov, 1961).

In the case of solid-state aging, the needle-type and/or chunky-type morphologies of Ni_3Sn_4 change into scallop-type due to the change in interfacial energy between Sn-3.5Ag solder and Ni_3Sn_4 intermetallic. The interfacial energy of intermetallics is highly anisotropic with molten pure Sn and it decreases with increasing the concentration of alloying element (Tu *et al.*, 2003). Thus, the interfacial energy between Ni_3Sn_4 and molten Sn-Ag solder with a small amount of Ag (less than 3.5 wt.%) can be understood to be highly anisotropic and this causes the Ni_3Sn_4 morphology to be faceted chunky-type. However, during solid-state aging, the interfacial energy between Ni_3Sn_4 and solid Sn-Ag solder becomes isotropic and consequently Ni_3Sn_4 morphology changes from faceted chunky-type to curved scallop-type.

3.4.7. Diffusion of Cu through Ni-P Layer

From interfacial microstructure analysis, it has been observed that Cu diffuses through the Ni_3P layer (Figs. 3.5d and 3.7). However, the mechanism of Cu diffusion needs to be understood. Electroless Ni-P UBM is a good diffusion barrier due to its amorphous structure. The amorphous structure lacks the grain boundaries and thus inhibits the grain boundary diffusion. The structure of electroless Ni-P generally depends upon its P concentration (Mallory and Hajdu, 1990); amorphous if P is higher than 12.5 at.% and nanocrystalline otherwise. Thus, the as-plated electroless Ni-P layer (with 16 at.% P) was amorphous in nature, which transformed into bi-layered Ni-P, crystalline Ni_3P layer on the electroless Ni-P layer, during reflow (Fig. 3.4a). This Ni_3P layer grew continuously at the expense of electroless Ni-P layer during aging (Fig. 3.5). Therefore, as this layer reached the Cu substrate, Cu started diffusing out through the grain boundaries of Ni_3P layer (Fig. 3.23).

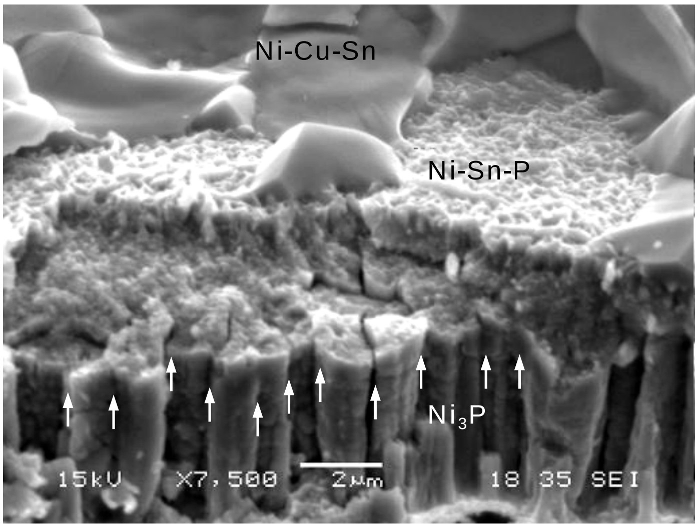

Fig. 3.23. Fracture surface of the Cu/electroless Ni-P/Sn-3.5Ag solder joint aged at 200 °C for 100 h showing micron-size columnar Ni_3P grains. The arrows indicate the diffusion paths in the grain boundaries of Ni_3P grains.

A schematic illustration of Cu diffusion through the Ni_3P layer is shown in Fig. 3.24. As Sn-3.5Ag/Ni-P interfacial reactions proceed, Ni diffuses out from the electroless Ni-P layer through the grain boundaries of Ni_3P layer to form Ni_3Sn_4 and thus results in the growth of Ni_3P layer (Fig. 9a). This process is continued until the Ni_3P layer reaches the Cu substrate, after that Cu starts diffusing out from the Cu substrate through the grain boundaries of Ni_3P layer to compensate the Ni supply (Fig. 3.24b). It is to be understood that as long as electroless Ni-P layer present on the Cu substrate, Cu cannot diffuse out due to the lack of grain boundaries in the electroless Ni-P. However, after its crystallization into Ni_3P, the grain boundaries of Ni_3P layer provide diffusion paths for Cu atoms. Thus, the diffusion of Cu from the Cu substrate can be inhibited by preventing the complete crystallization of electroless Ni-P layer.

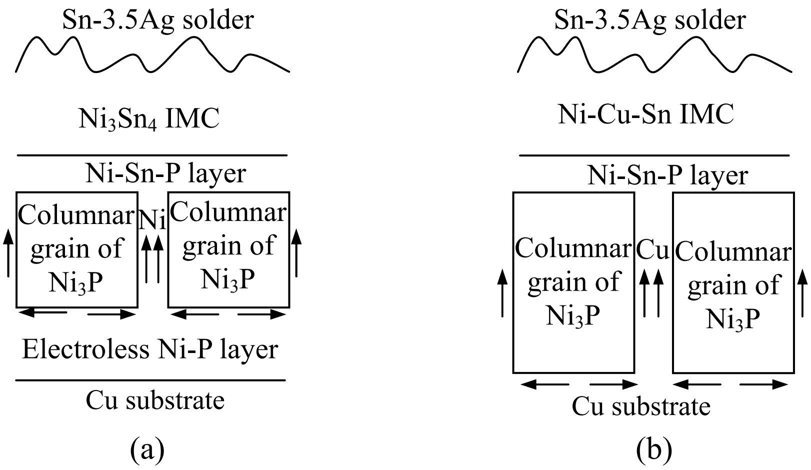
Sn-3.5Ag solder
Ni3Sn4 IMC
Ni-Sn-P layer
Columnar grain of Ni3P
Ni
Columnar grain of Ni3P
Electroless Ni-P layer
Cu substrate
(a)
Sn-3.5Ag solder
Ni-Cu-Sn IMC
Ni-Sn-P layer
Columnar grain of Ni3P
Cu
Columnar grain of Ni3P
Cu substrate
(b)

Fig. 3.24. Schematic illustration of Cu diffusion through the Ni_3P layer: (a) Growth of Ni_3P layer in between Ni_3Sn_4 intermetallic and electroless Ni-P layer and (b) Diffusing of Cu through the grain boundaries of Ni_3P layer.

3.4.8. Factors Affecting the Mechanical Properties of Solder Joint

The results obtained in this investigation clearly show that the mechanical properties of Cu/electroless Ni-P/Sn-3.5Ag solder joint are influenced by the interfacial reactions. However, the factors that are associated with the interfacial reactions and affect the mechanical properties of solder joint have to be identified. Based on the results, two main factors, growth of interfacial compounds and formation of a layer of Kirkendall voids at the Ni_3P/Cu interface, are identified and thus discussed in this section.

Growth of Interfacial Compounds

It was found that as long as electroless Ni-P layer remains on the Cu surface, neither the formation of Ni_3P and Ni-Sn-P compounds nor the formation of voids in the Ni_3P layer affect the solder joint strength directly. All the samples aged at 160 and 180 °C had the Ni_3P and Ni-Sn-P compounds; nevertheless, the fracture occurred inside the bulk solder and at the Ni_3Sn_4/Sn-3.5Ag interface (Fig. 3.14a, b, c, and d), respectively. However, the growth of Ni_3Sn_4 IMC was found to deteriorate the mechanical properties of solder joint owing to the several factors such as the development of intrinsic stresses, Ni_3Sn_4 morphology, and the accumulation of spalled Ni_3Sn_4 particles at the solder/Ni_3Sn_4 interface.

Development of Intrinsic Stresses

Owing to interfacial reactions, multiple compounds grow at the Cu/electroless Ni-P/Sn-3.5Ag interfaces. As mass is conserved during interfacial reactions, intrinsic-volumetric stresses are built up at the reaction interfaces due to the difference in density of reacting materials and resulting compounds. These volumetric stresses increase with the increase in the thickness of compound layer and eventually make the reaction interfaces more prone to failure.

Table 3.9 shows the density of reacting materials and resulting compounds in the Cu/electroless Ni-P/Sn-3.5Ag solder joint. The high density of Ni_3Sn_4 indicates that maximum volumetric stress generates with the growth of Ni_3Sn_4. This evidence supports our observation of the fracture at the Sn-3.5Ag/Ni_3Sn_4 interface in the samples aged at 180 °C (Fig. 3.16). In these samples even though both Ni_3Sn_4 and Ni_3P grew with aging, fracture occurred primarily at the Sn-3.5Ag/Ni_3Sn_4 interface. Apart from intrinsic stresses, there are a few other factors that also contribute to the failure at Sn-3.5Ag/Ni_3Sn_4 interface and will be discussed subsequently.

Table. 3.9. Density of reacting materials and resulting compounds in the Cu/electroless Ni-P/Sn-3.5Ag solder joint.

Reacting materials and resulting compounds	Density (g/cm^3)	References
Electroless Ni-P (16 at.% P)	7.9	ASM, 1994
Sn-3.5Ag	7.5	Qualitek, 2006
Ni_3Sn_4	8.64	Jang *et al.*, 1999
Ni_3P	7.82	Jang *et al.*, 1999
Ni_2SnP	7.56	Furuseth and Fjellvag, 1985

Ni_3Sn_4 Morphology

The morphology of IMCs formed between solder and UBM during interfacial reactions is an area of great interest for researchers. There are various investigations in which the morphology of IMCs formed at the solder/electroless Ni-P interface has been studied (He *et al.*, 2004b, d; Jang *et al.*, 1999, 2000a). However, limited experimental evidence is available about their influence on the mechanical properties of the solder joint. In this investigation, a clear correlation was observed between Ni_3Sn_4 morphology and the tensile properties of the solder joint. In the case of as-prepared samples, the tensile strength was ~ 45 MPa and ductile fracture occurred in the bulk solder (Figs. 3.11 and 3.13). The tensile strength slightly increased to ~ 50 MPa in the case of samples aged at 160 °C, however similar ductile fracture occurred in the bulk solder (Figs. 3.11, 3.14a, and 3.14b). On the other hand, in the case of samples aged at 180 °C, the strength decreased to ~ 28 MPa and mixed fracture occurred at the Sn-3.5Ag/Ni_3Sn_4 interface (Figs. 3.11, 3.15, and 3.16).

On comparing the interfacial microstructure of as-prepared and aged (at 160 and 180 °C) samples, the morphology of Ni_3Sn_4 was found to be one of the causes of mixed fracture at the Sn-3.5Ag/Ni_3Sn_4 interface in the samples aged at 180 °C. In the as-prepared samples, Ni_3Sn_4 IMC had needle-type and chunky-type morphologies (Fig. 3.4) and its morphology changed into scallop-type due to the solid-state aging at 160 °C (Figs. 3.5b and 3.6b). Although in the samples aged at 180 °C Ni_3Sn_4 morphology changed into scallop-type, in these samples the Sn-3.5Ag/Ni_3Sn_4 interface became more even due to the large growth of Ni_3Sn_4 as shown in Figs. 3.5c and 3.6c. The even Sn-3.5Ag/Ni_3Sn_4 interface resulted in the less contact surface area between Sn-3.5Ag solder and Ni_3Sn_4 IMC, and that made the Sn-3.5Ag/Ni_3Sn_4 interface more prone to failure.

Accumulation of Spalled Ni_3Sn_4 Particles at the Solder/Ni_3Sn_4 Interface

A number of Ni_3Sn_4 particles were observed to spall off the Sn-3.5Ag/Ni_3Sn_4 interface during reflow (Fig. 3.4a). Although the spalled Ni_3Sn_4 particles were found not to influence the mechanical properties directly, these particles accumulated at the Sn-3.5Ag/Ni_3Sn_4

interface due to the large growth of Ni_3Sn_4 IMC in the samples aged at 180 and 200 °C (Fig. 3.5c and d). The accumulated Ni_3Sn_4 particles decreased the contact surface area between Sn-3.5Ag solder and Ni_3Sn_4 IMC and caused the fracture to take place at the Sn-3.5Ag/Ni_3Sn_4 interface as shown in Figs. 3.15 and 3.16.

To make the effect of Ni_3Sn_4 spallation on the interfacial microstructure and strength of Cu/electroless Ni-P/Sn-3.5Ag solder joint more clear, a schematic illustration is shown in Fig 3.23. As shown in Fig. 3.25a, a number of Ni_3Sn_4 particles spall off the Sn-3.5Ag/Ni_3Sn_4 interface during reflow and remain close to the Sn-3.5Ag/Ni_3Sn_4 interface after reflow. The Ni_3Sn_4 IMC grows further during solid-state aging and eventually spalled Ni_3Sn_4 particles come in contact with growing Ni_3Sn_4 IMC. The large growth of Ni_3Sn_4 IMC causes the large accumulation of spalled Ni_3Sn_4 particles at the Sn-3.5Ag/Ni_3Sn_4 interface (Fig. 3.25b). These accumulated particles break the direct contact between solder and Ni_3Sn_4 IMC and thus reduce the adhesion between solder and Ni_3Sn_4 IMC.

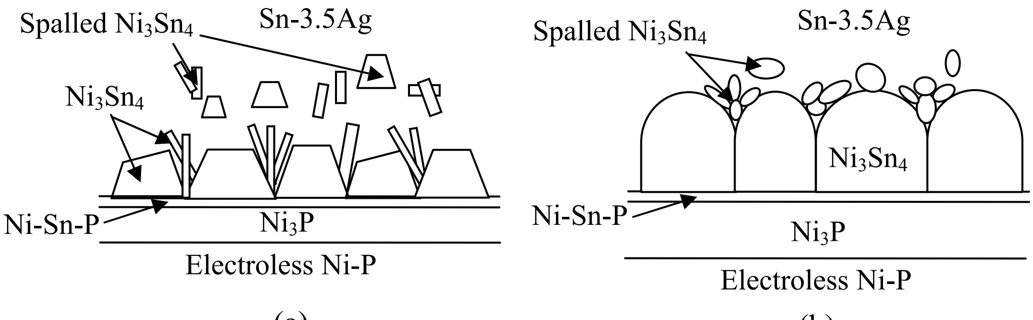

(a) (b)

Fig. 3.25. Schematic illustration for the effect of Ni_3Sn_4 spallation on the interfacial microstructure of solder joint: (a) Ni_3Sn_4 spallation during reflow and (b) Accumulation of spalled Ni_3Sn_4 particles at the solder/Ni_3Sn_4 interface due to the growth of Ni_3Sn_4 layer during aging.

Formation of a Layer of Kirkendall Voids at the Ni_3P/Cu Interface

It was observed that in the case of samples aged at 200 °C, the tensile strength decreased severely to ~12 MPa (Fig. 3.11) and brittle fracture occurred mainly at the Ni_3P/Cu interface (Figs. 3.17 and 3.18b). Appearance of Ni_3P/Cu interface as one of main fracture surfaces indicates that in these samples, the Cu surface lost its adhesion with the adjoining Ni_3P layer. In these samples, electroless Ni-P layer completely transformed into Ni_3P and Ni-Sn-P layers (Fig. 3.18a). Then, the Cu started depleting from the Cu surface to the Ni_3Sn_4 intermetallic through the Ni_3P and Ni-Sn-P layers (Fig. 3.23). The depletion of Cu from the Cu surface resulted in the formation of a layer of Kirkendall voids at the Cu/Ni_3P interface as shown in Figs. 3.7 and 3.18a. This layer of voids broke down the mechanical and atomic interlocking between Cu surface and Ni_3P layer; thus causing a severe decrease in solder joint strength with a brittle fracture at the Cu/Ni_3P interface (Fig. a. Tb).

Although all the mentioned factors reduced the solder joint strength and changed the failure mode from ductile to brittle, the solder joint became extremely weak due to the formation of a layer of Kirkendall voids at the Ni_3P/Cu interface. The Kirkendall voids at the Ni_3P/Cu interface were found to form only after the complete transformation of electroless Ni-P layer into Ni_3P layer, which opened the channel for Cu to diffuse from Cu surface to Ni_3Sn_4 intermetallic.

a.5. Conclusions

Interfacial reactions and mechanical properties of solder joint between Sn-3.5Ag solder and electroless Ni-P metallization on Cu substrate were investigated after reflow and high temperature solid-state aging. The following conclusions have been made based on the investigation

1. During interfacial reactions, mainly three compounds, Ni Sn , Ni-Sn-P, and Ni P, grow at the Sn-3.5Ag/electroless Ni-P interface. Ni_3Sn_4, Ni-Sn-P, and Ni_3P grow due to the reaction between Sn and Ni, reaction between Sn and Ni_3P, and depletion of Ni from electroless Ni-P, respectively. The depletion of Ni from electroless Ni-P layer results in the formation of columnar Kirkendall voids in the Ni_3P layer.
2. Ni_3Sn_4 grains with needle-type and chunky-type morphologies form during reflow;

however, their morphologies change into scallop-type after solid-state aging.

3. Ni_3Sn_4 and Ni_3P layers grow predominantly as long as electroless Ni-P layer is present at the reaction interface. However, after the complete transformation of electroless Ni-P layer into Ni_3P, Ni-Sn-P layer grows rapidly at the expanse of Ni_3P layer.
4. The growth of Ni_3Sn_4 and Ni_3P follows $t^{1/3}$ kinetics. Initially, the growth of ternary Ni-Sn-P compound also follows $t^{1/3}$ kinetics, but after the complete transformation of electroless Ni-P layer into Ni_3P, it follows linear (t^1) kinetics due to the dominating reaction of Sn with Ni_3P.
5. The apparent activation energies for the growth of Ni_3Sn_4, Ni-Sn-P, and Ni_3P compounds are found to be 98.9, 42.2, and 94.3 kJ/mol, respectively.
6. Interfacial reactions degrade the mechanical properties of Cu/electroless Ni-P/Sn-3.5Ag solder joint due to the extensive growth of Ni_3Sn_4 IMC and due to the depletion of Cu from the Cu surface. The mechanical properties are degraded more severely with the latter.
7. The growth of Ni_3Sn_4 IMC results in a mixed fracture at the Ni_3Sn_4/Sn-3.5Ag interface. The depletion of Cu from the Cu surface results in the formation of a layer of Kirkendall voids at the Cu/Ni_3P interface, which further degrades the joint strength and causes a brittle fracture at the Cu/Ni_3P interface.
8. Growth of other compounds such as Ni_3P and Ni-Sn-P does not affect the mechanical properties of solder joint as long as the electroless Ni-P layer remains on the Cu surface. However after the complete transformation of electroless Ni-P layer into Ni_3P, columnar Kirkendall voids of Ni_3P layer and fine grains of Ni-Sn-P layer help the fracture to transmit from the Ni_3P/Cu interface to the $(Ni_{1-x}Cu_x)_3Sn_4$/Ni-Sn-P and/or Ni-Sn-P/Ni_3P interfaces.

From this investigation, it is clear that the mechanical properties of Cu/electroless

Ni-P/Sn-3.5Ag solder joint are influenced by the interfacial reactions. Furthermore, it has been reported that the UBM/solder interfacial reactions are influenced by the UBM thickness itself (Choi and Lee, 1999; Huang *et al.*, 2003). Thus, the influence of Ni-P UBM thickness on the Cu/electroless Ni-P/Sn-3.5Ag interfacial reactions and solder joint strength has also been investigated and will be presented in the following chapter.

Chapter 4

Influence of Ni-P thickness on Cu/Electroless Ni-P/Sn-3.5Ag Interfacial Reactions and Solder Joint Strength

4.1. Introduction

Numerous studies have been done on the interfacial reactions between solder and electroless Ni-P UBM and their effect on solder joint strength (Ahat *et al.*, 2000, Alam *et al.*, 2003; Chonan *et al.*, 2002a; He *et al.*, 2005; Hung *et al.*, 2000a; Islam *et al.*, 2003; Liu and Shang, 2000a; Mei *et al.*, 1998; Yoon *et al.*, 2004). Nevertheless, understanding made so far on the influence of electroless Ni-P UBM thickness on interfacial reactions and solder joint strength is incomplete. Accordingly, in this part of the work, solid-state interfacial reactions and mechanical properties of solder joint between Sn-3.5Ag solder and electroless Ni-P UBM on Cu substrate have been studied for the different thicknesses of Ni-P UBM. An attempt has been made to correlate the mechanical properties of solder joint with the evolution of interfacial microstructure.

4.2. Experimental Procedures

4.2.1. Preparation of Test Samples

The procedure for test samples preparation was the same as described in section 3.2.1. However, in this study, electroless Ni-P metallization, of three different thicknesses, was plated on the Cu plate by selecting the three different deposition times (10, 20, and 30 min) under the same process conditions.

4.2.2. Thermal Aging of Test Samples

In this work, thermal aging of as-prepared test samples was carried out at 160, 180, and

200 °C for 48, 100, 225, and 400 h. After aging, the samples were removed from the oven and cooled in air to room temperature.

4.2.3. Tensile Testing of Test Samples

The same as described in section 3.2.3.

4.2.4. Microstructural Observations

The same as described in section 3.2.4.

4.3. Results

The thicknesses of three as-plated electroless Ni-P layers were measured to be around 3.9, 7.3, and 9.9 μm, while the P concentration was found to be around 16 at.%. According to their thicknesses, the electroless Ni-P layers are termed as thin, medium, and thick Ni-P.

4.3.1. Interfacial Microstructure Analysis

As-prepared Test Samples

Fig. 4.1 shows the back-scattered SEM images of Sn-3.5Ag/Ni-P/Cu interfaces in the as-prepared solder joints having electroless Ni-P layer of different thicknesses. Regardless of the Ni-P thickness, all the joints were found to have similar interfacial microstructure and chemistry. It can be seen that needle-type and chunky-type Ni_3Sn_4 intermetallic formed at the Sn-3.5Ag/Ni-P interface during the reflow, part of which spalled off into the molten solder. Underneath the Ni_3Sn_4, a ternary Ni-Sn-P layer of sub-micron thickness formed. Underneath the Ni-Sn-P layer, a dark thin Ni_3P layer having a large number of voids formed within the electroless Ni-P layer.

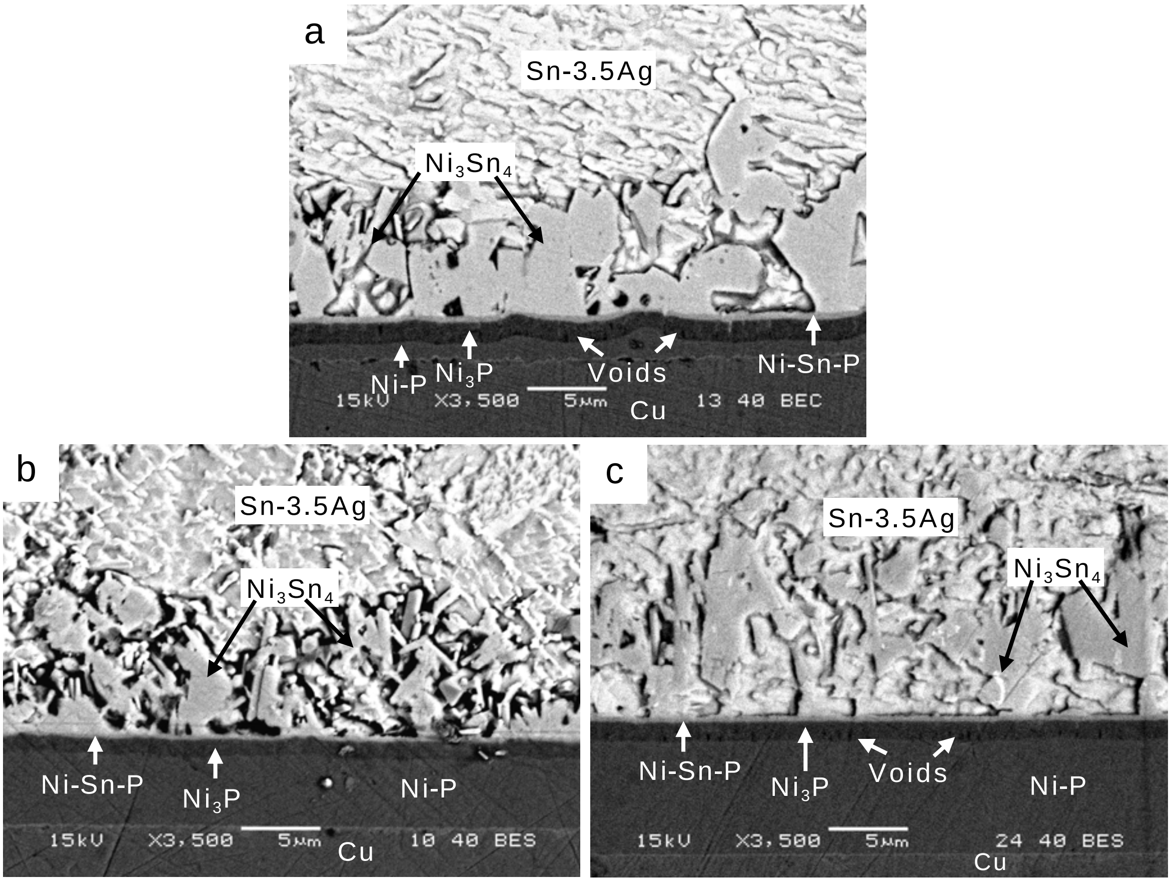
a
Sn-3.5Ag
Ni3Sn4
Ni-P
Ni3P
Voids
Ni-Sn-P
Cu
15kU X3,500 5µm 13 40 BEC
b
Sn-3.5Ag
Ni3Sn4
Ni-Sn-P
Ni3P
Ni-P
Cu
15kU X3,500 5µm 10 40 BES
c
Sn-3.5Ag
Ni3Sn4
Ni-Sn-P
Ni3P
Voids
Ni-P
Cu
15kU X3,500 5µm 24 40 BES

Fig. 4.1. Back-scattered SEM images of Sn-3.5Ag/Ni-P/Cu interfaces in the as-prepared samples having electroless Ni-P layers of thickness of (a) 3.9 µm, (b) 7.3 µm, and (c) 9.9 µm.

Thermally-Aged Test Samples

Fig. 4.2 is the back-scattered SEM images of Sn-3.5Ag/Ni-P/Cu interfaces in the samples aged at 160 °C for 225 h showing the growth of Ni_3Sn_4 intermetallic and Ni_3P layer. It can be observed that in the thin Ni-P sample, electroless Ni-P layer completely transformed into Ni_3P, whereas in other samples, it was still present underneath the Ni_3P layer. In all the samples, several voids formed in the Ni_3P layer due to the depletion of Ni. However, a layer of voids also formed at the Ni_3P/Cu interface in the thin Ni-P sample (Fig. 4.2a). In addition, in this sample, the Ni_3Sn_4 intermetallic was found to have Cu up to 5 at.%. The presence of Cu in the Ni_3Sn_4 and the formation of layer of voids at the Ni_3P/Cu interface imply that the Cu diffused out from the Cu substrate to the Ni_3Sn_4 in the thin Ni-P sample.

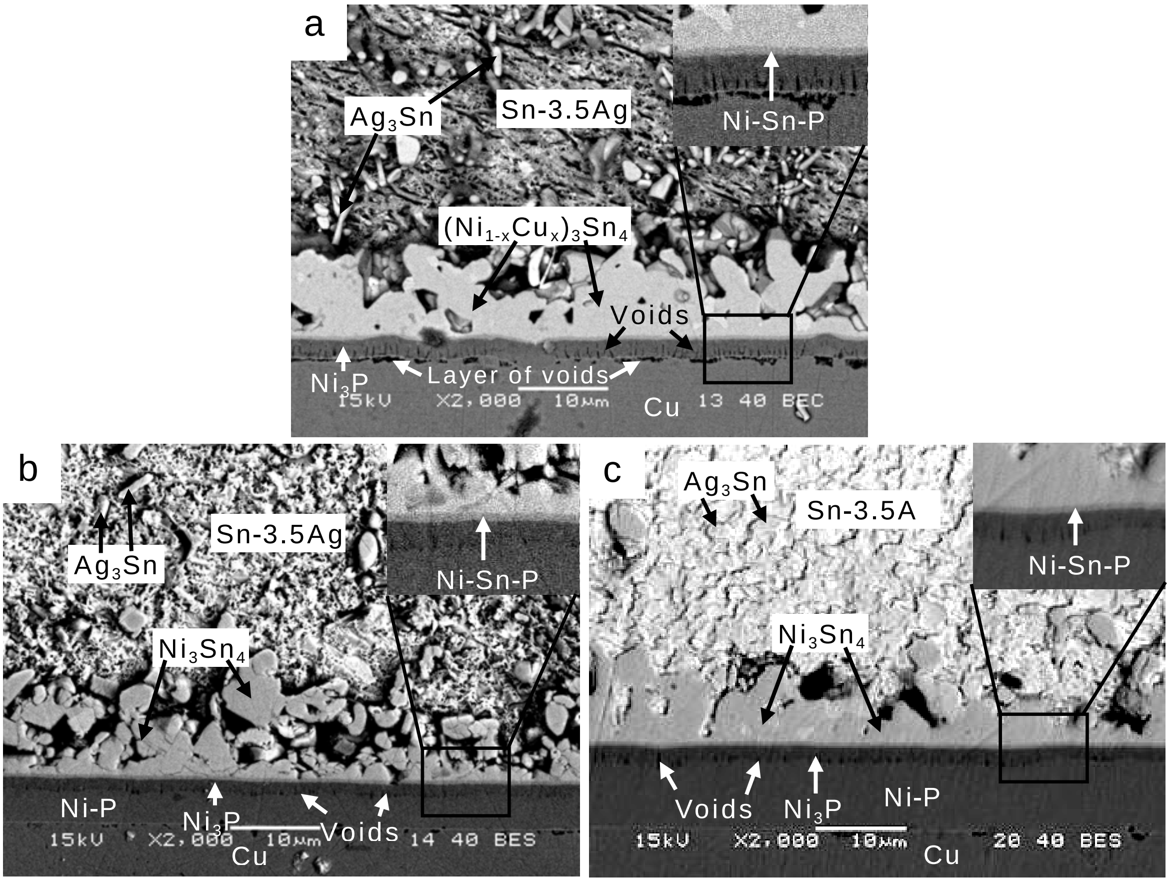
a
Ag_3Sn
Sn-3.5Ag
Ni-Sn-P
$(Ni_{1-x}Cu_x)_3Sn_4$
Voids
Ni_3P
Layer of voids
15kU X2,000 10µm
Cu
13 40 BEC
b
Ag_3Sn
Sn-3.5Ag
Ni-Sn-P
Ni_3Sn_4
Ni-P
Ni_3P
Voids
15kU X2,000 10µm
Cu
14 40 BES
c
Ag_3Sn
Sn-3.5A
Ni-Sn-P
Ni_3Sn_4
Voids
Ni_3P
Ni-P
15kU X2,000 10µm
Cu
20 40 BES

Fig. 4.2. Back-scattered SEM images of Sn-3.5Ag/Ni-P/Cu interfaces in the solder joints aged at 160 °C for 225 h and having (a) thin (3.9 µm), (b) medium (7.3 µm), and (c) thick (9.9 µm) Ni-P layers.

Fig. 4.3 is the back-scattered SEM images of Sn-3.5Ag/Ni-P/Cu interfaces in the samples aged at 180 °C for 225 h showing the growth of Ni_3Sn_4, Ni_3P, Ni-Sn-P, and Ni-Cu-Sn compounds. From the figure, it is clear that the thickness of electroless Ni-P UBM influences the growth of interfacial compounds. Along with the transformation of Ni-P layer into Ni_3P, only Ni_3Sn_4 grew predominantly in the thick Ni-P sample, whereas, Ni-Sn-P also grew in other samples. This Ni-Sn-P layer grew at the expense of Ni_3P layer (Fig. 4.3a and b). The chemical composition of this Ni-Sn-P layer was close to that of Ni_2SnP compound. It can be seen that in the thick Ni-P sample, the number of voids formed at the Ni_3P/Cu interface is negligible as compared to the other samples. In this sample, the Cu concentration of Ni_3Sn_4 intermetallic (<1 at.%) was also negligible as compared to the other samples that had Cu up to 7 at.%.

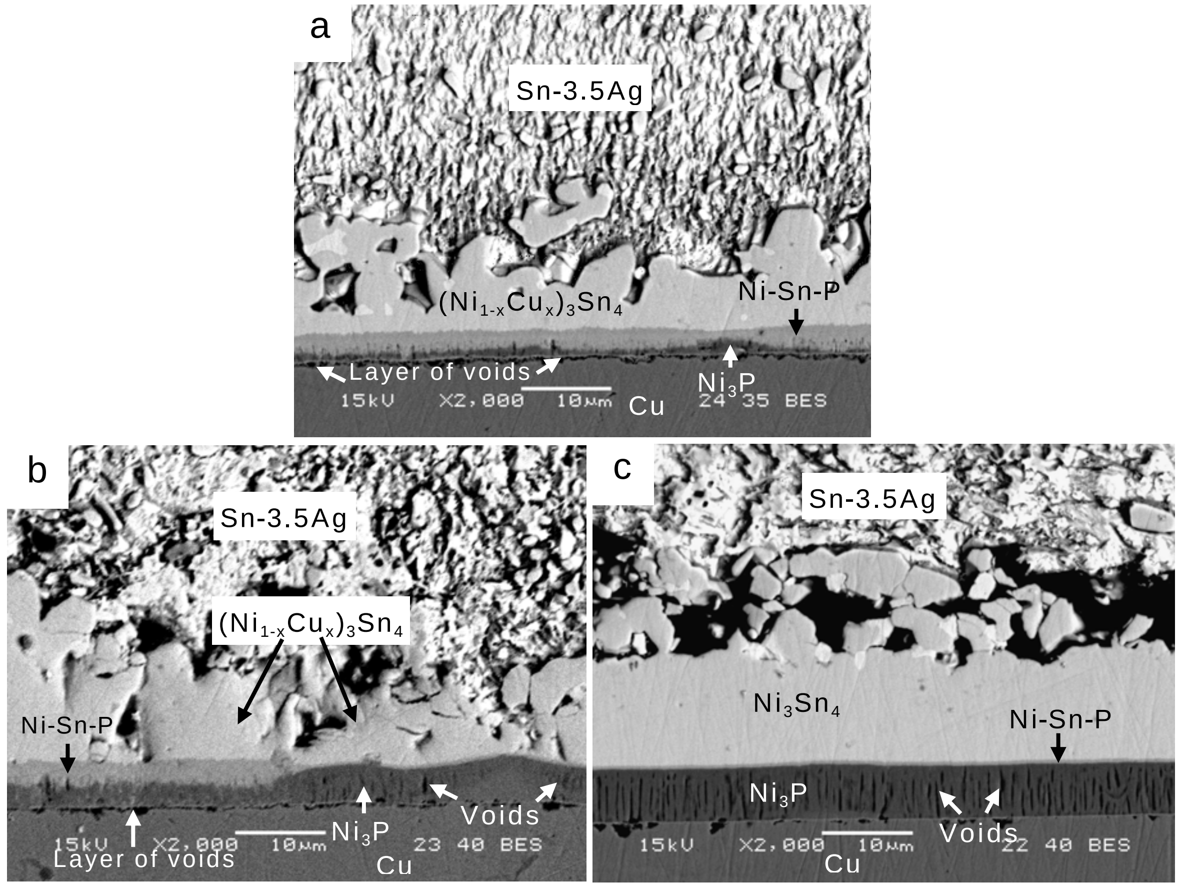
a
Sn-3.5Ag
(Ni1-xCux)3Sn4
Ni-Sn-P
Layer of voids
Ni3P
Cu
15kU X2,000 10µm 24 35 BES
b
Sn-3.5Ag
(Ni1-xCux)3Sn4
Ni-Sn-P
Layer of voids
Ni3P
Voids
Cu
15kU X2,000 10µm 23 40 BES
c
Sn-3.5Ag
Ni3Sn4
Ni-Sn-P
Ni3P
Voids
Cu
15kU X2,000 10µm 22 40 BES

Fig. 4.3. Back-scattered SEM images of Sn-3.5Ag/Ni-P/Cu interfaces in the samples aged at 180 °C for 225 h and having (a) thin (3.9 μm), (b) medium (7.3 μm), and (c) thick (9.9 μm) Ni-P layers.

Fig. 4.4 is the back-scattered SEM images of Sn-3.5Ag/Ni-P/Cu interfaces in the samples aged at 200 °C for 400 h showing the growth of Ni-Cu-Sn, Ni-Sn-P, and Cu-Sn compounds. It can be seen that electroless Ni-P layer completely dissolved into Ni-Sn-P in all the samples. In the sample with thin Ni-P, two layers of Cu-Sn IMCs, Cu_6Sn_5 and Cu_3Sn, formed at the Ni-Sn-P/Cu interface. The Cu_3Sn formed close to Cu substrate, understood to be due to the large availability of Cu from the Cu substrate. In the sample with thin Ni-P, two Ni-Cu-Sn intermetallics of distinct colors and chemical compositions, $(Ni_{1-x}Cu_x)_3Sn_4$ and $(Ni_{1-x}Cu_x)_6Sn_5$, also formed at the Ni_3Sn_4/Ni-Sn-P interface (Fig. 4.4a and Table 4.1). On the other hand, no Cu-Sn or $(Ni_{1-x}Cu_x)_6Sn_5$ intermetallics were found to form in the samples with medium and thick Ni-P, however, $(Ni_{1-x}Cu_x)_3Sn_4$ formed with Cu up to 6 at.%.

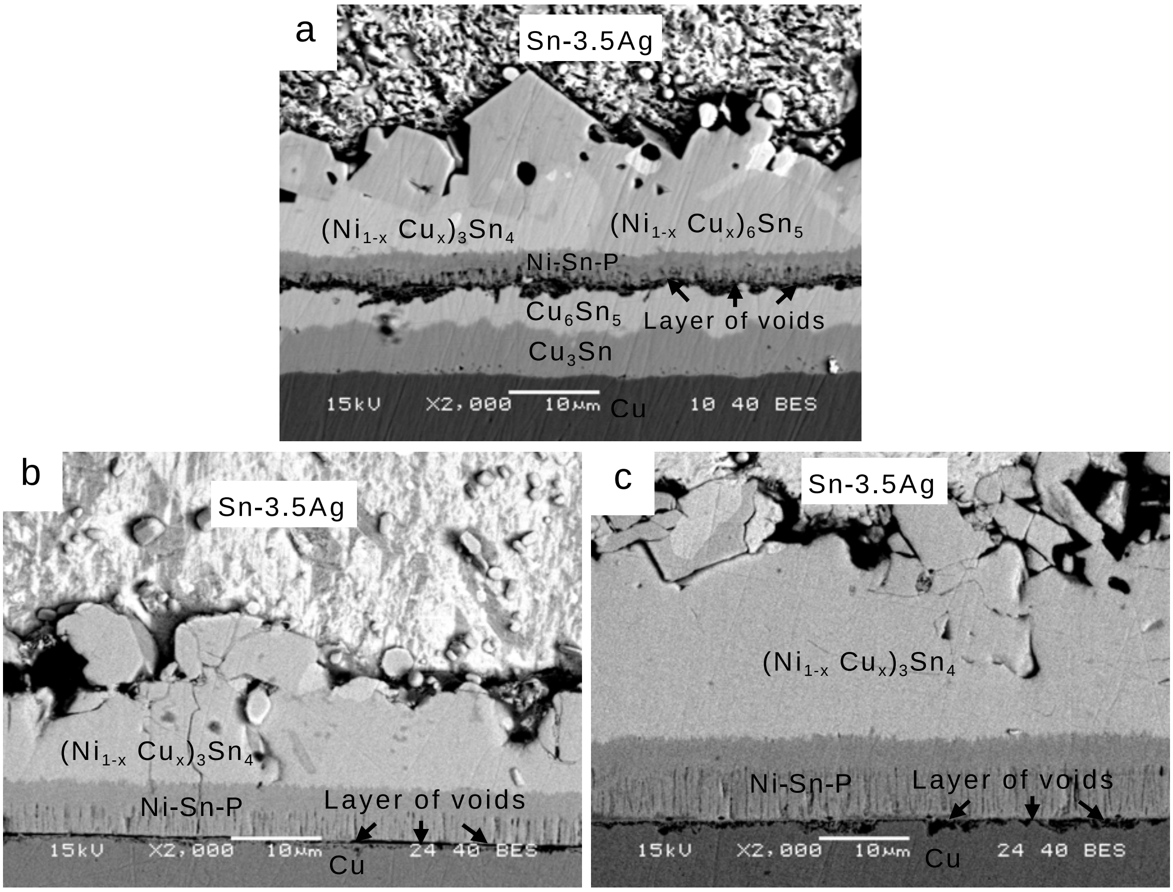
a
Sn-3.5Ag
(Ni1-x Cux)3Sn4
(Ni1-x Cux)6Sn5
Ni-Sn-P
Cu6Sn5
Layer of voids
Cu3Sn
15kV X2,000 10µm Cu 10 40 BES
b
Sn-3.5Ag
(Ni1-x Cux)3Sn4
Ni-Sn-P
Layer of voids
15kV X2,000 10µm Cu 24 40 BES
c
Sn-3.5Ag
(Ni1-x Cux)3Sn4
Ni-Sn-P
Layer of voids
15kV X2,000 10µm Cu 24 40 BES

Fig. 4.4. Back-scattered SEM images of Sn-3.5Ag/Ni-P/Cu interfaces in the samples aged at 200 °C for 400 h and having (a) thin (3.9 μm), (b) medium (7.3 μm), and (c) thick (9.9 μm) Ni-P layers.

Table 4.1. EDS results showing the chemical composition (at.%) of compounds formed at the Sn-3.5Ag/Ni-P/Cu interfaces in Fig. 4.4a.

Compounds	Ni	Cu	Sn	P
Ni-Sn-P	45±1.5	<2	29±1.5	24±1.5
$(Ni_{1-x}Cu_x)_3Sn_4$	33±1	8±1	59±1	-
$(Ni_{1-x}Cu_x)_6Sn_5$	25±1.5	29±2.5	46±1.5	-
Cu_6Sn_5	-	52±1.5	48±1.5	-
Cu_3Sn	-	73±1.5	27±1.5	-

The EDX element mapping analysis of Sn-3.5Ag/Ni-P/Cu interfaces of the sample having thin Ni-P layer and aged at 200 °C for 400 h is shown in Fig. 4.5. The presence of a dark red Ni-Sn-P layer in Fig. 4.5b and a dark black Ni-Sn-P layer in Fig. 4.5d, respectively, indicates that almost all the P atoms remain in the Ni-Sn-P layer and Cu atoms diffuse through the Ni-Sn-P layer without interacting with it. A number of Ag_3Sn particles, which formed in the solder matrix, were observed to accumulate at the solder/Ni-Cu-Sn interface due to the extensive growth of Ni-Cu-Sn layer (Fig. 4.5e and f).

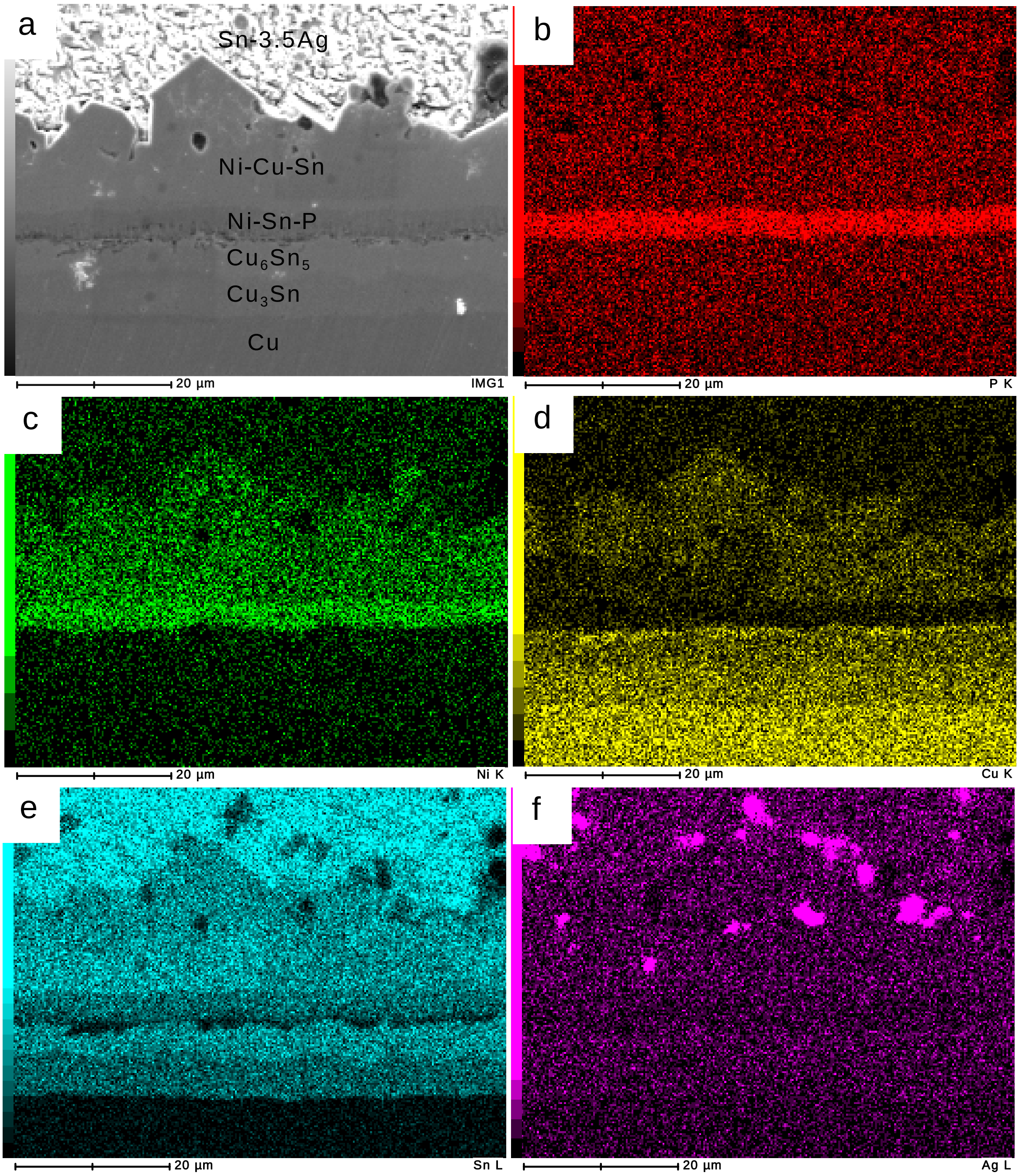
a
Sn-3.5Ag
Ni-Cu-Sn
Ni-Sn-P
Cu6Sn5
Cu3Sn
Cu
20 µm
IMG1
b
20 µm
P K
c
20 µm
Ni K
d
20 µm
Cu K
e
20 µm
Sn L
f
20 µm
Ag L

Fig. 4.5. EDS element mapping analysis of Sn-3.5Ag/Ni-P/Cu interfaces of the sample having thin (3.9 µm) Ni-P layer and aged at 200 °C for 400 h: (a) SEM image, (b) mapping for P, (c) mapping for Ni, (d) mapping for Cu, (e) mapping for Sn, and (f) mapping for Ag. The concentration of element decreases with the increase in intensity of black color.

4.3.2. Tensile Strength and Fracture Analysis

As-prepared Test Samples

Regardless of Ni-P thickness, the tensile strength and fracture behavior of all the three types of as-prepared samples were found nearly the same. Average tensile strength of all the three types of as-prepared samples was in the narrow range of 42-45 MPa (Fig. 4.7) and ductile fracture inside the bulk solder occurred in all the as-prepared samples (Figs. 3.13 and 4.6).

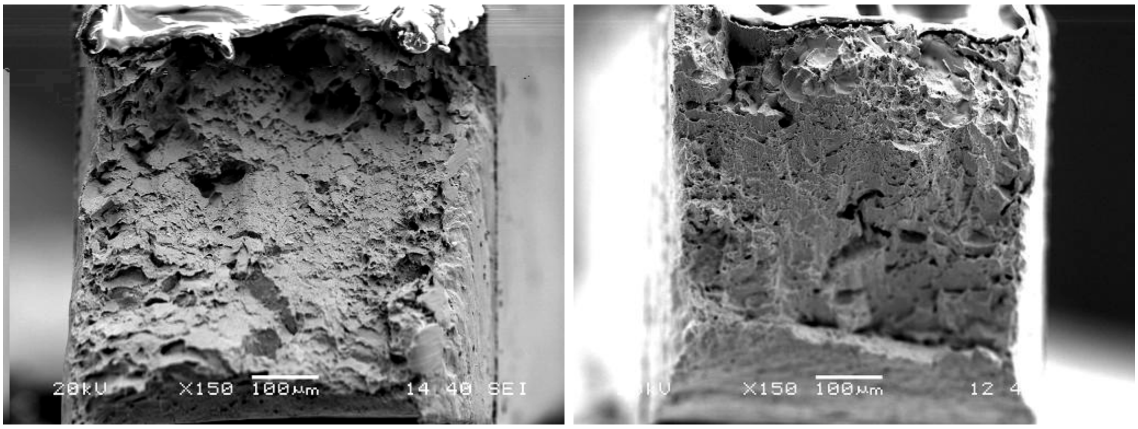

Fig. 4.6. Fracture surfaces of the as-prepared sample having thin (3.9 µm) Ni-P layer showing ductile fracture inside the bulk solder.

Thermally-Aged Test Samples

Samples Aged at 160 °C

Figs. 4.7 and 4.8 show the tensile strength and fracture energy (area under load-extension curve) of test samples having Ni-P layers of three different thicknesses as a function of aging duration at 160 °C. A considerable difference was noticed in the tensile strength and fracture energy depending upon the Ni-P thickness. In the case of thin (3.9 µm) Ni-P, the strength and fracture energy decreased with aging, while in the case of thicker Ni-P (7.3 and 9.9 µm) they increased with aging. Similarly, a significant difference was observed in the failure mode and fracture behavior of the samples having Ni-P layer of different thicknesses. Mainly, two types of failure mode were observed. First was a ductile failure in which the fracture occurred inside the bulk solder as shown in Figs. 4.9a and b and the second failure mode was a brittle failure in which fracture occurred at the interface between compounds (Figs. 4.9c and d). In the samples with medium and thick Ni-P layers, failure mode remained ductile throughout the aging, however in the samples with thin Ni-P, it gradually changed to brittle with the increase in aging duration as shown in Figs. 4.7 and 4.8.

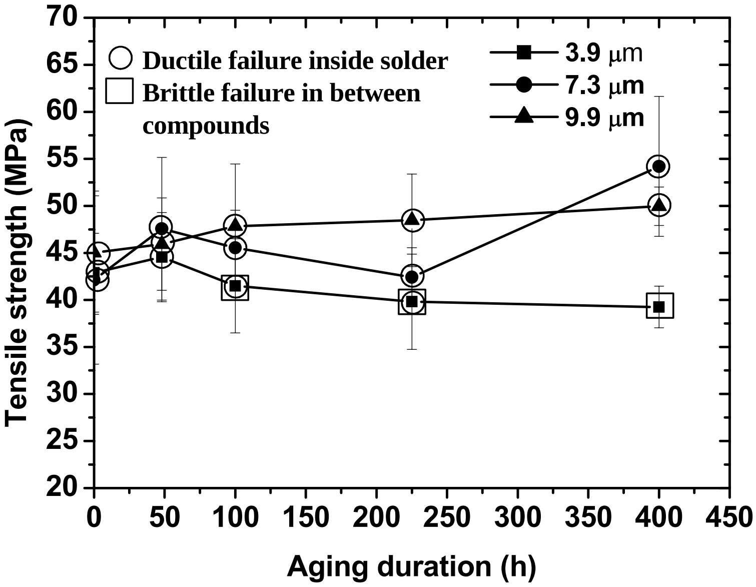

Fig. 4.7. Tensile strength of test samples having Ni-P layers of different thicknesses as a function of aging duration at 160 °C.

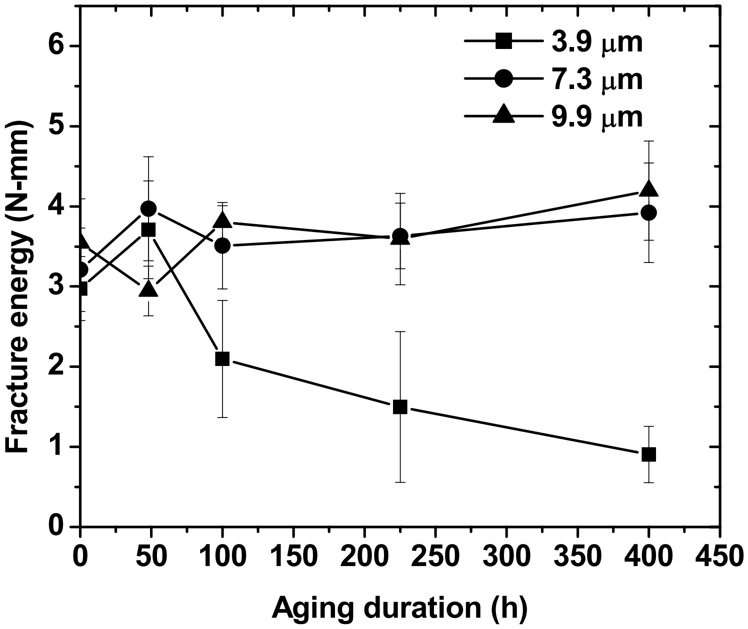

Fig. 4.8. Fracture energy of test samples having Ni-P layers of different thicknesses as a function of aging duration at 160 °C (typical load-extension curves are shown in the Fig. A.2 of appendix A).

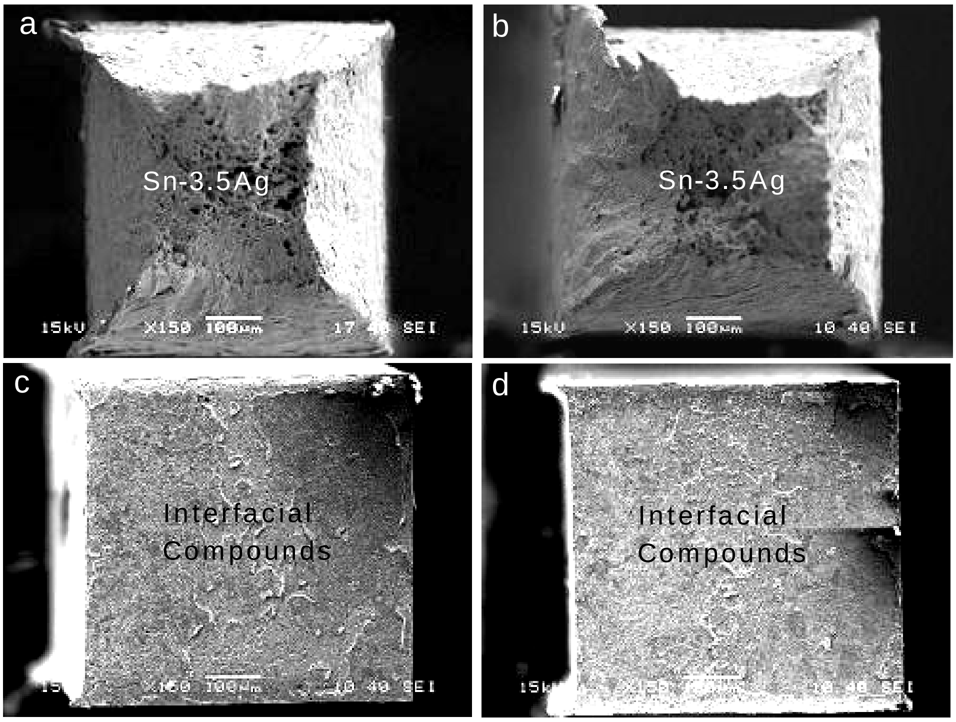
a
Sn-3.5Ag
15kV X150 100µm 17 40 SEI
b
Sn-3.5Ag
15kV X150 100µm 10 40 SEI
c
Interfacial
Compounds
X150 100µm 10 40 SEI
d
Interfacial
Compounds

Fig. 4.9. Fracture surfaces of the aged (at 160 °C for 100 h) samples having (a) thick Ni-P (one side), (b) thick Ni-P (other side), (c) thin Ni-P (one side), and (d) thin Ni-P (other side).

A detailed fracture analysis of the aged samples with thin (3.9 µm) Ni-P layer was carried out to understand its brittle failure. Fig. 4.10 shows the fracture surfaces of aged samples having thin Ni-P layer. After careful analysis, it was found that in these samples the fracture occurred at the mixed $(Ni_{1-x}Cu_x)_3Sn_4$/Ni-Sn-P and Ni_3P/Cu interfaces. This was further confirmed by the cross-sectional SEM images of tensile tested sample shown in Fig. 4.11. From the figure, it is clear that although brittle fracture occurred at both the Ni_3P/Cu and $(Ni_{1-x}Cu_x)_3Sn_4$/Ni-Sn-P interfaces, the Ni_3P/Cu interface was more susceptible to fracture. Interestingly, the Ni_3P layer having a large number of columnar voids was found not to be prone to fracture, nevertheless it helped the fracture to transmit from Ni_3P/Cu interface to the $(Ni_{1-x}Cu_x)_3Sn_4$/Ni-Sn-P interface through its columnar voids (Fig. 4.11b).

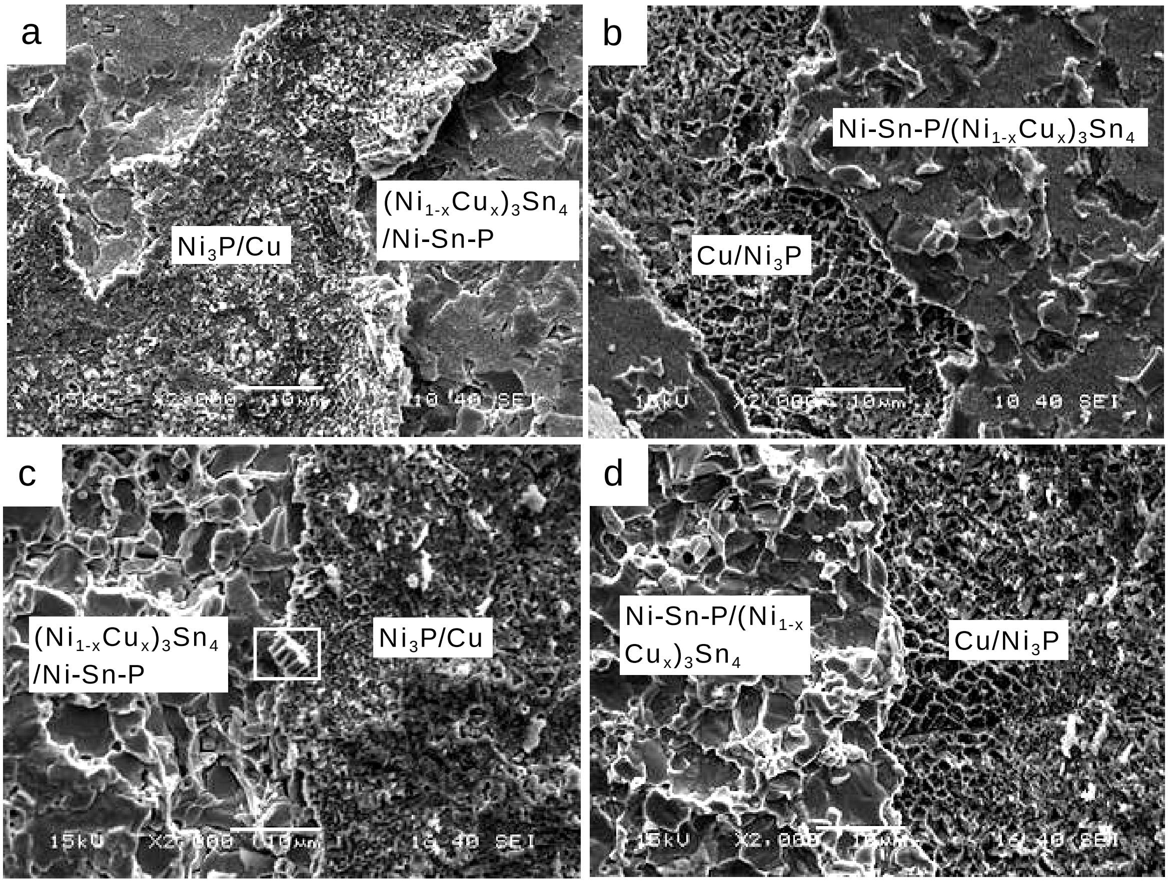
a
Ni3P/Cu
(Ni1-xCux)3Sn4 /Ni-Sn-P
15kU X2,000 10µm 10 40 SEI
b
Ni-Sn-P/(Ni1-xCux)3Sn4
Cu/Ni3P
15kU X2,000 10µm 10 40 SEI
c
(Ni1-xCux)3Sn4 /Ni-Sn-P
Ni3P/Cu
15kU X2,000 10µm 10 40 SEI
d
Ni-Sn-P/(Ni1-x Cux)3Sn4
Cu/Ni3P
15kU X2,000 10µm 10 40 SEI

Fig. 4.10. Fracture surfaces of the aged samples having thin (3.9 µm) Ni-P layer and aged at 160 °C for (a) 100 h (solder side), (b) 100 h (Cu side), (c) 400 h (solder side), and (d) 400 h (Cu side). Fracture surfaces are at the $(Ni_{1-x}Cu_x)_3Sn_4$/Ni-Sn-P and Ni_3P/Cu interfaces.

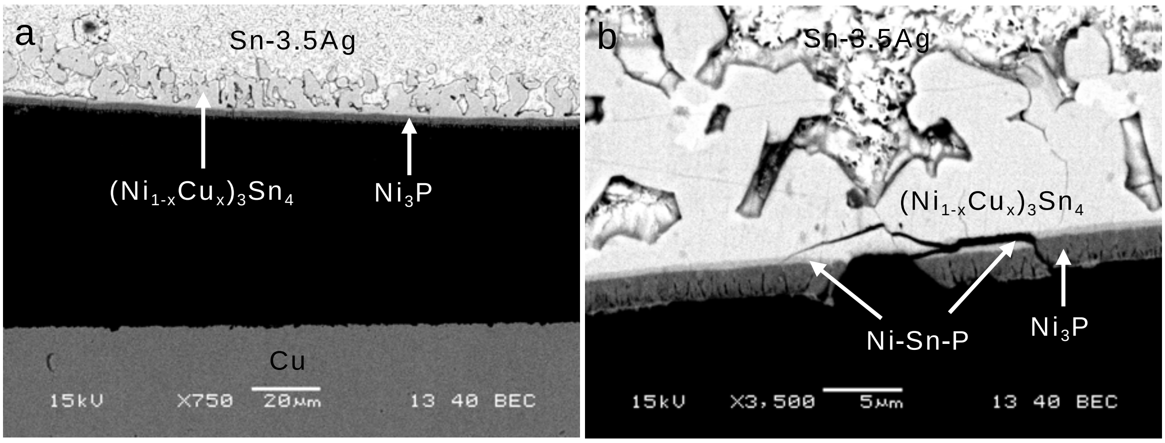
a
Sn-3.5Ag
(Ni1-xCux)3Sn4
Ni3P
Cu
15kU X750 20µm 13 40 BEC
b
Sn-3.5Ag
(Ni1-xCux)3Sn4
Ni-Sn-P
Ni3P
15kU X3,500 5µm 13 40 BEC

Fig. 4.11. SEM images showing fracture of the sample aged at 160 °C for 400 h and having thin (3.9 µm) Ni-P layer (a) Fracture occurring at the Ni_3P/Cu interface and (b) Fracture transmitting to the $(Ni_{1-x}Cu_x)_3Sn_4$/Ni-Sn-P interface through the Ni_3P layer.

Samples Aged at 180 °C

Fig. 4.12 shows the tensile strength of test samples having Ni-P layers of three different thicknesses as a function of aging duration at 180 °C. Regardless of Ni-P thickness, the tensile strength of all the three types of samples were nearly the same and followed similar trend, decreased with the increase in aging duration. However, a difference was observed in the failure mode and fracture surfaces of these samples. In the samples with thick (9.9 μm) Ni-P layer, mixed fracture occurred at the solder/Ni_3Sn_4 interface as shown in Figs. 3.15, 3.16, and 4.12. In the samples with medium (7.3 μm) Ni-P, at the beginning of aging, two types of factures, mixed fracture at the solder/Ni_3Sn_4 interface (Fig. 4.13a and b) and brittle fracture in the layer of Kirkendall voids between Ni_3P layer and Cu surface (Fig. 4.13c and d) occurred, however at later stage of aging, only brittle fracture occurred (Fig. 4.12). On the other hand, in the samples with thin (3.4 μm) Ni-P, only brittle facture was found to occur primarily in the layer of Kirkendall voids throughout the aging (Figs. 4.12 and 4.14).

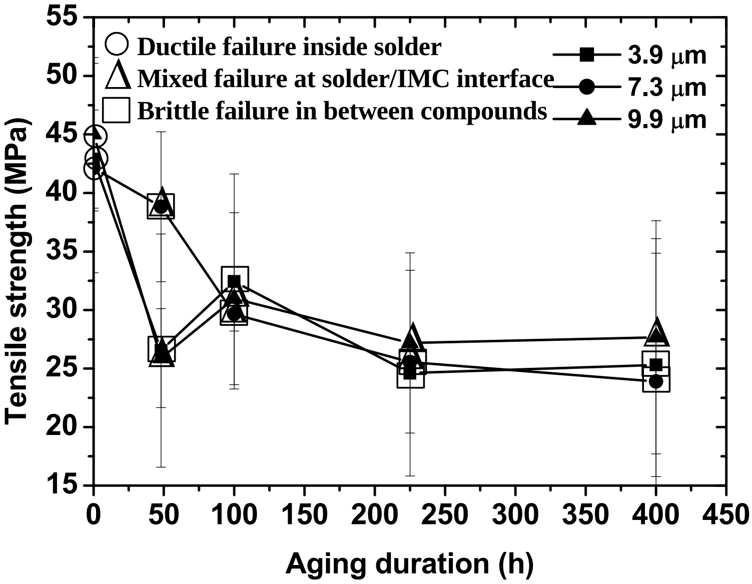

Fig. 4.12. Tensile strength of test samples having Ni-P layers of different thicknesses as a function of aging duration at 180 °C.

Samples Aged at 200 °C

The tensile strength of test samples having Ni-P layers of three different thicknesses as a function of aging duration at 200 °C is shown in Fig. 4.15. From the figure it is clear that all the three types of samples had nearly the same strength. In all the three types of samples, strength decreased mostly at the early stage of aging and then remained nearly constant. In addition, a similarity was also observed in the fracture behavior of all these samples. In all the samples, brittle fracture occurred in the layer of Kirkendall voids. However, the location of the layer of Kirkendall voids changed from Ni_3P/Cu interface to the Ni-Sn-P/Cu and finally to the Ni-Sn-P/Cu-Sn interface with aging as shown in Fig 4. 16.

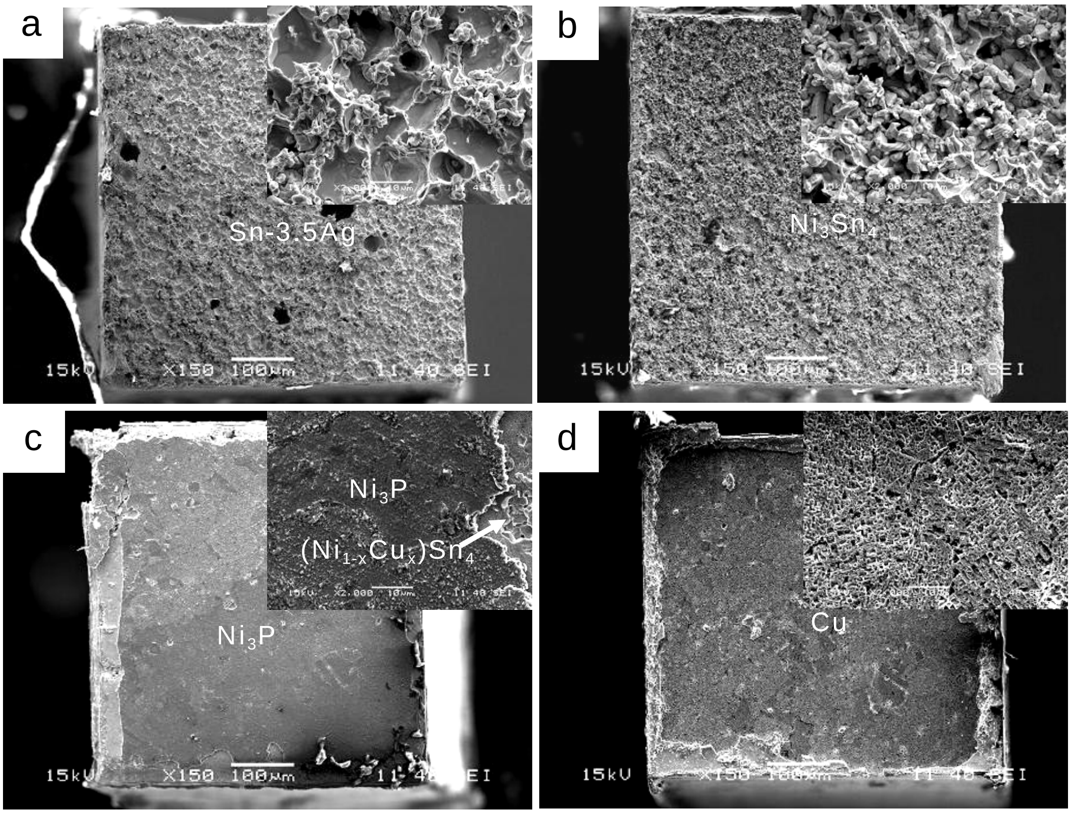
a
Sn-3.5Ag
15kV X150 100µm 11 40 SEI
b
Ni3Sn4
15kV X150 100µm 11 40 SEI
c
Ni3P
(Ni1-xCux)Sn4
Ni3P
15kV X150 100µm 11 40 SEI
d
Cu
15kV X150 100µm 11 40 SEI

Fig. 4.13. SEM image showing fracture at the solder/Ni_3Sn_4 interface (a and b) and Ni_3P/Cu interface (c and d) in the medium (7.3 µm) Ni-P samples aged at 180 °C for 48 h.

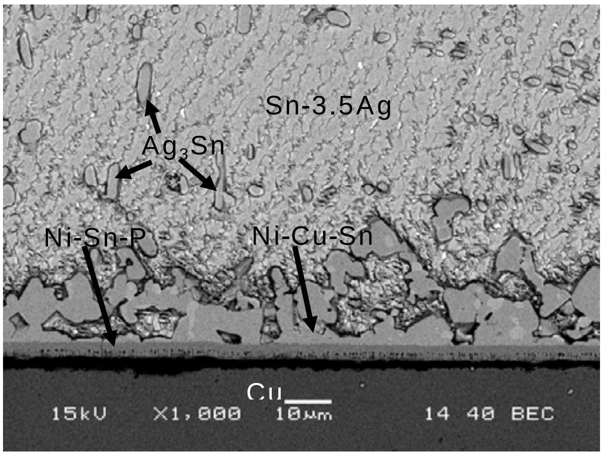
Sn-3.5Ag
Ag3Sn
Ni-Sn-P
Ni-Cu-Sn
Cu
15kV X1,000 10µm 14 40 BEC

Fig. 4.14. SEM image showing fracture in the layer of Kirkendall voids between Cu and Ni-Sn-P layer in the thin (3.4 µm) Ni-P sample aged at 180 °C for 400 h.

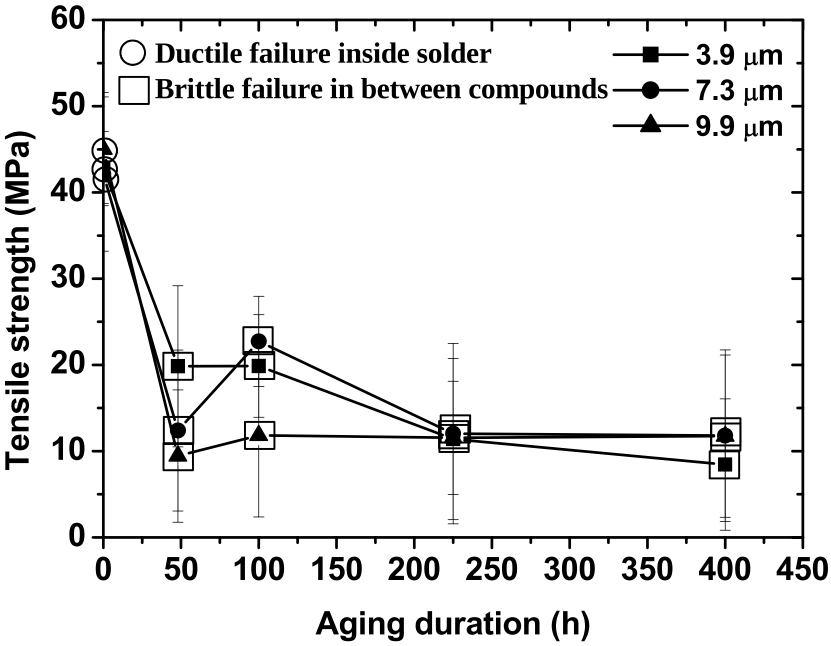

Fig. 4.15. Tensile strength of test samples having Ni-P layer of different thicknesses as a function of aging duration at 200 °C.

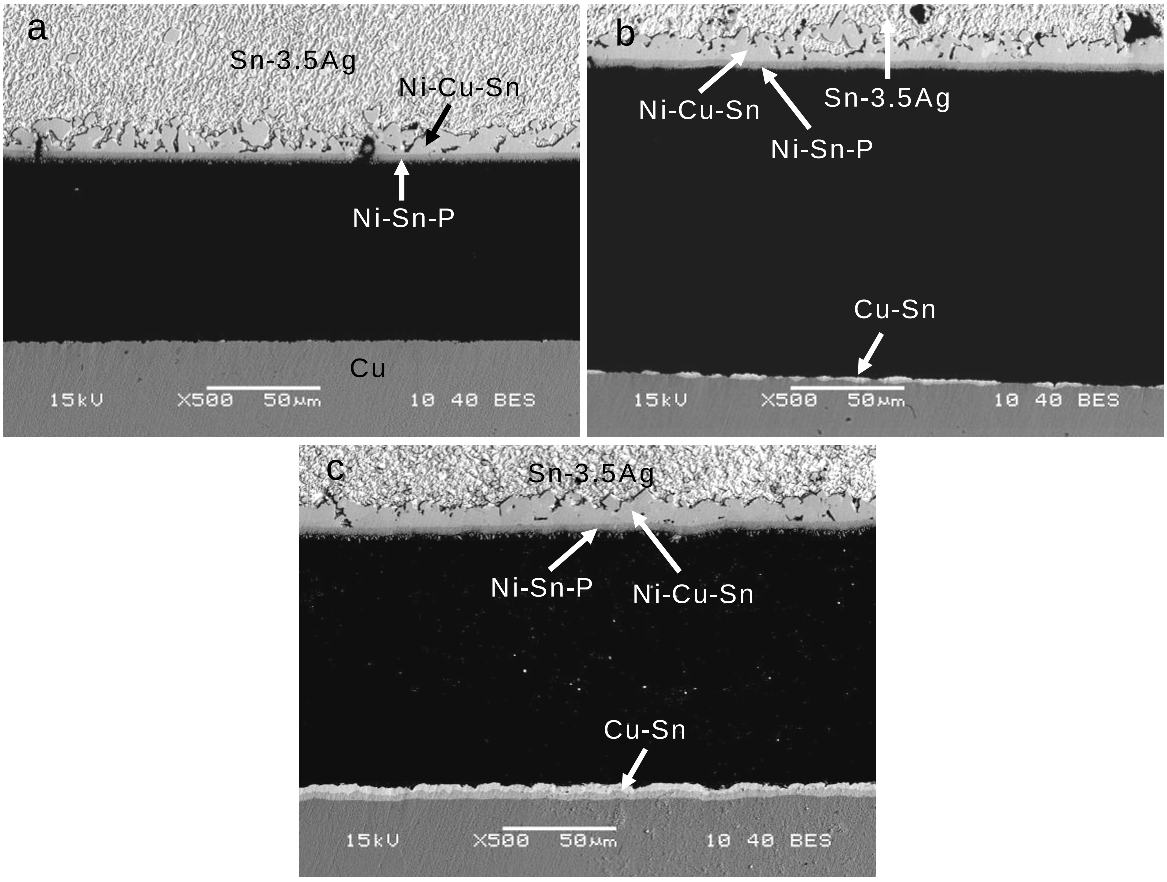
a
Sn-3.5Ag
Ni-Cu-Sn
Ni-Sn-P
Cu
15kV X500 50μm 10 40 BES
b
Ni-Cu-Sn
Sn-3.5Ag
Ni-Sn-P
Cu-Sn
15kV X500 50μm 10 40 BES
c
Sn-3.5Ag
Ni-Sn-P
Ni-Cu-Sn
Cu-Sn
15kV X500 50μm 10 40 BES

Fig. 4.16. Cross-sectional SEM images showing fracture path of the sample having thin (3.9 μm) Ni-P layer and aged at 200 °C for (a) 48 h, (b) 100 h, and (c) 400 h. Fracture typically occurred in the layer of Kirkendall voids.

4.4. Discussion

4.4.1. Growth Mechanism of Ni-Cu-Sn and Cu-Sn IMCs

In this study, various compounds such as Ni_3Sn_4, Ni-Sn-P, Ni_3P, $(Ni_{1-x}Cu_x)_xSn_4$, $(Ni_{1-x}Cu_x)_6Sn_4$, Cu_3Sn, and Cu_6Sn_5 were found to form during Sn-3.5Ag/Ni-P/Cu interfacial reactions. Although the formation of many of these compounds has been discussed in the previous chapter, the growth mechanism of Ni-Cu-Sn and Cu-Sn IMCs is still not clear. From the study reported in the previous chapter, it is clear that during Sn-3.5Ag/electroless Ni-P/Cu interfacial reactions, Ni_3Sn_4, Ni-Sn-P, and Ni_3P compounds grow due to the reaction between Sn and Ni, the reaction between Sn and Ni_3P, and the depletion of Ni from electroless Ni-P, respectively. For the growth of Ni_3Sn_4, Sn comes from the solder to the Ni_3Sn_4/Ni-Sn-P interface, where it reacts with Ni that is coming from the electroless Ni-P layer. The depletion of Ni from the electroless Ni-P layer causes its crystallization or transformation into Ni_3P compound. After the complete transformation of electroless Ni-P into Ni_3P layer, Cu starts diffusing out from the Cu surface to the Ni_3Sn_4 IMC through the grain boundaries of Ni_3P layer.

In this study, it was found that the diffusion of Cu from the Cu surface results in the formation of a layer of Kirkendall voids and $(Ni_{1-x}Cu_x)_3Sn_4$ IMCs at the Ni_3P/Cu and Ni_3Sn_4/Ni-Sn-P interfaces, respectively (Fig. 4.2a). Concurrently, Sn starts reacting with the Ni_3P layer to grow a Ni-Sn-P layer (Fig. 4.3a and b). After the complete transformation of the Ni_3P layer into a Ni-Sn-P layer, Sn reaches the Cu surface and forms Cu_3Sn and Cu_6Sn_5 IMCs at the Ni-Sn-P/Cu interface (Fig. 4.4a). As interfacial reactions proceed, extensive inter-diffusion of Sn and Cu causes the growth of thick Cu-Sn and Ni-Cu-Sn IMCs. Initially, the $(Ni_{1-x}Cu_x)_3Sn_4$ IMCs, with low Cu concentration, forms and then eventually the $(Ni_{1-x}Cu_x)_6Sn_5$ IMCs, with high Cu concentration, forms due to the continued supply of Cu (Figs. 4.3a and 4.4a and Table. 4.1).

A schematic illustration of compound growth in the Sn-3.5Ag/electroless Ni-P/Cu system is shown in Fig. 4.17. The complete growth mechanism can be divided in to three stages. In the stage I, three compounds, Ni_3Sn_4, Ni-Sn-P, and Ni_3P form at the reaction interfaces, whose thicknesses increase with thermal aging. After the complete transformation of electroless Ni-P layer into Ni_3P, the supply of Ni becomes insufficient and thus Cu starts diffusing from Cu surface to compensate the Ni supply causing the formation of a layer of Kirkendall voids and $(Ni_xCu_{1-x})_3Sn_4$ IMCs and simultaneously the Ni-Sn-P layer starts growing rapidly due to the reaction between Sn and Ni_3P (stage II). In the final stage III, after the conversion of the entire Ni_3P layer into Ni-Sn-P, Sn reaches the Cu substrate and forms Cu_3Sn and Cu_6Sn_5 IMCs at the Ni-Sn-P/Cu interface. The continuous supply of Cu from Cu surface causes the formation $(Ni_xCu_{1-x})_6Sn_5$ IMCs in the Ni-Cu-Sn layer.

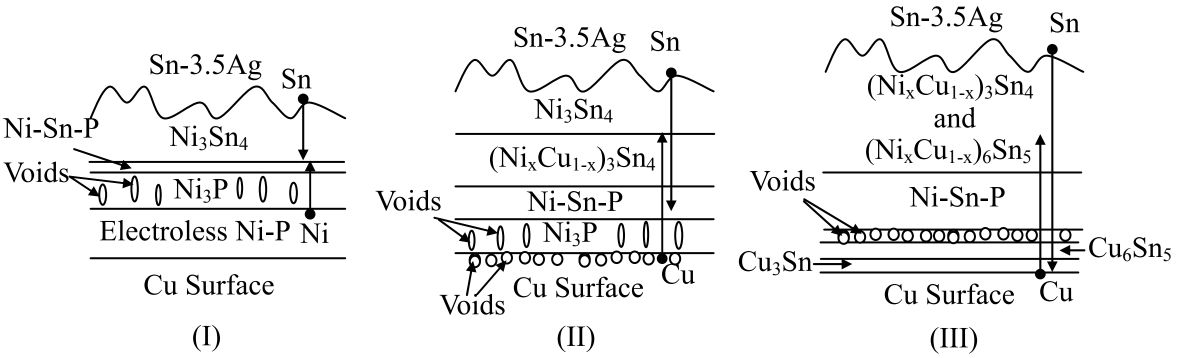
Sn-3.5Ag
Sn
Ni-Sn-P
Ni3Sn4
Voids
Ni3P
Electroless Ni-P
Ni
Cu Surface
(I)
Sn-3.5Ag
Sn
Ni3Sn4
(NixCu1-x)3Sn4
Voids
Ni-Sn-P
Ni3P
Cu
Voids
Cu Surface
(II)
Sn-3.5Ag
Sn
(NixCu1-x)3Sn4
and
(NixCu1-x)6Sn5
Voids
Ni-Sn-P
Cu3Sn
Cu6Sn5
Cu Surface
Cu
(III)

Fig. 4.17. Schematic illustration for the growth of interfacial compounds in Sn-3.5Ag/electroless Ni-P/Cu system showing different stages of growth: (I) Formation of Ni_3Sn_4, Ni-Sn-P, and Ni_3P compounds, (II) Formation of $(Ni_xCu_{1-x})_3Sn_4$ IMCs due to the reaction between Cu and Ni_3Sn_4 and growth of Ni-Sn-P layer due to the reaction between Sn and Ni_3P, and (III) Formation of Cu-Sn and $(Ni_xCu_{1-x})_6Sn_5$ IMCs due to the reaction between Sn and Cu and the large supply of Cu, respectively.

Since during Sn-3.5Ag/electroless Ni-P/Cu interfacial reactions, several compounds such as Ni-Sn-P, Cu-Sn, and Ni-Cu-Sn grow only after the complete transformation of electroless Ni-P UBM into Ni_3P. Thus, the growth of these compounds can be hindered by preventing the complete transformation of electroless Ni-P UBM and this can be easily achieved by increasing the Ni-P thickness.

4.4.2. Effect of Ni-P Thickness on the Mechanical Strength of Solder Joint

The mechanical strength of a solder interconnect is determined not only by the strength of solder alloy but also by the adhesion between interfacial layers growing at the solder/UBM interface. If the adhesion between interfacial layers is sufficiently high, fracture occurs inside the bulk solder. Whilst in the opposite case, fracture occurs at the weakest interface. Accordingly, in this study, fracture inside the bulk solder was observed in all the as-prepared samples and in the medium and thick Ni-P samples aged at 160 °C (Figs. 3.13, 4.6, 4.7, 4.9a, and 4.9b). Further, in all these joints, the microstructure of Sn-3.5Ag/electroless Ni-P/Cu interfaces comprised of Ni_3Sn_4, Ni-Sn-P, Ni_3P, and electroless Ni-P layers (Figs. 4.1, 4.2b, and 4.2c). The fracture shifted to the Ni_3P/Cu and $(Ni_{1-x}Cu_x)_3Sn_4$/Ni-Sn-P interfaces in the thin Ni-P samples aged at 160 °C (Figs. 4.10 and 4.11), in which microstructure of Sn-3.5Ag/electroless Ni-P/Cu interfaces changed into the $(Ni_{1-x}Cu_x)_3Sn_4$, Ni-Sn-P, and Ni_3P layers and a layer of voids (Fig. 4.2a).

On correlating the observed fracture behavior with the microstructure of Sn-3.5Ag/electroless Ni-P/Cu interfaces (Fig. 4.18), the cause of brittle failure of the solder joint with thin Ni-P layer can be understood. This correlation reveals that as long as electroless Ni-P layer is present at the Sn-3.5Ag/Ni-P/Cu interfaces, the adhesion between interfacial compounds remains quite high and Sn-3.5Ag solder is the weakest section in the solder joint. Thus during aging, the increase in tensile strength in the case of medium and thick Ni-P samples aged at 160 °C can be understood to be due to the growth of Ag_3Sn intermetallic (Fig. 4.2) that reinforced the solder. On the other hand, in the case of thin Ni-P samples aged at 160 °C, as the electroless Ni-P layer transformed completely into Ni_3P layer, Cu started depleting from the Cu surface through the grain boundaries or even the internal surface of the voids of the Ni_3P layer (Fig. 4.19) to compensate the Ni supply, thereby resulting in formation of a layer of Kirkendall voids at the Ni_3P/Cu interface (Fig. 4.2a). The layer of voids broke the mechanical and atomic interlocking between the Cu surface and the

Ni_3P layer and made the Ni_3P/Cu interface one of the weak sections in the solder joint.

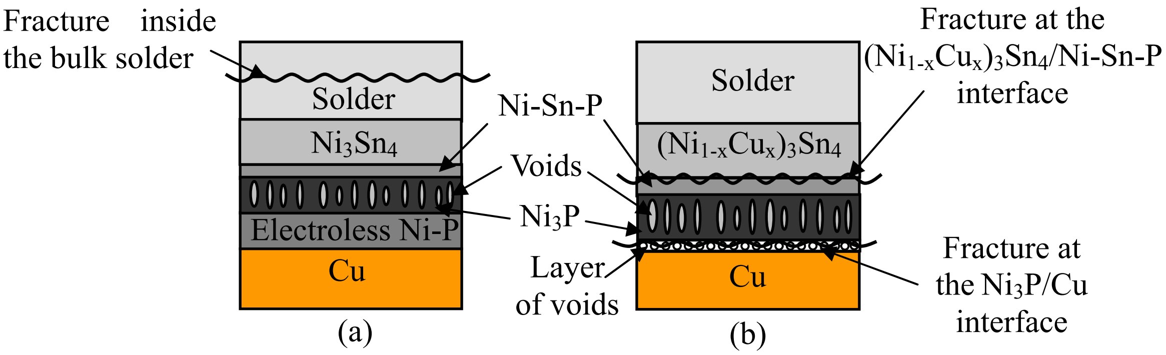
Fracture inside the bulk solder
Solder
Ni_3Sn_4
Electroless Ni-P
Cu
(a)
Ni-Sn-P
Voids
Ni_3P
Layer of voids
Solder
$(Ni_{1-x}Cu_x)_3Sn_4$
Cu
(b)
Fracture at the $(Ni_{1-x}Cu_x)_3Sn_4$/Ni-Sn-P interface
Fracture at the Ni_3P/Cu interface

Fig. 4.18. Schematic illustrations correlating the fracture behavior with the interfacial microstructure of Cu/electroless Ni-P/Sn-3.5Ag solder joint: (a) fracture inside the bulk solder and (b) fracture at the interfaces between two compounds.

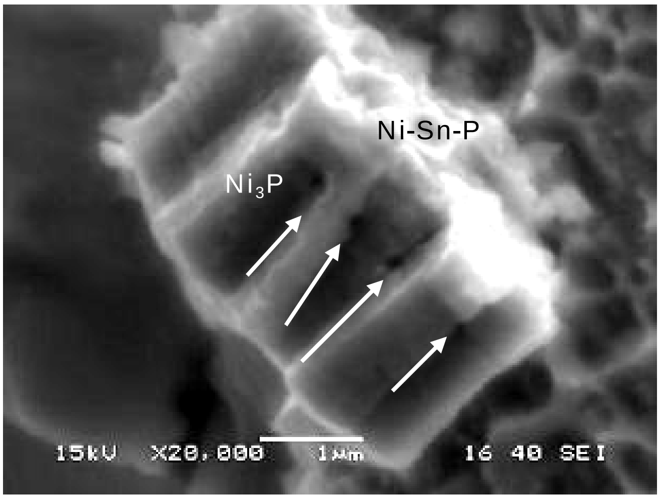
Ni-Sn-P
Ni_3P
15kV X20,000 1μm 16 40 SEI

Fig. 4.19. Magnified view of Ni_3P layer inside the rectangle frame in Figure 4.10c illustrating the Cu diffusion paths in the Ni_3P layer by the arrows.

The Ni-Sn-P layer was reported (Matsuki *et al.*, 2002) to be the weakest section in the electroless Ni-P/Sn-Pb solder joint. However, in this study, the interface of Ni-Sn-P layer with $(Ni_{1-x}Cu_x)_3Sn_4$ intermetallics was observed to be one of the weak sections in the solder joint and this was observed only after complete transformation of underlying electroless Ni-P layer into Ni_3P layer. From the previous chapter, it is known that after the complete transformation of the electroless Ni-P layer, Sn coming from the solder starts reacting with Ni_3P layer to grow Ni-Sn-P layer. On the other hand, Cu starts depleting from the Cu surface and forms Ni-Cu-Sn intermetallic compounds at the Ni_3Sn_4/Ni-Sn-P interface. Thus, there can be two possible reasons for the loss of adhesion between Ni-Sn-P and $(Ni_{1-x}Cu_x)_3Sn_4$ layers in the case of the solder joint with thin Ni-P. One is the relatively high growth of Ni-Sn-P and the other is the formation of $(Ni_{1-x}Cu_x)_3Sn_4$ intermetallic compound. Since no big difference was observed in the Ni-Sn-P thickness grown in all the samples aged at 160°C (Fig. 4.2), it can be concluded that the formation of $(Ni_{1-x}Cu_x)_3Sn_4$ might be a cause for the brittle fracture at the $(Ni_{1-x}Cu_x)_3Sn_4$/Ni-Sn-P interface. The formation of $(Ni_{1-x}Cu_x)_3Sn_4$ intermetallic at the Ni_3Sn_4/Ni-Sn-P interface can result in the generation of intrinsic stress at the interface and thereby in the loss of adhesion due to the breaking of mechanical interlocking and atomic bonding. Moreover, the contribution of fine morphology of Ni-Sn-P compound (Fig.4.20) in the loss of adhesion between Ni-Sn-P and $(Ni_{1-x}Cu_x)_3Sn_4$ layers can not be ruled out as fine morphology implies low mechanical interlocking.

Although the above mentioned discussion explains the brittle failure of the thin Ni-P sample aged at 160°C, it can also be used for the samples aged at higher temperatures (180 and 200°C). All these samples were found to have nearly the same strength and fracture behavior (except medium and thick Ni-P samples aged at 180°C, where mixed fracture occurred at the solder/Ni_3Sn_4 interface). As discussed in the previous chapter, the cause for the mixed fracture at the solder/Ni_3Sn_4 interface in the medium and thick Ni-P samples aged at 180°C can be understood to be due to the larger growth of Ni_3Sn_4 IMC. However in other samples, the layer of Kirkendall voids formed at the Ni_3P/Cu interface was the main cause of brittle fracture (Fig. 4.13c and d). The layer of Kirkendall voids remained the main cause of brittle fracture even after the transformation of the Ni_3P layer into Ni-Sn-P and the formation of Cu-Sn intermetallics at the Ni-Sn-P/Cu interface (Figs. 4.14 and 4.16).

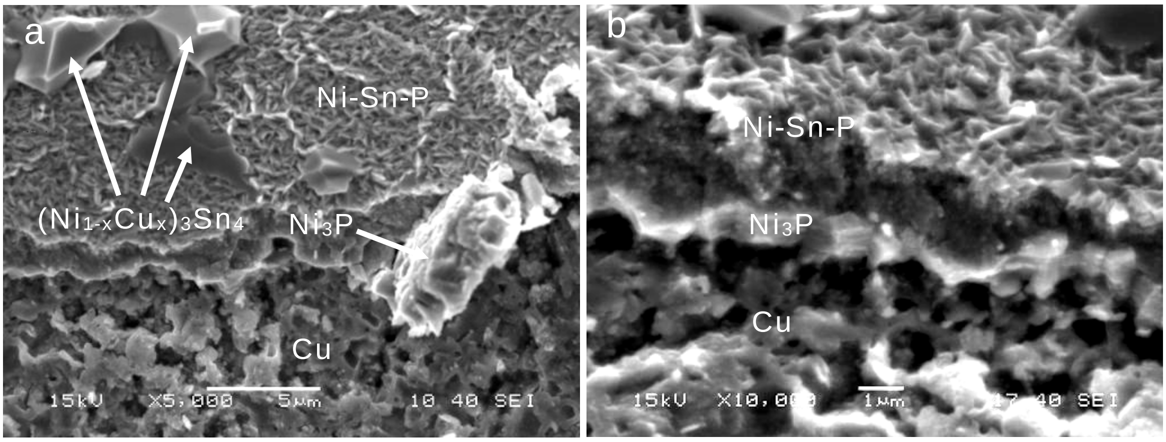

Fig. 4.20. (a) Top view and (b) titled view of fracture surface of the thin Ni-P sample aged at 180°C for 225 h showing fine morphology of Ni-Sn-P compound grown in between $(Ni_{1-x}Cu_x)_3Sn_4$ and Ni_3P compounds.

As the layer of Kirkendall voids form only after the complete transformation of electroless Ni-P layer into Ni_3P, it formed in the thin Ni-P samples much earlier than in the thicker Ni-P samples. As a result, brittle fracture was observed much earlier in the samples with thin Ni-P layer as compared to the samples with thicker Ni-P layers.

4.5. Conclusions

Interfacial microstructure, tensile strength, and fracture behavior of thermally aged Cu/electroless Ni-P/Sn-3.5Ag solder joint were investigated for three different Ni-P thicknesses (3.9, 7.3, and 9.9 µm). The following conclusions were made based on the investigation:

1. The thickness of electroless Ni-P UBM influences the growth of compounds at the Sn-3.5Ag/electroless Ni-P/Cu interfaces due to the amount of Ni available from the electroless Ni-P. In the samples with thin (3.9 µm) Ni-P, various compounds such as Ni-Sn-P, Cu_3Sn, Cu_6Sn_5, $(Ni_{1-x}Cu_x)_3Sn_4$, and $(Ni_{1-x}Cu_x)_6Sn_5$ grew at a lower aging temperature and within a shorter duration as compared to the samples with thicker (7.3 and 9.9 µm) Ni-P. Thus, the growth of these compounds can be avoided by using the Ni-P UBM of proper thickness.

2. The thickness of electroless Ni-P UBM influences the mechanical properties of Cu/electroless Ni-P/Sn-3.5Ag solder joint. In the thin Ni-P samples, brittle fracture at the Ni_3P/Cu and Ni-Cu-Sn/Ni-Sn-P interfaces was found to occur much earlier than that in the samples with thicker Ni-P layers.
3. The brittle fracture at the Ni_3P/Cu and Ni-Cu-Sn/Ni-Sn-P interfaces is observed only after the complete transformation of electroless Ni-P layer into Ni_3P. Through the Ni_3P layer, Cu starts depleting from Cu surface and thereby a layer of Kirkendall voids is formed at the Ni_3P/Cu interface. This layer of Kirkendall voids makes the Ni_3P/Cu interface one of the weak sections in the solder joint. The layer of Kirkendall voids remains the main cause of brittle fracture even after the transformation of Ni_3P layer into Ni-Sn-P and the formation of Cu-Sn intermetallics at the Ni-Sn-P/Cu interface.
4. Cu diffuses out from the Cu surface and forms Ni-Cu-Sn intermetallic compounds at the Ni_3Sn_4/Ni-Sn-P interface. The formation of Ni-Cu-Sn intermetallics results in loss of adhesion between Ni-Cu-Sn and Ni-Sn-P compounds.
5. Finally, it is clear that the brittle failure of Cu/electroless Ni-P/solder joint can be avoided by the selection of the electroless Ni-P UBM of proper thickness. For example, in this study, this thickness was found to be more than 3.9 μm (7.3 or 9.9 μm).

Based on the findings of this investigation, it can be said that the thickness of electroless Ni-P layer plays an important role in determining the mechanical reliability of Cu/electroless Ni-P/sn-3.5Ag solder joint. However, there is another Ni-P feature, the P concentration, which can potentially influence the interfacial reactions and thus solder joint strength. Therefore, in the following chapter, interfacial and mechanical studies focused on the P concentration of the electroless Ni-P layer will be presented.

Chapter 5

Influence of P Concentration on Cu/Electroless Ni-P/Sn-3.5Ag Interfacial Microstructure and Solder Joint Strength

5.1. Introduction

The influence of P concentration on the mechanical properties of electroless Ni-P/solder joint has been investigated in a few studies (Chonan *et al.*, 2002a; Alam *et al.*, 2003). However, different thicknesses of electroless Ni-P UBM were used for investigating and comparing the influence of P concentration on the joint strength. As the thickness of electroless Ni-P layer itself influences the mechanical properties of electroless Ni-P/solder joint. It is essential to separate the effect of electroless Ni-P thickness from the effect of P concentration. Accordingly, in this study, electroless Ni-P layers of different P concentrations, but of the same thickness, were used to investigate the effect of P concentration on the interfacial microstructure and tensile strength of Cu/electroless Ni-P/Sn-3.5Ag solder joint.

In electronic manufacturing, at least 2 reflows are required. The first reflow forms an area of solder bumps on a chip surface, while the second reflow bonds the chip to a substrate. Multiple reflows, in fact, are often experienced during subsequent surface mount, testing and repair of chips. In this study, multiple reflows up to 30 cycles were carried out. Our intention is to not only simulate the actual situation that a package may go through, but also drive the interfacial reactions to the extreme condition to reveal the endurance limit of different Ni-P alloys.

5.2. Experimental Procedures

5.2.1. Preparation of Test Samples

The procedure for test sample preparation was the same as described in section 3.2.1. However, in this study, different commercial electroless nickel solutions were used to coat three electroless Ni-P layers of different P concentrations and thus the electroless Ni-P layers of three different P concentrations, 6.1 wt.%, 8.8 wt.%, and 12.3 wt.%, were obtained. All electroless Ni-P layers were plated such that approximately the same thickness (~3 μm) was obtained.

5.2.2. Multiple Reflows of Test Samples

The as-prepared samples were subjected to multiple reflows of 2, 5, 10, 15, 20 and 30 cycles. The each reflow cycle followed the same temperature profile as the one used during sample preparation.

5.2.3. Tensile Testing of Test Samples

The same as described in the section 3.2.3.

5.2.4. Microstructural Observations

The same as described in the section 3.2.4.

5.3. Results and Discussion

5.3.1. Influence of P Concentration on Interfacial Microstructure

The cross-section of electroless Ni-P plated Cu substrate is shown in Fig. 5.1, in which an electroless Ni-P layer of uniform thickness of around 3 μm can be seen. Fig. 5.2 shows the interfacial microstructure of as-prepared samples. In all the three types of as-prepared samples, two distinct colored layers (light and dark grey) of compounds were observed at the electroless Ni-P/Sn-3.5Ag interface. The light grey layer was of Ni_3Sn_4 intermetallic and the relatively thinner continuous dark grey layer formed between Ni_3Sn_4 and electroless Ni-P layers was mainly consisted of Ni_3P compound. From previous electroless Ni-P/solder interfacial studies (He *et al.*, 2004a; Lee and Lin, 1994), it is known that during interfacial reactions, Ni diffuses toward the solder side while Sn diffuses toward the electroless Ni-P side forming Ni_3Sn_4 intermetallic at the electroless Ni-P/solder interface. Owing to the depletion of Ni from electroless Ni-P, phosphorus atoms are left behind in the Ni-P layer. Continued reactions between electroless Ni-P and solder cause a large depletion of Ni from the electroless Ni-P layer. Consequently, there is an accumulation of P atoms at the interface between electroless Ni-P and Ni_3Sn_4 resulting in the crystallization or transformation of electroless Ni-P layer into higher P concentration Ni-P (Ni_3P) layer (Jang *et al.*, 1999).

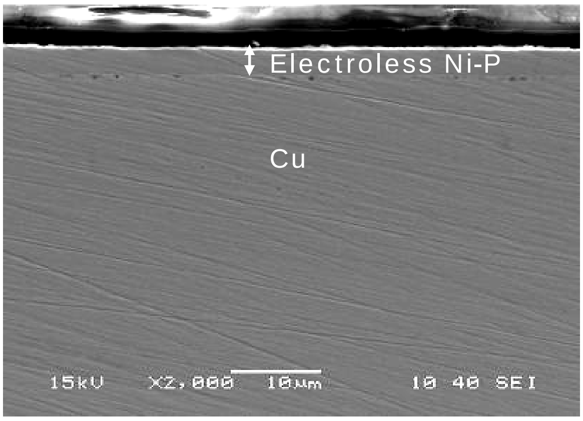

Fig. 5.1. Cross-section of electroless Ni-P plated Cu substrate.

Comparing Figs. 5.2a, b, and c, it is apparent that electroless Ni-P layer in low P sample was thinner than those in higher P samples. This shows that electroless Ni-P UBM with low P was consumed more rapidly by Sn to form Ni_3Sn_4. The lower P concentration of electroless Ni-P layers results in the higher concentration gradient of Ni from the electroless Ni-P to the solder. This in turn allows faster Ni diffusion to the solder to form Ni_3Sn_4 and thus the faster consumption of electroless Ni-P UBM. This finding is in agreement with the study, which has been done by Sohn *et al.* (2004a) on the interfacial reaction between pure

Sn and electroless Ni-P layers with different P concentrations. They observed that the thickness of Ni_3Sn_4 intermetallic increases, or in other words, the consumption of electroless Ni-P UBM increases with decreasing the P concentration of electroless Ni-P layer.

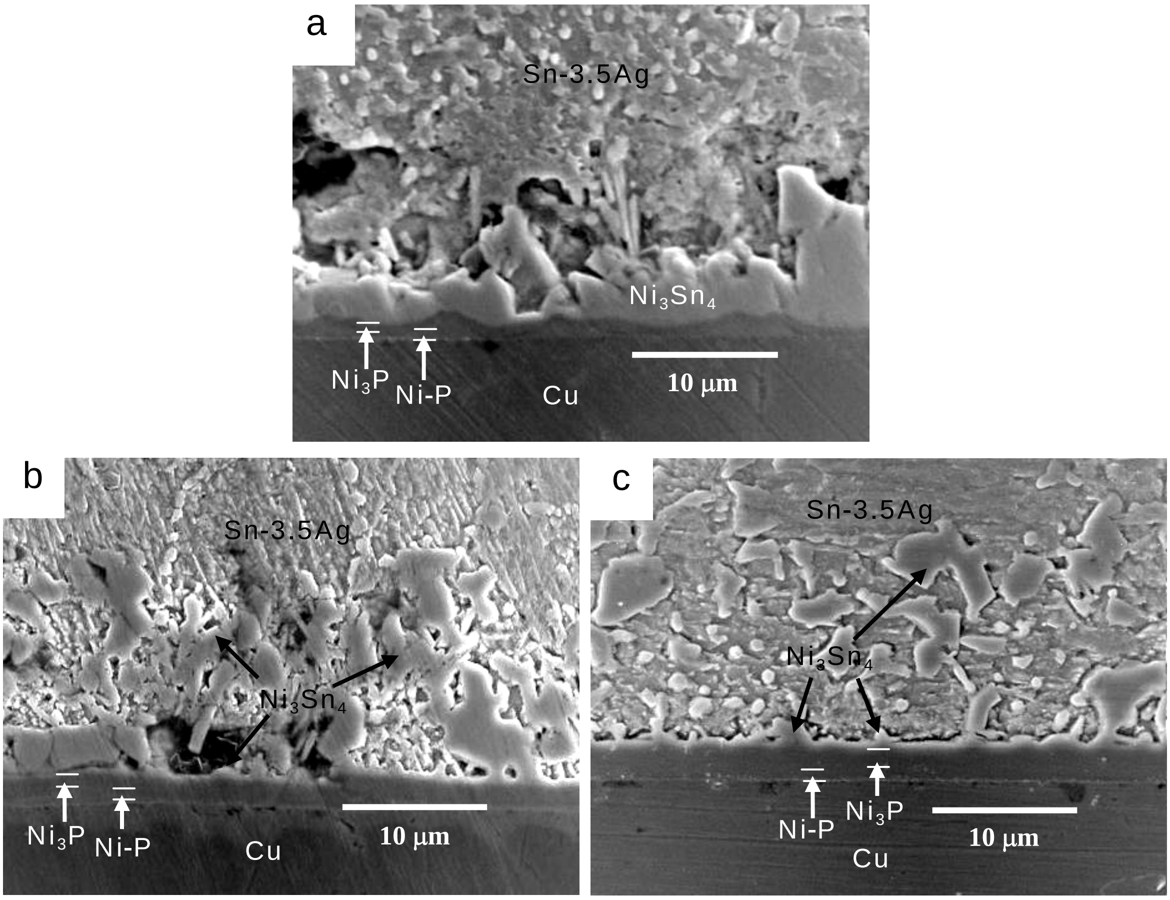

Fig. 5.2. Interfacial microstructures of as-prepared samples having electroless Ni-P layers of (a) low (6.1 wt.%), (b) medium (8.8 wt.%), and (c) high (12.3 wt.%) P concentrations.

In this study, the Ni_3P layer that grew between electroless Ni-P and Ni_3Sn_4 layers was found to be the thinnest in the low P sample. Similar phenomenon has been reported in previous interfacial studies between electroless Ni-P and different solders (Chonan *et al.*, 2002a; Alam *et al.*, 2003; Sohn *et al.*, 2004a). Sohn *et al.* (2004a) demonstrated differential scanning calorimetry (DSC) analyses of electroless Ni-P layers with different P concentrations. It was reported that the crystallization temperature of electroless Ni-P decreases while the heat of crystallization increases with increasing the P concentration of electroless Ni-P layer. These facts imply that the driving force for electroless Ni-P to transform into crystalline Ni_3P phase increases with increasing P concentration. Thus, it is reasonable to conclude that the higher P electroless Ni-P UBM would be able to supply more P atoms to facilitate Ni_3P formation and thus the Ni_3P layer would be thicker in the higher P sample.

In Fig. 5.2, it is worthwhile to notice that in the medium and high P samples, most of the Ni_3Sn_4 intermetallic compound spalled off into the solder leaving behind a thin layer of Ni_3Sn_4 adhering to the reaction interface. The spallation of Ni_3Sn_4 intermetallic during electroless Ni-P/solder interfacial reactions has been further confirmed from recent interfacial studies (Chen *et al.*, 2004; Sohn *et al.*, 2004b). Chen *et al.* (2004) have suggested that intermetallics spallation into the molten solder during liquid-state reaction could occur due to the mechanical stresses built up at the reaction interface. The mechanical stresses build at the reaction interface due to the growth of multi-layered compounds. As the compounds are generally of different densities, the growth of these compounds causes a volume change at the reaction interface and thereby results in volumetric stress generation. It has been known that the density of electroless Ni-P coatings is inversely proportional to their phosphorus concentration (ASM, 1994). The density of Ni_3Sn_4 is 8.64 g/cm^3 (Chen *et al.*, 2004), while the densities of electroless Ni-P layers containing 6.1, 8.8, and 12.3 wt.% P are approximately 8.2, 7.9, and 7.5 g/cm^3, respectively (ASM, 1994). The higher P concentration of electroless Ni-P UBM yields the larger density difference between electroless Ni-P and Ni_3Sn_4 layers. As Ni_3Sn_4 intermetallic forms, stresses generate between electroless Ni-P and Ni_3Sn_4 layers. These stresses increase as Ni_3Sn_4 grows thicker and at certain extent spallation of Ni_3Sn_4 may occur. Due to the larger density difference between higher P-containing electroless Ni-P UBM and Ni_3Sn_4 intermetallic, higher mechanical stresses build between electroless Ni-P and Ni_3Sn_4 layers causing more severe Ni_3Sn_4 spallation into the solder. As mentioned earlier, a thin layer of Ni_3Sn_4 remained adherent to the reaction interface in spite of the spallation. This implies that the reaction between Ni and Sn was still taking place when the Ni_3Sn_4 spallation occurred and the Ni_3Sn_4 had not grown to the extent that the stresses generated would cause further spallation to happen.

Fig. 5.3 shows the interfacial microstructure of the test samples subjected to 5 reflows. As compared to the as-prepared sample, it is apparent that the Ni_3Sn_4 intermetallic in the low P sample grew thicker with the number of reflows and thus the electroless Ni-P layer became thinner as the reaction between Ni and Sn continued (Fig. 5.3a). No trace of electroless Ni-P UBM was observed in the low P sample after 5 reflows. The thin dark Ni_3P layer was no longer a continuous layer, compared with the as-prepared sample shown in Fig. 5.2a. Instead, at many locations, it was dissolved and transformed into the Ni-Sn-P layer, which opened the channels for Sn to diffuse into the Cu substrate and for Cu to diffuse into the Ni_3Sn_4 layer. The diffusion of Sn and Cu through the “leaky” Ni_3P and Ni-Sn-P layers resulted in the formation of Ni-Cu-Sn and Cu-Sn IMCs at the reaction interface as shown in Fig. 5.3a. No such formation of Ni-Cu-Sn and Cu-Sn IMCs was observed in the samples with medium and high P electroless Ni-P UBM (Figs. 5.3b and c). This observation can be explained by considering the lower consumption of higher P-containing electroless Ni-P UBM. As discussed previously, the Ni_3P layer grows thicker with increasing the P concentration of electroless Ni-P UBM. The thicker Ni_3P layer will slow down the Ni diffusion from electroless Ni-P to the Ni_3Sn_4/Ni_3P interface due to the lower concentration gradient of Ni and consequently the consumption of electroless Ni-P UBM will be slowed down. This is the reason why there was still a continuous electroless Ni-P layer remaining in the medium and high P samples after 5 reflows. This remaining electroless Ni-P layer prevented the formation of Ni-Cu-Sn and Cu-Sn IMCs, by preventing the Sn and Cu diffusion.

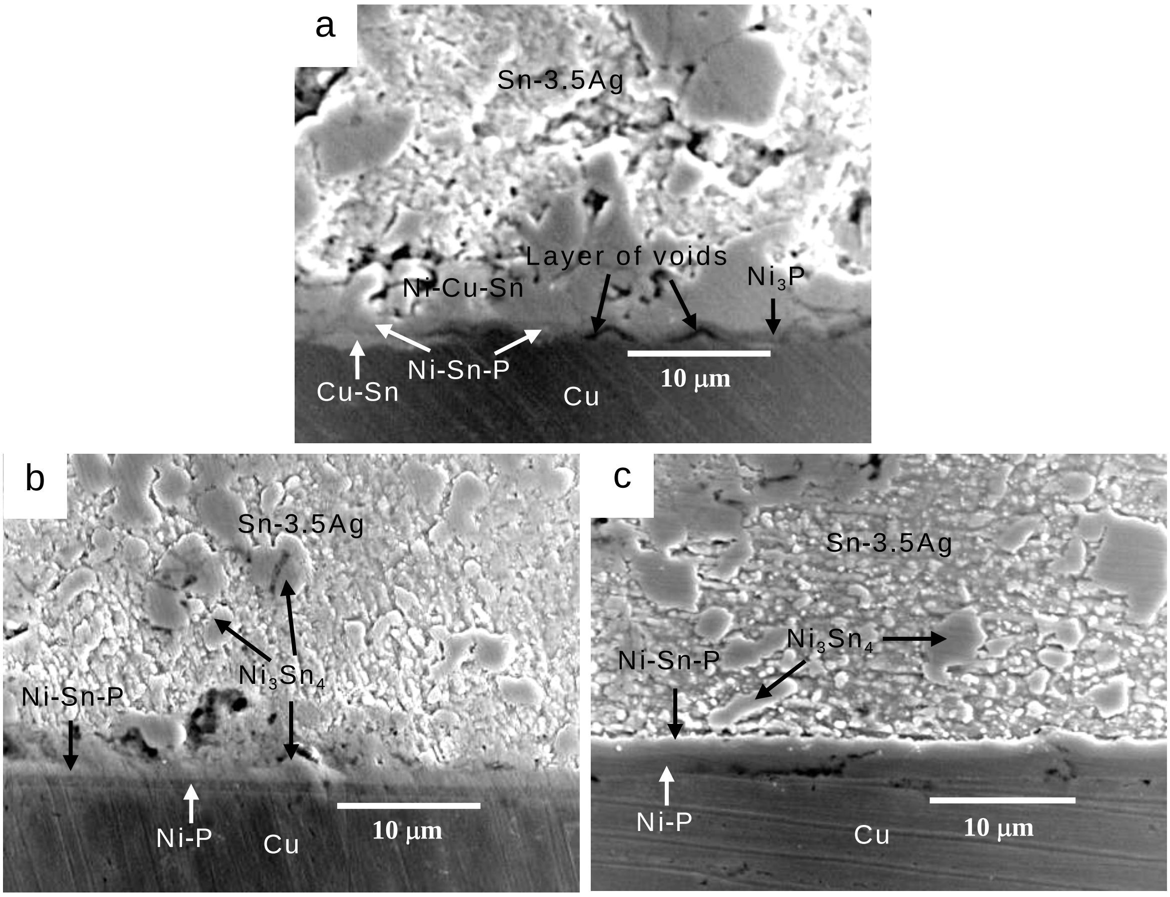

Fig. 5.3. Interfacial microstructures of the test samples having electroless Ni-P layers of (a) low (6.1 wt.%), (b) medium (8.8 wt.%), and (c) high (12.3 wt.%) P concentrations, after 5 reflows.

The interfacial microstructures of low (6.1 wt.%) , medium (8.8 wt.%), and high (12.3 wt.%) P samples after 20 reflows are depicted in Fig. 5.4. All samples contained some features in common. Quite a large amount of Ni-Cu-Sn and Cu-Sn intermetallics were present at the interface. Moreover, no trace of electroless Ni-P was found in all the samples and there was no more Ni_3Sn_4 present at the interface. The apparent distinction between the three samples was that the Ni-Cu-Sn and Cu-Sn IMCs formed in low P sample were the thinnest among all the samples. The presence of thick layers of Ni-Cu-Sn and Cu-Sn IMCs in the samples with medium and high P electroless Ni-P UBM can be understood to be due to the Ni_3Sn_4 spallation, which occurred typically in the medium and high P samples. From the study reported in previous chapter (Fig. 4.16), it is known that after the complete transformation of electroless Ni-P layer into Ni_3P and/or Ni-Sn-P layers, Cu starts diffusing out from Cu substrate and forms Ni-Cu-Sn intermetallics at the Ni_3Sn_4/Ni-Sn-P interface due to the reaction with Ni_3Sn_4. Moreover, Sn coming from solder eventually reaches the Cu substrate and forms Cu-Sn intermetallics at the Ni-Sn-P/Cu interface. Thus, in the case of medium and high P samples, owing to the Ni_3Sn_4 spallation, the Cu-Sn and Ni-Cu-Sn IMCs formation is expected to be rapid since the Ni_3Sn_4 spallation shortens the Sn and Cu diffusion path through the remaining compound layers.

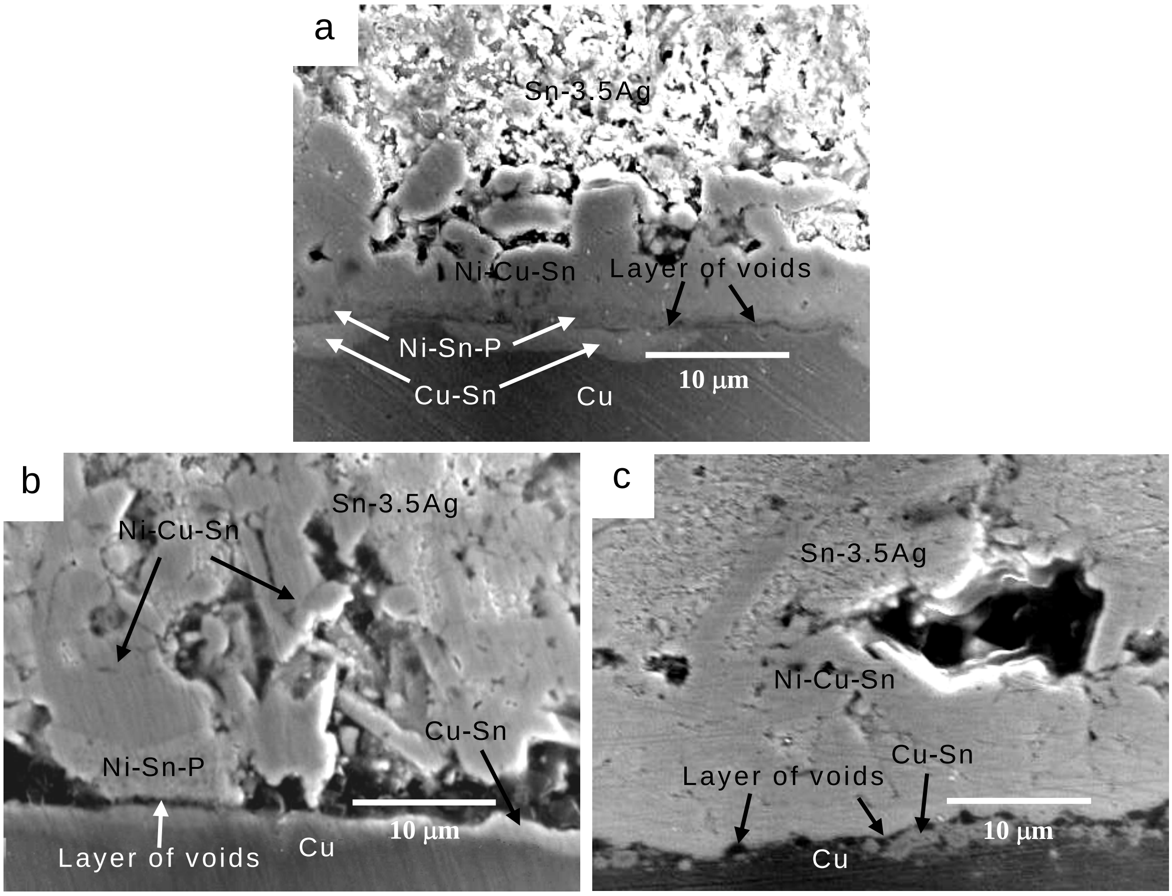
a
Sn-3.5Ag
Ni-Cu-Sn
Layer of voids
Ni-Sn-P
Cu-Sn
Cu
10 µm
b
Sn-3.5Ag
Ni-Cu-Sn
Cu-Sn
Ni-Sn-P
Layer of voids
Cu
10 µm
c
Sn-3.5Ag
Ni-Cu-Sn
Cu-Sn
Layer of voids
Cu
10 µm

Fig. 5.4. Interfacial microstructures of the samples having electroless Ni-P layers of (a) low (6.1 wt.%), (b) medium (8.8 wt.%), and (c) high (12.3 wt.%) P concentrations, after 20 reflows.

5.3.2. Influence of P Concentration on Mechanical Properties

Fig. 5.5 shows the variation in the average tensile strengths of low, medium, and high P samples as the samples underwent multiple reflows. From the figure, it is clear that the tensile strength of all the three types of samples (low, medium, and high P) decreases with increase in the number of reflows. All the three types of samples showed a similar tensile strength up to 5 reflows. However after 5 reflows, the strength of medium and high P samples decreased rapidly, while the strength of low P sample stabilized and remained nearly unchanged. The strengths of medium and high P samples were observed to be comparable to each other after 10 reflows. To sum up, low P samples exhibited the highest tensile strength among all after multiple reflows. In other words, the degradation in strength was the lowest in the case of low P sample.

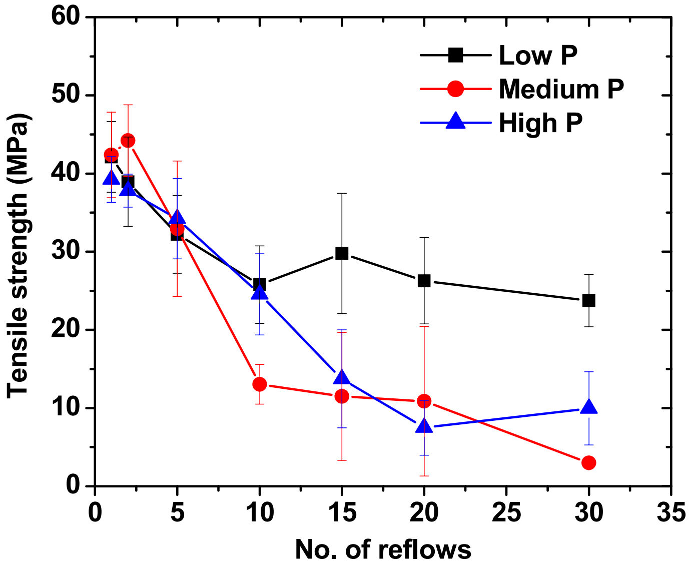

Fig. 5.5. The tensile strength of low, medium, and high P samples after multiple reflows.

In order to understand the reasons for degradation in the tensile strength of Cu/electroless Ni-P/Sn-3.5Ag solder joints having different P containing electroless Ni-P layers, in-depth study of fracture surfaces and fracture path were carried out. Figs. 5.6 and 5.7, respectively, show typical fracture path and fracture surfaces that occurred in the multiple reflowed samples. A general trend was observed in the fracture surfaces and fracture path of the samples having different P containing electroless Ni-P layers. For up to 2 reflows, in all the three types of samples, the fracture path was entirely inside the solder (Fig. 5.6a and 5.7a). However, as the number of reflows increased, the fracture path shifted from inside the bulk solder to the reaction interfaces between solder and Cu substrate (Fig. 5.6b and 5.7b). This indicates that in the samples reflowed more than twice, the cohesive strength of the compounds formed at the Cu/electroless Ni-P/Sn-3.5Ag interfaces and their adhesive strength with both the Cu substrate and solder were much lower than the cohesive strength of solder. From Figs. 5.6a and 5.7a, it is also apparent that the failure mode was ductile in the samples reflowed up to 2 times. The necking in the solder (see Fig. 5.6a) clearly indicates that the solder experienced quite large amount of plastic deformation before fracture. However, as shown in Figs. 5.6b and 5.7b, with increased number of reflows, the appearance of fracture surface changed macroscopically from rough to nearly flat surface, in other words, the failure mode changed from ductile to brittle.

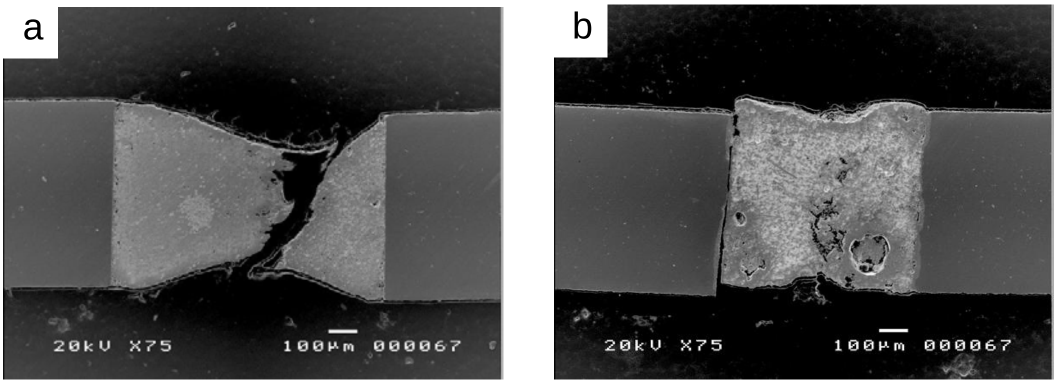

Fig. 5.6. Fracture path in low P sample (a) after 2 reflows, (b) after 20 reflows, showing the transition from ductile to brittle failure as the number of reflows increased.

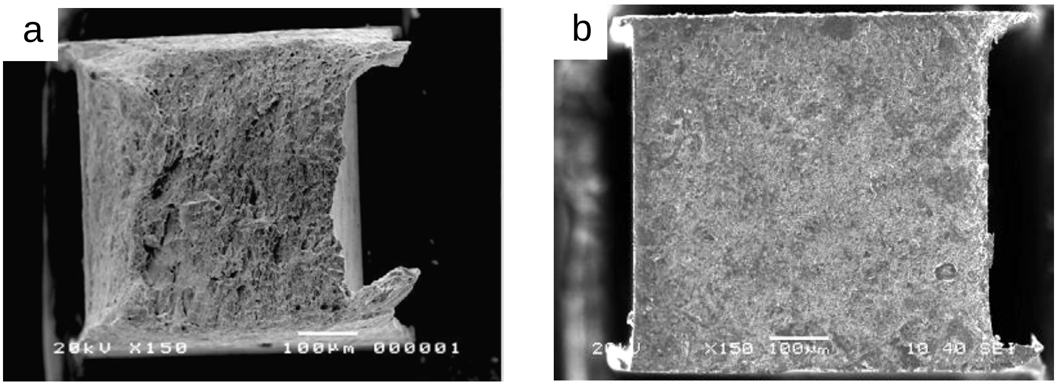

Fig. 5.7. Fracture surfaces of high P sample (a) after 2 reflows, (b) after 20 reflows, showing the transition from ductile to brittle failure as the number of reflows increased.

Fig. 5.8 shows the SEM images of fracture surfaces of medium P samples reflowed for multiple times. The figure shows a clear transition in the fracture surfaces. In the sample reflowed for 5 times, fracture surfaces were at the Cu/Ni_3P and Ni_3P/Ni-Cu-Sn interfaces (Fig 5.8a and b), which shifted to the Ni-Sn-P/Cu and Ni-Sn-P/Cu-Sn interfaces with the increase in reflow cycles (Fig. 5.8c and d). Finally, the fracture surfaces were at the Ni-Sn-P/Cu-Sn interface owing to the large growth of Cu-Sn intermetallics on the Cu substrate (Fig. 5.8e and f). The large growth of Cu-Sn intermetallics on the Cu substrate is further confirmed from the SEM images of fracture path shown in Fig. 5.9.

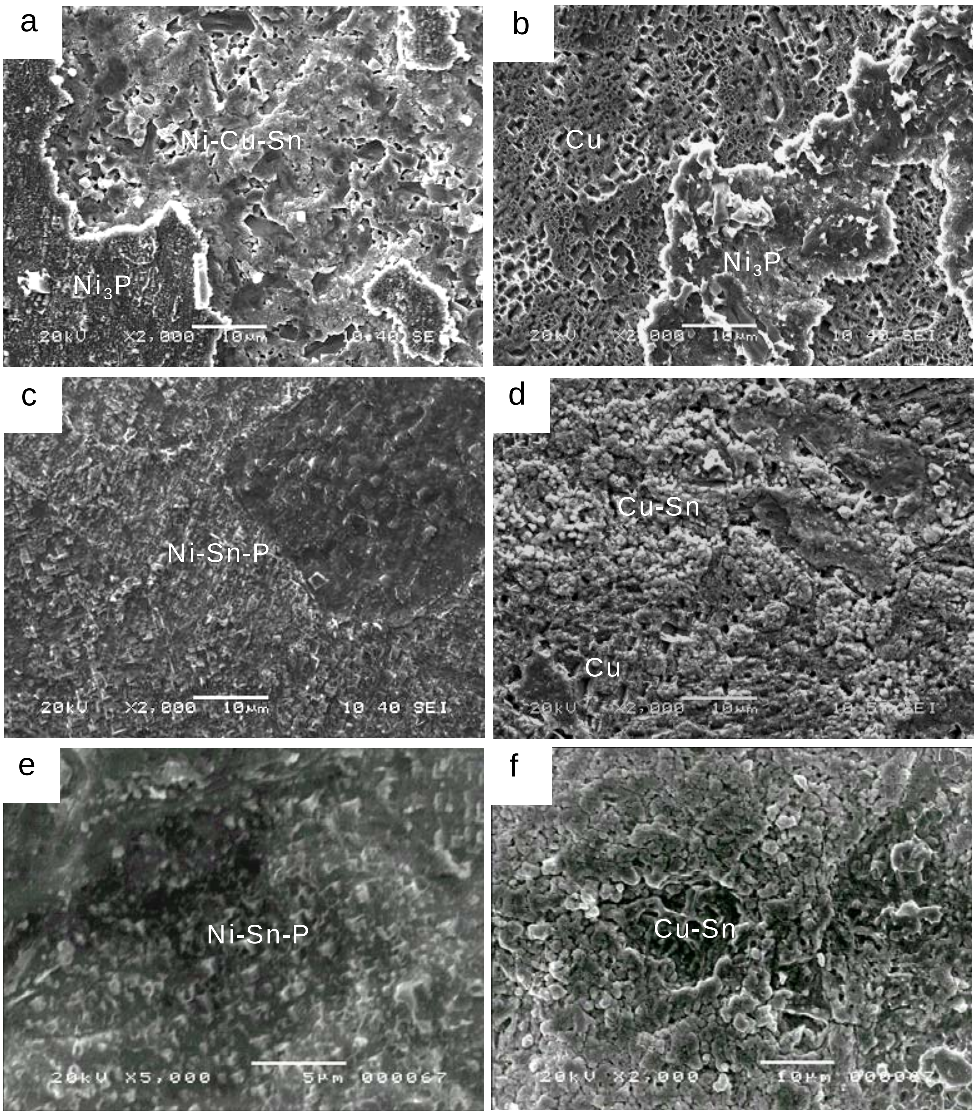
a
Ni-Cu-Sn
Ni_3P
20kU X2,000 10μm 10 40 SEI
b
Cu
Ni_3P
20kU X2,000 10μm 10 40 SEI
c
Ni-Sn-P
20kU X2,000 10μm 10 40 SEI
d
Cu-Sn
Cu
20kU X2,000 10μm 10 40 SEI
e
Ni-Sn-P
20kU X5,000 5μm 000067
f
Cu-Sn
20kU X2,000 10μm 000047

Fig. 5.8. Fracture surfaces of medium P samples after reflow for (a) 5 cycles (solder side), (b) 5 cycles (Cu substrate side), (c) 15 cycles (solder side), (d) 15 cycles (Cu substrate side), (e) 30 cycles (solder side), and (f) 30 cycles (Cu substrate side).

It has been shown in the previous chapters that the Ni_3P/Cu and Ni-Sn-P/Cu interfaces in the Cu/electroless Ni-P/Sn-3.5Ag solder joint are more prone to fracture due to the formation of a layer of Kirkendall voids at these interfaces. The layer of voids at the Ni_3P/Cu interface forms after complete transformation of electroless Ni-P layer into Ni_3P

layer and due to the depletion of Cu from the Cu substrate through the Ni_3P layer. The layer of voids remains at the reaction interface even after the formation of Ni-Sn-P and Cu-Sn compounds. In this study, a similar layer of voids was observed at the reaction interface after 5 reflows (Figs. 5.3 and 5.4), which caused the facture to occur at the Ni_3P/Cu interface (Fig. 5.8a and b). The growth of Ni-Sn-P and Cu-Sn compounds at the Ni_3P/Cu interface changed the appearance of fracture surfaces (5.8b, c, d, and e) and decreased the tensile strength severally (Fig. 5.5). Thus, the decrease in tensile strength during multiple reflows can be understood to be due to the formation of a layer of voids and growth of Ni-Sn-P and Cu-Sn compounds between the solder and Cu substrate.

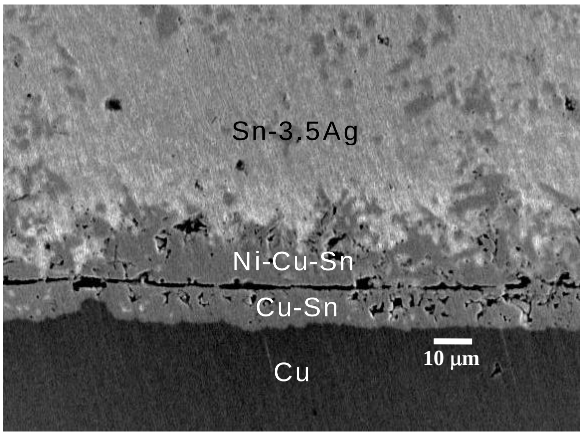

Fig. 5.9. SEM image of fracture path in the medium P sample reflowed for 30 cycles, showing the large growth of Cu-Sn intermetallics on the Cu substrate.

Although the cause of degradation in tensile strength of all the three types of reflowed samples is quite clear, the cause of relatively small decrease in tensile strength of low P sample has to be understood as well. As discussed in previous section, owing to the low intermetallic spalling, the growth of Cu-Sn IMCs in the low P samples was very low as compared to that of medium and high P samples. Since the growth of Cu-Sn IMCs severely deteriorated the tensile strength of solder joints (Figs. 5.5, 5.8, and 5.9), the small decrease in tensile strength of low P samples is attributed to the low growth rate of Cu-Sn IMCs. Another difference observed in the low P samples was the fracture surface, which consists of mixed paths along different interfaces. Unlike the ones for medium and high P samples

(Fig. 5.7b and 5.8), the fracture in low P sample occurred at the mixed interfaces even after 20 cycles of reflow (Fig. 5.10) and this mixed fracture could be the reason for no significant drop in tensile strength (Fig. 5.5). We tried to find out the cause for this mixed facture in the case of low P samples. From interfacial analysis, it was found that in the low P samples, the mixed fracture occurred due to the uneven growth of interfacial compounds as shown in Figs. 5.3a and 5.4a. Since in the medium and high P samples, most of the compounds spalled off the reaction interface, no such uneven growth of compounds took place in these samples (Figs. 5.3b, 5.3c, 5.4b, and 5.4c).

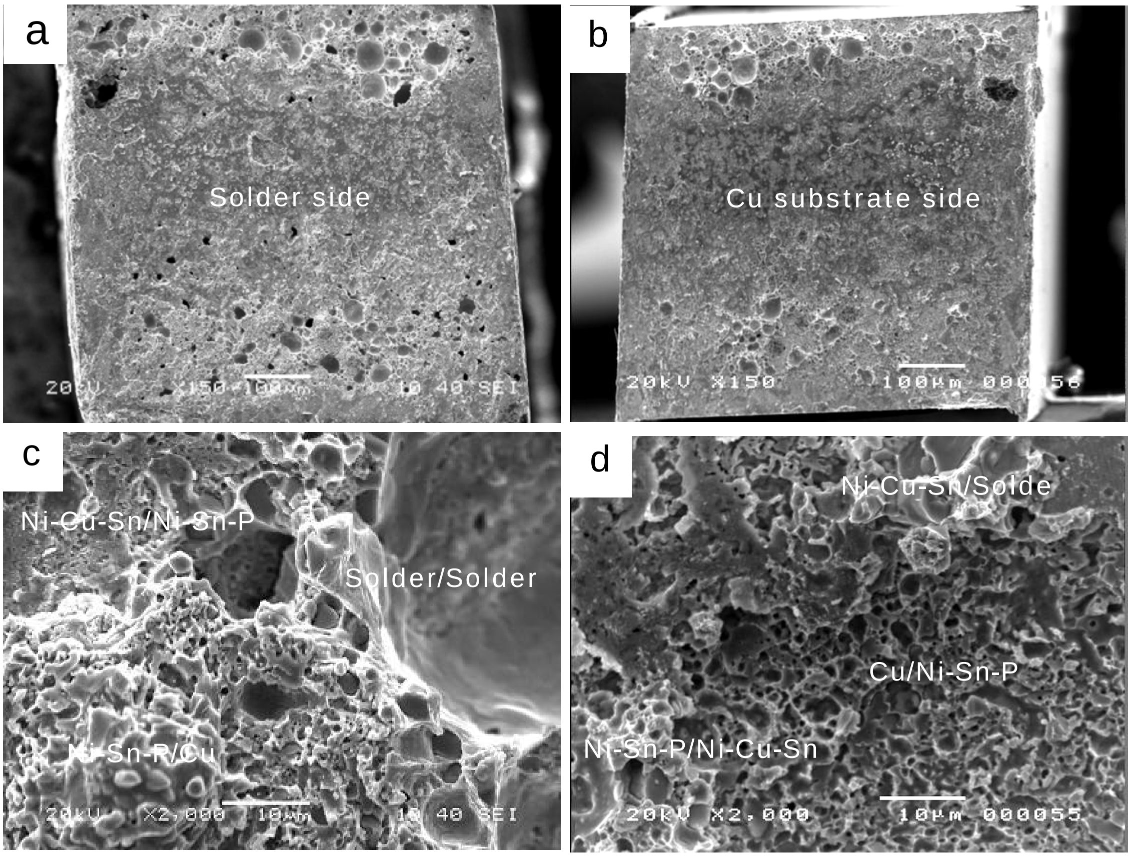
a
Solder side
20kV X150 100µm 10 40 SEI
b
Cu substrate side
20kV X150 100µm 000056
c
Ni-Cu-Sn/Ni-Sn-P
Solder/Solder
Ni-Sn-P/Cu
20kV X2,000 10µm 10 40 SEI
d
Ni-Cu-Sn/Solde
Cu/Ni-Sn-P
Ni-Sn-P/Ni-Cu-Sn
20kV X2,000 10µm 000055

Fig. 5.10. Fracture surfaces of low P sample after 20 reflows (a) solder side, (b) Cu substrate side, (c) magnified image of solder side, (d) magnified image of Cu substrate side, showing that fracture occurred at mixed solder/solder, solder/Ni-Cn-Sn, Ni-Cu-Sn/Ni-Sn-P, and Ni-Sn-P/Cu interfaces.

5.4. Conclusions

From this study, it is clear that the P concentration of electroless Ni-P layer influences the interfacial microstructure and mechanical strength of Cu/electroless Ni-P/Sn-3.5Ag solder joint. Low P samples exhibited the highest joint strength among all, with little drop in tensile strength. The strengths of medium and high P samples decreased rapidly with the increase in reflow cycles. In the early stage, low P electroless Ni-P layer consumed more rapidly by its reaction with Sn due to the high concentration gradient of Ni from electroless Ni-P layer to solder. However, Ni_3Sn_4 IMC in low P sample was found to remain at the reaction interface. In contrast, Ni_3Sn_4 IMC that formed in the medium and high P samples mostly spalled into the molten solder and eventually the electroless Ni-P layer was consumed rapidly as the reflow cycles progressed. Although Ni_3Sn_4 spallation was not found to influence the solder joint strength directly, it shortened the Cu and Sn diffusion path through the remaining compound layers and consequently, Ni-Cu-Sn and Cu-Sn IMCs grew rapidly with the number of reflows. The extensive growth of Ni-Cu-Sn and Cu-Sn IMCs and voids at the reaction interface decreased the tensile strength of medium and high P samples severely. Therefore, low P electroless Ni-P is the best electroless Ni-P UBM against multiple reflows because of high solder joint strength, low spallation of interfacial compounds, and slow growth of interfacial compounds and voids.

From this study, a qualitative understanding of the influence of P concentration on the interfacial microstructure and tensile strength of Cu/electroless Ni-P/Sn-3.5Ag solder joint has been made. In the next chapter, a quantitative account of the influence of P on the growth of interfacial compounds will be presented through analytical modeling.

Chapter 6

Mathematical Model for the Growth of Ni_3P and Ni_3Sn_4 Compounds

6.1. Introduction

Although much is known about the formation of multiple compounds in the electroless Ni-P/Solder (Sn-Pb and Sn-Ag) system, there are still a lot of issues such as the variation in growth kinetics of compounds and the influence of P concentration on the growth of compounds, to be understood. A wide variation in Ni_3Sn_4 growth kinetics ranging from $t^{1/2}$ to $t^{1/4}$ has been reported in different studies (He *et al.*, 2004d; Jang *et al.*, 1999; Jeon *et al.*, 2003b; Yoon *et al.*, 2003; Yoon and Jung, 2004). As this variation cannot be explained simply with the help of the state of reaction (liquid or solid) or IMC grain coarsening, a thorough investigation is needed to explain it. Further, in a recent interfacial study (Sohn *et al.*, 2004a), the P concentration of electroless Ni-P layer has been reported to influence the growth of Ni_3P and Ni_3Sn_4 compounds. From these studies, it is clear that the growth mechanism and kinetics of Ni_3P and Ni_3Sn_4 compounds are closely associated with the electroless Ni-P UBM. However, the exact mechanism behind these findings is still not clear.

The Ni_3P layer that formed in the electroless Ni-P layer under short reflow or liquid-state thermal aging has been reported to have nanocrystalline columnar grains (Chen *et al.*, 2004; He *et al.*, 2004a; Jang *et al.*, 1999). However in the present study, after long solid-state thermal aging, this layer has been found to have columnar grains of micron-size (Figs. 3.21 and 4.18). This implies that the growth of columnar Ni_3P grain takes place during soldering reaction. Thus, considering the growth of columnar Ni_3P grain, in this study, we developed a mathematical model for the growth of Ni_3P and Ni_3Sn_4 compound layers. The model not only can describe the variation in Ni_3P and Ni_3Sn_4 growth kinetics, but also can help to understand the influence of P concentration on Ni_3P and Ni_3Sn_4 growth.

6.2. Derivation of Growth Model

In modeling the growth of Ni_3P and Ni_3Sn_4 compounds, we considered the following facts based on the previous studies (Chen *et al.*, 2004; He *et al.*, 2004a; Jang *et al.* 1999; Lee and Lin, 1994; Matsuki *et al.*, 2002): (a) Columnar Ni_3P grains grow in electroless Ni-P layer due to the depletion of Ni and depleted Ni reacts with Sn to form Ni_3Sn_4 (Chen *et al.*, 2004; He *et al.*, 2004a; Jang *et al.*, 1999), (b) Ni diffuses through the grain boundaries of Ni_3P layer and there is no out flux of P from electroless Ni-P layer, in other wards, P is completely consumed within electroless Ni-P layer to form Ni_3P (Chen *et al.*, 2004; Jang *et al.*, 1999; Matsuki *et al.*, 2002), and (c) Sn is the main diffusing element in Ni_3Sn_4, in other words, the Sn-Ni reaction takes place only at the Ni_3P/Ni_3Sn_4 interface (Lee and Lin, 1994). Some assumptions were also made in the modeling, which are: (a) the interface between electroless Ni-P layer and Ni_3P shifts due to the depletion of Ni (Kirkendall effect); however, formation of Kirkendall voids is ignored for convenience, (b) the thickness of Ni_3P grain boundary 'δ' is very small as compared to the width of the Ni_3P gain 'W', (c) the geometrical shape of a columnar Ni_3P grain can be represented by perfect rectangular column, and (d) the growth of ternary Ni-Sn-P compound can be neglected as this compound does not grow unless and until electroless Ni-P layer is completely transformed into Ni_3P.

Fig. 6.1 is a one-dimensional schematic diagram that shows the growth of columnar Ni_3P compound in the electroless Ni-P layer. Considering the symmetry in Ni_3P grains, in the model, only the growth of one Ni_3P grain is taken into account. Lets at time t, ΔX_1 and ΔX_2 are the thickness of Ni_3P and Ni_3Sn_4 layers, respectively. If in time Δt, due to the depletion of Ni from electroless Ni-P layer, ΔX_L is the shift in the interface between electroless Ni-P and Ni_3P layers and ΔX_K is the attenuation in electroless Ni-P layer, then the number of Ni and P atoms present per unit cross-sectional area of electroless Ni-P layer before and after its transformation into Ni_3P will be

Before transformation:

$$N_{Ni}^{before} = \frac{|\Delta X_L|}{\Omega} C_0 \tag{6.1}$$

and

$$N_P^{before} = \frac{|\Delta X_L|}{\Omega} (1 - C_0) \tag{6.2}$$

After transformation:

$$N_{Ni}^{after} = \frac{(|\Delta X_L| - |\Delta X_K|)}{\Omega} C_i = \frac{(|\Delta X_L| - |\Delta X_K|)}{\Omega} \frac{3}{4} \tag{6.3}$$

and

$$N_P^{after} = \frac{(|\Delta X_L| - |\Delta X_K|)}{\Omega} (1 - C_i) = \frac{(|\Delta X_L| - |\Delta X_K|)}{\Omega} \frac{1}{4} \tag{6.4}$$

where, C_0 and C_i, respectively, are the atomic fraction of Ni in electroless Ni-P and Ni_3P layers, and Ω is the molar volume.

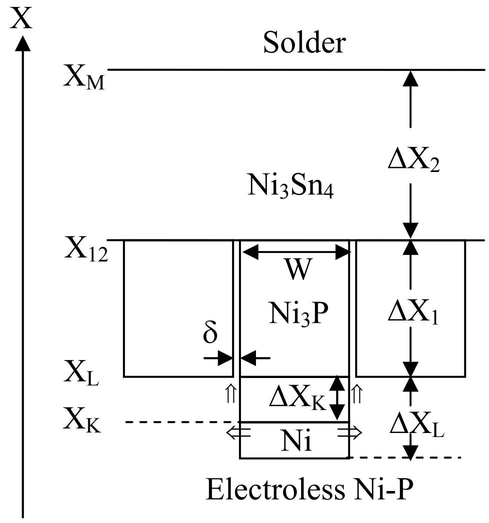

Fig. 6.1. Schematic illustration of the growth of Ni_3P grain in the electroless Ni-P layer due to the depletion of Ni during soldering reaction.

Since P is completely consumed within electroless Ni-P layer to form Ni_3P layer, thus

$$N_P^{before} = N_P^{after} \tag{6.5}$$

$$|\Delta X_K| = |\Delta X_L|(4C_0 - 3) \tag{6.6}$$

Since $\Delta X = V\Delta t$, thus

$$V_K = V_L(4C_0 - 3) \tag{6.7}$$

where, V_K and V_L are the velocity of interfaces X_K and X_L, respectively.

The number of Ni atoms that freed from electroless Ni-P layer in time Δt owing to its transformation into Ni_3P can be calculated as

$$\Delta N_{Ni} = N_{Ni}^{before} - N_{Ni}^{after} \tag{6.8}$$

$$\Delta N_{Ni} = \frac{|\Delta X_L|}{\Omega}\left(C_0 - \frac{3}{4}\right) + \frac{|\Delta X_K|}{\Omega}\frac{3}{4} \tag{6.9}$$

After substituting the value of ΔX_K from Eq. 6.6, we get

$$\Delta N_{Ni} = \frac{|\Delta X_L|}{\Omega}(4C_0 - 3) \tag{6.10}$$

Since all the freed Ni atoms diffuse through the Ni_3P layer, thus from mass balance for Ni, the flux of Ni diffusing through the Ni_3P layer must be equal to

$$J_{Ni} = \frac{\Delta N_{Ni}}{\Delta t} = \frac{|\Delta X_L|}{\Omega \Delta t}(4C_0 - 3) \tag{6.11}$$

Flux of Ni atom diffusing through the Ni_3P layer can also be represented by

$$J_{Ni} = -\frac{1}{\Omega} D_{Ni}^{eff} \frac{\Delta C_1}{\Delta X_1} \tag{6.12}$$

where, D_{Ni}^{eff} is the effective diffusivity of Ni in Ni_3P layer, and $\Delta C_1 / \Delta X_1$ is the gradient of the atomic fraction of Ni along the Ni_3P layer. From Eqs. 6.11, and 6.12,

$$\frac{|\Delta X_L|}{\Omega \Delta t}(4C_0 - 3) = -\frac{1}{\Omega} D_{Ni}^{eff} \frac{\Delta C_1}{\Delta X_1} \tag{6.13}$$

Since $|\Delta X_L| = -V_L \Delta t$, thus

$$V_L = \left(\frac{1}{4C_0 - 3}\right) D_{Ni}^{eff} \frac{\Delta C_1}{\Delta X_1} \tag{6.14}$$

Since the velocity of interface X_{12}, V_{12}, is equal to V_K, then after substituting the value of V_L in Eq. 6.7, we can get

$$V_{12} = V_K = D_{Ni}^{eff} \frac{\Delta C_1}{\Delta X_1} \tag{6.15}$$

Considering the flux of Sn at the interface X_M, the velocity of the interface V_M can be determined as

$$\left(C_{Sn}^{'} - C_{Sn}^{''}\right)V_M = \Omega\left(J_{Sn}^{'} - J_{Sn}^{''}\right) \tag{6.16}$$

where, $J_{Sn}^{'}$ and $J_{Sn}^{''}$ are the flux of Sn atoms diffusing through the solder and Ni_3Sn_4, respectively, and $C_{Sn}^{'}$ and $C_{Sn}^{''}$ are the mole fraction of Sn in solder and Ni_3Sn_4, respectively. After assuming Sn-3.5Ag solder as a pure Sn, the flux of Sn atoms diffusing through the Ni_3Sn_4 layer can be determined as

$$\left(1 - \frac{4}{7}\right)V_M = \Omega\left\{0 - (-\left|J_{Sn}^{''}\right|)\right\} \tag{6.17}$$

$$\left|J_{Sn}^{''}\right| = \frac{1}{\Omega}\frac{3}{7}V_M \tag{6.18}$$

In electroless Ni-P/solder system, the growth of Ni_3P and Ni_3Sn_4 layers are controlled by the diffusion of Ni through the Ni_3P layer (Chen *et al.*, 2004; Jang *et al.*, 1999; Matsuki *et al.* 2002), thus for the growth of Ni_3Sn_4 at the Ni_3Sn_4/Ni_3P interface, the flux of Sn atoms coming from the solder through the Ni_3Sn_4 layer must be equal to the 4/3 times of the flux of Ni atoms coming from the electroless Ni-P through the Ni_3P layer i.e.

$$\left|J_{Sn}^{''}\right| = \frac{4}{3}J_{Ni} \tag{6.19}$$

After substituting the value of J_{Ni} from Eq. 6.11, we get

$$\left|J''_{Sn}\right| = \frac{4}{3}\frac{\left|\Delta X_L\right|}{\Omega \Delta t}\left(4C_0 - 3\right) \tag{6.20}$$

Since $\left|\Delta X_L\right| = -V_L \Delta t$, then

$$\left|J''_{Sn}\right| = \frac{1}{\Omega}\frac{4}{3}\left(4C_0 - 3\right)\left(-V_L\right) \tag{6.21}$$

After substituting the value of $\left|J''_{Sn}\right|$ from Eq. 6.18, we get the velocity of interface X_M

$$V_M = \frac{28}{9}\left(4C_0 - 3\right)\left(-V_L\right) \tag{6.22}$$

And after putting the value of V_L from Eq. 6.14, we get

$$V_M = -\frac{28}{9} D_{Ni}^{eff} \frac{\Delta C_1}{\Delta X_1} \tag{6.23}$$

Now, the growth rate of Ni_3P layer can be determined as

$$\frac{d\Delta X_1}{dt} = V_{12} - V_L = -4\left(\frac{1 - C_0}{4C_0 - 3}\right) D_{Ni}^{eff} \frac{\Delta C_1}{\Delta X_1} \tag{6.24}$$

and the growth rate of Ni_3Sn_4 IMC layer will be

$$\frac{d\Delta X_2}{dt} = V_M - V_{12} = -4.11 D_{Ni}^{eff} \frac{\Delta C_1}{\Delta X_1} \tag{6.25}$$

From Eqs. 6.24 and 6.25, the ratio between thickness of Ni_3Sn_4 and Ni_3P layers can be determined as

$$\frac{\Delta X_2}{\Delta X_1} = 1.03 \frac{4C_0 - 3}{1 - C_0} \tag{6.26}$$

If f is the structural factor depending upon the Ni_3P grain's structure, δ is the thickness of grain boundary, and D_{Ni}^{gb} is the grain boundary diffusivity of Ni through Ni_3P layer, then the effective diffusivity of Ni in Ni_3P layer will be

$$D_{Ni}^{eff} = f\frac{\delta}{W}D_{Ni}^{gb}$$

For columnar grain of square cross-section, $f = 1$, thus

$$D_{Ni}^{eff} = \frac{\delta}{W}D_{Ni}^{gb} \tag{6.27}$$

On considering the lateral growth of Ni$_3$P grain, two possibilities exist for D_{Ni}^{eff}. The first, when D_{Ni}^{eff} is constant due to the constant W and the second, when D_{Ni}^{eff} is varying with time due to the change in W.

Case I: If there is no lateral growth in Ni$_3$P grain, then W is constant, and thus from Eqs. 6.24 and 6.27,

$$\frac{d\Delta X_1}{dt} = -4\left(\frac{1-C_0}{4C_0-3}\right)\frac{\delta}{W}D_{Ni}^{gb}\frac{\Delta C_1}{\Delta X_1} \tag{6.28}$$

On integrating we get,

$$\Delta X_1^2 = 8\left(\frac{1-C_0}{4C_0-3}\right)\frac{\delta}{W}D_{Ni}^{gb}\Delta C_1 t + const \tag{6.29}$$

Since at t=0, $\Delta X_1 = 0$, then

$$\Delta X_1^2 = 8\left(\frac{1-C_0}{4C_0-3}\right)\frac{\delta}{W}D_{Ni}^{gb}\Delta C_1 t \tag{6.30}$$

After putting the value of ΔX_1 in Eq. 6.26, ΔX_2 will be

$$\Delta X_2^2 = 8.45\left(\frac{4C_0-3}{1-C_0}\right)\frac{\delta}{W}D_{Ni}^{gb}\Delta C_1 t \tag{6.31}$$

Thus in this case, $\Delta X_1 \propto t^{1/2}$; $\Delta X_2 \propto t^{1/2}$

Case II: The previous case is an ideal one, however in practice, as soldering reaction proceeds, Ni$_3$P grains grow in lateral direction also (as seen in Figs. 3.21 and 4.18). Thus in this case, W will not be a constant. Therefore in this case, we can assume that $W \approx K\Delta X_1^m$, where K and m are the constants that depend upon the kinetics of grain growth. After putting the value of W in Eq. 6.28, we get

$$\frac{d\Delta X_1}{dt} = -4\left(\frac{1-C_0}{4C_0-3}\right)\frac{\delta}{K}D_{Ni}^{gb}\frac{\Delta C_1}{\Delta X_1^{1+m}} \tag{6.33}$$

On integrating we get,

$$\Delta X_1^{(2+m)} = 4(2+m)\left(\frac{1-C_0}{4C_0-3}\right)\frac{\delta}{K}D_{Ni}^{gb}\Delta C_1 t + const \tag{6.34}$$

If at t=0, $\Delta X_1 = 0$, then

$$\Delta X_1^{(2+m)} = 4(2+m)\left(\frac{1-C_0}{4C_0-3}\right)\frac{\delta}{K}D_{Ni}^{gb}\Delta C_1 t \tag{6.35}$$

After putting the value of ΔX_1 in Eq. 6.26, ΔX_2 will be

$$\Delta X_2^{(2+m)} = 4(2+m)(1.03)^{2+m}\left(\frac{4C_0-3}{1-C_0}\right)^{1+m}\frac{\delta}{K}D_{Ni}^{gb}\Delta C_1 t \tag{6.36}$$

Thus in this case, $\Delta X_1 \propto t^{1/(2+m)}$; $\Delta X_2 \propto t^{1/(2+m)}$

From both cases, it is clear that the Ni_3P and Ni_3Sn_4 compounds can follow not only $t^{1/2}$ but also $t^{1/(2+m)}$ growth kinetics depending upon the lateral growth of Ni_3P grain. If the lateral growth of Ni_3P grain is negligible, then the Ni_3P and Ni_3Sn_4 compounds follow $t^{1/2}$ growth kinetics, otherwise, they follow $t^{1/(2+m)}$ growth kinetics. Thus, it is reasonable to conclude that for the short period of soldering reaction, when width of Ni_3P grain is approximately constant, Ni_3P and Ni_3Sn_4 follow $t^{1/2}$ growth kinetics. However for the long period of soldering reaction, the width of Ni_3P grain increases, and eventually the Ni_3P and Ni_3Sn_4 compounds follow $t^{1/(2+m)}$ growth kinetics.

Schaefer *et al.* (1998) has showed that IMC could follow $t^{1/3}$ growth kinetics due to the grain growth by considering isometric grain growth. Similarly, if we assume isometric grain growth ($m \approx 1$) then our model also suggests $t^{1/3}$ growth kinetics. Gusak and Tu (2002) also reported the existence of $t^{1/3}$ IMC growth kinetics owing to the grain coarsening of IMC.

They considered an open system and assumed that during grain coarsening or ripening, the total surface area of grain undergoing coarsening remains constant while the total volume of the grain grows. However in practice, grain growth could be an-isometric in nature and there could be a change in the surface area along with the change in the volume of grain. And that is why there are several studies (He *et al.*, 2004d; Jeon *et al.*, 2003b;Schaefer *et al.*, 1998), which reported $t^{1/(2+m)}$ (m > 1) growth kinetics of IMC.

To explain $t^{1/(2+m)}$ (m > 1) growth kinetics of compound, we considered that two driving forces, the reduction of surface energy (Lifshitz and Slyozov, 1961) and the gain of bulk free energy (Gusak and Tu, 2002), work together in the process of grain growth. When the gain of bulk free energy is much larger than the reduction of surface energy (normally in the early stage and short duration of aging when concentration or potential gradient and net atomic flux are large due to the thin layer of compound and a large number of grain boundaries, respectively), flux-driven grain growth is more likely to dominate. However, once the gain of bulk free energy becomes low (normally in long duration aging where potential gradient and net atomic flux become low due to the thick layer of compound and a small number of grain boundaries, respectively), the reduction of surface energy will be the dominant driving force for grain growth and then the width of grain (W) will grow at much faster rate than the length (ΔX), or in other word, the value of m in Eqs. 6.34 and 6.35 will be more than 1.

6.3. Comparison with Experimental Results

6.3.1. Growth Kinetics of Ni_3P and Ni_3Sn_4 Compounds

Growth kinetics of Ni_3P and Ni_3Sn_4 compounds in the electroless Ni-P/solder (Sn-Ag and Sn-Pb) joints has been examined in several interfacial studies (He *et al.*, 2004d; Jang *et al.*, 1999; Jeon *et al.*, 2003b; Yoon *et al.*, 2003; Yoon and Jung, 2004). It has been reported that these compounds follow both $t^{1/2}$ (Jang *et al.*, 1999; Jeon *et al.*, 2003b) and $t^{1/(2+m)}$ (m > 0) (He *et al.*, 2004d; Jeon *et al.*, 2003b; Yoon *et al.*, 2003; Yoon and Jung, 2004) growth kinetics. However, the cause for this difference in growth kinetics is not clear as Ni_3Sn_4 has been reported to follow both $t^{1/2}$ (Jeon *et al.*, 2003b) and $t^{1/3}$ (He *et al.*, 2004d) growth kinetics under liquid state aging. Since previously reported Ni_3Sn_4 growth kinetics cannot be explained with the help of state (liquid or solid) of aging, we used our model to explain this by considering the duration of the aging. As discussed in the previous section, for short soldering reaction, Ni_3P and Ni_3Sn_4 compounds follow $t^{1/2}$ growth kinetics because the lateral growth in Ni_3P grain is negligible as compared to the longitudinal growth (see the aspect ratio of Ni_3P grain is around 1/4 in Figs. 3.21 and 4.18), whereas, for long soldering reaction, compounds follow the $t^{1/(2+m)}$ growth kinetics due to the large increase in the width of Ni_3P grain. This explanation matches quite well with all previously reported results because $t^{1/2}$ growth kinetics was reported for short (up to a few minutes) liquid-state aging (Jang *et al.*, 1999; Jeon *et al.*, 2003b), whereas, $t^{1/(2+m)}$ growth kinetics was reported for long (a few hours) liquid-state aging (He *et al.*, 2004d) as well as for long (a few hundreds hours) solid-state aging (Jeon *et al.*, 2003b; Yoon *et al.*, 2003; Yoon and Jung, 2004).

6.3.2. Influence of P Concentration on the Growth of Ni_3P and Ni_3Sn_4

In the growth model, Eq. 6.26 shows a non-linear relationship between thicknesses of Ni_3P and Ni_3Sn_4 layers growing at the electroless Ni-P/solder interface. From the equation, it is clear that thickness ratio of Ni_3Sn_4 to Ni_3P layers decreases with increase in the P concentration of electroless Ni-P UBM. The relationship between Ni_3P and Ni_3Sn_4 thicknesses was verified from the experimental results of various electroless Ni-P/solder interfacial studies. To do this, the thickness of Ni_3P and Ni_3Sn_4 layers were obtained from different electroless Ni-P/solder interfacial studies, which used electroless Ni-P UBM of different P concentrations. The obtained thickness of Ni_3P and Ni_3Sn_4 layers were tabulated in Table 6.1 and their ratio was plotted as a function of P in Fig. 6.2 to compare with the modeling results. Fig. 6.2 shows a good agreement between modeling and experimental results.

Eq. 6.24 shows that the P concentration of electroless Ni-P layer is a crucial factor in determining the growth rate of Ni_3P layer. From the equation it is clear that Ni_3P growth rate increases with increasing the P concentration of electroless Ni-P UBM. These results are in agreement with the results reported in previous interfacial studies between electroless Ni-P and different solders (Alam *et al.*, 2003; Chonan *et al.*, 2002a; Sohn *et al.*, 2003; Sohn *et al.* 2004a). Chonan *et al.* (2002a) measured the growth of P-enriched Ni-P (Ni_3P) layer in the solder joints having electroless Ni-P layers of different P concentrations. It was observed that the growth of P-enriched Ni-P layer increases with the increase in P concentration of electroless Ni-P layer. Sohn *et al.* (2004a) also demonstrated with the help of differential scanning calorimetry (DSC) analysis that the driving force for electroless Ni-P to transform into crystalline Ni_3P phase increases with increasing the P concentration. Thus, it can easily be understood that higher P electroless Ni-P UBM would be able to supply more P atoms to facilitate Ni_3P formation and thereby the Ni_3P layer would grow faster.

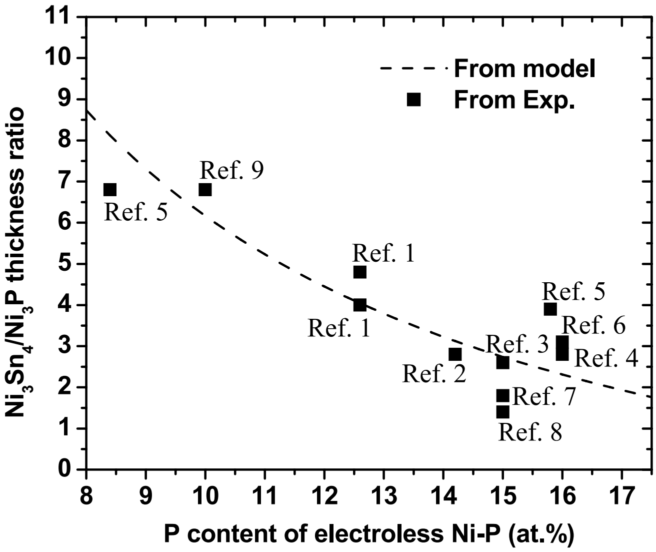

Fig. 6.2. A plot of Ni_3Sn_4/Ni_3P thickness ratio versus P concentration of electroless Ni-P UBM showing good agreement of equation 6.26 with the experimental results.

Table 6.1. Thickness ratio of Ni_3Sn_4 to Ni_3P layers obtained from previous interfacial studies that used electroless Ni-P UBM of different P concentrations.

Ni_3Sn_4 thickness (µm)	Ni_3P thickness (µm)	P concent-ration (at.%)	Ni_3Sn_4/Ni_3P thickness ratio	Solder (wt.%)	Experimental condition	Reference	Ref. No.
3.8	0.8	12.6	4.8	Sn-3.5Ag	16 min reflow at 250 °C	Jeon *et al.*, 2001	1
1.6	0.4	12.6	4	Sn-37.5Pb	16 min reflow at 210 °C	Jeon *et al.*, 2001	1
1.1	0.4	14.2	2.8	eutc. Sn-Pb	2 min reflow above 183 °C (max. 245 °C)	Matsuki *et al.*, 2002	2
3.9	1.5	15.0	2.6	eutc. Sn-Pb	One reflow at 220 °C + 20 min aging at 220 °C	Jang *et al.*, 1999	3
5.4	1.9	16.0	2.8	Sn-3.5Ag	1 min reflow at 250 °C + 225 h aging at 160 °C	From present study	4
7.0	1.8	15.8	3.9	Pure Sn	10 min reflow at 250 °C	Sohn *et al.*, 2004a	5
7.5	1.1	8.4	6.8	Pure Sn	10 min reflow at 250 °C	Sohn *et al.*, 2004a	5
2.0	0.65	16	3.1	Pure Sn	Heating up to 300 °C at a rate of 5 °C/min	Sohn *et al.*, 2003	6
2.2	1.2	15	1.8	Sn-3.5Ag-5Bi	Reflow up to 40 °C above solder-melting temperature + 15 days aging at 170 °C	Yoon *et al.*, 2003	7
3.0	2.1	15	1.4	Sn-3.5Ag	Reflow up to 40 °C above solder-melting temperature + 60 days aging at 170 °C	Yoon and Jung, 2004	8
3.4	0.5	10	6.8	Sn-3.5Ag	30 min reflow at 240 °C	Sharif *et al.*, 2005	9

6.4. Conclusions

A mathematical model has been developed for the growth of Ni_3P and Ni_3Sn_4 compounds in the electroless Ni-P/solder system. The modeling results match very well with the experimental results. The model shows that $t^{1/2}$ to $t^{1/(2+m)}$ ($m > 0$) transition in the growth kinetics of compounds is not due to grain boundary diffusion, but due to the lateral growth of Ni_3P grain. The influence of the P concentration of electroless Ni-P UBM on the growth of Ni_3P and Ni_3Sn_4 has also been clearly understood with the help of growth model.

In this and previous parts of the work, the focus is given to Cu/electroless Ni-P/Sn-3.5Ag interfacial reactions and/or their effect on the solder joint strength. In the next chapter, the effect of electromigration will be presented on the Cu/electroless Ni-P/Sn-3.5Ag interfacial reactions and solder joint strength.

Chapter 7

Effect of Electromigration on the Interfacial Microstructure and Mechanical Properties of UBM/Solder Joints

7.1. Introduction

The trend of miniaturization of VLSI devices is causing the requirements of smaller size and higher I/O density solder flip chip and ball grid array (BGA) packages. A higher I/O density results in the finer pitch and smaller size interconnects. As the size of interconnects is decreasing, the current density of electric current passing thorough them is increasing. High current density (~10^4 A/cm^2) causes the electrical failure of solder interconnects due to the electromigration and current crowding (Lee *et al.*, 2001a, b; Yeh *et al.*, 2002). Even at moderate current density (~10^3 A/cm^2), electromigration influences the IMC formation at the UBM/solder interface (Chen and Chen, 2001; Chen *et al.*, 1998; Gan and Tu, 2005). Moreover, there are a few examples in which moderate electric current density (~ 10^3 A/cm^2) has been found to influence the IMC formation, precipitation, recrystallization, and grain coarsening in different materials (Conrad, 2000). As all these microstructural changes can influence the mechanical properties of a material, it is imperative to study the effect of electric current on the mechanical properties of solder joints. Accordingly in this study, the effect of electric current has been investigated on the interfacial microstructure and mechanical properties of UBM/solder joint. Three UBM/solder systems, electroless Ni-P/Sn-3.5Ag, Ni/Sn-3.5Ag, and electroless Ni-P/Sn-37Pb, are compared in terms of microstructure and mechanical properties to achieve a complete understanding.

7.2. Experimental Procedures

7.2.1. Preparation of Test Samples

The preparation method of the electroless Ni-P/Sn-3.5Ag test samples has been described in section 3.2.1. For the electroless Ni-P/Sn-37Pb test samples, the preparation method was the same, but Sn-37Pb solder was used instead of Sn-3.5Ag and the thickness of electroless Ni-P metallization deposited on Cu plate was around 7 µm. Even for the Ni/Sn-3.5Ag test samples, a similar preparation method was followed. However in this case, Ni plate was used instead of Cu and immersion Au was deposited directly on the surface cleaned Ni plate without depositing electroless Ni-P (see Fig. 7.1). Pure Ni/Sn-3.5Ag solder joint was prepared by cutting the Au coated Ni plate into two plates of sizes of 40 mm × 25 mm × 6 mm and 30 mm × 25 mm × 6 mm, and then joining them using Sn-3.5Ag solder wires as described in section 3.2.1. Finally, the joined plates were cut into a number of small test sample shown in Fig. 7.2.

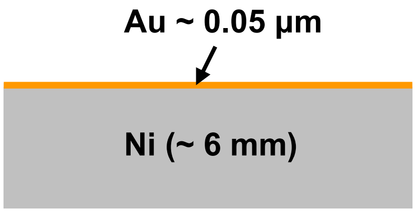

Fig. 7.1. Schematic of metallization layout on Ni plate.

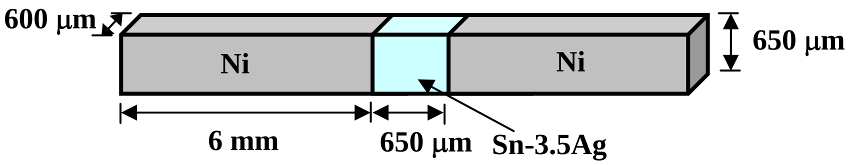

Fig. 7.2. Schematic diagram of Ni/Sn-3.5Ag test sample.

7.2.2. Thermal Aging and Electrical Stressing of Test Samples

The experimental setup used for electrical stressing of test samples is shown in Fig. 7.3. As-prepared test samples were connected to a current source with the help of a specially designed sample holder. The sample holder had a ceramic base and several Cu electrodes to hold the Cu or Ni part of the test samples. The upper surface of Cu electrodes was insulated with the ceramic plates to disconnect them electrically from the sample holder's metallic body. These Cu electrodes were directly connected to a current source.

For thermal aging with electrical stressing, the experimental setup was kept in the oven and as-prepared test samples were aged at 160 °C for 100 h with different DC current densities ranging from 0 to 3×10^3 A/cm^2. For zero current density, test samples were aged without current. After aging, samples were removed from the oven and cooled in air to room temperature.

Electric current results in Joule heating, hence the increase in temperature due to the electrical stressing was measured with the help of a thermocouple. As shown in Fig. 7.3, a thermocouple was kept at the center of test sample with the help of high temperature thermo-tape. The increase in temperature was monitored at the room temperature with increasing current density. A maximum increase in temperature of around 5 °C was observed at the highest 3×10^3 A/cm^2 current density used. This small increase in temperature due to the passage of electric current was neglected as compared to the thermal aging temperature of 160 °C.

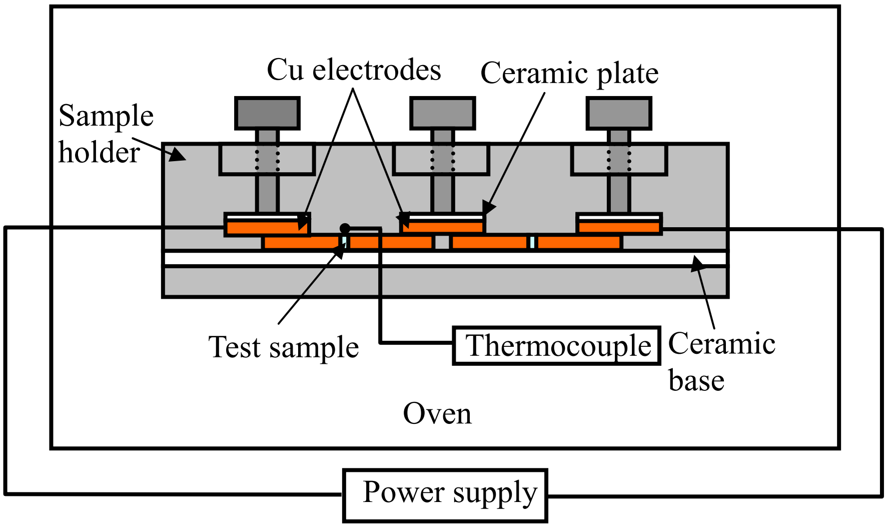

Fig. 7.3. Schematic diagram of experimental setup used to pass the electric current through test samples during thermal aging in oven.

7.2.3. Mechanical Testing of Test Samples

Two types of mechanical testing were carried out in this study. The first was tensile testing that has been described in section 3.2.3 and the second was nano-indentation. The nano-indentation test was carried out using a nano-indentation tester (Micro Materials NanoTest) having a Berkovich diamond pyramid tip. Twelve indentations in the solder matrix of a sample (six on one side and six on the opposite side) were performed. Before indentations, the samples were cold mounted in epoxy and polished down to 1 μm finish to make the solder surface smooth. Nano-indentations were performed in force-controlled mode with a loading rate of 0.2 mN/s to a maximum load of 10 mN. The dwelling time of 20s was used with an unloading rate of 0.2 mN/s. A distance of 30 μm was maintained in between two subsequent indentations, so that the previous indentation cannot affect the new one.

7.2.4. Microstructural Observations

The same as described in section 3.2.4.

7.3. Results

7.3.1. Tensile Strength of UBM/Solder Joints

Fig. 7.4 shows the tensile strength of Ni-P/Sn-3.5Ag, Ni-P/Sn-37Pb, and Ni/Sn-3.5Ag solder joints as a function of current density. It can be observed that the average tensile strength of Ni-P/Sn-3.5Ag and Ni-P/Sn-37Pb joints increased slightly or remained the same after aging with current as compared to aging without current. The average tensile strength of Ni/Sn-3.5Ag solder joint, however, decreased slightly with an increase in current density. In the case of Sn-3.5Ag solder, as shown in Fig. 7.4a and c, the variation among the individual tensile strength of the solder joints aged with the same current density increased with an increase in current density.

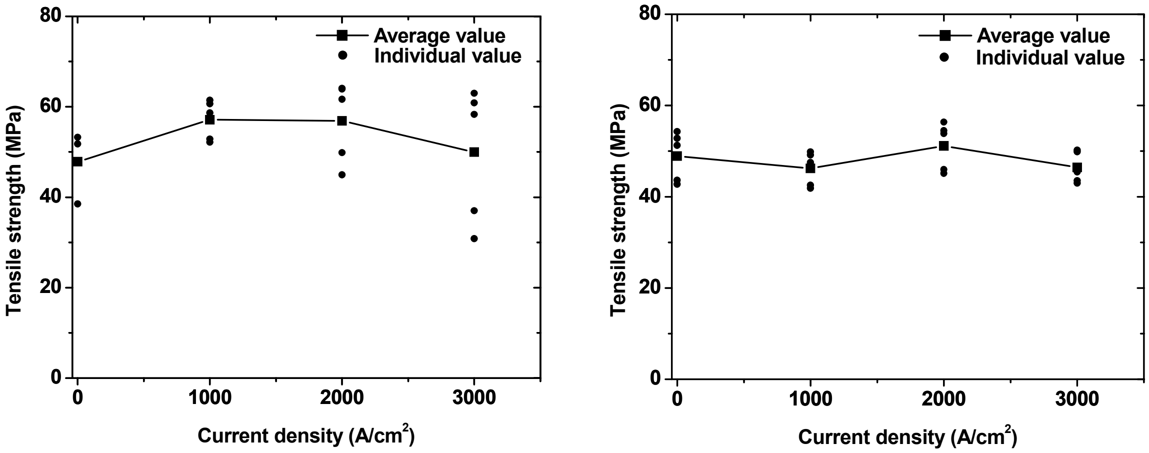
(a) Ni-P/Sn-3.5Ag

(b) Ni-P/Sn-37Pb

(c) Ni/Sn-3.5Ag

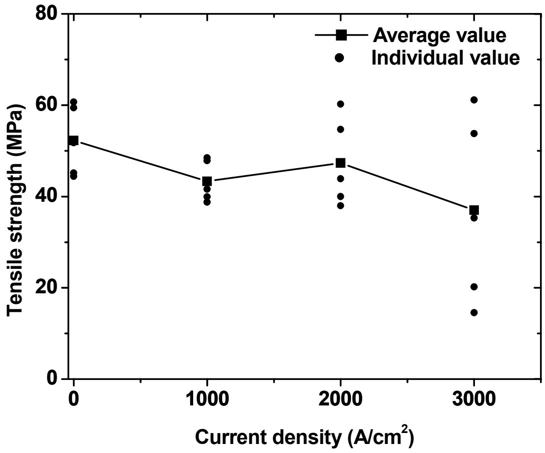

Fig. 7.4. Tensile strength of (a) Ni-P/Sn-3.5Ag (b) Ni-P/Sn-37Pb and (c) Ni/Sn-3.5Ag solder joints as a function of current density.

7.3.2. Fracture Energy of UBM/Solder Joints

In this study, the fracture energy of UBM/solder joint is defined by the area under load versus extension curve of tensile tested sample. The high fracture energy indicates the ductile failure of solder joint, while low indicates brittle failure. The fracture energy of different UBM/solder joints is plotted as a function of current density in Fig. 7.5. From the figure, it is clear that the average fracture energy of all three types of solder joints decreased with an increase in current density. However, the decrease in fracture energy was more severe in the case of Ni-P/Sn-37Pb and Ni/Sn-3.5Ag solder joints (Fig. 7.5b and c) as compared to the Ni-P/Sn-3.5Ag solder joint (Fig. 7.5a).

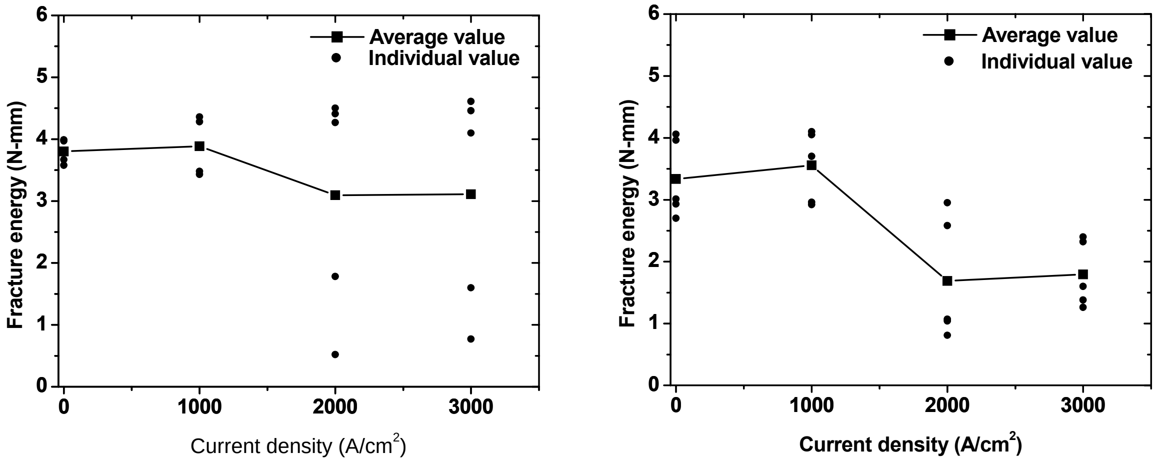
(a) Ni-P/Sn-3.5Ag

(b) Ni-P/Sn-37Pb

(c) Ni/Sn-3.5Ag

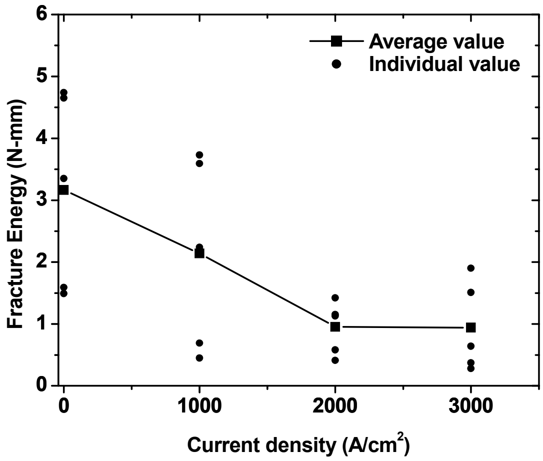

Fig. 7.5. Fracture energy of (a) Ni-P/Sn-3.5Ag (b) Ni-P/Sn-37Pb and (c) Ni/Sn-3.5Ag solder joints as a function of current density.

A difference was also observed in the variation among the individual fracture energy of all three types of solder joints aged with the same current density. In the case of Ni-P/Sn-3.5Ag and Ni-P/Sn-37Pb solder joints, the variation was relatively high in the samples aged with high 2 × 10^3 and 3 × 10^3 A/cm^2 current densities (Fig. 7.5a and b). However, in the case of Ni/Sn-3.5Ag, it was high in the samples aged without current or with a low 1 × 10^3 A/cm^2 current density and became relatively small in the samples aged with the higher current densities (Fig. 7.5c). The reason for this trend of variation of individual fracture energy was that in the case of Ni-P/Sn-3.5Ag and Ni-P/Sn-37Pb solder joints, all the five samples aged without current or with the low current density had ductile failure (Fig. 7.6a), whereas a few of the five samples aged with the higher current densities had brittle or mixed failure (Fig. 7.6b). On the other hand, in the case of Ni/Sn-3.5Ag solder joint, a few of the five samples aged without current or with the low current density had brittle failure (Fig. 7.7a), while all the five samples aged with the higher current densities had brittle or mixed failure (Fig. 7.7b).

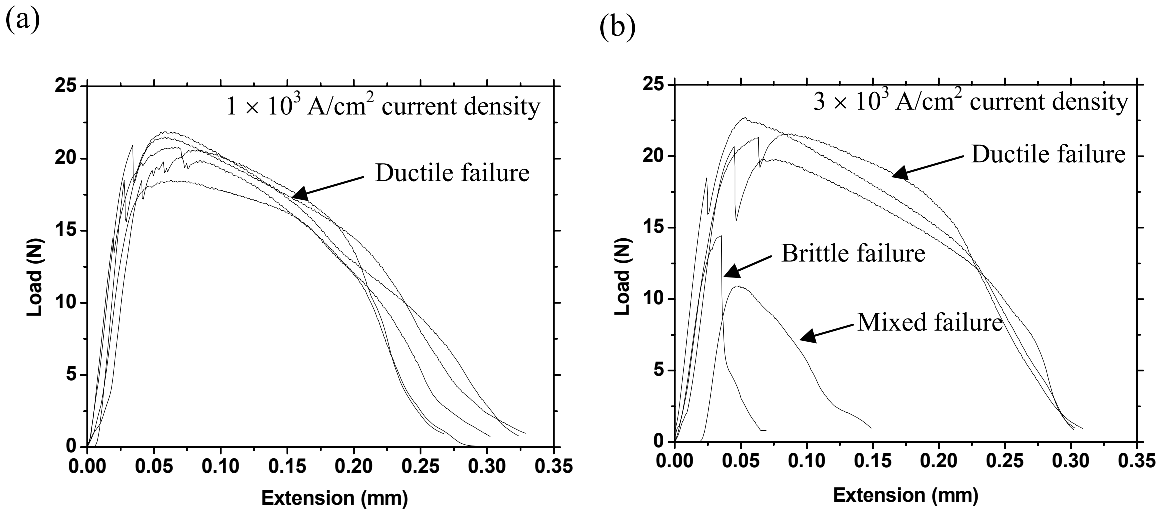

Fig. 7.6. Load vs. Extension curves of the Ni-P/Sn-3.5Ag solder joints aged with (a) 1 × 10^3 A/cm^2 and (b) 3 × 10^3 A/cm^2 current densities, showing ductile, brittle, and mixed failures.

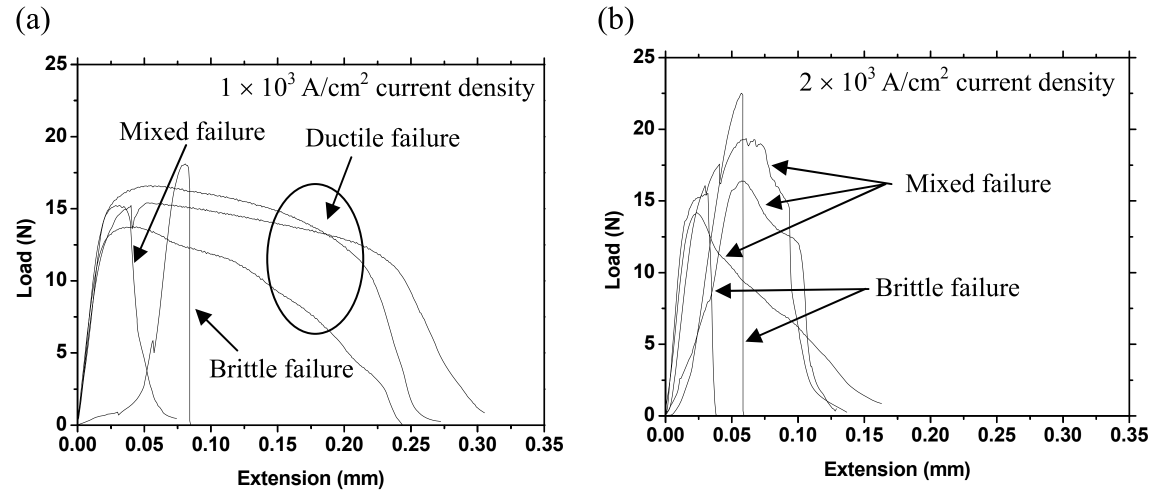

Fig. 7.7. Load vs. Extension curves of the Ni/Sn-3.5Ag solder joints aged with (a) 1 × 10^3 A/cm^2 and (b) 2 × 10^3 A/cm^2 current densities, showing ductile, brittle, and mixed failures.

7.3.3. Fracture Analysis

Fracture analysis was carried out to examine the fracture behaviour of all three types of solder joints.

Electroless Ni-P/Sn-3.5Ag Samples

In all the Ni-P/Sn-3.5Ag samples aged without current or with a low 1 × 10^3 A/cm^2 current density, as shown in Figs. 7.5a and 7.8, failure was ductile and fracture path was inside the bulk solder. However in the case of samples aged with higher current densities, a few samples had brittle or mixed failure (Figs. 7.5a and 7.9) and in these samples fracture was primarily at the Ni_3Sn_4/Sn-3.5Ag interface (Fig. 7.10). No polarity effect of electric current was observed on the brittle failure of solder joint, as the failure occurred at both the anode and cathode side Ni_3Sn_4/ Sn-3.5Ag interfaces.

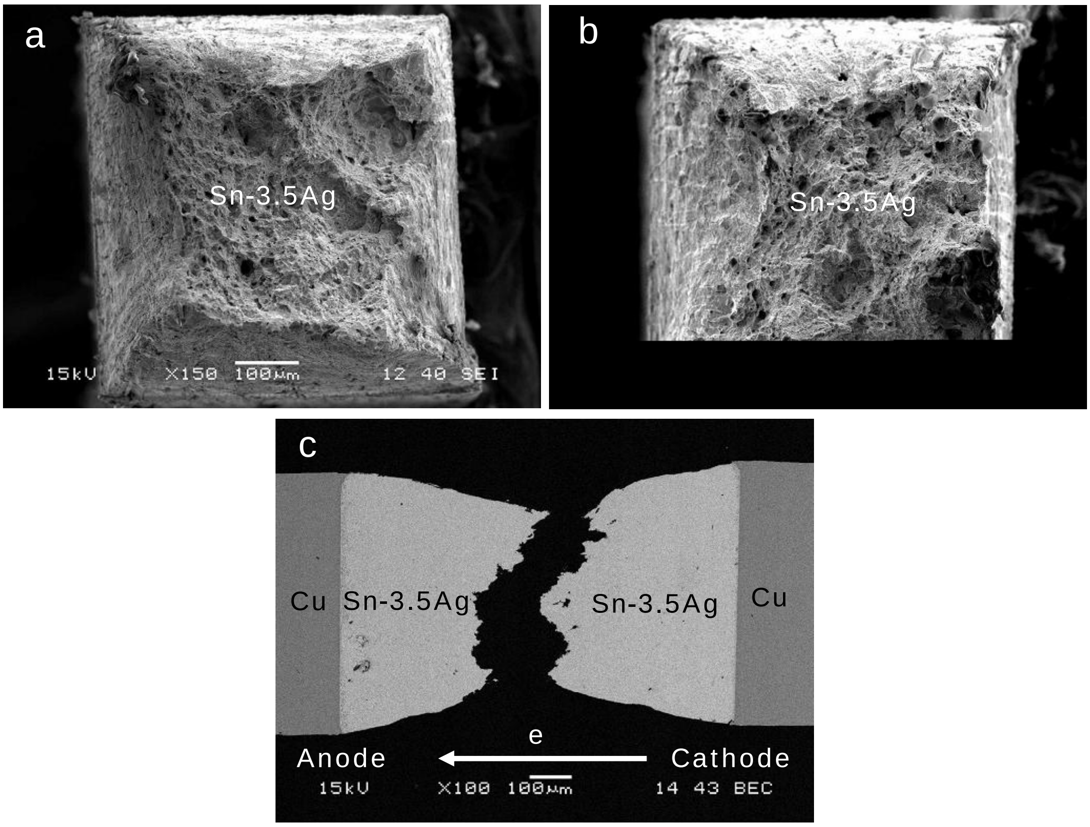

Fig. 7.8. SEM images showing fracture in the electroless Ni-P/Sn-3.5Ag solder joint aged at 160 °C for 100 h with 1 × 10^3 A/cm^2 current density: (a) Anode side top view, (b) cathode side tope view, and (c) cross-sectional view. Neck formation in the bulk solder indicates the ductile failure of solder joint.

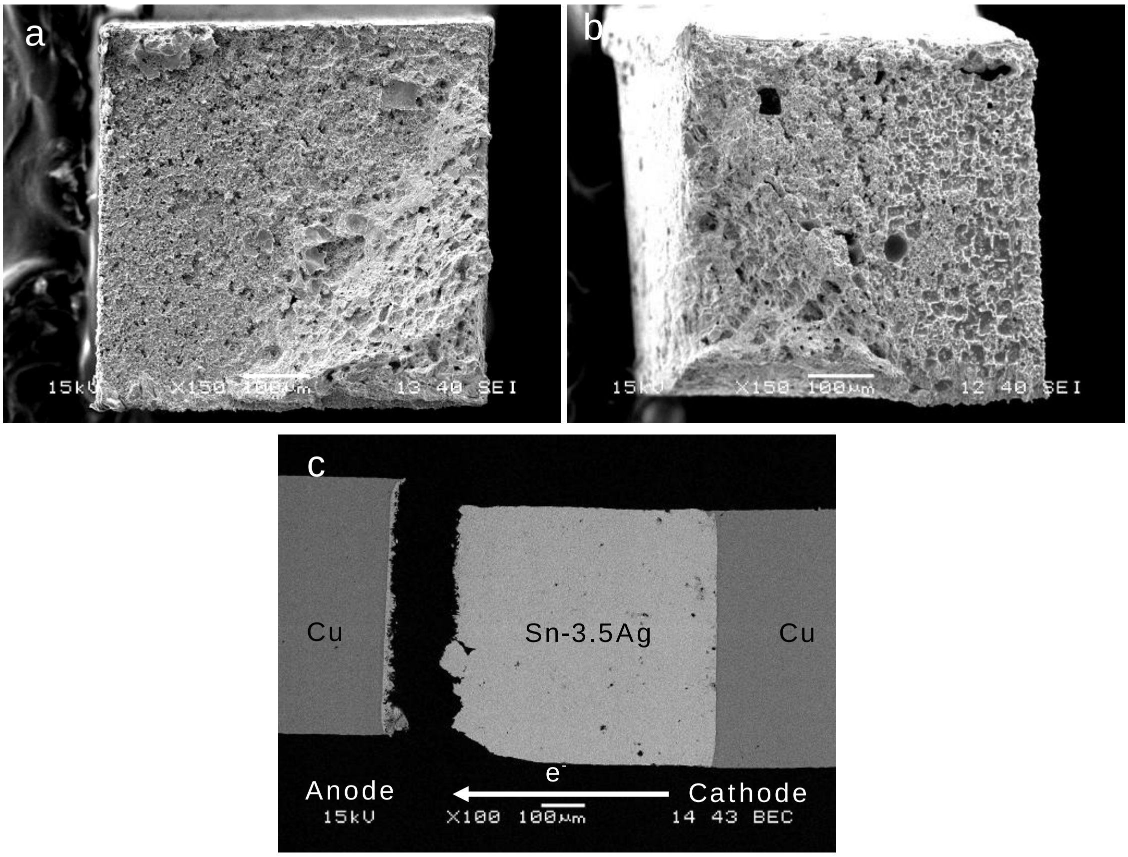
a
15kV X150 100µm 13 40 SEI
b
15kV X150 100µm 12 40 SEI
c
Cu
Sn-3.5Ag
Cu
Anode
e-
Cathode
15kV X100 100µm 14 43 BEC

Fig. 7.9. SEM images showing fracture in the electroless Ni-P/Sn-3.5Ag solder joint aged at 160 °C for 100 h with 3×10^3 A/cm^2 current density: (a) Anode side top view, (b) cathode side tope view, and (c) cross-sectional view. Brittle failure occurred at the Ni_3Sn_4/Sn-3.5Ag interface.

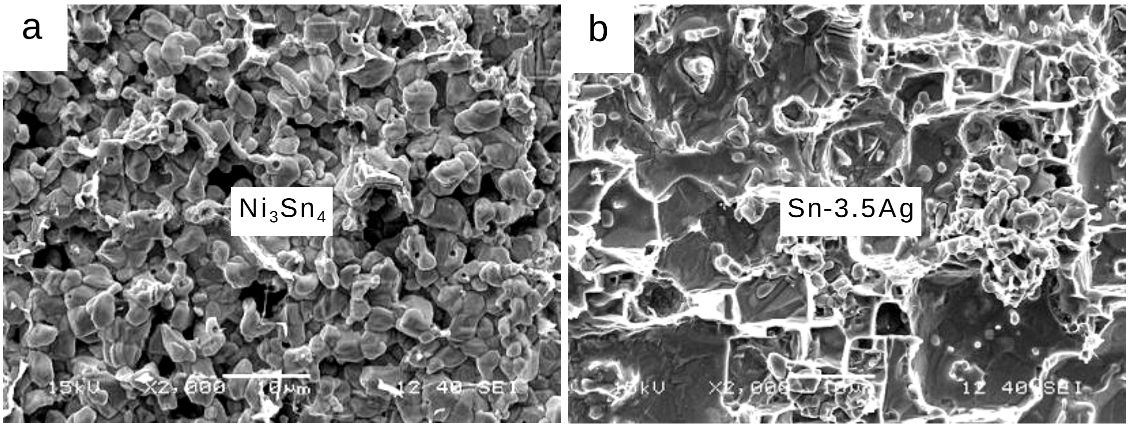
a
Ni_3Sn_4
15kV X2,000 10µm 12 40 SEI
b
Sn-3.5Ag
15kV X2,000 10µm 12 40 SEI

Fig. 7.10. Fracture surfaces of the electroless Ni-P/Sn-3.5Ag solder joint aged at 160 °C for 100 h with 3×10^3 A/cm^2 current density: (a) Anode side and (b) cathode side.

Pure Ni/Sn-3.5Ag Samples

In the case of Ni/Sn-3.5Ag samples, some of the samples aged without current had ductile fracture inside the bulk solder (Fig. 7.11) and some had brittle or mixed fracture at the Sn-3.5Ag/Ni_3Sn_4, Ni-Sn IMC/Ni-Sn IMC, and Ni-Sn IMC/Ni interfaces (Fig. 7.12). The tendency of brittle fracture increased with the increase in current density and almost all the samples aged with the current density higher than 1×10^3 A/cm^2 had brittle fracture (Figs. 7.13 and 7.5c). In most of the brittle-failed samples, fracture surfaces were found to have very fine Ni-Sn grains as shown in Fig. 7.14. Similar to the Ni-P/Sn-3.5Ag samples, no polarity effect of electric current was observed on the brittle failure of Ni/Sn-3.5Ag samples.

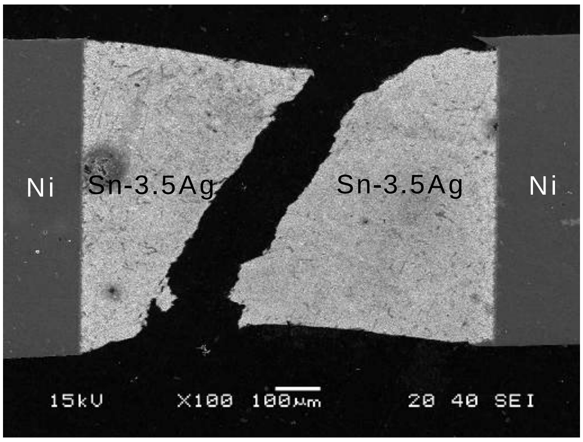

Fig. 7.11. Fracture in the Ni/Sn-3.5Ag solder joint aged at 160 °C for 100 h without current showing ductile failure inside the bulk solder.

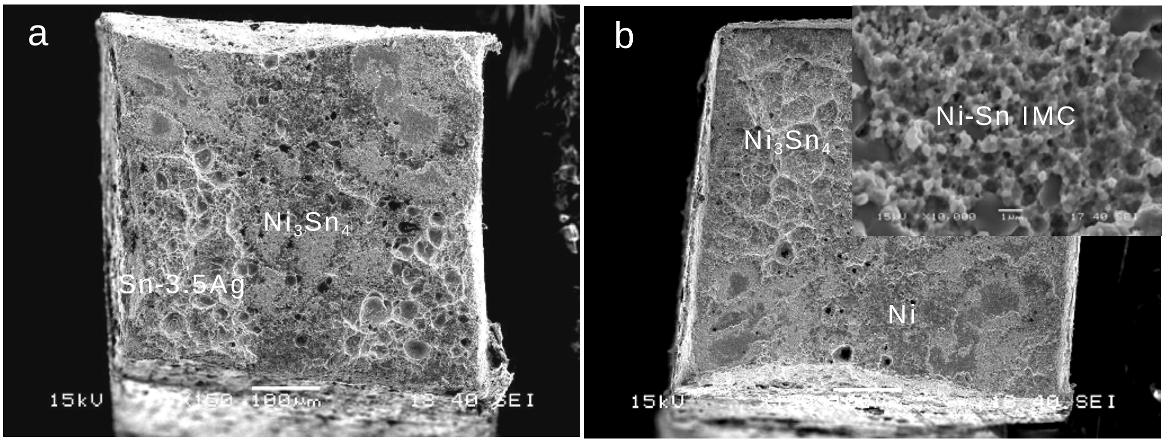

Fig. 7.12. Fracture surfaces of the Ni/Sn-3.5Ag solder joint aged at 160 °C for 100 h without current: (a) solder side and (b) Ni side. Brittle fracture occurred at the mixed Sn-3.5Ag/Ni_3Sn_4, Ni-Sn IMC/Ni-Sn IMC, and Ni-Sn IMC/Ni interfaces.

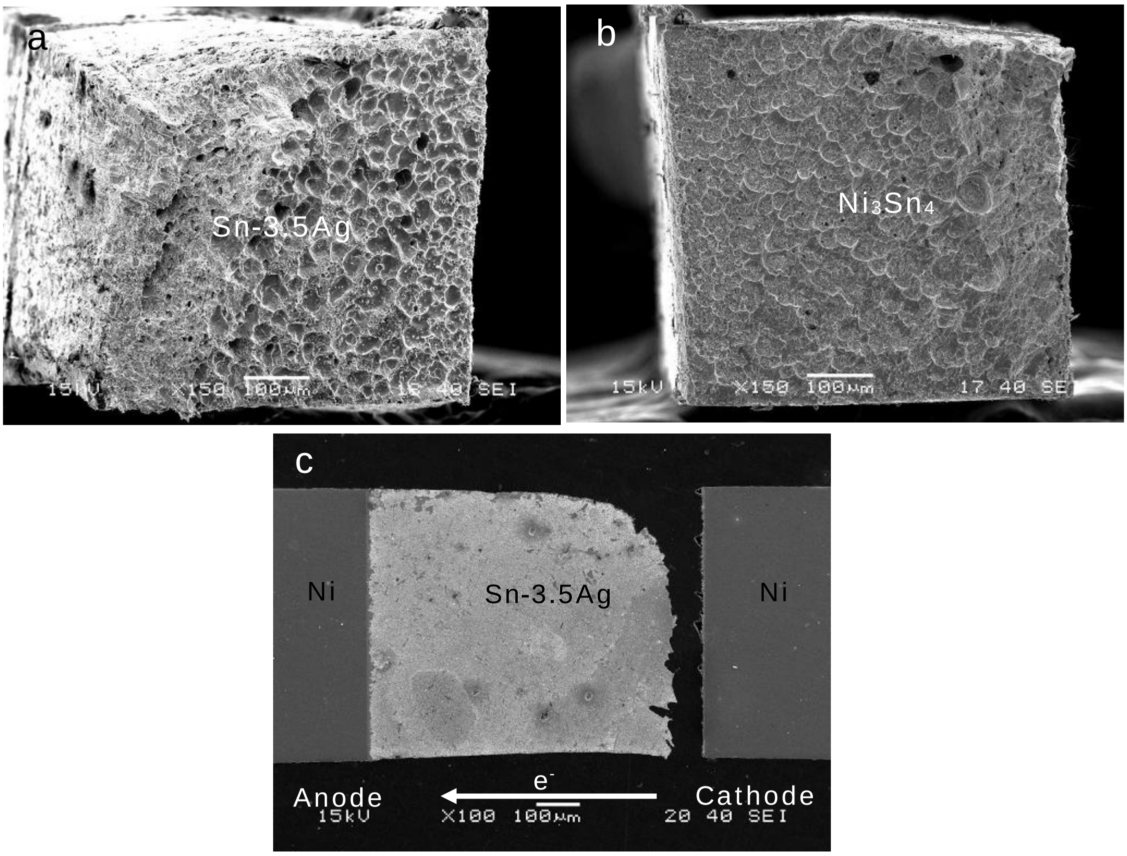
a
Sn-3.5Ag
15kV X150 100µm 16 40 SEI
b
Ni3Sn4
15kV X150 100µm 17 40 SEI
c
Ni
Sn-3.5Ag
Ni
Anode
e-
Cathode
15kV X100 100µm 20 40 SEI

Fig. 7.13. SEM images showing mixed fracture in the Ni/Sn-3.5Ag solder joint aged at 160 °C for 100 h with 2 × 10^3 A/cm^2 current density: (a) Anode side top view, (b) cathode side tope view, and (c) cross-sectional view.

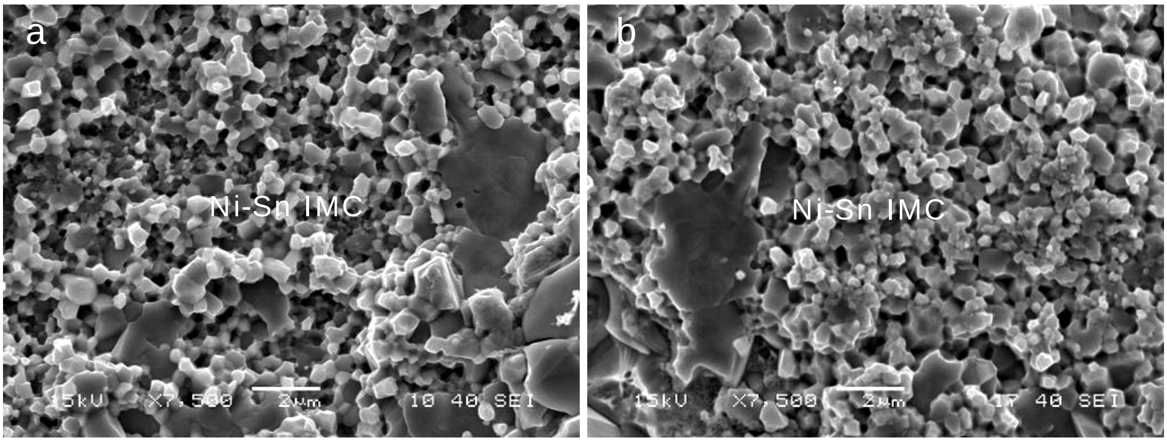
a
Ni-Sn IMC
15kV X7,500 2µm 10 40 SEI
b
Ni-Sn IMC
15kV X7,500 2µm 17 40 SEI

Fig. 7.14. Fracture surfaces of the Ni/Sn-3.5Ag solder joint aged at 160 °C for 100 h with 3 × 10^3 A/cm^2 current density, showing fine grains of Ni-Sn IMC at both the fracture surfaces.

Electroless Ni-P/Sn-37Pb Samples

In most of the electroless Ni-P/Sn-37Pb samples aged without current or with a low 1 ×

10^3 A/cm^2 current density, ductile fracture occurred inside the bulk solder (Fig. 7.15). However, with an increase in current density, fracture became brittle or mixed and always occurred at the cathode side Ni_3Sn_4/solder interface of the sample (Fig. 7.16).

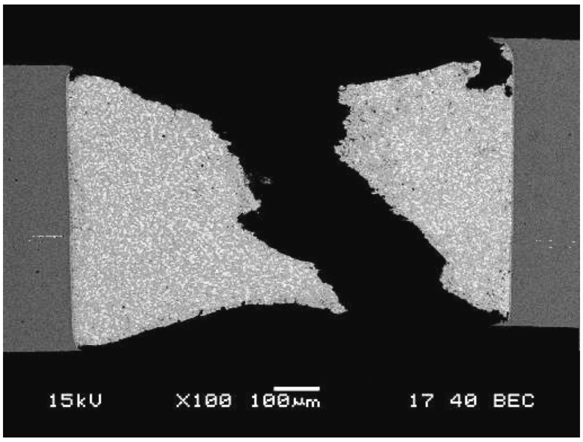
15kV
X100
100µm
17 40 BEC

Fig. 7.15. Fracture in the Ni-P/Sn-37Pb solder joint aged at 160 °C for 100 h with 1 × 10^3 A/cm^2 current density, showing ductile failure inside the bulk solder.

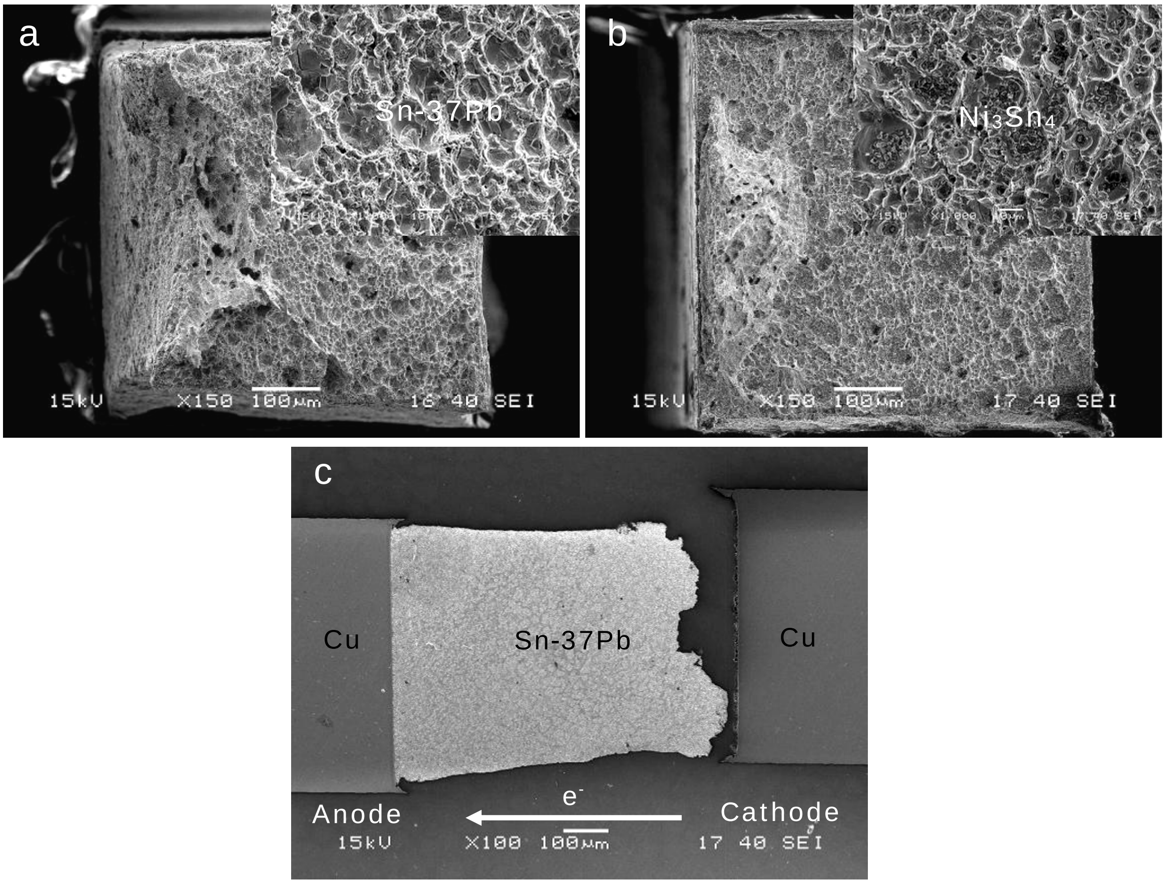
a
Sn-37Pb
15kV
X150
100µm
16 40 SEI
b
Ni3Sn4
15kV
X150
100µm
17 40 SEI
c
Cu
Sn-37Pb
Cu
e-
Anode
Cathode
15kV
X100
100µm
17 40 SEI

Fig. 7.16. SEM images showing mixed fracture in the electroless Ni-P/Sn-37Pb solder joint aged at 160 °C for 100 h with 3 × 10^3 A/cm^2 current density: (a) Anode side top view, (b) cathode side tope view, and (c) cross-sectional view.

7.3.4. Nano-indentation Test

Nano-indentation tests were carried out to investigate the effect of electric current on the mechanical properties such as modulus and hardness of solder. All three types of solder joints were tested after aging without current and with 2×10^3 A/cm^2 current density. To get reliable results, twelve indentations in the solder matrix of a sample, six on one side and six on the opposite side, were performed (Fig. 7.17). The measured values of reduced modulus and hardness of solder in different solder joints are tabulated in the Table 7.1. From these values, it is clear that the reduced modulus and hardness of solder increased slightly due to the thermal aging with current as compared to the thermal aging without current. Similar trend of increase in the modulus and hardness of eutectic Sn-Pb solder due to the electric current was observed by Ye *et al.* (2003b). However, they attributed that increase to experimental error. This interpretation is based on the expectation that, normally, the modulus and hardness of a material should decrease as defects nucleate, assisted by electric current in this case. However, we believe that in the case of UBM/solder joints, electrical current can increase the modulus and hardness of solder by accumulating the defects at certain locations, thereby reducing the defect density of rest of the solder matrix.

Though in this work no visible accumulation of defects took place, however in several previous studies with higher current densities (~ 10^4 A/cm^2), defects or vacancies were seen to accumulate in the form of voids at the cathode side solder/IMC interface (Hsu *et al.*, 2003; Gan and Tu, 2005; Lee *et al.*, 2001a, b; Shao *et al.*, 2004). Thus, the high-density electric current can increase the modulus and hardness of solder by reducing the defect density of bulk solder by accumulating the defects at the cathode side solder/IMC interface.

Table 7.1. Reduced modulus and hardness of solders in different solder joints at different experimental conditions.

Solder joints / Experimental Conditions	Electroless Ni-P/Sn-3.5Ag				Ni/Sn-3.5Ag				Electroless Ni-P/Sn-37Pb			
	Reduced Modulus (GPa)		Hardness (GPa)		Reduced Modulus (GPa)		Hardness (GPa)		Reduced Modulus (GPa)		Hardness (GPa)	
	Side 1	Side 2	Side 1	Side 2	Side 1	Side 2	Side 1	Side 2	Side 1	Side 2	Side 1	Side 2
Aged at 160 °C for 100 h without current	70.9 ± 3.5	71.7 ± 4.8	0.27 ± 0.04	0.27 ± 0.03	71.0 ± 5.5	67.1 ± 6.2	0.27 ± 0.04	0.24 ± 0.01	27.3 ± 3.8	28.1 ± 7.2	0.15 ± 0.01	0.16 ± 0.02
Aged at 160 °C for 100 h with 2×10^3 A/cm^2 current density	71.7 ± 6.0	72.4 ± 3.1	0.28 ± 0.02	0.29 ± 0.05	75.0 ± 4.0	76.8 ± 6.0	0.28 ± 0.02	0.26 ± 0.02	28.1 ± 8.5	28.9 ± 4.8	0.16 ± 0.01	0.16 ± 0.01

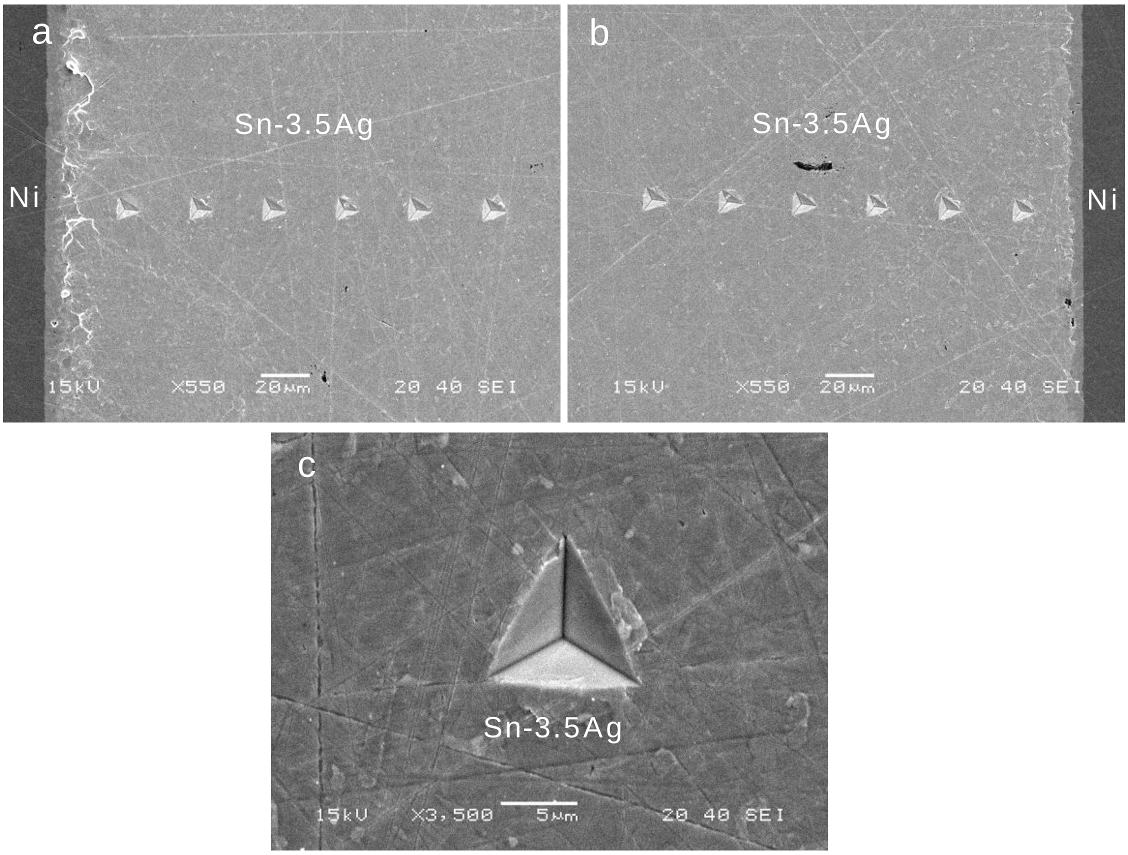

Fig. 7.17. SEM images showing nano-indentation marks in the Ni/Sn-3.5Ag sample aged at 160 °C for 100 h with 2×10^3 A/cm^2 current density: (a) Anode side, (b) cathode side, and (c) magnified view of a single mark.

7.3.5. Microstructural Analysis

Microstructural analysis of all three types of samples was carried out to analyse the formation of IMC and to understand the evolution of microstructure.

Electroless Ni-P/Sn-3.5Ag Samples

Fig. 7.18 shows the cross-sectional SEM images of the electroless Ni-P/Sn-3.5Ag interfaces of the sample aged at 160 °C for 100 h without current. It can be observed that mainly Ni_3Sn_4 and Ni_3P compounds grew during aging. The interface between Ni_3Sn_4 IMC and Sn-3.5Ag solder was very uneven. In the electrically stressed sample also, as shown in Fig. 7.19, mainly two compounds, Ni_3Sn_4 and Ni_3P, grew and the Ni_3Sn_4/Sn-3.5Ag interface was very rough. No significant difference was observed in the thickness of Ni_3Sn_4 grown at the anode side and cathode side Ni-P/Sn-3.5Ag interfaces (Fig. 7.19).

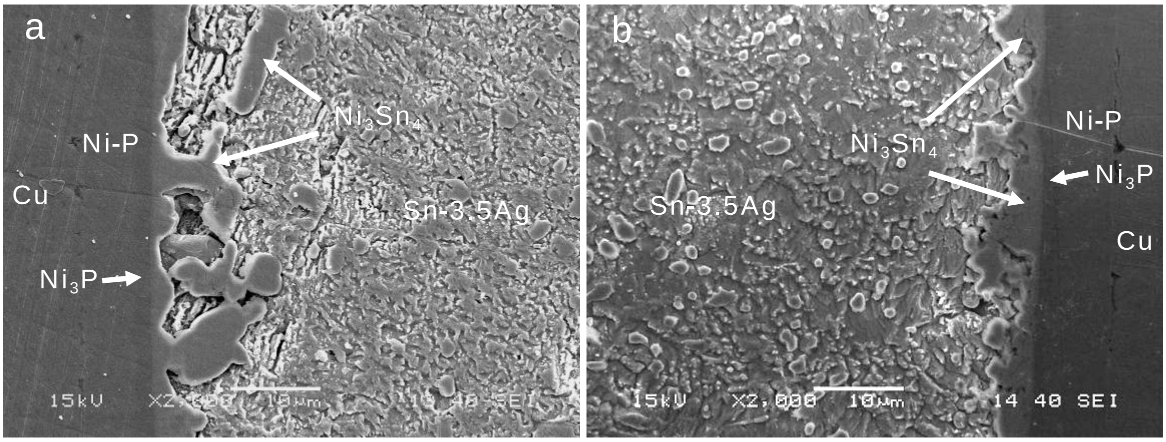
a
Ni-P
Cu
Ni3P
Ni3Sn4
Sn-3.5Ag
15kV X2,000 10μm 14 40 SEI
b
Ni3Sn4
Sn-3.5Ag
Ni-P
Ni3P
Cu
15kV X2,000 10μm 14 40 SEI

Fig. 7.18. Cross-sectional SEM images of electroless Ni-P/Sn-3.5Ag interfaces of the sample aged at 160 °C for 100 h without current.

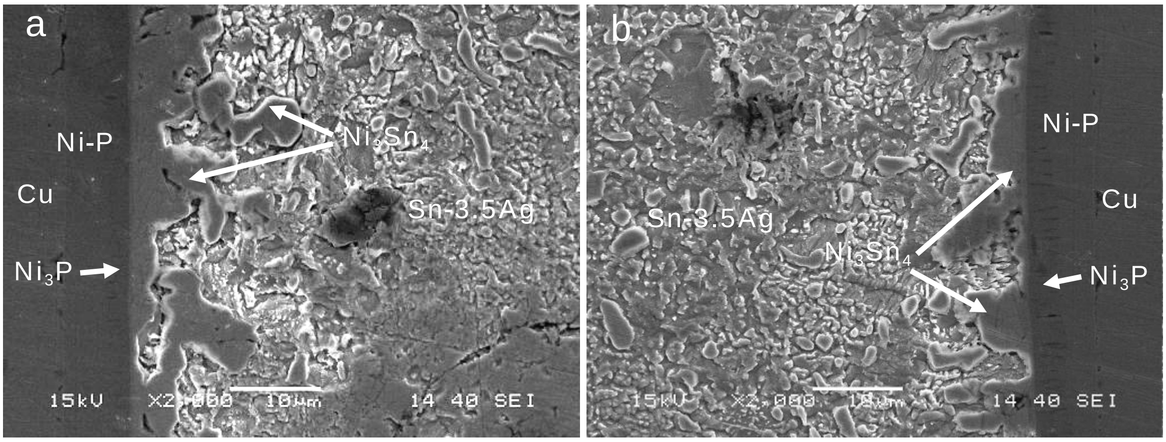
a
Ni-P
Cu
Ni3P
Ni3Sn4
Sn-3.5Ag
15kV X2,000 10μm 14 40 SEI
b
Ni-P
Cu
Sn-3.5Ag
Ni3Sn4
Ni3P
15kV X2,000 10μm 14 40 SEI

Fig. 7.19. Cross-sectional SEM images of electroless Ni-P/Sn-3.5Ag interfaces of the sample aged at 160°C for 100 h with 2 × 10^3 A/cm^2 current density: (a) anode side and (b) cathode side.

Pure Ni/Sn-3.5Ag Samples

In the case of Ni/Sn-3.5Ag samples, mainly one compound, Ni_3Sn_4, grew during thermal aging without and with electric current as shown in Figs. 7.20 and 7.21, respectively. As compared to the electroless Ni-P/Sn-3.5Ag samples, the Ni_3Sn_4/Sn-3.5Ag interface was very smooth in these samples. Another difference observed was the higher thickness of Ni_3Sn_4 IMC grown at the anode side Ni/Sn-3.5Ag interface than that of Ni_3Sn_4 IMC grown at the cathode side interface of the samples aged with electric current (Fig. 7.21).

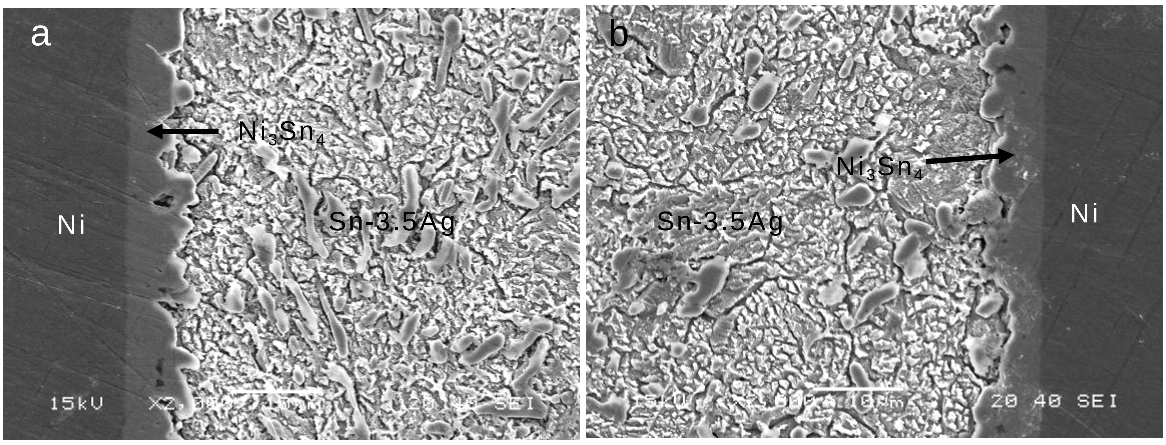

Fig. 7.20. Cross-sectional SEM images of Ni/Sn-3.5Ag interfaces of the sample aged at 160 °C for 100 h without current.

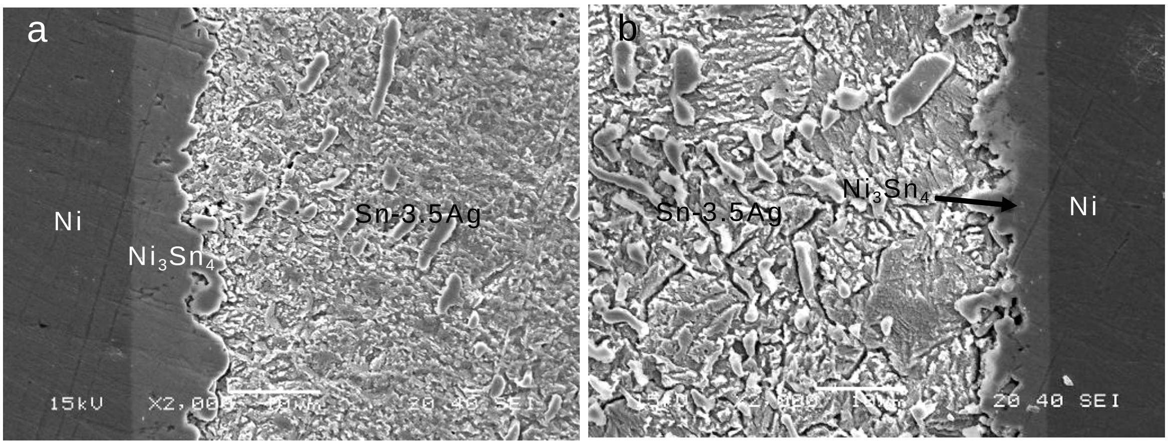

Fig. 7.21. Cross-sectional SEM images of Ni/Sn-3.5Ag interfaces of the sample aged at 160°C for 100 h with 2 × 10^3 A/cm^2 current density: (a) anode side and (b) cathode side.

Electroless Ni-P/Sn-37Pb Samples

Similar to the electroless Ni-P/Sn-3.5Ag samples, in electroless Ni-P/Sn-37Pb samples also, mainly two compounds, Ni_3Sn_4 and Ni_3P, grew during thermal aging without and with electric current as shown in Figs. 7.22 and 7.23, respectively. However, in these samples, the Ni_3Sn_4/solder interface was relatively even, which can be understood to be due to the relatively low growth of Ni_3Sn_4 IMC. Similar to the electrically stressed Ni-P/Sn-3.5Ag samples, no big difference was observed in the thickness of Ni_3Sn_4 IMC grown at the anode and cathode side Ni-P/Sn-37Pb interfaces of electrically-stressed samples (Fig. 7.23).

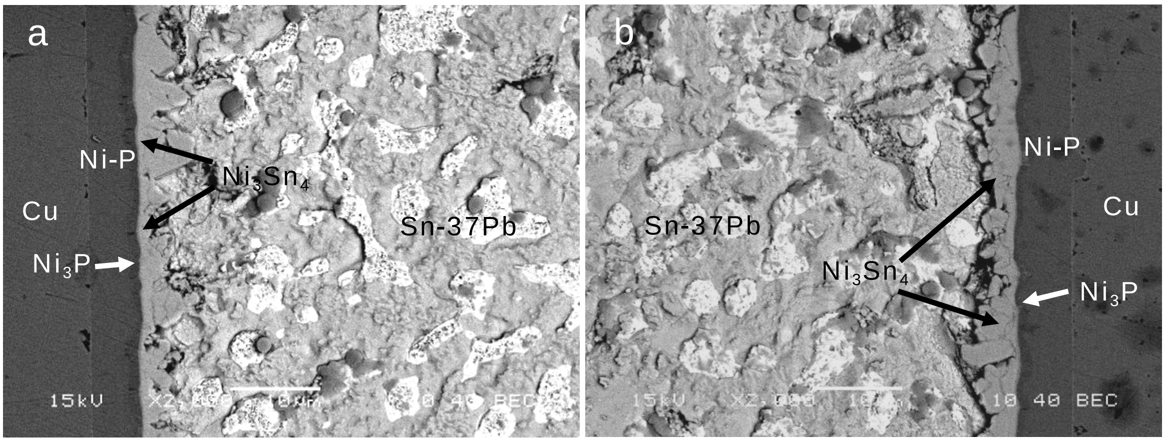

Fig. 7.22. Cross-sectional SEM images of electroless Ni-P/Sn-37Pb interfaces of the sample aged at 160 °C for 100 h without current.

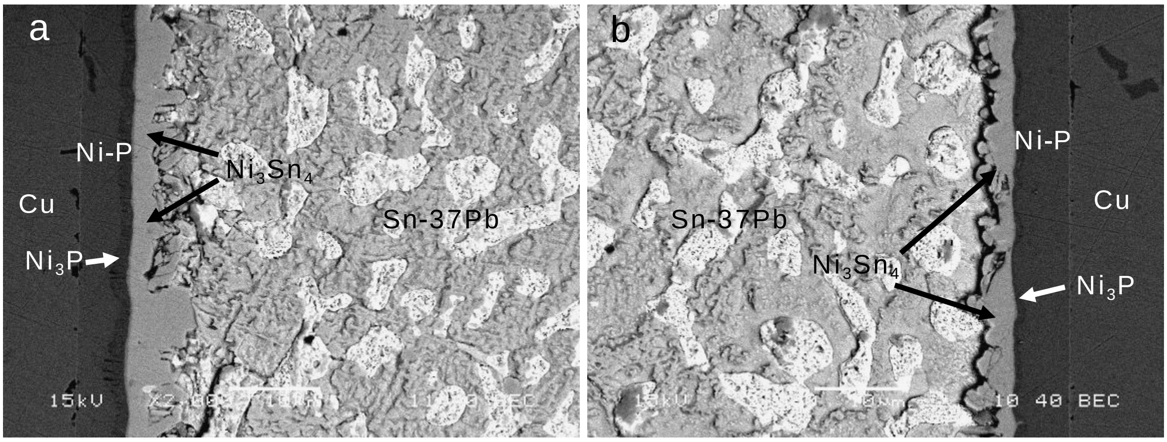

Fig. 7.23. Cross-sectional SEM images of electroless Ni-P/Sn-37Pb interfaces of the sample aged at 160°C for 100 h with 2×10^3 A/cm^2 current density: (a) anode side and (b) cathode side.

Fig. 7.24 shows the SEM images of the microstructure of Sn-37Pb solder in the samples aged at 160 °C for 100 h with different current densities. From the figure, it is clear that grain coarsening takes place in the Sn-37Pb solder due to the electric current and it increases with the increase in current density. The grain coarsening in Sn-Pb solder owing to the electric current has been also observed in previous electrical studies (Chen *et al.*, 2006; Ye *et al.*, 2004). In a material, grain coarsening takes place during thermal aging due to the diffusion of atoms across the grain boundaries. During grain coarsening, the larger grain grows at the expense of the smaller one and the reduction of surface energy acts as a driving force for atomic diffusion (Lifshitz and Slyozov, 1961). Thus, in the presence of high electric current, fast grain growth is expected to be due to the extensive diffusion of atoms owing to the additional electromigration force.

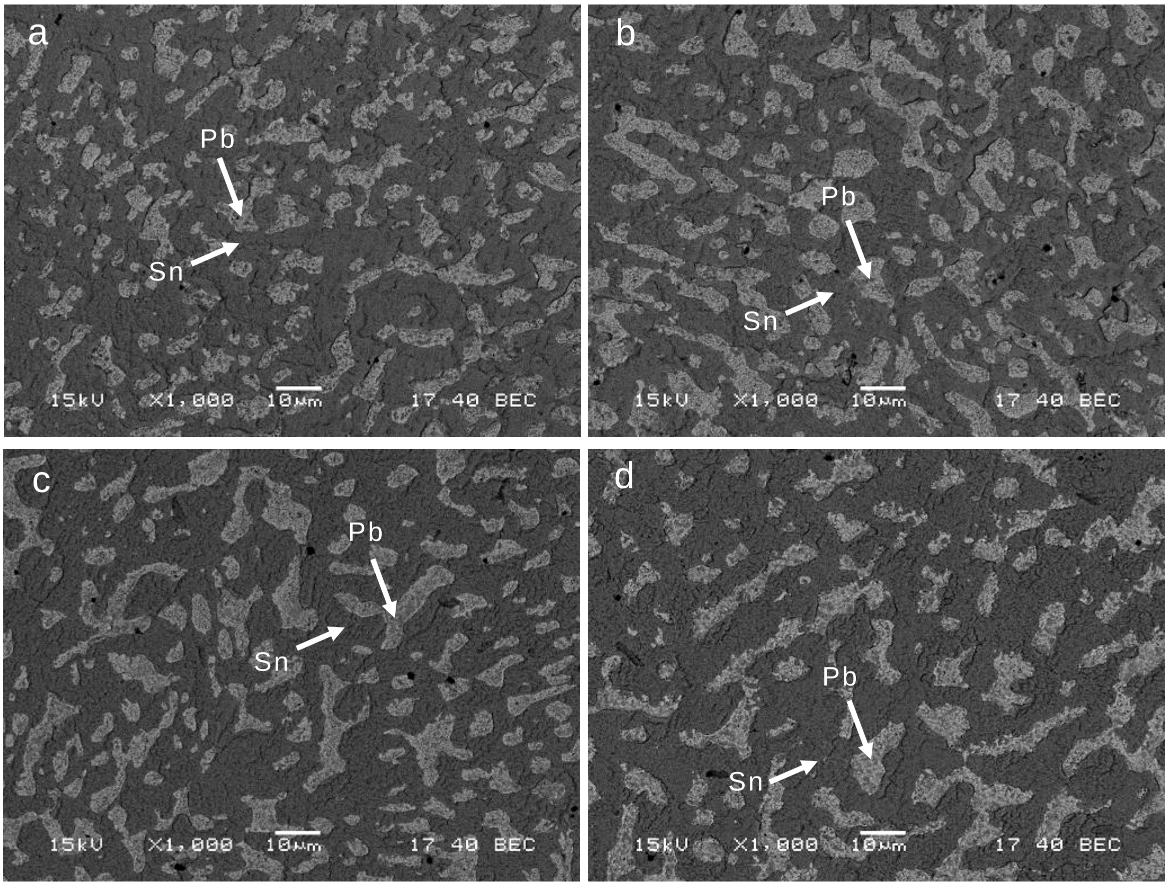
a
Pb
Sn
15kV X1,000 10μm 17 40 BEC
b
Pb
Sn
15kV X1,000 10μm 17 40 BEC
c
Pb
Sn
15kV X1,000 10μm 17 40 BEC
d
Pb
Sn
15kV X1,000 10μm 17 40 BEC

Fig. 7.24. Microstructure of Sn-37Pb solder in the samples aged at 160 °C for 100 h with (a) 0 A/cm^2, (b) 1 × 10^3 A/cm^2, (c) 2 × 10^3 A/cm^2, and (d) 3 × 10^3 A/cm^2 current densities, showing Pb and Sn grains coarsening.

7.3.6. Growth of Ni_3Sn_4 IMC

Fig. 7.25 shows the thickness of Ni_3Sn_4 IMC in the samples aged at 160 °C for 100 h, as a function of current density. In the samples aged with current, thickness was measured at both the anode side interface (where the flow of electrons was from solder to metallization) and the cathode side interface (where the flow was from metallization to solder). In the samples aged without current, Ni_3Sn_4 thicknesses at both the interfaces were nearly the same; therefore only the average value is reported. From Fig. 7.25, it is apparent that electric current influenced Ni_3Sn_4 growth significantly in the case of Ni metallization (Fig. 7.25b), whereas its effect was relatively negligible in the case of electroless Ni-P metallization (Fig. 7.25a and c). In the case of Ni metallization, the thickness of Ni_3Sn_4 IMC that formed at the anode side Ni/Sn-3.5Ag interface increased with an increase in current density, whereas the thickness of Ni_3Sn_4 IMC that formed at the cathode side Ni/Sn-3.5Ag interface decreased slightly with current density (Fig. 7.25b). On the other hand, in the case of electroless Ni-P metallization, no big difference was observed in the thickness of Ni_3Sn_4 IMC grown at the anode and cathode side electroless Ni-P/solder interfaces with an increase in current density (Fig. 7.25a and c).

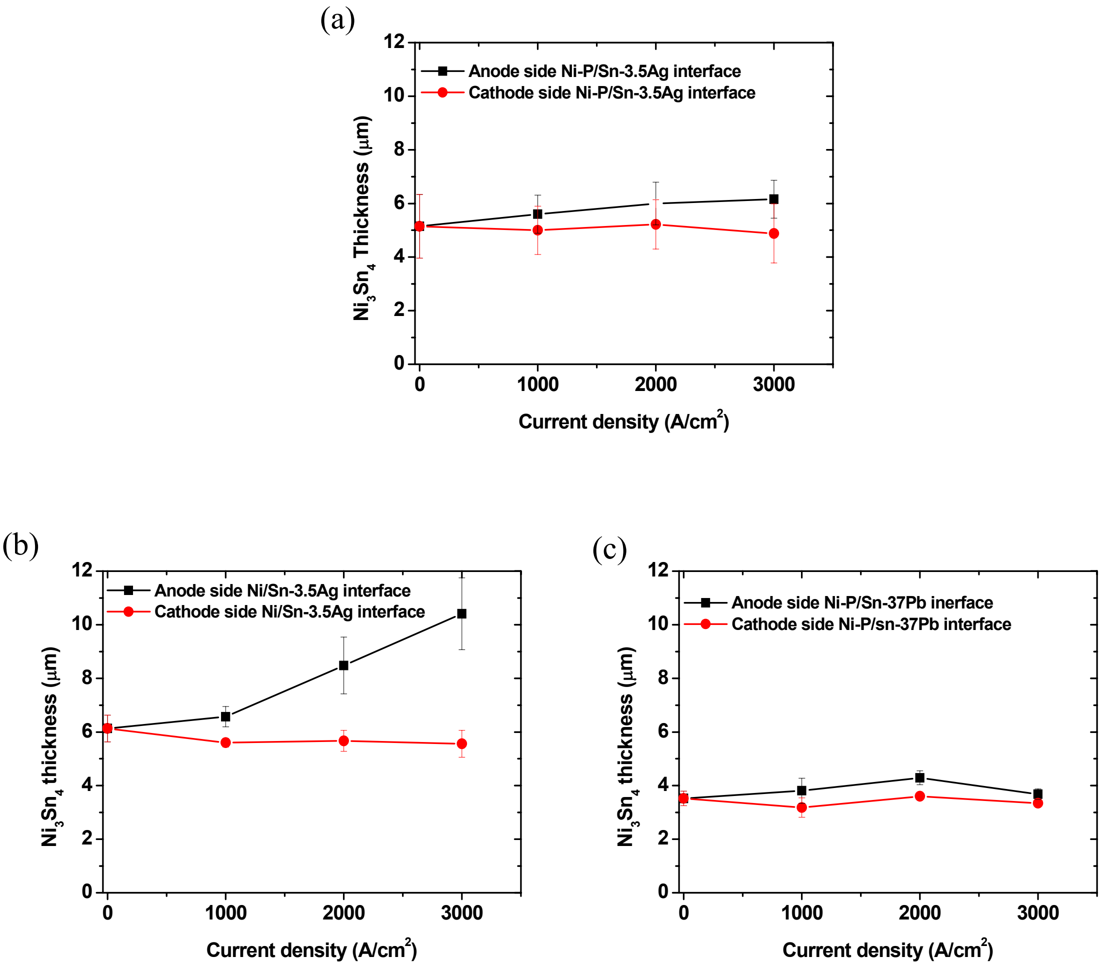

Fig. 7.25. Thickness of Ni_3Sn_4 IMC in the (a) electroless Ni-P/Sn-3.5Ag, (b) Ni/Sn-3.5Ag, and (c) electroless Ni-P/Sn-37Pb samples aged at 160 °C for 100 h, as a function of current density.

7.4. Discussion

7.4.1. Electromigration-Induced Brittle Failure of Solder Joints

In this study, it was observed that electric current causes the brittle failure of UBM/solder joints. Electric current was also observed to increase the mechanical properties such as hardness and modulus of bulk solder in the solder joints (Table. 7.1). These observations imply that electrical current increases the mechanical strength of solder and thus causes the failure to occur at the brittle solder/IMC and/or in the IMC layers rather than inside the ductile solder. Though electric current-induced brittle failure occurred in all three types of UBM/solder joints, its occurrence varied significantly with the type of UBM/solder joint. For example, among all the three types of solder joints, electroless Ni-P/Sn-3.5Ag solder joint mechanically performed best, whereas the mechanical performance of Ni/Sn-3.5Ag solder joint was the worst (Fig. 7.5). Similarly, a polarity effect of electric current was observed on the brittle failure of electroless Ni-P/Sn-37Pb solder joint (Fig. 7.16); however, no polarity effect was observed in the electroless Ni-P/Sn-3.5Ag solder joints (Fig. 7.9). All these findings suggest that UBM and solder materials themselves play an important role in determining the effect of electric current on the brittle failure of UBM/solder joint and hence their role has been discussed here in detail.

Effect of Solder on the Electromigration-Induced Brittle Failure

In this work, two types of solders, lead-free Sn-3.5Ag and eutectic lead Sn-37Pb were investigated with the same electroless Ni-P metallization. It was found that the effect of electric current is more detrimental on the mechanical properties of Sn-37Pb solder joint than that of Sn-3.5Ag solder joint (Fig. 7.5). While in the case of both solders, electric current-induced brittle fracture occurred at the solder/Ni_3Sn_4 interface, fracture energy decreased more severely with current density in the case of Sn-37Pb. In addition, a clear polarity effect of electric current was observed on the brittle failure of Sn-37Pb solder joint.

These observations indicate that electric current effect was more prominent in Sn-37Pb solder than that in Sn-3.5Ag. The larger effect of electric current in eutectic lead solder than that in lead-free solder was further confirmed from the previous electromigration study in eutectic Sn-Pb and Sn-3.8Ag-0.7Cu solders (Lee *et al.*, 2001a). It was reported that the atomic flux driven by electromigration in eutectic Sn-Pb is much faster (around 10 times faster) than that in Sn-3.8Ag-0.7Cu due to the lower melting temperature of eutectic Sn-Pb (183 °C) than that of Sn-3.8Ag-0.7Cu (220 °C). As solders used in the present study have nearly the same compositions and melting temperatures, Sn-37Pb (183 °C) and Sn-3.5Ag (221 °C), the same difference of electromigration effect can be expected in these solders. Thus in the case of Sn-37Pb, large electromigration-induced atomic flux from cathode to anode caused the large accumulation of vacancies at the cathode side Sn-37Pb/Ni_3Sn_4 interface, making this interface more prone to failure. As electromigration effect on the atomic flux in Sn-3.5Ag solder was not so prominent, no such failure was observed.

Effect of Metallization on the Electromigration-Induced Brittle Failure

Two types of metallizations, pure Ni and electroless Ni-P, with the same Sn-3.5Ag solder were investigated in this work. Although in these solder joints, no polarity effect of electromigration was observed, but electromigration-induced brittle failure was most prominent in the case of pure Ni/Sn-3.5Ag solder joint (Fig. 7.5). The absence of polarity effect is understood to be due to the low electromigration effect on the atomic flux in Sn-3.5Ag solder, however the brittle failure of these joint has to be understood.

The mechanical strength of a solder joint is determined not only by the cohesive strength of solder alloy but also by the adhesive strength of interfacial layers. If the adhesion between interfacial layers is sufficiently high, fracture occurs inside the ductile solder. Whilst in the opposite case, fracture occurs at the brittle solder/IMC interface and/or in the brittle IMC layers. Accordingly, in this investigation, fracture at the brittle Sn-3.5Ag/Ni_3Sn_4

interface and/or in the brittle Ni-Sn IMCs was observed in some of the electrically-stressed Ni-P/Sn-3.5Ag samples and in most of the electrically-stressed Ni/Sn-3.5Ag samples due to the increase in cohesive strength of Sn-3.5Ag solder (see Table 7.1). A large occurrence of brittle-interfacial fracture in the Ni samples as compared to the electroless Ni-P samples indicates that the interfacial strength of Ni/Sn-3.5Ag solder joint was much lower than that of Ni-P/Sn-3.5Ag. Moreover, the fracture and microstructure analyses of these solder joints revealed the presence of smooth Ni_3Sn_4/solder interface (Fig. 7.21) and a large number of small Ni-Sn IMC grains (Fig. 7.14) in the Ni/Sn-3.5Ag solder joints. Since smooth Ni_3Sn_4/solder interface and fine IMC grains imply low mechanical interlocking and less atomic bonding, the low interfacial strength of Ni/Sn-3.5Ag solder joint can be understood. Thus, it can be said that in metallization/Sn-3.5Ag solder joint, Ni metallization assists the electromigration-induced brittle failure by forming a weak Ni/Sn-3.5Ag interface. On the other hand, rough Ni_3Sn_4/Sn-3.5Ag interface formed in the case of electroless Ni-P metallization hinders the electromigration-induced brittle failure of electroless Ni-P/Sn-3.5Ag solder joint.

7.4.2. Effect of Electromigration on Ni_3Sn_4 Growth

In several studies (Bertolino *et al.*, 2001; Chen and Chen, 2001; Chen *et al.*, 1998; Chen and Chen, 2003; Gan and Tu, 2005; Liu *et al.*, 1998; Vanhecke *et al.*, 1993), electromigration has been reported to influence the interfacial reactions in various metallic systems in terms of phase formation and/or growth of IMCs. In this work also, electromigration was found to influence the Ni_3Sn_4 growth in the Ni/Sn-3.5Ag samples (Fig. 7.25b); however, such an electromigration effect was relatively negligible in the Ni-P/solder samples (Fig. 7.25a and c). Moreover, no electromigration effect was observed on the phase formation of interfacial compound as in all the three types of UBM/solder systems, the same compound(s) formed during aging with or without an electric current.

Effect of Metallization on the Electromigration-Induced Ni_3Sn_4 Growth

The growth of IMC in a UBM/solder joint depends upon the direction of atomic fluxes at the reaction interface. If atomic fluxes flowing toward the reaction interface are larger than the fluxes flowing outward, then IMC grows; otherwise, it shrinks. As electromigration influences the atomic flux of species in heterogeneous materials system (Bertolino *et al.*, 2001; Chen and Chen, 2001; Chen *et al.*, 1998; Gan and Tu, 2005; Liu *et al.*, 1998), in most of the systems, electromigration increases the atomic flux of species when electrons flow in the direction of species diffusion driven by concentration gradient, whereas it reduces the atomic flux of species when electrons flow in the opposite direction. In this study, it was observed that in the Ni/Sn-3.5Ag system, electromigration increases the Ni_3Sn_4 growth at the anode side interface with the increase in current density, whereas it suppresses the Ni_3Sn_4 growth at the cathode side interface (Fig. 7.25b). A similar electromigration effect on the growth of Ni_3Sn_4 IMC in the Ni/Sn-3.5Ag system during aging at different temperatures and durations was observed by Chen and Chen (2001). They found that electromigration influences the Sn flux through the Ni_3Sn_4, whereas it does not have significant effect on the Ni flux through the Ni_3Sn_4. Thus, as shown in Fig. 7.26a, in the Ni/solder system, electromigration enhances the Ni_3Sn_4 growth at the anode side interface (where electrons flow from solder to Ni) by increasing the influx of Sn, whereas it suppresses the Ni_3Sn_4 growth at the cathode side interface (where electrons flow from Ni to solder) by reducing the influx of Sn.

On the other hand, in the electroless Ni-P/solder system, as mentioned in the previous chapters, Ni_3Sn_4 grows at the Ni-Sn-P/Ni_3Sn_4 interface, for which Ni comes from the electroless Ni-P layer through the Ni_3P and Ni-Sn-P layers and Sn comes from the solder through the Ni_3Sn_4 layer. The presence of Ni_3P and Ni-Sn-P layers in between the electroless Ni-P and Ni_3Sn_4 layers plays an important role in defining the electromigration effect in the electroless Ni-P/solder system. Fig. 7.26b illustrates the electromigration effect on Ni_3Sn_4 growth in the electroless Ni-P/solder system. During the passage of electron current through the Ni-P/solder/Ni-P sample, at the anode side interface (where electrons flow from solder to Ni-P), electromigration enhances the Sn flux through the Ni_3Sn_4 but retards the Ni flux through the Ni_3P, whereas at the cathode side interface (where electrons flow from solder to Ni-P), it retards the Sn flux but enhances the Ni flux. As a result, the net effect of electromigration on Ni_3Sn_4 growth in the Ni-P/solder system remains negligible.

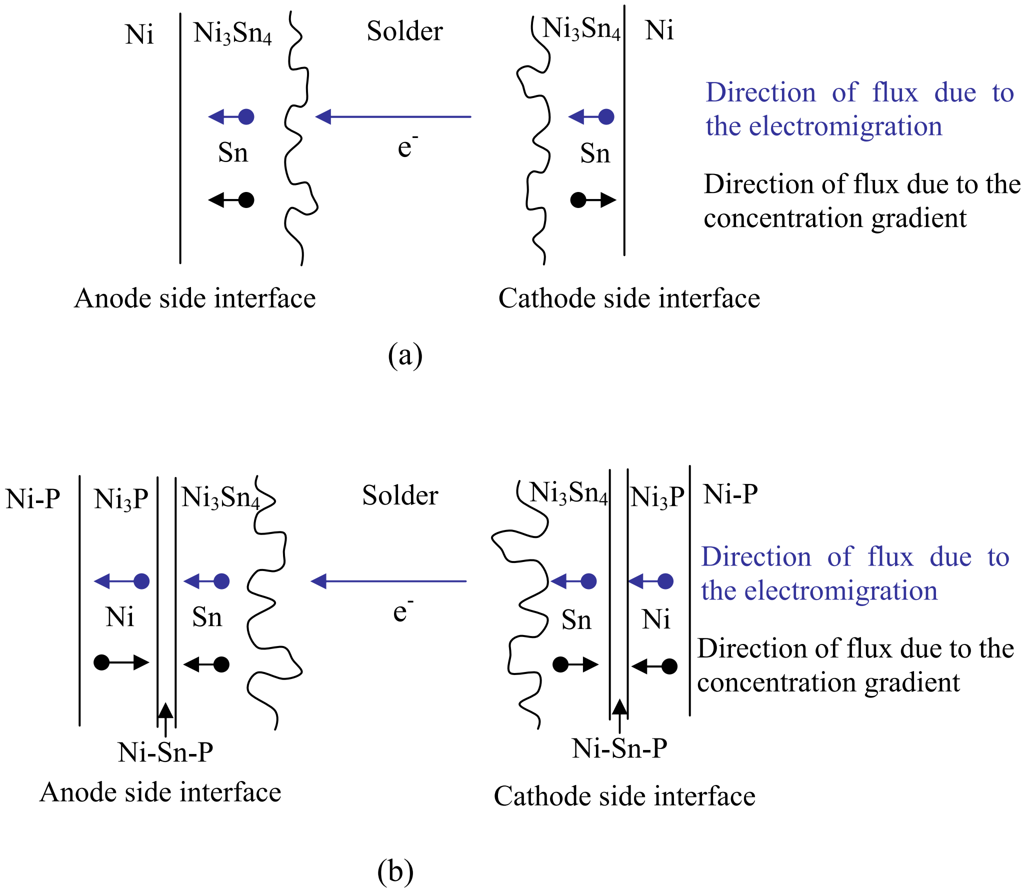
Ni
Ni3Sn4
Solder
Ni3Sn4
Ni
Direction of flux due to the electromigration
Sn
e-
Sn
Direction of flux due to the concentration gradient
Anode side interface
Cathode side interface
(a)
Ni-P
Ni3P
Ni3Sn4
Solder
Ni3Sn4
Ni3P
Ni-P
Direction of flux due to the electromigration
Ni
Sn
e-
Sn
Ni
Direction of flux due to the concentration gradient
Ni-Sn-P
Anode side interface
Ni-Sn-P
Cathode side interface
(b)

Fig. 7.26. Schematic illustration for electromigration effect on the growth of Ni_3Sn_4 IMC in (a) Ni/solder and (b) electroless Ni-P/solder systems.

7.5. Conclusions

In this study, the effect of electromigration on the interfacial microstructure and mechanical properties of three UBM/solder joint, Ni-P/Sn-3.5Ag, Ni/Sn-3.5Ag, and Ni-P/Sn-37Pb was investigated. The following conclusions can be drawn from this study:

1. Electromigration causes the brittle failure of solder joint and the tendency of brittle failure increases with an increase in current density. Electromigration causes the fracture to occur at the brittle solder/IMC interface and/or in the brittle IMCs rather than inside the ductile solder.
2. A higher cohesive strength of metallization/solder interface results in a better performance of solder joint against electromigration-induced brittle failure. The electroless Ni-P/Sn-3.5Ag solder joint performed best among all investigated solder joints due to the high cohesive strength of the electroless Ni-P/Sn-3.5Ag interface.
3. A lower melting temperature of solder results in a larger tendency of electromigration-induced brittle failure. A clear polarity effect of electric current on the electromigration-induced brittle failure of electroless Ni-P/Sn-37Pb solder joint was observed due to the low melting temperature of Sn-37Pb solder. A significant grain coarsening in Sn-37Pb solder also takes place due to electromigration and that increases with the increase in current density.
4. Electromigration influences the IMC growth depending on the metallization. In the case of pure Ni metallization, Ni_3Sn_4 IMC grows thicker at the anode side Ni/Sn-3.5Ag interface (where electrons flow from solder to Ni) as compared to the cathode side Ni/Sn-3.5Ag interface (where electrons flow from Ni to solder).
5. In the case of electroless Ni-P metallization, electromigration does not appear to have significant effect on Ni_3Sn_4 growth. In the current density range investigated in this study, this behavior of electromigration in electroless Ni-P/solder joint is understood to be due to the presence of the Ni_3P layer in between the electroless Ni-P and Ni_3Sn_4 layers.

Chapter 8

Conclusions and Recommendations

8.1. Conclusions

The main objective of this work was to study the effects of interfacial reactions and electromigration on the mechanical behavior of Cu/electroless Ni-P/Sn-3.5Ag solder joint. For a complete understanding, several process and material parameters, such as aging temperature, aging duration, Ni-P thickness, P concentration of Ni-P, and current density were varied systematically and their effect was studied on the solder joint strength. From this work, the following conclusions can be drawn:

The Cu/electroless Ni-P/Sn-3.5Ag interfacial reactions results in the formation of multiple interfacial compounds, such as Ni_3Sn_4, Ni_2SnP, Ni_3P, Cu_6Sn_5, Cu_3Sn, $(Ni_{1-x}Cu_x)_6Sn_5$, and $(Ni_{1-x}Cu_x)_6Sn_5$, and a number of Kirkendall voids in the Ni_3P layer and at the Ni_3P/Cu interface. The extensive growths of Ni_3Sn_4 IMC at the Ni_3Sn_4/solder interface and Kirkendall voids at the Ni_3P/Cu interface degrade the solder joint strength. The extensive growth of Ni_3Sn_4 IMC decreases the solder joint strength from ~ 45 MPa to ~ 28 MPa and changes the fracture mode from ductile to mixed (macroscopically brittle, but microscopically ductile). The mechanical properties of the solder joint further degrade due to the growth of Kirkendall voids at the Ni_3P/Cu interface, which decreases the solder joint strength to ~ 12 MPa and causes a brittle fracture at Ni_3P/Cu interface.

The mechanical properties of Cu/electroless Ni-P/Sn-3.5Ag solder can be improved by increasing the thickness of electroless Ni-P layer. A thick layer of electroless Ni-P delays the complete transformation of electroless Ni-P into the Ni_3P layer and thereby hinders the brittle failure of solder joint by hindering the growth of Kirkendall voids at the Ni_3P/Cu interface. The P concentration of electroless Ni-P layer also influences the mechanical properties of Cu/electroless Ni-P/Sn-3.5Ag solder joint. The lower P concentration of Ni-P layer results in the lesser spallation of Ni_3Sn_4 into molten solder and thereby in slower growth of voids and Ni-Cu-Sn and Cu-Sn IMCs. Due to the slow growth of voids and IMCs, the lowest P samples exhibit the highest joint strength.

Electromigration causes the brittle failure of solder joint and the tendency of brittle failure increases with increasing current density. In the case of high current density, fracture occurs at the brittle solder/IMC interface rather than inside the ductile solder. This effect of electromigration depends upon the microstructure and the physical properties of UBM/solder joint. Against electromigration-induced brittle failure, the Ni-P/Sn-3.5Ag solder joint performs best among the Ni-P/Sn-3.5Ag, Ni/Sn-3.5Ag, and Ni-P/Sn-37Pb solder joints due to high Ni-P/Sn-3.5Ag interfacial strength and high melting temperature of Sn-3.5Ag solder. Electromigration also influences the growth of Ni_3Sn_4 IMC, depending on the metallization. In the case of pure Ni metallization, thicker Ni_3Sn_4 forms at the anode side Ni/Sn-3.5Ag interface as compared to the cathode side Ni/Sn-3.5Ag interface. However, in the case of electroless Ni-P metallization, electromigration does not have significant effect on the Ni_3Sn_4 growth due to the presence of the Ni_3P layer in between electroless Ni-P and Ni_3Sn_4 layers.

This work has clearly shown that the thickness and the P concentration of Ni-P layer play an important role in determining the mechanical reliability of Cu/electroless Ni-P/Sn-3.5Ag solder joint. A thicker electroless Ni-P metallization with a lower P concentration is needed to achieve good mechanical reliability of the solder joint. Considering the thermal aging (160 °C for 1000 h) and multiple reflows requirements of advanced packages, the usage of ~ 10 μm thick Ni-P metallization with ~ 12 at.% P concentration is proposed to achieve reliable electroless Ni-P/solder joint. Moreover, as shown in this study, the amount of current density that would pass through the solder joint has to be taken in account for the mechanical reliability of the solder joint. The amount of current density should not be more than 1×10^3 A/cm^2, otherwise it can cause the brittle failure of solder joint much earlier than the formation of electromigration-induced voids and hillocks. The amount of current density can be easily controlled by changing the metallization pad and solder ball sizes.

8.2. Recommendations for Future Work

Based on the understanding of present work, the following work is recommended for further studies:

The present work has shown that the concentration of P in electroless Ni-P plays an important role in determining the mechanical reliability of electroless Ni-P/solder joint and a low P concentration is desirable for a reliable solder joint. Recently, a few researchers (Balaraju and Rajam, 2005; Bangwei and Haowen, 2000; Yu *et al.*, 2001) developed a number of ternary electroless Ni-P-X (Cu, W, Sn, Mo, Co) alloys and reported that the addition of a third element reduces the P concentration of electroless Ni-P-X layer. Thus, the interfacial and mechanical studies of these electroless alloys with lead-free solders should be carried out to produce the next generation UBM which would be more reliable and economical.

The growth of Kirkendall voids at the Ni_3P/Cu interface has been found to be very detrimental for the reliability of Cu/electroless Ni-P/solder joint. Thus, an effort should be made to determine the growth kinetics of these voids. This can be determined by choosing the appropriate experimental conditions, such as Ni-P thickness, aging temperature, and aging duration.

In the present work, it has been found that the effect of electromigration on the mechanical properties of solder joint depends not only on current density but also on UBM/solder system. Though in the present study we have studied three UBM/solder systems, more work should be done using other promising solders such as Sn-Cu and Sn-Ag-Cu and UBMs such as electrolytic Ni and Ni-V.

References

Ahat, S., Du, L., Sheng, M., Luo, L., Kempe, W., and Freytag, J. (2000). Effect of aging on the microstructure and shear strength of SnPbAg/Ni-P/Cu and SnAg/Ni-P/Cu solder Joints. *J. Electron. Mater.*, 29, 1105-1109.

Ahat, S., Sheng, M., and Luo, L. (2001). Effects of static thermal aging and thermal cycling on the microstructure and shear strength of $Sn_{95.5}Ag_{3.8}Cu_{0.7}$ solder joints. *J. Mater. Res.*, 16, 2914-2921.

Alam, M. O., Chan, Y. C., and Tu, K. N. (2003). Effect of reaction time and P content on mechanical strength of the interface formed between eutectic Sn-Ag solder and Au/electroless Ni(P)/Cu bond pad. *J. Appl. Phys.*, 94, 4108-4115.

ASM International Handbook Committee (1994). *Surface Engineering.* Materials Park, OH: ASM International, vol.5, pp. 295.

Balaraju, J.N., and Rajam, K.S. (2005). Electroless deposition of Ni–Cu–P, Ni–W–P and Ni–W–Cu–P alloys. *Surface and Coatings Technology*, 195, 154-161.

Bangwei, Z., and Haowen, X. (2000). Effect of alloying elements on the amorphous formation and corrosion resistance of electroless Ni–P based alloys. *Materials Science and Engineering A*, 281, 286–291.

Bertolino, N., Garay, J., Tamburini, U. A., and Munir, Z. A. (2001). Electromigration Effect in Al-Au multilayers. *Scripta Materialia,* 44, 737-742.

Binnewies, M., and Mike, E. (2002). *Thermochemical Data of Elements and Compounds*, 2nd Edition, Wiley-VCH, Weinheim.

Bleach, I. A. (1976). Electromigration in thin aluminum films on titanium nitride. *J. Appl. Phys.*, 47, 1203-1208.

Blech, I. A., and Herring, C. (1976). Stress generation by electromigration. *Appl. Phys. Lett.*, 29, 131-133.

Blech, I. A., and Sello, H. (1966). Physics of Failures in Electronics 5. *USAF-RADC Series*, pp. 496.

Brandenburg, S., and Yeh, S. (1998). Electromigration studies of flip chip bump solder joints. In: *Proceedings of Surface Mount International Conference and Exposition*, 337-342.

Braunovic, M., and Alexandrov, N. (1994). Intermetallic Compounds at Aluminum-to-Copper Electrical Interfaces: Effect of Temperature and Electric Current. *IEEE Trans. Comp. Packag. Manufact. Technol. Part A*, 17, 78-85.

Bruinsma, N.A. (2001). Lead-free soldering-legislative issues: The road towards lead-free soldering, Eindhoven.

Campbell, D. R., and Huntington, H. B. (1969). Thermomigration and Electromigration in Zirconium. *Phys. Rev.*, 179, 601-612.

Chan, Y.C., Fan, S.H., and Lai, J.K.L. (2003). The effect of cooling rate on the growth of Cu-Sn intermetallics in annealed PBGA solder joints. *Journal of Electronic Packaging*, 125, 153-156.

Chandler, J.H. (1981) *Practical Methods in Electron Microscopy: X-Ray Microanalysis in the Electron Microscope*, Edited by Glauert, A.M., First edition, North-Holland, Amsterdam, 472-475.

Chen, C. M., and Chen, S. W. (2001). Electromigration effect upon the Sn-0.7 wt% Cu/Ni and Sn-3.5 wt% Ag/Ni interfacial reactions. *J. Appl. Phys.*, 90, 1208-1214.

Chen, C. M., and Chen, S. W. (1999) Electric Current Effects on Sn/Ag Interfacial Reactions. *J. Electron. Mater.*, 28, 902-906.

Chen, C. M., and Chen, S.W. (2002). Electromigration effect upon the Sn/Ag and Sn/Ni interfacial reactions at various temperatures. *Acta Materialia*, 50, 2461-2469.

Chen, C. M., and Chen, S. W. (2003). Electromigration effects upon the low-temperature Sn/Ni interfacial reactions. *J. Mater. Res.*, 18, 1293-1296.

Chen, S.-W., Chen, C.-M, and Liu, W. C. (1998). Electric Current Effects Upon the Sn/Cu and Sn/Ni Interfacial Reactions. *J. Electron. Mater.*, 27, 1193-1199.

Chen, Z., He, M., and Qi, G.J. (2004). Morphology and Kinetic Study of the Interfacial Reaction between Sn-3.5Ag Solder and Electroless Ni-P Metallization. *J. Electron. Mater.*, 33, 1465-1472.

Chen, K.M., Wu, J.D., and Chiang, K.N. (2006, in press). Effect of pre-bump probing and bumping processes on eutectic solder bump electromigration. *Microelectronics Reliability*.

Choi, W.K.**,** and Lee, H.M. (1999). Effect of Ni layer thickness and soldering time on intermetallic compound formation at the interface between molten Sn-3.5Ag and Ni/Cu substrate. *Journal of Electronic Materials*, 28, 1251-1255.

Chonan, Y., Komiyama, T., Onuki, J., Urao, R., Kimura, T., and Nagano, T. (2002a). Influence of phosphorus concentration in electroless plated Ni-P alloy film on interfacial structures and strength between Sn-Ag-(-Cu) solder and plated Ni-P alloy film. *Materials Transactions*, 43, 1840-1846.

Chonan, Y., Komiyama, T., Onuki, J., Urao, R., Kimura, T., and Nagano, T. (2002b). Influence of P content in electroless plated Ni-P alloy film on interfacial structures and strength between Sn-Zn solder and plated Au/Ni-P alloy film. *Materials Transactions*, 43, 1887-1890.

Christon, A. (1994). *Electromigration and electronic device degradation*. New York: John Wiley Sonc Inc., Chapter-9, pp. 259.

Conrad, H. (2000). Effect of electric current on solid state phase transformations in metals. *Mater. Sc. Eng. A*, 287, 227-237.

Durkan, C., Schneider, M. A., and Welland, M. E. (1999). Analysis of failure mechanisms in electrically stresses Au nanowires. *J. Appl. Phys.*, 86, 1280-1286.

Fan, S.H., Chan, Y.C., Tang, C.W., and Lai, J.K.L. (2001). Effect of cooling rate on the isothermal fatigue behavior of CBGA solder joints in shear. *IEEE Transactions on Advanced Packaging*, 24, 10-16.

Frear, D.R., Burchett, S.N., Morgan, H.S., and Lau, J.H. (1994). *The Mechanics of Solder Alloy Interconnects*. New York: Van Nostrand Reinhold, pp. 60.

Frear, D.R., Hosking, F.M., and Vianco, P.T. (1991). *Materials Developments in Microelectronic Packaging*. Ed: P.J. Singh, ASM International, 229-240.

Furuseth, S., and Fjellvag, H. (1985). Crystal structure and properties of Ni_2SnP. *Acta Chemica Scandinavica A*, 39, 537-544.

Gan, H., and Tu, K. N. (2005). Polarity effect of electromigration on kinetics of intermetallic compound formation in Pb-free solder V-groove samples. *J. Appl. Phys.*, 97, (063514)1-10.

Gao, F., and Takemoto, T. (2006, in press). Mechanical properties evolution of Sn-3.5Ag based lead-free solders by nanoindentation. *Materials Letters*.

Ghosh, G. (2000a). Interfacial microstructure and the kinetics of interfacial reaction in diffusion couples between Sn-Pb solder and Cu/Ni/Pd metallization. *Acta Mater.*, 48, 3719-3738.

Ghosh, G. (2000b). Coarsening kinetics of Ni_3Sn_4 scallops during interfacial reaction between liquid eutectic solders and Cu/Ni/Pd metallization. *Journal of Applied Physics*, 88, 6887-6896.

Goldstein, J.I., Romig, A.D., Newbury, D.E, Lyman, C.E., Echlin, P., Fiori, C.E., Joy, D.C., Lifshin, E. (1992). *Scanning Electron Microscopy and X-Ray Microanalysis: A Text for*

Biologists, Material Scientists, and Geologists, 2nd Edition, Plenum Press, New York, 399-401.

Golopentia, D.A., and Huntington, H. B. (1978). A study of electromigration of nickel in lead. *J. Phys. Chem. Solids*, 39, 975-984.

Goyal, D., Lane, T., Kinzie, P., Panichas, C., Chong, K.M., and Villalobos, O. (2002). Failure Mechanism of Brittle Solder Joint Fracture in the Presence of Electroless Nickel Immersion Gold (ENIG) Interface. In: *Proceedings of the 52nd Electronic Components and Technology Conference*, 732 -739.

Gupta, D., and Ho, P. S. (1988). *Diffusion phenomena in thin films and microelectronic materials*. New Jersey: Noyes Publications, Chapter-7, 369-431.

Gusak, A. M., and Tu, K. N. (2002). Kinetic theory of flux-driven ripening. *Physical Review B*, 66, 1154031-11540314.

Haseeb, A.S.M.A., Chakraborty, P., Ahmed, I., Caccavale, F., and Bertoncello, R. (1996). XRD, XPS and SIMS investigations on electrodeposited nickel-phosphorous alloy coatings. *Thin Solid Films*, 283, 140-144.

He, M., Chen, Z., and Qi, G. J. (2005). Mechanical Strength of Thermally Aged Sn-3.5Ag/Ni-P Solder Joints. *Metall. Mater. Trans. A*, 36, 65-75.

He, M., Chen, Z., and Qi, G.J. (2004a). Solid state interfacial reaction of Sn-37Pb and Sn-3.5Ag solders with Ni-P metallization. *Acta Materialia*, 52, 2047-2056.

He, M., Kumar, A., Yeo, P.T., Qi, G.J., and Chen, Z. (2004b). Interfacial Reaction between Sn-Rich Solders and Ni-Based Metallization. *Thin Solid Films*, 462-463, 387-394.

He, M., Chen, Z., Qi, G.J., Wong, C.C., and Mhaisalkar, S. (2004c). Effect of post-reflow cooling rate on intermetallic compound formation between Sn-3.5Ag solder and Ni-P under bump metallization. *Thin Solid Films*, 462-463, 363-369.

He, M., Lau, W.H., Qi, G.J., and Chen, Z. (2004d). Intermetallic compound formation between Sn-3.5Ag solder and Ni-based metallization during liquid state reaction. *Thin Solid Films*, 462-463, 376-383.

Hsieh, M. Y., and Huntington, H. B. (1978).Electromigration of copper in lead. *J. Phys. Chem. Solids*, 39, 867-871.

Hsu, Y. C., Shao, T. L., Yang, C. J., and Chen, C. (2003). Electromigration Study in SnAg3.8Cu0.7 Solder Joints on Ti/Cr-Cu/Cu Under-Bump Metallization. *J. Electron. Mater.*, 32, 1222-1227.

Huang, C. S., Duh, J. G., Chen, Y. M., and Wang, J. H. (2003). Effects of Ni Thickness and Reflow Times on Interfacial Reactions between Ni/Cu Under-Bump Metallization and Eutectic Sn-Pb Solder in Flip-Chip Technology. *J. Electron. Mater.*, 32, 89-94.

Hung, K.C., and Chan, Y.C. (2000). Study of Ni_3P Growth Due to Solder Reaction-assisted Crystallization of Electroless Ni-P Metallization. *Journal of Materials Science Letters*, 19, 1755-1757.

Hung, K.C., Chan, Y.C., and Tang, C.W. (2000a). Metallurgical reaction and mechanical strength of electroless Ni-P solder joints for advanced packaging applications. *Journal of Materials Science*: *Materials in Electronics*, 11, 587-593.

Hung, K.C., Chan, Y.C., Tang, C.W., and Ong, H.C. (2000b). Correlation between Ni_3Sn_4 Intermetallics and Ni_3P Due to Solder Reaction-assisted Crystallization of Electroless Ni-P Metallization in Advanced Packages. *Journal of Materials Research*, 15, 2534-2539.

Huntington, H. B., Hu, C. K., and Mei, S. N. (1984). *Diffusion in Solids: Recent Developments*. Ed: M. A. Dayanada and G. E. Murch (Warrendale, PA: TMS), 97-119.

Hwang, C.W., Suganuma, K., Kiso, M., and Hashimoto, S. (2003). Interface microstructures between Ni-P alloys plating and Sn-Ag-(Cu) lead-free solders. *J. Mater. Res.*, 18, 2540-2543.

Islam, M. N., Chan, Y. C., Sharif, A., and Alam, M. O. (2003). Comparative study of the dissolution kinetics of electrolytic Ni and electroless Ni-P by the molten Sn3.5Ag0.5Cu solder alloy. *Microelectronics Reliability*, 43, 2031-2037.

Jang, J.W., Frear, D.R., Lee, T.Y., and Tu, K.N. (2000a). Morphology of interfacial reaction between lead-free solders and electroless Ni-P under bump metallization. *Journal of Applied Physics*, 88, 6359-6363.

Jang, J.W., Kim, P.G., Tu, K. N., Frear, D. R., and Thompson, P. (1999). Solder reaction-assisted crystallization of electroless Ni-P under bump metallization in low cost flip chip technology. *J. Appl. Phys.*, 85, 8456-8463.

Jeon, Y.D., and Paik, K.W. (2002). Stresses in Electroless Ni–P Films for Electronic Packaging Applications. *IEEE Trans. Comp. Packag. Technol.*, 25, pp.169.

Jeon, Y. D., Paik, K. W., Bok, K. S., Choi, W. S., and Cho, C. L. (2001). Studies on Ni-Sn Intermetallic Compound and P-rich Layer at the Electroless Nickel UBM-Solder Interface and Their Effects on Flip Chip Solder Joint Reliability. In: *Proc. 51st Electron. Comp. Technol. Conf., IEEE, New York,* 1326-1332.

Jeon, Y.D., Paik, K.W., Bok, K.S., Choi, W.S., and Cho, C.L. (2002). Studies of Electroless Nickel Under Bump Metallurgy - Solder Interfacial Reactions and Their Effects on Flip Chip Solder Joint Reliability. *Journal of Electronics Materials*, 31, pp.520.

Jeon, Y.D., Nieland, S., Ostmann, A., Reichl, H., and Paik, K.W. (2003a). Study on Interfacial Reactions between Electroless Ni-P Under Bump Metallization and 95.5Sn-4.0Ag-0.5Cu Alloy. *Journal of Electronic Materials*, 32, 548-557.

Jeon, Y. D., Ostmann, A., Reichl, H., and Paik, K. W. (2003b). Comparison of Interfacial Reactions and Reliabilities of Sn3.5Ag, Sn4.0Ag0.5Cu, and Sn0.7Cu Solder Bumps on Electroless Ni-P UBMs. In: *Proc. IEEE Electron. Comp. Technol. Conf., New Orleans*, 1203-1208.

Kawashima, K., Ito, T., and Sakuragi, M. (1992). Strain-rate and temperature-dependent stress-strain curves of Sn-Pb eutectic alloy. *J. Mater. Sci.*, 28, 6387-6390.

Kim, H.K., and Tu, K.N. (1996). Kinetic analysis of the soldering reaction between eutectic SnPb alloy and Cu accompanied by ripening. *Physical Review B*, 53, 16027-16034.

Kim, H.K., Tu, K.N., and Totta, P.A. (1996). Ripening-assisted asymmetric spalling of Cu-Sn compound spheroids in solder joints on Si wafers. *Journal of Applied Physics*, 68, 2204-2206.

Kim, P. G., Jang, J. W., Lee, T. Y., and Tu, K. N. (1999). Interfacial reaction and wetting behavior in eutectic SnPb solder on Ni/Ti thin films and Ni foils. *Journal of Applied Physics*, 86, 6746-6751.

Koppenaal, T.J., and Simcoe, C.R. (1963). The effect of electric current on the aging of an Al–4wt.%Cu alloy. *Transactions of the AIME*, 227, 615–617.

Kubaschewski, O., Alcock, C. B., and Spencer, P. J. (1993) *Materials Thermo-chemistry*, 6th Edition, Pergamon Press, New York.

Kulojarvi, K., Vuorinen, V., and Kivilahti, J. (1998). Effect of dissolution and intermetallic formation on the reliability of FC joints. *Microelectronics International*, 15, 20-24.

Kumar, K.M., Kripesh, V., Shen, L., Zeng, K., and Tay, A.A.O. (2006). Nanoindentation study of Zn-based Pb free solders used in fine pitch interconnect applications. *Mater. Sc. Eng. A*, 423, 57-63.

Lai, Z.H., Conrad, H., Chao, Y.S., Wang, S.Q., and Sun, J. (1989). Effect of electropulsing on the microstructure and properties of iron-based amorphous-alloys. *Scripta Metallurgica*, 23, 305–310.

Lai, Z.H., Chao, Y.S., Conrad, H., and Chu, K. (1995). Hyperfine-structure changes in iron-base amorphous-alloys produced by high current density electropulsing. *Journal of Materials Research*, 10, 900–906.

Lau, J.H. (1996). *Flip chip technologies*. McGraw-Hill.

Lee, T.Y., Choi, W.J., Tu, K.N., and Jang, J.W. (2002). Morphology, kinetics, and thermodynamics of solid-state aging of eutectic SnPb and Pb-free solders (Sn–3.5Ag, Sn–3.8Ag–0.7Cu and Sn–0.7Cu) on Cu. *J. Mater. Res.*, 17, 291-301.

Lee, C.Y., and Lin, K.L. (1994). The interaction kinetics and compound formation between electroless Ni-P and solder. *Thin Solid Films*, 249, 201-206.

Lee, C.Y., and Lin, K.L. (1995). Bonding fracture mechanism between SnPb solder and electroless nickel alloy deposits. In: *Proc. of INTERpack 95*, 2, 26-30.

Lee, T. Y., Tu, K. N., and Frear, D. R. (2001a). Electromigration of eutectic SnPb and $SnAg_{3.8}Cu_{0.7}$ flip chip solder bumps and under-bump metallization. *J. Appl. Phys.*, 90, 4502-4508.

Lee, T. Y., Tu, K. N., Kuo, S. M., and Frear, D. R. (2001b). Electromigration of eutectic SnPb solder interconnects for flip chip technology. *J. Appl. Phys.*, 89, 3189-3194.

Li, H., Chen, H., Dong, S., Yang, J., and Deng, J.F. (1998). Study on the crystallization process of Ni-P amorphous alloy. *Applied Surface Science*, 125, 115-119.

Lifshitz, I. M., and Slyozov, V. V. (1961). The kinetics of precipitation from supersaturated solid solutions. *J. Phys. Chem. Solids*, 19, 35-50.

Lin, K.L., and Liu, Y.C. (1999). Reflow and property of Al/Cu/Electroless Nickel/Sn-Pb solder bumps. *IEEE Transactions on Advanced Packaging*, 22, 568-574.

Liu, W. C., Chen, S. W., and Chen, C. M. (1998). The Al/Ni Interfacial Reactions Under the Influence of Electric Current. *J. Electron. Mater.*, 27, L5-L9.

Liu, C.Y., Chen, C., Liao, C. N., and Tu, K. N. (1999). Microstructure-electromigration correlation in a thin stripe of eutectic SnPb solder stressed between Cu electrodes. *Appl. Phys. Lett.*, 75, 58-60.

Liu, C. Y., Chen, C., Liao, C. N., and Tu, K. N. (2000a). Electromigration in Sn-Pb solder strips as a function of alloy composition. *J. Appl. Phys.*, 88, 5703-5709.

Liu, A.A., Kim, H.K., and Tu, K.N. (1996). Spalling of Cu_6Sn_5 Spheroids in the Soldering Reaction of Eutectic SnPb on Cr/Cu/Au Thin Films. *J. Appl. Phys.*, 80, 2774-2780.

Liu, P.L., Xu, Z., and Shang, J.K. (2000b). Thermal stability of electroless-nickel/solder interface: Part A. Interface chemistry and microstructure. *Metallurgical and Materials Transactions A,* 31, 2857-2866.

Liu, P.L., and Shang, J.K. (2000a). Thermal stability of electroless-nickel/solder interface: Part B. Interfacial fatigue resistance. *Metallurgical and Materials Transactions A*, 31, 2867-2875.

Liu, P.L., and Shang, J.K. (2000b). A comparative fatigue study of solder/electroless-nickel and solder/copper interfaces. *Journal of Materials Research*, 15, 2347-2355.

Lyman, C.E., Newbury, D.E, Goldstein, J.I., Williams, D.B., Romig, A.D., Armstrong, J.T., Echlin, P., Fiori, C.E., Joy, D.C., Lifshin, E., Peters, K.R. (1990). *Scanning Electron Microscopy, X-Ray Microanalysis, and Analytical Electron Microscopy: A Laboratory Workbook*, Plenum Press, New York, 39-40 and 114.

Mallory, G.O., and Hajdu, J.B. (1990). *Electroless Plating: Fundamentals and Applications*. Orlando, FL: Amer. Electroplaters Surf. Finishes Soc., 111-113.

Massalski, T.B. (1986). *Binary alloy phase diagrams*. American Society for Metals, Metals Park, Ohio, ASM International.

Matsuki, H., Ibuka, H., and Saka, H. (2002). TEM observation of interfaces in a solder joint in a semiconductor device. *Science and Technology of Advanced Materials*, 3, 261-270.

Mei, Z., and Dauskardt, R.H. (1999). Reliability of electroless processed thin layered solder joints. In: *Proc. of MRS Spring Meeting Symposium M; Materials Reliability in Microelectronics IX*, 1-6.

Mei, Z., Kaufmann, M., Eslambolchi, A., and Johnson, P. (1998). Brittle Interfacial Fracture of PBGA Packages Soldered on Electroless Nickel/Immersion Gold. In: *Proc. IEEE Electron. Comp. Technol. Conf., New York*, 952-961.

Oliver, W. C., and Pharr, G. M. (1992). An improved technique for determining hardness and elastic modulus using load and displacement sensing indentation experiments. *J. Mater. Res.*, 7, 1564-1583.

Pierce, D. G., and Brusius, P. G. (1997). Electromigration: A Review. *Microelectron. Reliab.*, 37, 1053-1072.

Porter, D. A. and Easterling, K. E. (1991). *Phase Transformations in Metals and Alloys*, Chapman and Hall, London, Chapter 1.

Qualitek (2006). http://www.qualitek.com/ppalloyc.html: Physical property alloy comparison analysis.

Routbort, J. L. (1968). Electromigration in Zinc Single Crystals. *Phys. Rev.*, 176, 796-803.

Ren, F., Nah, J. W., Suh, J. O., Tu, K. N., Xiong, B. S., Xu, L. H., and Pang, J. H. L. (2005). Effect of Electromigration on Mechanical Behavior of Solder Joints. In: *Proceedings of International Symposium on Advanced Packaging Materials: Processes, Properties and Interfaces*, 66-69.

Schaefer, M., Fournelle, R.A., and Liang, J. (1998). Theory for intermetallic phase growth between Cu and liquid Sn-Pb solder based on grain boundary diffusion control. *Journal of Electronic Materials*, 27, 1167.

Sharif, A., Chan, Y. C., Islam, M. N., Rizvi, M. J. (2005). Dissolution of electroless Ni metallization by lead-free solder alloys. *J. Alloys Comp.*, 388, 75-82.

Shao, T. L., Chen. Y. H., Chiu, S. H., and Chen C. (2004). Electromigration failure mechanisms for SnAg 3.5 solder bumps on Ti/Cr-Cu/Cu and Ni(P)/Au metallization pads. *J.*

Appl. Phys., 96, 4518-4524.

Shi, F. X., Cao, L. L., Yao, W. Q., and Ye, X. Y. (2000). Electric field induced interfacial reaction of Au-Ag bimetal film on SiO_2 surface. *J. Mater. Sc.*, 35, 3655-3658.

Sohn, Y. C., Yu, J., Kang, S. K., Choi, W. K., and Shih, D. Y. (2003). Study of the reaction mechanism between electroless Ni-P and Sn and its effect on the crystallization of Ni-P. *J. Mater. Res.*, 18, 4-7.

Sohn, Y. C., Yu, J., Kang, S. K., Shih, D. Y., and Choi, W. K. (2004a). Effects of Phosphorus Content on the Reaction of Electroless Ni-P with Sn and Crystallization of Ni-P. *J. Electron. Mater.*, 33, 790-795.

Sohn, Y. C., Yu, J., Kang, S. K., Shih, D. Y., and Lee, T. Y. (2004b). Spalling of intermetallic compounds during the reaction between lead-free solders and electroless Ni-P metallization. *J. Mater. Res.*, 19, 2428-2436.

Sohn, Y. C., Yu, J., Kang, S. K., Shih, D. Y., and Lee, T. Y. (2005). Effect of Intermetallics Spalling on the Mechanical Behavior of Electroless Ni(P)/Pb-free Solder Interconnection. In: *Proc. IEEE Electronic Components and Technology Conference*, 83-87.

Stepniak, F. (1997). Solder flip chip employing electroless nickel: An evaluation of reliability and coast. In: *Proc. Advances in Electronic Packaging, ASME, New York*, 1, 353-358.

Sullivan, G. A. (1967). Electromigration and Thermal Transport in Sodium Metal. *Phys. Rev.*, 154, 605-613.

Takemoto, T., and Matsunawa, A. (1997). Tensile test for estimation of thermal fatigue properties of solder alloys. *Journal of Materials Science*, 32, 4077-4084.

Teng, G.Q., Chao, Y.S., Lai, Z.H., Dong, L. (1996). Microstructural study of the low-temperature nanocrystallization of amorphous Fe78B13Si9. *Physica Status Solidi A-Applied Research*, 156, 265–276.

Tu, K.N., Gusak, A. M., and Li, M. (2003). Physics and materials challenges for lead-free solders. *J. Appl. Phys*., 93, 1335-1353.

Tu, K.N., Ku, F., and Lee, T.Y. (2001a). Morphology stability of solder reaction products in flip chip technology. *Journal of Electronic Materials*, 30, 1129-1132.

Tu, K.N., Lee, T.Y., Jang, J.W., Li, L., and Frear, D.R. (2001b). Wetting reaction versus solid state aging of eutectic SnPb on Cu. *Journal of Applied Physics*, 89, 4843-4849.

Tu, K.N., and Zeng, K. (2001). Tin-lead (SnPb) solder reaction in flip chip technology. *Materials Science and Engineering R*, 34, 1-58.

Tummala, R.R. (2001). *Fundamentals of Microsystems packaging*. McGraw Hill, New York,1-12 and 391.

Vafaei-Makhsoos, E. (1980). Electron diffraction study of newly discovered nickel phosphides in partially crystallized amorphous electrodeposited Ni-P thin films. *J. Appl. Phys.*, 51, 6366-6376.

Vanhecke, B., Schepper, L. D., Ceuninck, W. D., Haeger, V. D., Olieslaegers, M. D., Beyne, E., Roggen, J., and Stals, L. (1993). Electromigration: Investigation of heterogeneous systems. *Microelectron. Reliab.*, 33, 1141-1157.

Vianco, P.T. (1999). *Soldering Handbook*. 3rd Edition, American Welding Society, FL.

Wang, S.J., and Liu, C.Y. (2003). Retarding growth of Ni_3P crystalline layer in Ni(P) substrate by reacting with Cu-bearing Sn(Cu) solders. *Scripta Materialia*, 49, 813-818.

WEEE (2000). *Directive of The European Parliament And of The Council on Waste Electrical and Electronic Equipment, on the restriction of the use of certain hazardous substances in electrical and electronic equipment, Commission of The European Communities*. Brussels, June 13, 59-83.

Xu, L., and Pang, J. H. L. (2006, in press). Nanoindentation on SnAgCu lead-free solder joints and analysis. *J. Electron. Mater.*.

Yao, D.P., and Shang, J.K. (1996). Effect of cooling rate on interfacial fatigue-crack growth in Sn-Pb solder joints. *IEEE Trans. Comp. Packag. Manu. Technol. Part B*, 19, 154-165.

Ye, H., Basaran, C., and Hopkins, D. C. (2003a). Thermomigration in Pb-Sn solder joints under joule heating during electric current stressing. *Appl. Phys. Lett.*, 82, 1045-1047.

Ye, H., Basaran, C., and Hopkins, D. C. (2003b). Damage mechanics of microelectronics solder joints under high current densities. *International Journal of Solids and Structures*, 40, 4021-4032.

Ye, H., Basaran, C., and Hopkins, D. C. (2004). Pb phase coarsening in eutectic Pb/Sn flip chip solder joints under electric current stressing. *International Journal of Solids and Structures*, 41, 2743-2755.

Yeh, E. C. C., Choi, W. J., Tu, K. N., Elenius, P., and Balkan, H. (2002). Current-crowding-induced electromigration failure in flip chip solder joints. *Appl. Phys. Lett.*, 80, 580-582.

Yeh, E. C. C., and Tu, K. N. (2000). Numerical simulation of current crowding phenomena and their effects on electromigration in very large scale integration interconnects. *J. Appl. Phys.*, 88, 5680-5686.

Yokomine, K., Shimizu, N., Miyamoto, Y., Iwata, Y., Love, D., and Newman, K. (2001). Development of electroless Ni/Au plated build-up flip chip package with high reliable solder joints. In: *Proc. of IEEE Electronic Components and Technology Conference*, 346-352.

Yoon, J. W., and Jung, S. B. (2004). Growth kinetics of Ni_3Sn_4 and Ni_3P layer between Sn-3.5Ag solder and electroless Ni-P substrate. *J. Alloys Comp.*, 376, 105-110.

Yoon, J. W., and Jung, S. B. (2005). Interfacial reaction between Sn-0.4Cu solder and Cu substrate with or without ENIG plating layer during reflow reaction. *J. Alloys Comp.*, 396, 122-127.

Yoon J. W., Kim, S. W., and Jung, S. B. (2004). Effect of reflow time on interfacial reaction and shear strength of Sn-0.7Cu solder/Cu and electroless Ni-P BGA joints. *J. Alloys Comp.*, 385, 192-198.

Yoon, J. W., Lee, C. B., and Jung, S. B. (2003). Growth of an Intermetallic Compound Layer with Sn-3.5Ag-5Bi on Cu and Ni-P/Cu during Aging Treatment. *J. Electron. Mater.*, 32, 1195-1202.

Yoon, S.W., Park, C.J., Hong, S.H., Moon, J.T., Park, I.S., and Chun, H.S. (2000). Interfacial reaction and solder joint reliability of Pb-free solders in lead frame chip scale packages (LF-CSP). *Journal of Electronic Materials*, 29, 1233-1240.

Yu, H.S., Luo, S.F., and Wang, Y.R. (2001). A comparative study on the crystallization behavior of electroless Ni–P and Ni–Cu–P deposits. S*urface and Coatings Technology*, 148, 143-148.

Zeng, K., and Tu, K. N. (2002). Six cases of reliability study of Pb-free solder joints in electronic packaging technology. *Materials Science and Engineering R*, 38, 55-105.

Zeng, K.J., Vuorinen, V., and Kivilahti, J.K. (2002). Interfacial reactions between lead-free SnAgCu solder and Ni(P) surface finish on printed circuit boards. *IEEE Trans. Electron. Packag. Manuf.*, 25, 162-169.

Zeng, K., Stierman, R., Chiu, T. C., Edwards, D., Ano, K., and Tu, K. N. (2005). Kirkendall void formation in eutectic SnPb solder joints on bare Cu and its effect on joint reliability. *J. Appl. Phys.*, 97, 024508-024516.

List of Publications

1. **Kumar, A.**, Chen, Z., Mhaisalkar, S. G., Wong, C. C., Teo, P. S., and Kripesh, V. (2006). Effect of Ni-P thickness on solid-state interfacial reactions between Sn-3.5Ag solder and electroless Ni-P metallization on Cu substrate. *Thin Solid Films*, 504, 410-415.
2. **Kumar, A.,** and Chen, Z., (2006). Influence of solid-state interfacial reactions on the tensile strength of Cu/Electroless Ni-P/Sn-3.5Ag solder joint. *Mater. Sc. Eng. A*, 423, 175-179.
3. **Kumar**, **A.,** He, M., and Chen, Z. (2005). Barrier properties of thin Au/Ni-P under bump metallization for Sn-3.5Ag solder. *Surf. Coat. Technol.*, 198, 283-286.
4. **Kumar**, **A.,** He, M., Chen, Z., and Teo, P. S. (2004). Effect of electromigration on interfacial reactions between electroless Ni-P and Sn-3.5%Ag solder. *Thin Solid Films*, 462-463, 413-418.
5. He, M., **Kumar**, **A.,** Yeo, P. T., Qi, G. J., and Chen, Z. (2004). Interfacial reaction between Sn-rich solders and Ni-based metallization. *Thin Solid Films*, 462-463, 387-394.
6. **Kumar, A.,** and Chen, Z. (2006). Effect of Ni-P Thickness on the Tensile Strength of Cu/Electroless Ni-P/Sn-3.5Ag Solder Joint. *IEEE Trans. Comp. Packag. Technol.*, 29, 886-892.
7. **Kumar**, **A.,** Chen, Z., Wong, C. C., Mhaisalkar, S. G., and Kripesh, V. (2006). Effect of Electric Current on the Mechanical Properties and Interfacial Microstructure of Ni-P/Sn-3.5Ag and Ni/Sn-3.5Ag Solder Joints. *Proc. 8th Electron. Packag. Technol. Conf.,* IEEE, Singapore, 203-210.
8. **Kumar**, **A.,** Chen, Z., Wong, C. C., and Kripesh, V. (2006). Influence of Electric Current on the Mechanical Properties and Microstructure of Solder Joints. *Proc. International Conf. Mater. Processing Properties Performance (MP3),* Singapore, 5, 72-74.
9. **Kumar**, **A.,** Chen, Z., Wong, C. C., Mhaisalkar, S. G., and Kripesh, V. (2007). Factors Affecting the Mechanical Properties of Cu/electroless Ni-P/Sn-3.5Ag Solder Joint. *Proc. of MRS 2006 Fall meeting*, Boston, MA, USA, 968, 0968-V04-04.
10. **Kumar**, **A.,** Chen, Z., Wong, C. C., Mhaisalkar, S. G., and Kripesh, V. (2007). Electric Current Induced Brittle Failure of Lead and Lead-free Solder Joints with Electroless Ni-P Metallization. *Proc. MRS 2006 Fall meeting*, Boston, MA, USA, 968, 0968-V05-06.

11. Chen, Z., He, M., **Kumar, A.,** and Qi, G. J. (2007). Effect of Interfacial Reaction on the Tensile Strength of Sn-3.5Ag/Ni-P and Sn-37Pb/Ni-P Solder Joints. *J. Electron. Mater.*, 36, 17-25.
12. Chen, Z., **Kumar**, **A.,** and Mona (2006). Effect of Phosphorus Content on Cu/Ni-P/Sn-3.5Ag Solder Joint Strength after Multiple Reflow. *J. Electron. Mater.*, 35, 2126-2134.
13. Mona, **Kumar**, **A.,** and Chen, Z. (2007). Influence of Phosphorus Content on the Interfacial Microstructure between Sn-3.5Ag Solder and Electroless Ni-P Metallization on Cu Substrate. *IEEE Trans. Adv. Packag.*, 30, 68-72.

Appendix A

Typical Load-Extension Curves

Typical load-extension curves of the samples having 9.9 μm thick Ni-P layer and aged for 225 h at different temperatures are shown in Fig. A.1. These curves help in identifying the failure mode of Cu/Ni-P/Sn-3.5Ag solder joint. A clear difference can be seen in the shape of load-extension curves and the extensions in solder joint, indicating the ductile and brittle failure of the solder joint.

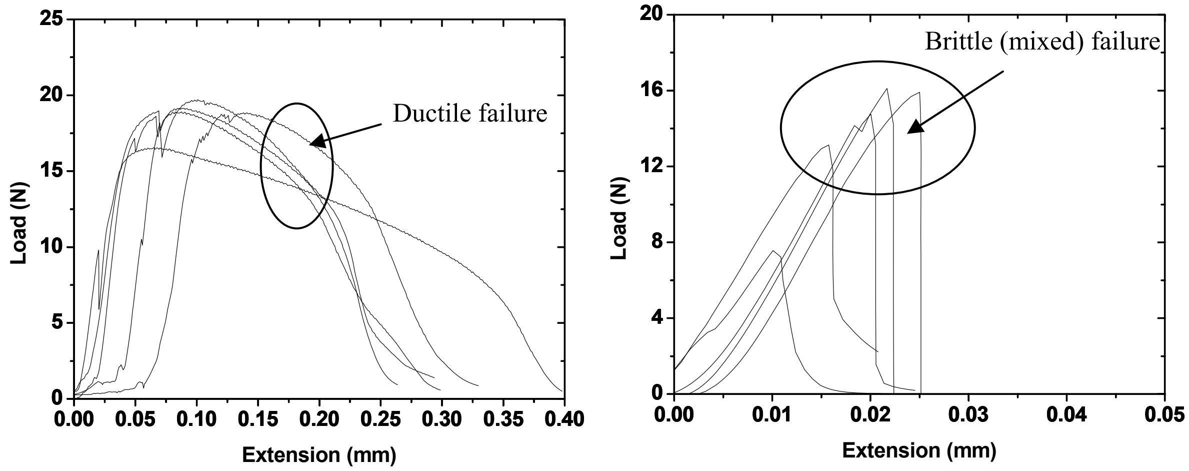

(a) 160 °C

(b) 180 °C

(c) 200 °C

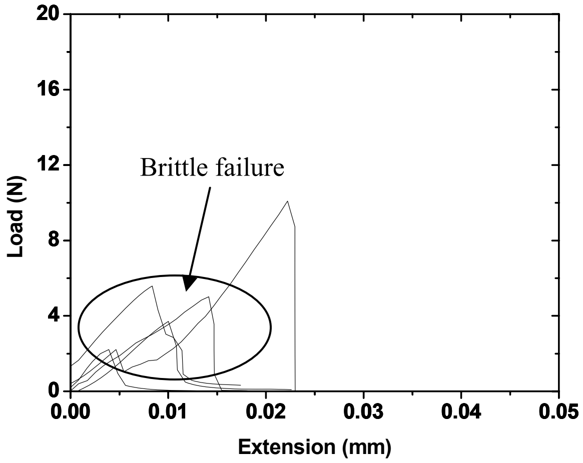

Fig. A.1. Load-extension curves of the samples having 9.9 μm thick Ni-P layer and aged for 225 h at (a) 160 °C, (b) 180 °C, and (c) 200 °C, showing ductile and brittle failures.

Fig. A.2 shows the typical load-extension curves of the samples having Ni-P layers of different thicknesses. The area under these load-extension curves has been reported in the Fig. 4.8.

(a) 3.9 µm Ni-P

(b) 7.3 µm Ni-P

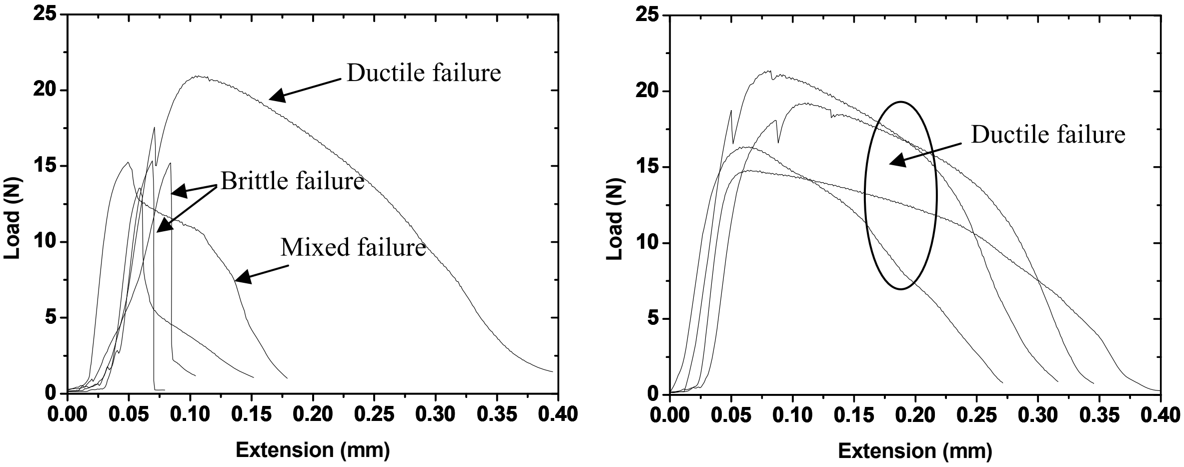

(c) 9.9 µm Ni-P

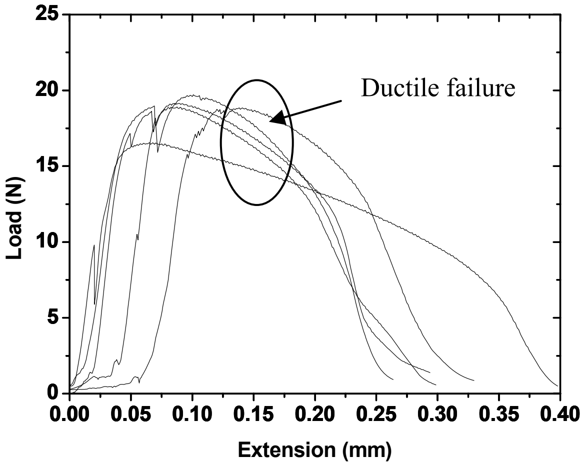

Fig. A.2. Load-extension curves of the samples aged at 160°C for 225 h and having (a) thin (3.9 µm), (b) medium (7.3 µm), and (c) thick (9.9 µm) Ni-P layers, showing ductile, mixed and brittle failures.

Appendix B

Quantitative EDS Analysis

This section describes quantitative EDS analysis in the SEM to yield the elemental composition of different compounds. On-line processing of EDS data from unknown and simple standards can yield quantitative analysis with detection limits of around 0.1 wt% and relative error of ± 3 % (Lyman *et al.*, 1990). The basis for quantitative EDS analysis is that (Lyman *et al.*, 1990; Goldstein *et al.*, 1992):

$$\frac{C_i}{C_{(i)}} \propto \frac{I_i}{I_{(i)}} = k_i \qquad \text{(B.1)}$$

where C_i and $C_{(i)}$ are the composition in weight concentration of element i in the specimen (unknown) and in the standard, respectively. I_i and $I_{(i)}$ are the measured characteristic x-ray intensity for i element in the specimen and in the standard, respectively, and their ratio, $I_i/I_{(i)}$ is called as "k ratio". The proportionality sign in equation B.1 indicates that the relationship between concentration and intensity is not exact. In most quantitative chemical analyses, the measured intensities from specimen and standard need to be corrected for differences in electron backscattering, density, and X-ray energy loss and absorption within the solid in order to get the proportionality constant between the intensity ratio and the concentration ratio (Goldstein *et al.*, 1992). These corrections are referred to as matrix corrections. There are a number of types of matrix correction methods, such as "ZAF", "phi or ϕ (ρz)", and "empirical". In present work, ZAF method has been used to determine the elemental composition of compounds and thus it will be discussed in this section. In ZAF method, matrix effects are divided into those due to atomic number, Z; X-ray absorption, A; and X-ray fluorescence, F. Using these matrix effects, the most common form of the correction equation is (Lyman *et al.*, 1990; Goldstein *et al.*, 1992)

$$\frac{C_i}{C_{(i)}} = [ZAF]\frac{I_i}{I_{(i)}} = [ZAF]k_i \qquad \text{(B.2)}$$

Since equation B.2 is the common basis for X-ray microanalysis in the SEM, it is important to develop a good understanding about the origin and procedure of ZAF matrix correction.

B.1. ZAF Factors in X-Ray Microanalysis

The matrix effects Z, A, and F all contribute to the corrections for X-ray microanalysis as given in equation B.2. This section discusses the origin of each of the matrix effects individually.

Atomic Number Effect (Z)

Electrons entering the surface of a specimen both penetrate the specimen and are scattered by it. The effects of these processes on X-ray emission are considered in terms of the two factors R and S (Chandler, 1981). The electrons that are backscattered from the specimen surface do not contribute to X-ray production. The fraction of the incident electrons that enters the sample and remains within it is called R. Specimens of low atomic number produce less backscattering and consequently a higher value of R.

The electrons that penetrate the specimen may cause ionizations, producing X-rays, or they may be scattered within it. The production of X-ray by ionization depends on the critical ionization potential of the specimen and thus on its composition. Elements of low atomic number (Z) have lower critical ionization potential, are more easily ionized, and have greater stopping power per unit mass. The stopping power of the specimen is called as S, and is higher for elements of low atomic number.

The initial energy (E_0) of the electrons affects the values of R and S also. Higher energy electrons may more readily be backscattered and escape from a sample, producing a lower value of *R*, while stopping power of the sample may be reduced, producing a lower value for *S*.

Thus we have *R* and *S* varying inversely with both E_0 and *Z*. This is fortunate since the atomic number correction to be applied depends on the ratio of *R* and *S* as (Chandler, 1981)

$$Z = \frac{R}{S} \tag{B.3}$$

Thus the two factors tend to cancel each other out as both the atomic number and electron accelerating voltage vary. Although the atomic number correction is minimized in this way, it is still important part of the matrix correction.

Absorption Effect (A)

X-rays traveling through a material of density ρ suffer absorption, which can be represented as (Chandler, 1981; Goldstein *et al.*, 1992)

$$\frac{I_t}{I_0} = \exp\left(-\left(\frac{\mu}{\rho}\right).\rho t\right) \tag{B.4}$$

where I_t is the transmitted X-ray intensity, I_0 is the original intensity, μ/ρ is the mass absorption coefficient, and *t* is the distance traveled by the X-rays. The value of μ/ρ depends on the X-ray energy as well as on the composition of the specimen. For a specimen composed of a number of elements the value for μ/ρ is given by the sum of the individual absorption coefficients multiplied by their mass fractions.

X-rays are generated at different depths within a specimen and hence must travel through different distances to leave the sample. They are thus absorbed to different degree. The correction for this absorption, *A*, takes into account the shape of the volume of specimen producing the X-rays, the angle at which the X-rays are collected from the specimen surface, the angle at which the incident electron beam enters the specimen surface, and the composition of the specimen.

Fluorescence Effect (F)

The absorption of X-rays traveling through the sample occurs when the X-ray photons give up their energy in ionizing other atoms (Chandler, 1981). Thus if an X-ray photon of element Z_1 has an emission energy which is slightly more than the energy required to ionize element Z_2, that photon is very likely to be absorbed, and element Z_2 will emit X-ray photons. Thus, if element Z_2 is being measured, its intensity will be raised and its apparent concentration will be artificially increased. The degree of enhancement depends on the relative excitation probability, the fluorescent yield, and the depth of electron penetration and X-ray production within the sample.

In addition, X-ray enhancement may occur due to the fluorescence by the white radiation, the effect being greatest in specimens of high atomic number that produces the greatest bremsstrahlung.

The combination of these parameters makes up the correction factor for fluorescence (F).

B.2. Procedure for ZAF Matrix Correction

The ZAF matrix correction procedure is complex mathematically and thus is carried out on a computer (Chandler, 1981). In the usual experiment, one determines a set of k ratios, but the factors Z, A, and F depend upon the true composition of the specimen, which is unknown. This problem is handled by using the measured k ratios as the first estimate of concentration (Goldstein *et al.*, 1992). In this way,

$$C_i = \frac{k_i}{\sum_i k_i} \qquad \text{(B.5)}$$

for all elements i in the specimen. These first-estimate concentrations are normalized to sum of 100%. The resulting mass fractions are used to compute the initial ZAF factors for each element. The estimated concentrations and ZAF factors for each element are used to calculate k_i values that are then compared to the measured k_i values. Iteration proceeds until results converge.

B.3. Quantitative EDS Analysis using Standard ZAF Correction Method

The most effective strategy for quantitative EDS analysis is to record and archive spectra from standards (pure elements or simple compounds) under standardized electron beam and X-ray spectrometer conditions (Lyman *et al.*, 1990). The archived standard spectra may be used to process X-ray spectra from the specimen to calculated k ratio. The ZAF matrix correction method may then be applied to the k ratio to produce the final measured composition.

In present work, EDS results were analyzed using standard ZAF matrix correction method to determine the chemical composition of compounds. This section includes the experimental procedure as well as the results of the quantitative EDS analysis.

B.3.1. Experimental Procedures for Standard ZAF Correction Method

The following steps were followed to analyze the EDS results using standard ZAF matrix correction method:

1. Preparation of standards: Pure (99.9 wt%) Ni, Sn, and Cu metals and GaP compound were used as standards for Ni, Sn, Cu, and P to do standard ZAF quantitative analysis. These standards were prepared in the same way as the specimens were prepared for EDS analysis. Sample preparation method for EDS analysis has been described in the section 3.2.4 of chapter 3. It should be noted that the samples for EDS analysis were not etched as etching causes a rough surface and rough surface may cause an error in the acquisition of EDS spectra (Lyman *et al.*, 1990).
2. EDS spectrum acquisition from the standard: In standard ZAF quantitative analysis

the EDS operating condition are kept same for recording the spectra of standards and specimen. As our SEM system did not have probe current detector (PCD) system, the probe current was calibrated manually. For this purpose, a stable metal sample known as “calibration sample” is normally used. In present work, Cu was used as “calibration sample” and following steps were followed to acquire standards spectra:

   a. The calibration sample was mounted in sample holder along with standards.
   b. Acquisition conditions selected were as 20.0 kV accelerating voltage, 10 mm working distance, 60 sec real time, 90.0 deg incidence angle, 35.0 deg. take-off angle, and 0.0 deg tilt.
   c. The spot size was adjusted at a fix value using the calibration Cu sample to achieve 30% dead time or 1600 cps.
   d. 1nA probe current was selected as an acquisition condition.
   e. Acquired standard spectrum from pure Cu, Ni, Sn and GaP and then registered it. During registration, a standard file will be created automatically in the computer for standard analysis. Fig. B.1 shows the spectra from different standards acquired and used in the present work.

3. EDS spectrum acquisition from the specimen: The EDS spectrum acquisition procedure for specimen was the same as of standard. Different locations of the samples subjected to different experimental conditions were analyzed to determine the chemical compositions of compounds. After acquiring the EDS spectrum from the specimen (Fig. B.2), analytical software was used to do standard ZAF matrix correction by selecting appropriate options as shown in Fig. B.3a. The same software can be used for standardless ZAF matrix correction (Fig. B.3b).

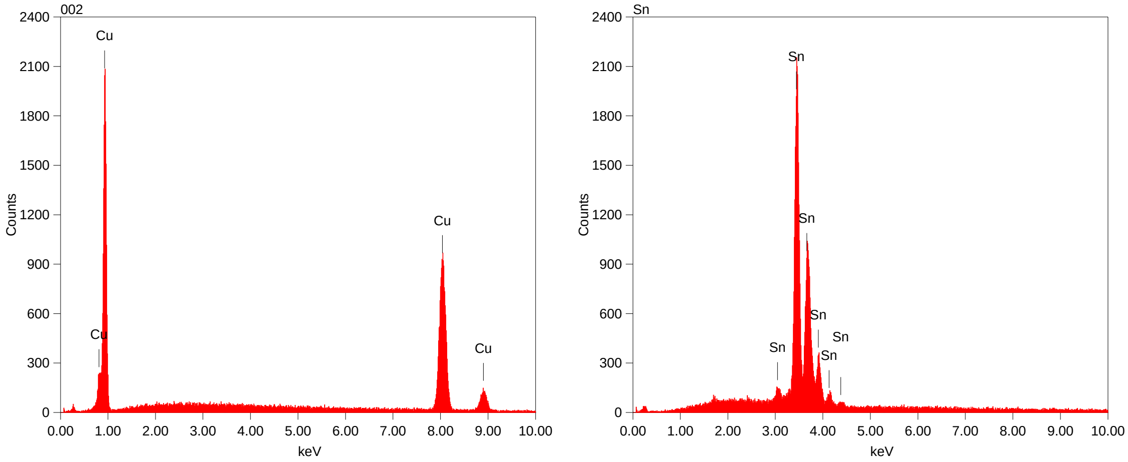

(a) Cu Standard

(b) Sn Standard

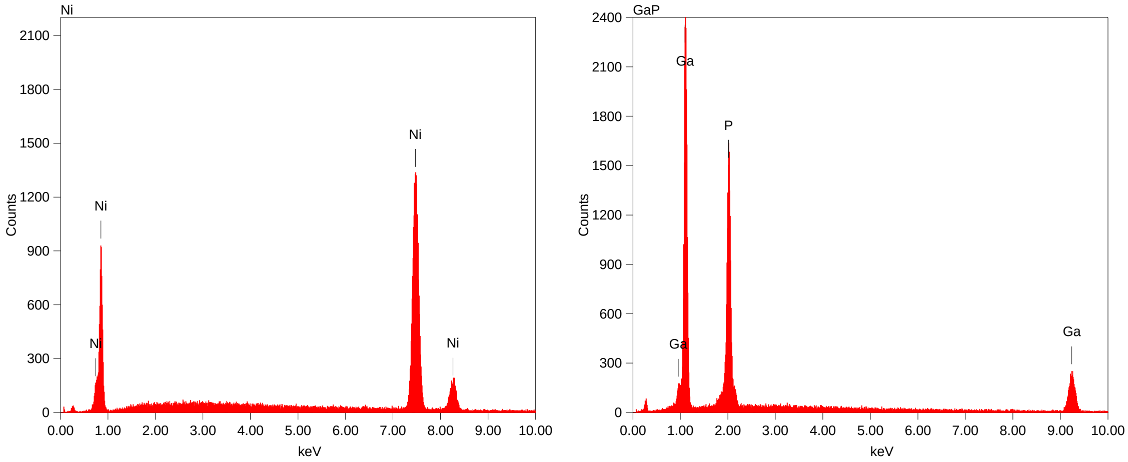

(c) Ni Standard

(d) GaP Standard

Fig. B.1. EDS spectra from (a) pure Cu, (b) pure Sn, (c) pure Ni, and (d) GaP standards.

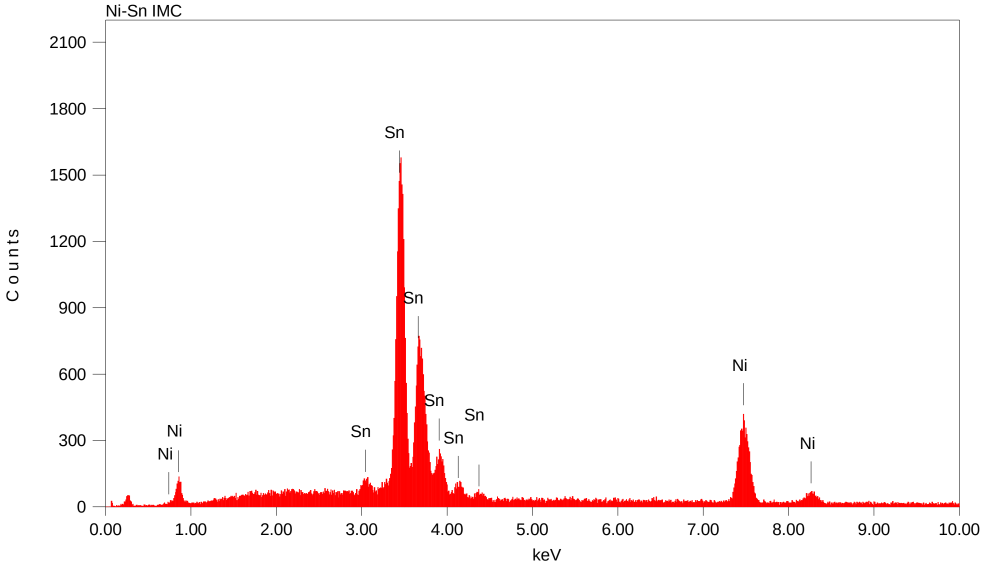

Fig. B.2. EDS spectrum from the Ni/Sn-3.5Ag sample aged at 160 °C for 100 h showing formation of Ni-Sn IMC.

(a)

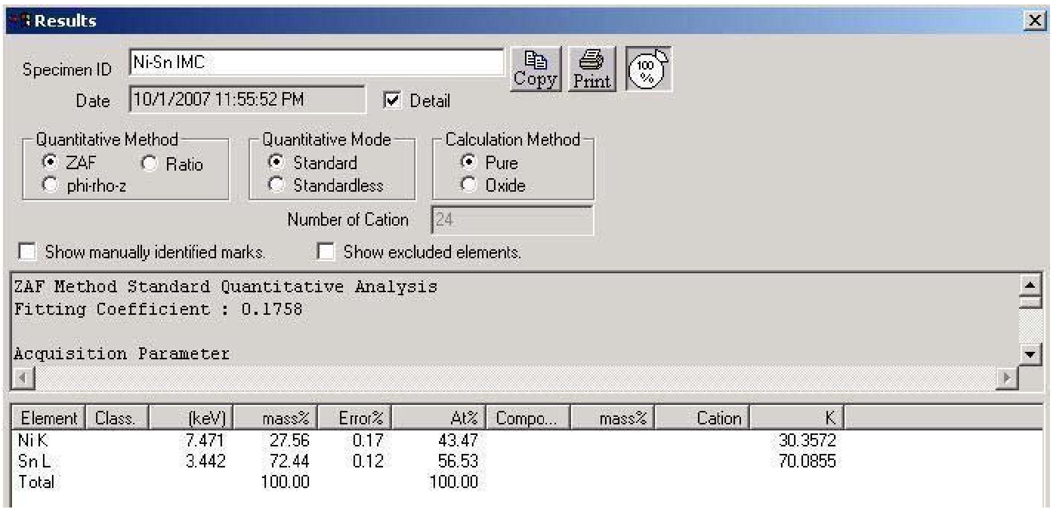

Specimen ID: Ni-Sn IMC

Date: 10/1/2007 11:55:52 PM

☑ Detail

Quantitative Method: ● ZAF ○ Ratio ○ phi-rho-z

Quantitative Mode: ● Standard ○ Standardless

Calculation Method: ● Pure ○ Oxide

Number of Cation: 24

☐ Show manually identified marks. ☐ Show excluded elements.

```
ZAF Method Standard Quantitative Analysis
Fitting Coefficient : 0.1758

Acquisition Parameter
```

Element	Class.	(keV)	mass%	Error%	At%	Compo...	mass%	Cation	K
Ni K		7.471	27.56	0.17	43.47				30.3572
Sn L		3.442	72.44	0.12	56.53				70.0855
Total			100.00		100.00				

(b)

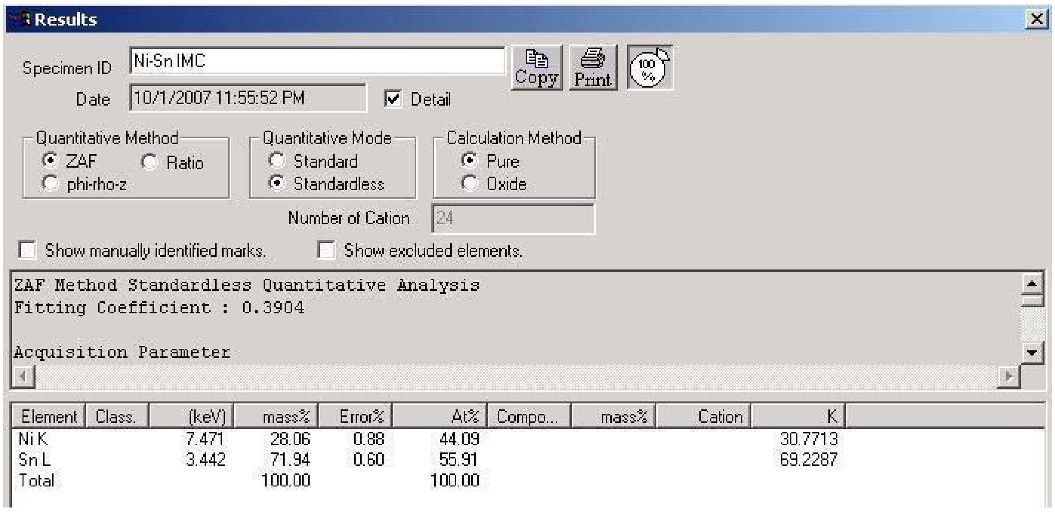

Specimen ID: Ni-Sn IMC

Date: 10/1/2007 11:55:52 PM

☑ Detail

Quantitative Method: ● ZAF ○ Ratio ○ phi-rho-z

Quantitative Mode: ○ Standard ● Standardless

Calculation Method: ● Pure ○ Oxide

Number of Cation: 24

☐ Show manually identified marks. ☐ Show excluded elements.

```
ZAF Method Standardless Quantitative Analysis
Fitting Coefficient : 0.3904

Acquisition Parameter
```

Element	Class.	(keV)	mass%	Error%	At%	Compo...	mass%	Cation	K
Ni K		7.471	28.06	0.88	44.09				30.7713
Sn L		3.442	71.94	0.60	55.91				69.2287
Total			100.00		100.00				

Fig. B.3. ZAF (a) standard and (b) standardless quantitative analyses of Ni-Sn spectrum from the sample aged at 160 °C for 100 h, indicating the formation of Ni_3Sn_4 IMC.

B.3.2. Quantitative EDS Analyses of Compounds Observed in Present Study

Fig. B.4 shows the SEM images of the Sn-3.5Ag/Ni-P/Cu interfaces of the samples having 9.9 μm electroless Ni-P layer and aged at different experimental conditions. The quantitative EDS analyses (with standard ZAF matrix correction) of the compounds formed at the interfaces were carried out and the results are shown in Fig. B.5. The elemental compositions of these compounds indicate the formation of Ni_3Sn_4, Ni_3P, and Ni_2SnP phases.

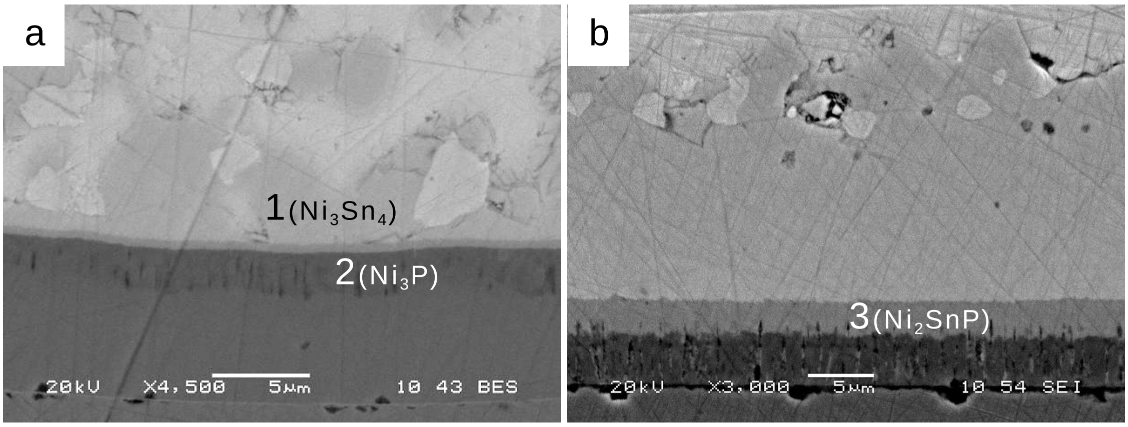
a
1(Ni$_3$Sn$_4$)
2(Ni$_3$P)
20kV X4,500 5µm 10 43 BES
b
3(Ni$_2$SnP)
20kV X3,000 5µm 10 54 SEI

Fig. B.4. SEM images of the Sn-3.5Ag/Ni-P/Cu interfaces of the samples having 9.9 µm electroless Ni-P layer and aged at (a) 160 °C for 400 h and (b) 200 °C for 100 h.

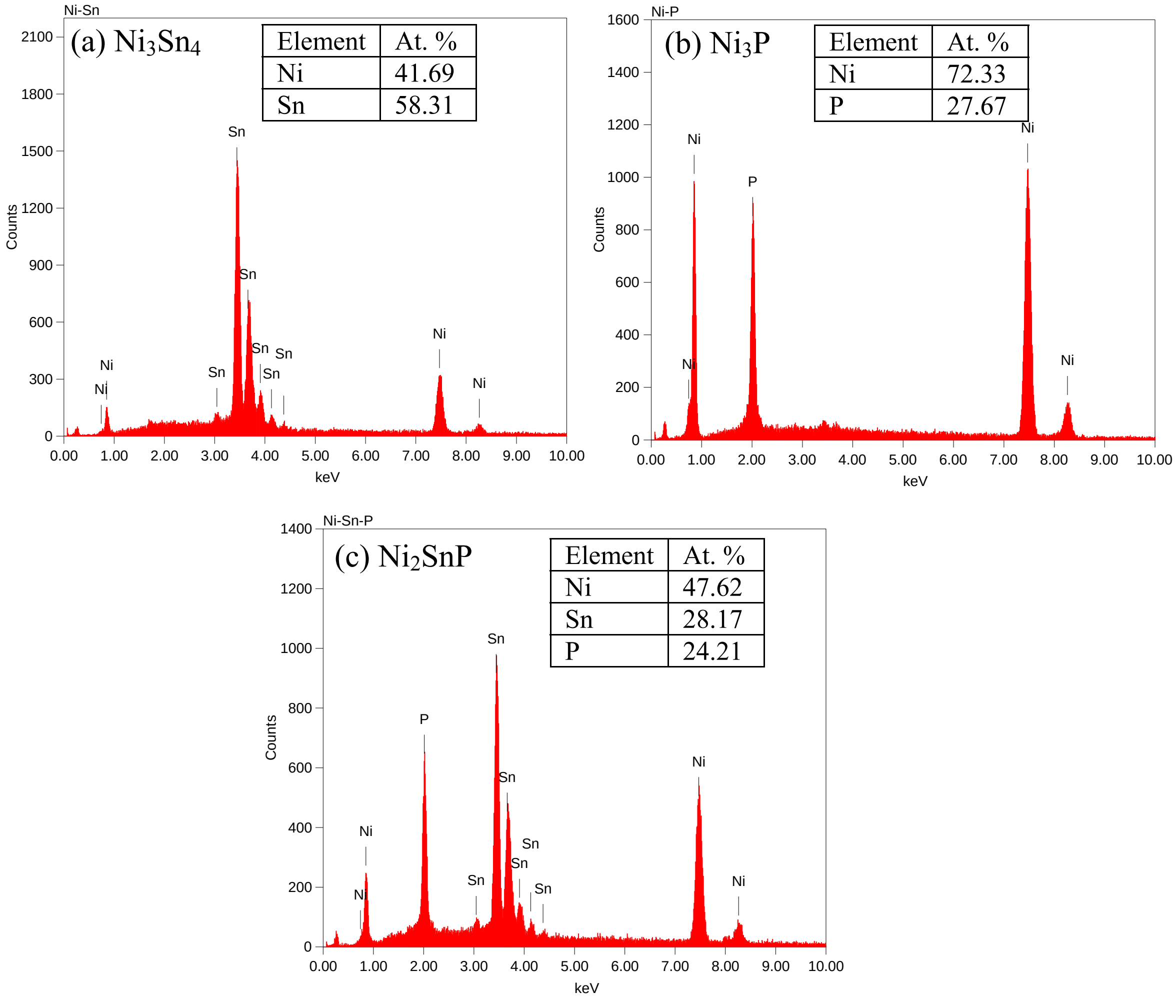

(a) Ni$_3$Sn$_4$

Element	At. %
Ni	41.69
Sn	58.31

(b) Ni$_3$P

Element	At. %
Ni	72.33
P	27.67

(c) Ni$_2$SnP

Element	At. %
Ni	47.62
Sn	28.17
P	24.21

Fig. B.5. EDS analyses of the points (a) 1, (b) 2, and (c) 3 that shown in the Fig B.4, indicating the formation of Ni$_3$Sn$_4$, Ni$_3$P, and Ni$_2$SnP phases, respectively.

Fig. B.6 shows the SEM image of the Sn-3.5Ag/Ni-P/Cu interfaces of the sample having 3.9 µm electroless Ni-P layer and aged at 200 °C for 400h. The EDS analyses of the points 1, 2, 3, and 4 that shown in the Fig. B.6 clearly indicate the formation of $(Ni_{1-x}Cu_x)_3Sn_4$, $(Ni_{1-x}Cu_x)_6Sn_5$, Cu_6Sn_5, Cu_3Sn IMCs, respectively.

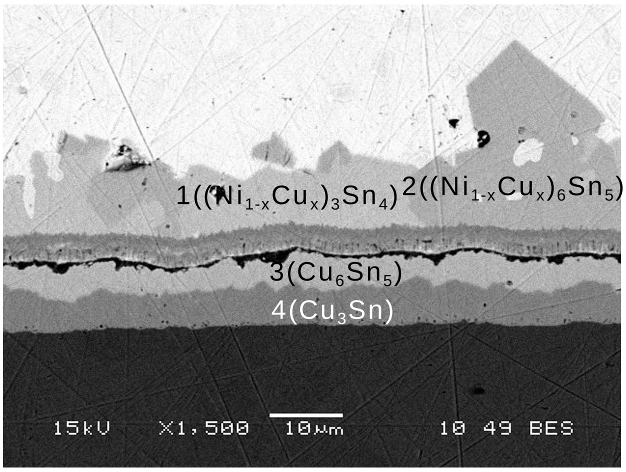
1((Ni$_{1-x}$Cu$_x$)$_3$Sn$_4$)
2((Ni$_{1-x}$Cu$_x$)$_6$Sn$_5$)
3(Cu$_6$Sn$_5$)
4(Cu$_3$Sn)
15kV X1,500 10μm 10 49 BES

Fig. B.6. SEM image of the Sn-3.5Ag/Ni-P/Cu interfaces of the sample having 3.9 μm electroless Ni-P layer and aged at 200 °C for 400 h.

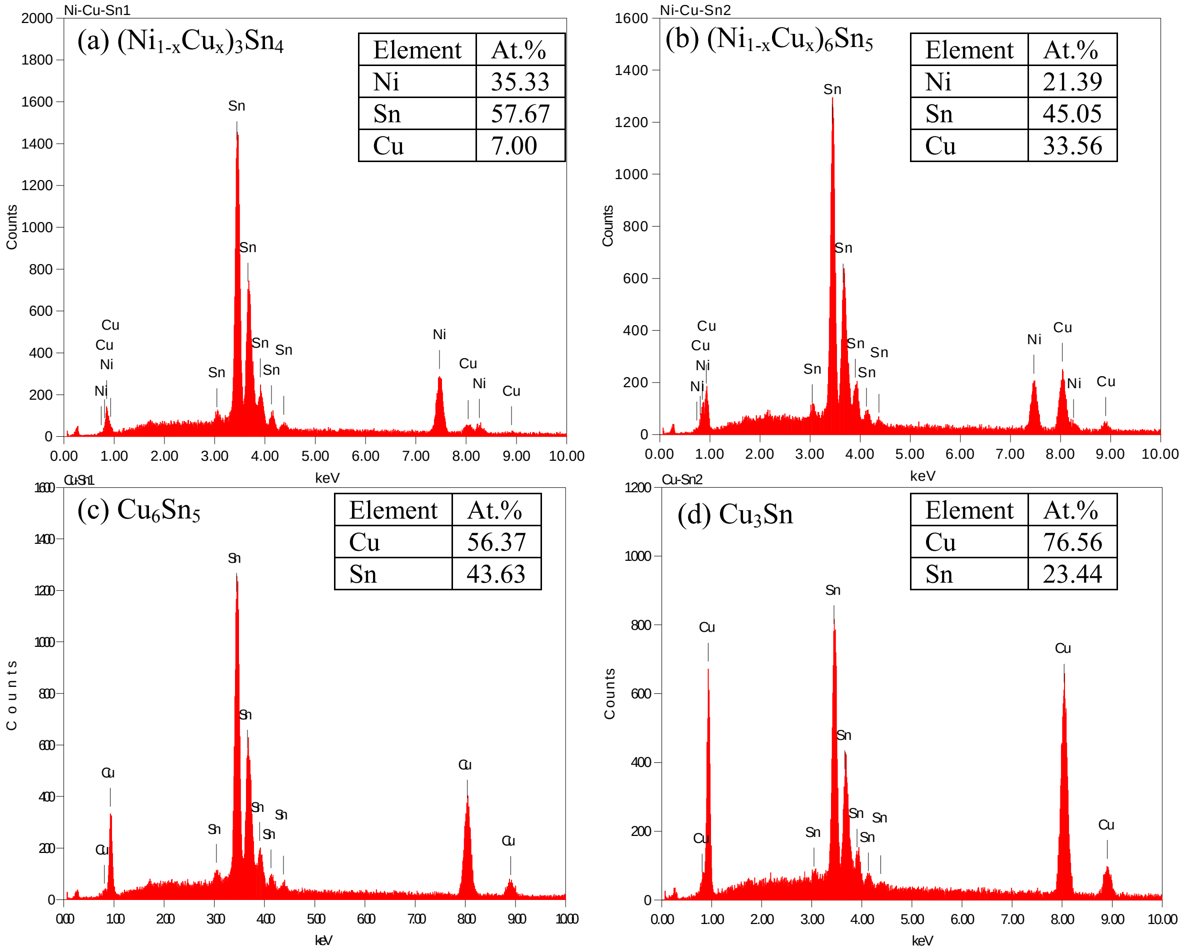

(a) $(Ni_{1-x}Cu_x)_3Sn_4$

Element	At.%
Ni	35.33
Sn	57.67
Cu	7.00

(b) $(Ni_{1-x}Cu_x)_6Sn_5$

Element	At.%
Ni	21.39
Sn	45.05
Cu	33.56

(c) Cu_6Sn_5

Element	At.%
Cu	56.37
Sn	43.63

(d) Cu_3Sn

Element	At.%
Cu	76.56
Sn	23.44

Fig. B.7. EDS analyses of the points (a) 1, (b) 2, (c) 3, and (d) 4 that shown in the Fig B.6, indicating the formation of $(Ni_{1-x}Cu_x)_3Sn_4$, $(Ni_{1-x}Cu_x)_6Sn_5$, Cu_6Sn_5, Cu_3Sn IMCs, respectively.

B.3.3. Comparison between the Results from Standard and Standardless ZAF Correction Methods

Table B.1 shows the elemental composition of different compounds that measured using standard and standardless ZAF matrix corrections. From the table it is clear that both standard and standardless ZAF corrections give nearly the same elemental composition and the measured composition is close to the ideal composition (Massalski, 1986) of the compound.

Table B.1. Elemental composition (at.%) of different compounds that measured using standard and standardless ZAF matrix corrections.

Compounds	Elemental composition using standard ZAF method (at.%)	Elemental composition using standardless ZAF method (at.%)
Ni_3Sn_4	41.69% Ni, 58.31% Sn	42.45% Ni, 57.55% Sn
Ni_3P	72.33% Ni, 27.67% P	76.45% Ni, 23.55% P
Ni_2SnP	47.62% Ni, 28.17% Sn, 24.21% P	50.41% Ni, 29.15% Sn, 20.43% P
$(Ni_{1-x}Cu_x)_3Sn_4$	35.33% Ni, 7.0% Cu, 57.67% Sn	36.38% Ni, 6.23% Cu, 57.39% Sn
$(Ni_{1-x}Cu_x)_6Sn_5$	21.39% Ni, 33.56% Cu, 45.05% Sn	22.74% Ni, 31.03% Cu, 46.23 % Sn
Cu_6Sn_5	56.37%Cu, 43.63%Sn	53.99%Cu, 46.01% Sn
Cu_3Sn	76.56% Cu, 23.44% Sn	74.65 % Cu, 25.35% Sn